

The Return Period of Soil Liquefaction

Roy T. Mayfield

A dissertation submitted in partial fulfillment
of the requirements for the degree of

Doctor of Philosophy

University of Washington

2007

Program Authorized to Offer Degree:
Department of Civil and Environmental Engineering

UMI Number: 3252875

INFORMATION TO USERS

The quality of this reproduction is dependent upon the quality of the copy submitted. Broken or indistinct print, colored or poor quality illustrations and photographs, print bleed-through, substandard margins, and improper alignment can adversely affect reproduction.

In the unlikely event that the author did not send a complete manuscript and there are missing pages, these will be noted. Also, if unauthorized copyright material had to be removed, a note will indicate the deletion.

UMI[®]

UMI Microform 3252875

Copyright 2007 by ProQuest Information and Learning Company.

All rights reserved. This microform edition is protected against unauthorized copying under Title 17, United States Code.

ProQuest Information and Learning Company
300 North Zeeb Road
P.O. Box 1346
Ann Arbor, MI 48106-1346

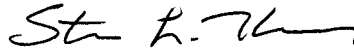
University of Washington
Graduate School

This is to certify that I have examined this copy of a doctoral dissertation by

Roy T. Mayfield

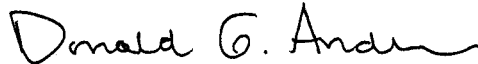
and have found that it is complete and satisfactory in all respects,
and that any and all revisions required by the final
examining committee have been made.

Chair of the Supervisory Committee:



Steven L. Kramer

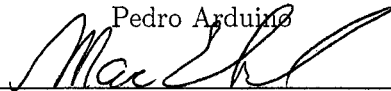
Reading Committee:



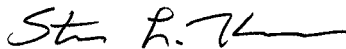
Donald G. Anderson



Pedro Arduini



Marc O. Eberhard



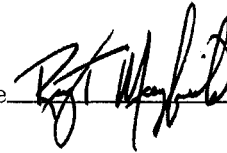
Steven L. Kramer

Date:

FEBRUARY 21, 2007

In presenting this dissertation in partial fulfillment of the requirements for the doctoral degree at the University of Washington, I agree that the Library shall make its copies freely available for inspection. I further agree that extensive copying of this dissertation is allowable only for scholarly purposes, consistent with "fair use" as prescribed in the U.S. Copyright Law. Requests for copying or reproduction of this dissertation may be referred to Proquest Information and Learning, 300 North Zeeb Road, Ann Arbor, MI 48106-1346, 1-800-521-0600, to whom the author has granted "the right to reproduce and sell (a) copies of the manuscript in microform and/or (b) printed copies of the manuscript made from microform."

Signature



Date

FEBRUARY 20, 2007

University of Washington

Abstract

The Return Period of Soil Liquefaction

Roy T. Mayfield

Chair of the Supervisory Committee:

Professor Steven L. Kramer

Department of Civil and Environmental Engineering

Soil liquefaction is one of the most damaging effects of earthquake shaking. Current methods of predicting liquefaction have proven to be effective for a given intensity of earthquake shaking but, because they consider only a single intensity at a time, their ability to communicate total liquefaction hazard is limited.

The goal of this research is to improve the assessment of seismically-induced soil liquefaction potential by including the entire range of the hazard due to ground shaking and by describing the liquefaction potential in a form that can be more easily used by other stakeholders in hazard and risk analysis. This has been accomplished by implementing two methods of liquefaction analysis into the performance-based earthquake engineering framework developed by the Pacific Earthquake Engineering Research Center. In this framework, a probabilistic liquefaction analysis is combined with a probabilistic seismic hazard analysis in a manner that accounts for the hazard from all possible earthquake scenarios with proper consideration of their likelihoods of occurrence.

The first method is based on the widely-used cyclic stress ratio as the measure of ground shaking intensity and soil resistance, for which the necessary data and predictive relationships are readily available. Implementation of this method, however, required modification of the scalar PEER framework to accommodate the magnitude-distance vector of loading information that forms the cyclic stress ratio. The second method is based on the recently-developed variant of cumulative absolute velocity, CAV_5 , for which no liquefaction analysis

procedures exist. A collection of case-histories and ground motion records was assembled and modeled with logistic regression to produce a relationship that predicts liquefaction probability from CAV_5 and soil penetration resistance.

The research shows that current methods of liquefaction analysis produce inconsistent estimates of the liquefaction hazard across different seismic environments. This occurs because they consider only a single ground shaking intensity whereas the total liquefaction hazard is composed of contributions from all shaking intensities. These inconsistent hazard estimates result in the application of different levels of safety to different locations. Because the performance-based approach incorporates all shaking intensities, it produces consistent estimates of liquefaction hazard across different seismic environments. The future use of performance-based liquefaction analyses is discussed.

The new CAV_5 method offers several conceptual advantages over the cyclic stress method, but its full implementation into the performance-based framework is hampered at this time by the lack of a robust attenuation relationship needed for the development of CAV_5 seismic hazard curves.

TABLE OF CONTENTS

	Page
List of Figures	v
List of Tables	x
Chapter 1: Introduction	1
1.1 Organization of the work	3
Chapter 2: The Performance-based Framework	5
2.1 Background	5
2.2 The PEER framework	7
2.2.1 Probabilistic seismic hazard analysis	8
2.2.2 The PEER framing equation	9
2.2.3 An alternate form of the framing equation	12
2.2.4 A graphical interpretation	13
2.3 Uncertainty within the PEER framework	16
2.3.1 The effect of uncertainty on hazard estimates	17
2.3.2 Predictability, efficiency, and sufficiency	19
Chapter 3: Intensity Measures for Liquefaction Assessment	22
3.1 Soil liquefaction	22
3.2 Cyclic shear stress method	23
3.2.1 The simplified method	25
3.2.2 Overburden stress correction	32
3.2.3 Static shear stress correction	33
3.2.4 Current form of <i>CSR</i> method equations	33
3.2.5 Probabilistic interpretations of <i>CRR</i>	35
3.2.6 Summary of the <i>CSR</i> method	37
3.3 Cyclic strain method	39
3.4 Energy approach	42

3.4.1	Arias intensity method	42
3.4.2	CAV_5	47
3.5	Intensity measures for performance-based liquefaction assessment	59
Chapter 4:	Performance-based cyclic stress method	61
4.1	IM hazard curve	61
4.1.1	Peak ground acceleration	62
4.1.2	Magnitude	63
4.2	IM - EDP fragility curves	67
4.2.1	Uncertainty terms in Çetin's probability of liquefaction	69
4.2.2	Useful $EDPs$	72
4.2.3	Relating FS_L and N_{req}	73
4.2.4	Magnitude dependence	75
4.3	The return period of soil liquefaction in Seattle	75
4.3.1	Comparison with conventional liquefaction analyses	77
4.3.2	Equivalent return periods of liquefaction	81
4.3.3	Deaggregation of liquefaction hazard	82
4.4	The return period of soil liquefaction across the U. S.	84
4.4.1	Deaggregation of liquefaction hazard	86
4.4.2	Comparison with conventional liquefaction analyses	88
4.4.3	Equivalent return periods of liquefaction	91
4.5	Development of a performance-based liquefaction criterion	93
4.5.1	An appropriate liquefaction return period	93
4.5.2	A suitable liquefaction evaluation procedure	94
4.6	Liquefaction hazard maps for Washington State	95
4.7	Adjustment of mapped N_{req} values for site-specific conditions	96
4.7.1	Comparison with conventional liquefaction analyses	99
4.8	Summary of the performance-based CSR approach	104
Chapter 5:	CAV_5 reduction coefficient	107
5.1	Previous work	108
5.1.1	Cyclic stress and strain approaches	109
5.1.2	Energy approach	117
5.2	Theoretical considerations for a CAV_5 depth reduction coefficient	119
5.3	Form of the predictive model	122
5.4	Dataset	125

5.4.1	1- and 2-d data exploration	131
5.5	Regression	132
Chapter 6:	Estimating liquefaction potential using CAV_5	140
6.1	Model parameters	140
6.2	Case history database	141
6.2.1	Penetration resistance	142
6.2.2	Effective confining pressure	143
6.2.3	CAV_5	144
6.2.4	Database summary	149
6.3	Transformation of model parameters	149
6.4	Logistic regression	152
6.4.1	Bayesian updating	153
6.4.2	Sampling bias	154
6.5	Liquefaction relationship including parameter and modeling uncertainty	155
6.5.1	Overburden stress correction	156
6.5.2	Liquefaction curves	156
6.5.3	Use of the CAV_5 liquefaction relationship	159
6.5.4	Limitations and potential sources of bias	160
6.5.5	Deterministic CAV_5 liquefaction relationship	161
6.5.6	Relating FS_L and N_{req}	162
6.6	Parameter uncertainty	163
6.6.1	Liquefaction relationship with parameter uncertainty removed	166
6.7	Alternative forms of the CAV_5 liquefaction model	168
6.8	Estimation of CAV_5 at initial liquefaction	173
6.9	Summary	177
Chapter 7:	Performance-based implementation of the CAV_5 method	179
7.1	IM hazard curve	179
7.1.1	Soil amplification factor	180
7.2	The return period of soil liquefaction in Seattle	181
7.3	The return period of soil liquefaction across the U. S.	185
7.4	Liquefaction hazard maps for Washington State	191
7.5	Adjustment of mapped N_{req} values for site-specific conditions	195
7.6	Modification of the CAV_5 attenuation relationship	196
7.7	Summary of the performance-based CAV_5 approach	205

Chapter 8: Summary, conclusions, and recommendations	206
8.1 Recommendations for future work	212
Bibliography	214
Appendix A: Estimates of parameter variance in Çetin's equation for probability of liquefaction	227
A.1 Overview of the approach	227
A.2 Example condition	229
A.3 Standard penetration resistance	229
A.4 Cyclic stress ratio	230
A.5 Earthquake magnitude	233
A.6 Effective vertical stress	234
A.7 Fines content	234
A.8 Model uncertainty	235
A.9 Putting it all together	235
Appendix B: Adjustment of liquefaction hazard maps for site specific conditions . .	236
B.1 Components of the adjustment	236
B.2 Stress component of the adjustment	238
B.3 Soil amplification adjustment	241
B.4 Adjustment for depth reduction factor	241
B.5 Calculating the shear wave velocity	243
B.6 Prediction error of adjustment	243
Appendix C: Data for CAV_5 logistic regression	249
Appendix D: CAV_5 at the start of liquefaction	265

LIST OF FIGURES

Figure Number	Page
1.1 Damage from soil liquefaction in Niigata, Japan, and Anchorage, Alaska. . . .	2
2.1 A conceptual representation of building performance levels after earthquake loading.	7
2.2 Examples of <i>IM</i> hazard and <i>IM-EDP</i> fragility curves.	14
2.3 Integration of <i>IM</i> hazard and <i>IM-EDP</i> fragility curves to produce an <i>EDP</i> hazard curve.	15
2.4 Graphical representation of PEER framework.	16
2.5 Effect of varying uncertainty levels on the drift ratio hazard.	18
2.6 The effect of uncertainty in site characterization on <i>EDP</i>	21
3.1 Correlation between cyclic resistance ratio and corrected penetration resistance.	24
3.2 Depth reduction coefficient.	27
3.3 Correlation between peak ground acceleration causing liquefaction in the field and relative density of sand.	27
3.4 Overburden stress corrections for penetration resistance.	30
3.5 Correlation between stress ratio causing liquefaction in the field and penetration resistance of sand.	32
3.6 Probabilistic <i>CRR</i> curves from Liao et al., Youd and Noble, Toprak et al., and Çetin et al.	36
3.7 Pore pressure generation from small and large strains.	40
3.8 Acceleration time history of Kawagishi-cho EW component 1964 Niigata earthquake and Hachirogata NS component 1983 Nihonkai-Chubu earthquake.	43
3.9 Time history of acceleration; pore pressure ratio, r_u ; and Arias intensity from the Wildlife site, 1987 Superstition Hills earthquake.	44
3.10 Depth reduction factor and liquefaction plot for the Arias intensity method. .	45
3.11 Cumulative absolute velocity (<i>CAV</i>) from acceleration time history.	48
3.12 <i>CAV</i> from velocity time history.	49
3.13 <i>CAV</i> from acceleration vs duration curve.	50
3.14 Mitchell's generic soil profile.	51
3.15 CAV_5 from acceleration time history and acceleration vs duration curve. . . .	52

3.16	Correlation between spectral acceleration and a_{max} , I_a , and CAV_5	55
3.17	Efficiency and sufficiency of a_{max} , I_a , and CAV_5 in predicting pore pressures generated due to seismic loading.	57
3.18	Correlation between average pore pressure ratio and a_{max} , I_a , and CAV_5 at the ground surface.	58
4.1	Hazard curves for a_{max} for six U. S. cities.	62
4.2	Extrapolation of the a_{max} hazard curve for Seattle.	64
4.3	PSHA deaggregation of the 475-yr a_{max} for Seattle.	65
4.4	Hazard curves for Seattle.	66
4.5	Illustration of the relationship between CRR and penetration resistance, and the effect of fines content on the factor of safety against liquefaction.	74
4.6	Subsurface profile used in assessing the return period of liquefaction in Seattle.	76
4.7	EDP hazard curves for FS_L and N_{req} at the Seattle site.	77
4.8	Performance-based FS_L and N_{req} depth profiles at the Seattle site.	78
4.9	Deterministic FS_L and N_{req} depth profiles at Seattle from the NCEER and Çetin methods.	80
4.10	Equivalent performance-based return periods of N_{req}^{det} at the Seattle site.	82
4.11	Deaggregation of 475-yr and 2475-yr return period liquefaction hazard for 6-m depth at Seattle.	83
4.12	Total a_{max} hazard curves for ten cities across the U. S.	85
4.13	EDP hazard curves for FS_L and N_{req} at 6-m depth for ten U. S. cities.	86
4.14	Deaggregation of 475-yr return period liquefaction hazard for 6-m depth at ten U. S. cities.	87
4.15	Performance-based FS_L and N_{req}^{pb} depth profiles at ten U. S. cities for the 475-yr return period.	88
4.16	Deterministic FS_L and N_{req} depth profiles at ten U. S. cities for the 475-yr return period a_{max} from the NCEER and Çetin methods.	89
4.17	Equivalent liquefaction return periods of 475-yr N_{req}^{det} for 6-m depth at ten U. S. cities from NCEER and Çetin methods.	91
4.18	Reference soil profile for performance-based analysis across Washington State.	96
4.19	475-yr and 2475-yr N_{req} at 6-m depth in reference profile for Washington State.	97
4.20	Correction factors for N_{req} maps.	100
4.21	475-yr and 2475-yr N_{req} at 6-m depth in reference profile for Washington State from conventional analyses using Çetin's method.	101
4.22	Equivalent liquefaction return period of 475-yr and 2475-yr N_{req} from conventional analyses at 6-m depth in reference profile for Washington State.	102

4.23	Difference between 475-yr and 2475-yr N_{req} from conventional analyses and 400-yr and 1700-yr N_{req} from performance-based analyses at 6-m depth in reference profile for Washington State.	103
4.24	Factors of safety implied by N_{req} difference in Figure 4.23 at 475-yr and 2475-yr return periods.	105
5.1	Comparison of average r_d from linear and nonlinear methods, after Golesorkhi (1989).	108
5.2	Depth reduction factor, r_d , vs depth, after Youd et al. (2001).	110
5.3	Depth reduction factor, r_d , vs depth, after Ishihara (1977).	111
5.4	Depth reduction coefficients based on ground response analyses and soil profiles vs depth.	113
5.5	Comparison of Iwasaki's average r_d and the range of results from Seed and Idriss, after Iwasaki (1978).	113
5.6	Depth reduction factor, r_d , vs depth after Imai et al. (1981).	113
5.7	Depth reduction coefficients based on linear equivalent (SHAKE) ground response analyses, after Golesorkhi (1989).	115
5.8	The effect of magnitude on r_d , after Golesorkhi (1989).	115
5.9	Depth reduction factor, r_d , vs depth for Magnitudes 5.5 to 8.0, after Idriss (1999).	115
5.10	Depth reduction factor, r_d , vs depth, after Çetin et al. (2004).	117
5.11	Arias intensity depth reduction factor, r_b , vs depth, after Kayen and Mitchell (1998).	117
5.12	Illustration of the shear wave velocity parameters, V_{s0} and dV_s , for shear wave velocity measurements in the upper 12 m of a soil deposit.	121
5.13	Shear wave velocity and CAV_5 depth reduction coefficient profiles from SHAKE91 analyses using simple soil profiles.	123
5.14	Illustration of the general form of the normalized r_c offset term.	124
5.15	CAV_5 vs a_{max} from dataset produced by SHAKE91 runs.	129
5.16	r_c vs depth from the dataset produced by SHAKE91 runs.	130
5.17	Plots of r_c vs depth for bins of V_{s0} and CAV_5 in the dataset.	133
5.18	Plot of r_c model.	135
5.19	Plot of r_c residuals vs depth, V_{s0} , dV_s , and CAV_5	136
5.20	Comparison of datasets and models for r_c from this study and r_d from Çetin and Seed (2003) and Çetin et al. (2004).	137
5.21	Comparison of r_c and r_d profiles investigating the sensitivity of CAV_5 and a_{max} to nonlinear soil behavior.	138
5.22	Plot of r_c residuals vs earthquake magnitude.	139

6.1	CAV_5 attenuation curves for reverse faulting from Kramer and Mitchell (2006).	146
6.2	Quantile plots of non-liquefaction and liquefaction cases for key liquefaction model parameters.	150
6.3	Liquefaction state boundary curves with parameter and model uncertainty included.	157
6.4	Case histories and liquefaction state boundary curves with parameter and model uncertainty included.	158
6.5	Liquefaction state boundary curves with only model uncertainty.	168
6.6	Case histories and liquefaction state boundary curves with only model uncertainty.	169
6.7	Liquefaction state boundary curves with CAV_5 estimated from Kramer and Mitchell's attenuation relationship.	171
6.8	Case histories and liquefaction state boundary curves with CAV_5 estimated from Kramer and Mitchell's attenuation relationship.	172
6.9	Estimation of CAV_5 at the start of liquefaction.	174
6.10	CAV_5 at the initiation of liquefaction compared with the liquefaction state boundary curves from Figure 6.3.	176
7.1	Subsurface profile used in assessing the return period of liquefaction in Seattle.	181
7.2	CAV_{5surf} and a_{max} hazard curves for Seattle.	182
7.3	FS_L and N_{req} hazard curves at the Seattle site using the CAV_5 and CSR methods.	184
7.4	Performance-based FS_L and N_{req} depth profiles at the Seattle site from the CAV_5 and CSR methods.	186
7.5	CAV_{5surf} and a_{max} hazard curves for ten cities across the U. S.	187
7.6	FS_L and N_{req} hazard curves at 6-m depth for ten U. S. cities using the CAV_5 and CSR methods.	189
7.7	Performance-based FS_L and N_{req}^{pb} depth profiles at ten U. S. cities for the 475-yr return period from the CAV_5 and CSR .	190
7.8	Reference soil profile for the performance-based analyses across Washington State.	191
7.9	475-yr N_{req} at 6-m depth in reference profile for Washington State from the CAV_5 and CSR methods.	192
7.10	2475-yr N_{req} at 6-m depth in reference profile for Washington State from the CAV_5 and CSR methods.	193
7.11	Adjustment factors for CAV_5 -based N_{req} maps.	197
7.12	Comparison of the Kramer and Mitchell attenuation relationship with CAV_{5rock} estimates from the Cascadia subduction zone.	198

7.13	Adjusted CAV_{5surf} and a_{max} hazard curves for Seattle.	200
7.14	475-yr CAV_{5surf} for Washington State from the original and adjusted Kramer and Mitchell attenuation relationship.	201
7.15	2475-yr CAV_{5surf} for Washington State from the original and adjusted Kramer and Mitchell attenuation relationship.	202
7.16	475-yr N_{req} at 6-m depth in reference profile for Washington State from the original and adjusted Kramer and Mitchell attenuation relationship.	203
7.17	2475-yr N_{req} at 6-m depth in reference profile for Washington State from the original and adjusted Kramer and Mitchell attenuation relationship.	204
B.1	The ΔN_{σ} adjustment factor for a range of depths and groundwater depth ratios.	240
B.2	The ΔN_{r_d} adjustment factor for a range of depths and shear wave velocities.	243
B.3	N_{req} prediction error of site-specific adjustment factor for 475-yr and 2475-yr return periods, $z_w/z = 0$, and parameter uncertainty corresponding to a detailed site investigation ($\sigma_E = 4.21$).	245
B.4	N_{req} prediction error of site-specific adjustment factor for 475-yr and 2475-yr return periods, $z_w/z = 1$, and parameter uncertainty corresponding to a detailed site investigation ($\sigma_E = 4.21$).	246
B.5	N_{req} prediction error of site-specific adjustment factor for 475-yr and 2475-yr return periods, $z_w/z = 0$, and no parameter uncertainty ($\sigma_E = 2.70$).	247
B.6	N_{req} prediction error of site-specific adjustment factor for 475-yr and 2475-yr return periods, $z_w/z = 1$, and no parameter uncertainty ($\sigma_E = 2.70$).	248
D.1	Case 110, 1987 Superstition Hills earthquake, Wildlife Refuge: (top) NS component, (bottom) EW component.	266
D.2	Case 142, 1989 Loma Prieta earthquake, Treasure Island: (top) NS component, (bottom) EW component.	267
D.3	Cases 145 and 146, 1993 Kushiro-oki earthquake, Kushiro Port: (top) NS component, (bottom) EW component.	268
D.4	Case 156, 1995 Hyogoken-Nambu earthquake, Port Island: (top) NS component, (bottom) EW component.	269
D.5	Case 208, 1999 Chi-chi earthquake, Chiaya CHY104: (top) NS component, (bottom) EW component.	270
D.6	Case 209, 1999 Chi-chi earthquake, Yuan-lin TCU110: (top) NS component, (bottom) EW component.	271

LIST OF TABLES

Table Number	Page
1.1 Terminology in the PEER framework.	3
3.1 Relative ranking of the <i>IMs</i> ' efficiency, sufficiency, and predictability.	59
4.1 Estimates of parameter variances for high and low levels of uncertainty for example soil element.	72
4.2 Peak horizontal ground accelerations and mean magnitudes for deterministic analyses at Seattle site.	79
4.3 Peak accelerations for 10 U. S. cities from the USGS deaggregation web site.	84
4.4 Required penetration resistances and ratios of equivalent factors of safety for 475-yr liquefaction hazard at 6-m depth in the idealized site at ten U. S. cities.	90
4.5 Equivalent liquefaction return periods of 475-yr and 2475-yr N_{req}^{det} for 6-m depth at ten U. S. cities.	92
5.1 Soft soil sites used to develop r_c	126
5.2 Soil types used in SHAKE91 analyses to develop r_c	127
5.3 Input motions used to develop r_c	128
5.4 Statistical parameters of variables in dataset used to develop r_c	131
5.5 Correlation matrix for variables in dataset used to develop r_c	131
5.6 Comparison of r_c calculated using model with r_c measured at the Wildlife seismic array.	137
6.1 Coefficients for Kramer and Mitchell's CAV_5 attenuation relationship.	145
6.2 Statistical parameters of the CAV_5 case history database.	151
6.3 Model coefficients from regression with model and parameter uncertainty.	155
6.4 Correlation matrix for coefficients from regression with model and parameter uncertainty.	155
6.5 Model coefficients from regression with only model uncertainty.	167
6.6 Correlation matrix for coefficients from regression with only model uncertainty.	167
6.7 Model coefficients from regression using estimates of CAV_5 only from Kramer and Mitchell's attenuation relationship.	170
6.8 Correlation matrix for coefficients from regression using estimates of CAV_5 only from Kramer and Mitchell's attenuation relationship.	170

6.9	CAV_5 at the start of softening and when fully softened for liquefaction sites at which a time history was recorded.	175
7.1	CAV_{5surf} and a_{max} for 10 U. S. cities.	188
7.2	Actual and apparent magnitudes from Green's function data for Kramer and Mitchell's CAV_5 attenuation relationship.	199
B.1	Correlations between SPT blowcount and shear wave velocity.	244
C.1	Vertical effective stress parameters for CAV_5 logistic regression.	250
C.2	Penetration resistance parameters for CAV_5 logistic regression.	255
C.3	CAV_5 parameters for CAV_5 logistic regression.	260

ACKNOWLEDGMENTS

It is unfair that only I am credited with authoring this dissertation because it is only through the support and assistance of many people and organizations that it has come to fruition.

I am grateful for the financial support from the Washington State Department of Transportation, and especially to Tony M. Allen.

Assembling the earthquake records and site conditions for the CAV_5 liquefaction relationship in Chapters 5 and 6 was made much easier and more effective by the kind assistance of the following individuals, organizations, and sources:

- The PhD dissertation of Professor K. Önder Çetin;
- Dr. Robert Kayen, U. S. Geological Survey;
- Dr. Mladen Kostadinov of SNC Lavalin, Canada, and Professor Fumio Yamazaki of Chiba University, Japan, for providing earthquake records from their paper, “Detection of soil liquefaction from strong motion records” (Earthquake Engng. Struct. Dyn. 2001, (30), 173–193);
- The National Geophysical Data Center (NGDC) of the National Oceanographic and Atmospheric Administration’s Satellite and Information Service;
- The K-net and KiK-net earthquake databases of Japan’s National Institute for Earth Science and Disaster Prevention (NIED);
- The Pacific Earthquake Engineering Research Center including the PEER Strong Motion Database and the Consortium of Organizations for Strong-Motion Observation Systems (COSMOS);

- Information from Strong-Motion Earthquake Observation in Japanese Ports provided by Dr. Takahiro Sugano of the Port and Airport Research Institute, Yokosuka, Japan;
- Taiwan's Central Weather Bureau;
- Professor Yasuo Tanaka, Kobe University Research Center for Urban Safety and Security;
- Professor Kohji Tokimatsu, Tokyo Institute of Technology;
- Dr. Sarah Upsall of Hart Crowser, Seattle, for providing the data that allowed the correlation between spectral acceleration and the intensity measures in Figure 3.16.

My fellow graduate students were a constant source of encouragement and entertainment and have made the work more pleasant. I especially appreciate the companionship of my office-mate, Hyung-Suk Shin, and the assistance of Yi-Min Hwang in finding soil profile information for recording sites affected by the Chi-chi earthquake and in organizing data for the a_{max} hazard curves for Washington State.

I offer my thanks to the supervisory and reading committees for this dissertation; your encouragement and support continue to be appreciated.

I am truly grateful for the opportunity to have worked on this project with my advisor, Steve Kramer. The high standards that he sets for himself have continually challenged me to produce a body of work that is far better than I imagined possible. Any errors or flaws that remain in this dissertation are evidence of the poor material he has had to work with rather than any lack of effort on his part.

Finally, my friends and family have given me unfailing and unstinting support at every stage of this work, even while I have ignored them. Thank you all.

DEDICATION

For Betty
(again)

Chapter 1

INTRODUCTION

It is a bitter and humiliating thing to see works, which have cost men so much time and labour, overthrown in one minute; yet compassion for the inhabitants is almost instantly forgotten, from the interest excited in finding that state of things produced in a moment of time, which one is accustomed to attribute to a succession of ages.

—Charles Darwin, March 1835, reporting the ruin of Concepción, Chile

Earthquakes have commanded our attention since the dawn of recorded history. That the earth's surface, upon which our entire existence is founded, suddenly begins to shake and heave both horrifies and fascinates us. The physical processes that cause earthquakes occur on a scale so enormous that we struggle to maintain proper perspective as we attempt to understand them, and the effects due to earthquakes are so varied and widespread that we struggle to maintain our focus as we can begin to develop that understanding.

One of the most dramatic effects of earthquake shaking is *soil liquefaction*, the loss of strength and stiffness that can occur due to excess pore water pressure generated when loose, saturated sand or non-plastic silt is shaken or sheared. Although the areas experiencing soil liquefaction are relatively small compared to the total area shaken by an earthquake, the inflicted damage is often disproportionately high. Low-lying areas near rivers, lakes, and other bodies of water that are desirable for human settlement are also the areas most susceptible to liquefaction. In addition, the damage from soil liquefaction can be very dramatic. The toppled apartment buildings in Niigata, Japan, and the destroyed subdivision in Anchorage, Alaska (Figure 1.1) are startling examples of soil liquefaction's devastating effects. Extending far beyond the obvious structural damage, liquefaction causes damage to

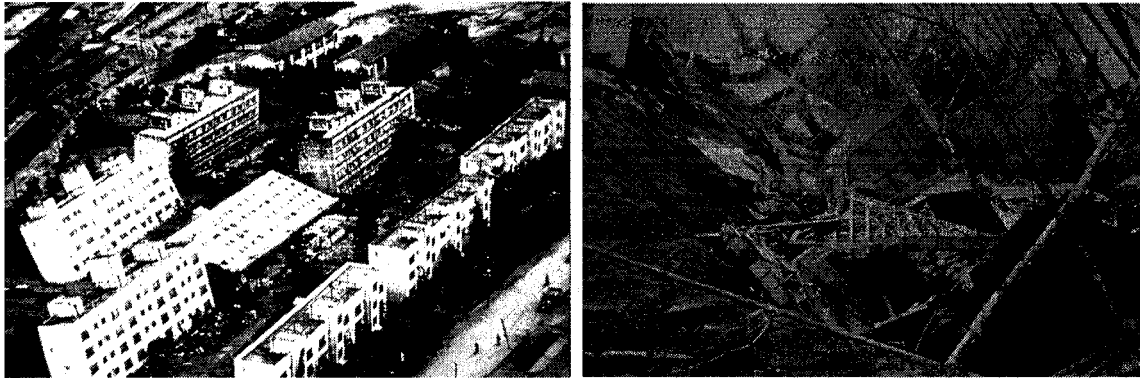


Figure 1.1: Damage from soil liquefaction in Niigata, Japan, and Anchorage, Alaska.

buried utilities and roads, disruption of lifelines, secondary damage caused by fires started as a result of structural damage or ruptured gas lines, injuries and loss of life, and tertiary costs such as business downtime and temporary relocation of residents. Assessing the risk from such a wide range of damage involves not only engineers but owners, government officials, bankers, and insurers. Apportioning and accumulating—simply communicating—the risk within this diverse group of stakeholders is an enormous challenge, one that is not well served by the current methods of liquefaction analysis used by geotechnical engineers.

The goal of this research is to improve the assessment of seismically-induced liquefaction potential by incorporating more comprehensively the hazard due to ground shaking and by describing the liquefaction potential in a form that can be more easily used by other stakeholders in hazard and risk analysis.

The Pacific Earthquake Engineering Research Center (PEER) has developed a probabilistic, performance-based framework that allows for the propagation of hazard from earthquake ground motions to ground motion response, measures of damage due to ground motion response, and finally to parameters that describe the cost of those damages. Table 1.1 describes PEER's terminology within PEER's framework. Each parameter in the framework is the main focus of a certain group of stakeholders: *IM* to seismologists, *EDP* to engineers, *DM* to loss analysts, and *DV* to decision-makers such as owners, government regulators, and the public. To allow for communication between these groups, the hazard associated

Table 1.1: Terminology in the PEER framework.

Stage	PEER term	Example
Ground motion	Intensity Measure, <i>IM</i>	Peak ground accel, Arias Intensity
Response	Engineering Demand Parameter, <i>EDP</i>	Interstory drift, liquefaction
Damage	Damage Measure, <i>DM</i>	Column cracking, slope displacement
Cost parameter	Decision Variable, <i>DV</i>	Repair cost, loss of life

with each variable is expressed as a mean annual rate of exceedance, which is the inverse of the return period of exceedance. With this representation, the information from each level of the framework is useful at other levels.

Using this framework and these terms, the goal of this research project can be restated as the development of a method for estimating the mean annual rate of exceedance of an *EDP*—the initiation of soil liquefaction—conditional upon some *IM*. The estimation method will combine the mean annual exceedance rate of the *IM* of interest as determined from a probabilistic seismic hazard analysis (PSHA) with the conditional probability of liquefaction given that *IM*. This combination will be integrated across the entire range of the *IM*. Stated more succinctly, the research will develop a method for estimating the return period of soil liquefaction.

1.1 Organization of the work

This dissertation begins by examining PEER's performance-based framework. Chapter 2 presents the background to its development and the key components required for its implementation. The role of prediction and parameter uncertainty is also discussed with the aim of selecting suitable ground motion intensity measures for assessing liquefaction potential.

Chapter 3 focuses on these *IMs*. It opens with a review of conventional methods of liquefaction assessment, including those based on the well-known cyclic stress ratio as well

as the less common cyclic strain and energy-based *IMs*. The chapter closes with an introduction of a new and potentially useful *IM* called CAV_5 , which is based on cumulative absolute velocity. The advantages and disadvantages of the different *IMs* are compared with respect to their suitability for implementation into the performance-based framework, and cyclic stress ratio and CAV_5 are selected for further study.

Chapter 4 describes in detail the assessment of liquefaction potential using cyclic stress ratio to describe the loading on the soil column due to earthquake shaking and the capacity of the soil to resist liquefaction. Conventional deterministic and probabilistic methods of analysis are discussed and the probabilistic procedure developed by Çetin [21, 24] is singled out for implementation into the performance-based framework. Results from conventional analyses and the new performance-based method are compared at ten U. S. cities and on a grid of 247 points across Washington State to conclude that the conventional analyses produce an inconsistent representation of liquefaction potential in different seismic environments.

The next three chapters describe the development of a liquefaction assessment method based on CAV_5 . Chapter 5 presents a depth reduction coefficient, r_c , which allows the estimation of CAV_5 at the depth of interest within a soil profile based on ground motions recorded at the ground surface. This coefficient is derived from theoretical considerations and from equivalent linear analyses on a wide range of soil profiles excited by a series of scaled earthquake motions. Chapter 6 applies r_c to nearly 200 liquefaction and non-liquefaction case histories to provide a database for regression of a probabilistic CAV_5 -based method for assessing liquefaction potential. The behavior of this new method is compared with that of the *CSR* method and limitations for its use are discussed. In Chapter 7, the CAV_5 method is implemented into the PEER performance-based framework and used to analyze the liquefaction potential of the ten U. S. cities and the Washington grid. The results are again compared with those from the *CSR* method.

Chapter 8 ends the dissertation with a summary of the main conclusions from the work and a list of topics for further investigation.

Chapter 2

THE PERFORMANCE-BASED FRAMEWORK

Performance-based engineering is an approach to the design, construction, maintenance, and rehabilitation of facilities that focuses on meeting the needs of the facility stakeholders—owners, users, government, and the general public—rather than on satisfying the minimum requirements defined in a building code. This is a major change for engineers. Instead of designing for “failure” prevention by providing a capacity that exceeds the specified load by some margin of safety, the goal is to relate loading levels to damage and provide answers to such questions as

- What is the likelihood, frequency, and risk of various damage levels?
- What are the annualized costs of prevention, repair, and mitigation of various damage levels?
- Which components of a facility contribute most to the overall risk?

Although performance-based engineering is not a new concept, it has gained prominence over the last ten years because it allows for a more transparent development of options and selection of choices about the desired performance of an engineered facility, especially as a result of earthquake loading. This wider range of options has been particularly beneficial for the upgrading of existing facilities in which it is often not appropriate to impose the prescriptions of a building code.

2.1 Background

May [89] presented a survey of the progression of performance-based engineering starting with ancient Babylon’s Code of Hammurabi, which decreed death to a builder if one of his

structures fell down. From the time of that abundantly clear performance goal until the mid-1990s, building codes gradually became less performance-based and more prescriptive; that is, they specified the design methods and building materials that should be used rather than an end result. In the prescriptive approach, there is the tacit assumption that following the stated procedures will achieve the desired performance. But what if the facility stakeholders want a higher level of performance than is implied in the building code? Having to satisfy mandatory prescriptions that are applicable for a lower standard while trying to implement a different design approach is expensive and frustrating.

The first procedures for performance-based earthquake engineering (PBEE) for buildings in the United States were proposed by the Applied Technology Council [4] and the Federal Emergency Management Agency [37]. They considered various levels of earthquake-induced loading that might result in nonlinear response and corresponding levels of damage: elastic limit (minor damage), immediate occupancy, life safety, collapse prevention, and collapse (Figure 2.1). Three premises are implicit in the performance-based approach [42]:

1. Performance levels and objectives can be quantified;
2. Performance can be reliably predicted; and,
3. The cost of improved performance can be evaluated so that rational trade-offs can be based on considerations of life-cycle cost rather than on construction costs alone.

The representation in Figure 2.1 partly addressed the first premise but identified difficulties with the remaining two. Each stakeholder had a different way of describing and analyzing performance, and there was no way to coordinate these disparate views into a final prediction of performance. Owners were interested in dollars and downtime, government regulators and the public were focused on public safety, engineers calculated factors of safety and stresses, and seismologists studied magnitudes and distances. Developing a framework for communicating, apportioning, and accumulating performance parameters within this diverse group of stakeholders has been one of the major achievements of the Pacific Earthquake Engineering Research Center.

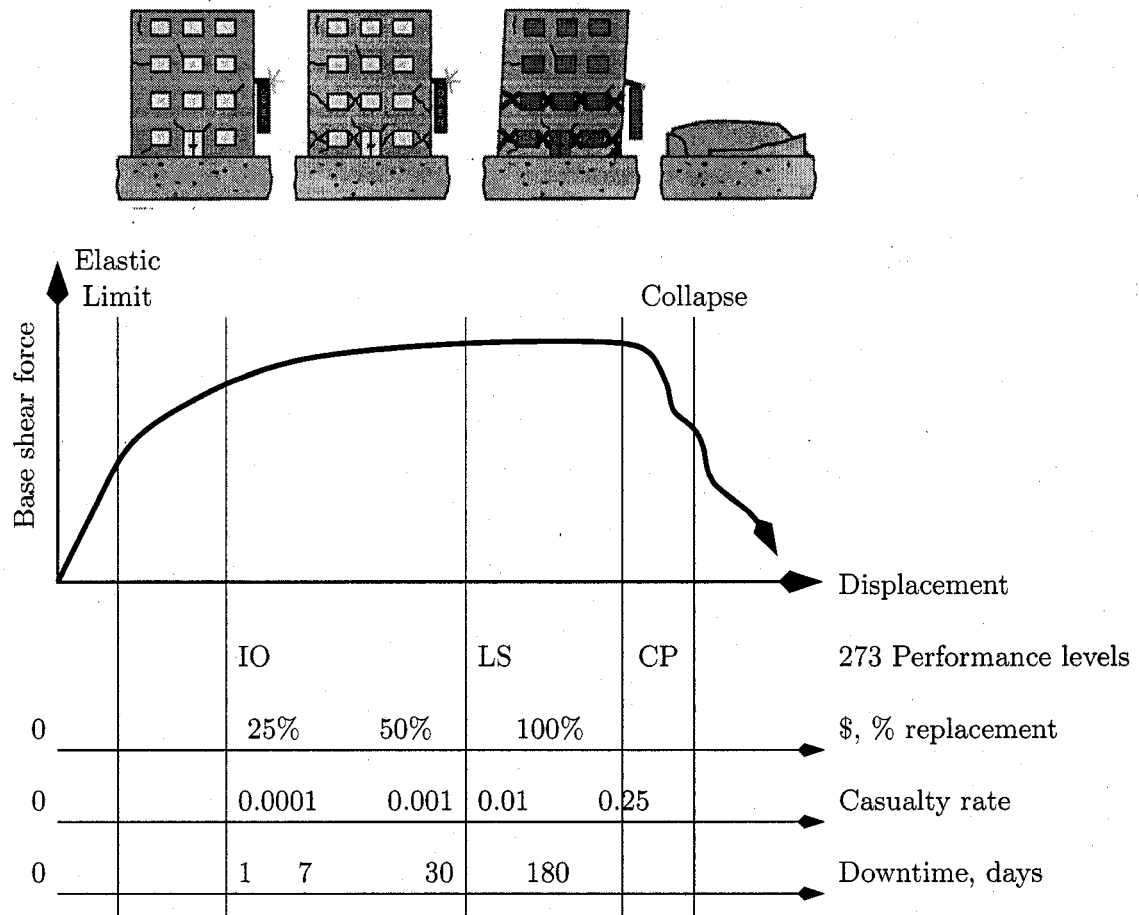


Figure 2.1: A conceptual representation of building performance levels after earthquake loading. IO stands for Immediate Occupancy, LS for Life Safety, and CP for Collapse Prevention. After Moehle and Deierlein [91].

2.2 The PEER framework

The National Science Foundation established the Pacific Earthquake Engineering Research Center (PEER) in October 1997 as one of three national earthquake engineering research centers. PEER's mission is to

develop and disseminate technologies to support performance-based earthquake engineering. The approach is aimed at improving decision-making about seismic risk by making the choice of performance goals and the tradeoffs that they entail

apparent to facility owners and society at large. The approach has gained world-wide attention in the past ten years with the realization that urban earthquakes in developed countries—Loma Prieta, Northridge, and Kobe—impose substantial economic and societal risks above and beyond potential loss of life and injuries. By providing quantitative tools for characterizing and managing these risks, performance-based earthquake engineering serves to address diverse economic and safety needs. . . .

—<http://peer.berkeley.edu/PEERCenter/mission.html>

One of PEER's significant achievements has been the development of a general framework for consistent treatment of risk, a consistency that allows rational discussion of hazard levels, appropriate design return periods, public safety issues, and investment risk among all project stakeholders. This is important for satisfying the first premise listed above. It also facilitates the other premises—analytical prediction of performance and cost evaluation of performance alternatives—by allowing these complex and multidisciplinary problems to be broken down into a series of logical and modular elements [28, 91].

The ultimate goal in PEER's PBEE framework is to describe the mean annual rate (frequency) of exceedance of one or more key *Decision Variables*, such as repair cost, downtime, injuries, or loss of life. However, predicting these *DVs* directly from earthquake source parameters—magnitude and distance, for example—is not usually possible because the performance of different facilities is influenced by a wide range of conditions such as soil type, structure type, and level of occupancy. The PEER framework separates the prediction into smaller components for which predictions of hazard and risk can be made with less uncertainty, then aggregates the individual hazard contributions into a final estimate of the performance. This deaggregation and reaggregation is similar to the approach used in Cornell's probabilistic seismic hazard analysis [27].

2.2.1 Probabilistic seismic hazard analysis

In 1968, Cornell [27] presented a method for estimating the seismic ground motion hazard based on the frequency and probability of occurrence of all possible earthquake magnitudes

of interest at all possible source-to-site distances. Through application of the total probability theorem, the mean annual rate that the ground motion intensity measure, IM , exceeds a particular level, im , can be expressed as:

$$\lambda_{IM}(im) = \sum_{i=1}^{N_S} \nu_i \sum_{j=1}^{N_M} \sum_{k=1}^{N_R} P[IM > im | M = m_j, R = r_k] P[M_i = m_j] P[R_i = r_k] \quad (2.1)$$

in which N_S is the number of seismic source zones potentially affecting the site; ν_i is the mean annual rate of exceedance of the minimum magnitude of interest for the i^{th} seismic source zone; N_M is the number of discretized increments of magnitude, M , in the i^{th} seismic source zone; N_R is the number of discretized increments of source-to-site distance, R in the i^{th} seismic source zone; $P[IM > im | M = m_j, R = r_k]$ is the probability that $IM > im$ conditional upon the particular magnitude, $M = m_j$ and source-to-site distance, $R = r_k$; $P[M_i = m_j]$ is the probability of occurrence of the particular discretized magnitude increment, m_j , in the i^{th} source zone; and $P[R_i = r_k]$ is the probability of occurrence of the particular discretized distance increment, r_k , in the i^{th} source zone [73]. The reciprocal of the mean annual rate of exceedance is commonly referred to as the return period. Collecting the information for Equation (2.1) and performing the calculations is called a Probabilistic Seismic Hazard Analysis, or PSHA.

According to the total probability theorem,

$$P[IM > im]_i = \sum_{j=1}^{N_M} \sum_{k=1}^{N_R} P[IM > im | M = m_j, R = r_k] P[M_i = m_j] P[R_i = r_k]$$

Thus,

$$\lambda_{IM}(im) = \sum_{i=1}^{N_S} \nu_i P[IM > im]_i \quad (2.2)$$

The mean annual rate of exceedance, then, is the product of a complementary cumulative probability distribution, $P[IM > im]$, and a scalar value defining the mean annual rate of exceedance of the threshold magnitude.

2.2.2 The PEER framing equation

PEER has extended Cornell's approach to propagate the ground motion hazard, λ_{IM} , from a PSHA through to the Decision Variable hazard, λ_{DV} , according to the following rationale:

- The ground motion at the site of interest is described by an *Intensity Measure*, IM , such as peak horizontal ground acceleration, spectral acceleration, or Arias intensity;
- The IM causes some level of response at the site described by an *Engineering Demand Parameter*, EDP , such as interstory drift, foundation settlement, or pore pressure rise;
- The EDP results in some level of physical damage to the facility described by a *Damage Measure*, DM , such as crack width or column failure; and,
- The DM results in some cost described by a *Decision Variable*, DV , such as the number of casualties, downtime, or economic loss.

The first part of the framing equation uses the IM hazard from a PSHA to estimate the EDP hazard. From the total probability theorem,

$$P[EDP > edp] = \sum_{im} P[EDP > edp | IM = im] P[IM = im]$$

The term $P[IM = im]$ is the discrete form of a probability density function, which can be determined either from a cumulative probability distribution ($\Delta P[IM < im]$) or from a complementary cumulative probability distribution ($|\Delta P[IM > im]|$). Thus,

$$P[EDP > edp] = \sum_{im} P[EDP > edp | IM = im] |\Delta P[IM > im]|$$

As noted in Equation (2.2), complementary cumulative distributions can be converted to mean annual rates of exceedance by multiplying them by the mean annual rate of threshold magnitude exceedance, ν :

$$\begin{aligned} \lambda_{IM}(im) &= \nu P[IM > im] \\ \lambda_{EDP}(edp) &= \nu P[EDP > edp] \\ &= \sum_{im} P[EDP > edp | IM = im] |\Delta \lambda_{IM}(im)| \end{aligned} \quad (2.3)$$

The absolute value operation is necessary because the slope of a complementary cumulative distribution is negative and none of the terms in Equation (2.3) can be less than zero. From

this point forward in the dissertation, the absolute value operation will not be explicitly noted.

Equation (2.3) defines the first component of the PEER framing equation in which the IM hazard is used to estimate the EDP hazard. It can also be expressed in continuous form:

$$\lambda_{EDP}(edp) = \int P[EDP > edp | IM = im] \frac{d\lambda_{IM}(im)}{dIM} dIM \quad (2.4)$$

As noted earlier, an absolute value operation is implicitly applied to the $d\lambda_{IM}$ term. The second step in the framing equation—using the EDP hazard to estimate the DM hazard—is similar to the first:

$$\lambda_{DM}(dm) = \int P[DM > dm | EDP = edp] \frac{d\lambda_{EDP}(edp)}{dEDP} dEDP$$

in which, from Equation (2.4),

$$\frac{d\lambda_{EDP}(edp)}{dEDP} = \int \frac{dP[EDP > edp | IM = im]}{dEDP} \frac{d\lambda_{IM}(im)}{dIM} dIM$$

Taking the derivative of λ_{EDP} with respect to EDP affects only the conditional probability term because λ_{IM} is independent of EDP . Using this result,

$$\lambda_{DM}(dm) = \iint P[DM > dm | EDP = edp] \frac{dP[EDP > edp | IM = im]}{dEDP} \frac{d\lambda_{IM}(im)}{dIM} dIM dEDP \quad (2.5)$$

or in discrete form,

$$\lambda_{DM}(dm) = \sum_{edp} \sum_{im} P[DM > dm | EDP = edp] P[EDP = edp | IM = im] \Delta\lambda_{IM}(im) \quad (2.6)$$

This can be extended once more to produce the full PEER framing equation for λ_{DV} :

$$\lambda_{DV}(dv) = \iiint P[DV > dv | DM = dm] \frac{dP[DM > dm | EDP = edp]}{dDM} \frac{dP[EDP > edp | IM = im]}{dEDP} \frac{d\lambda_{IM}(im)}{dIM} dIM dEDP dDM \quad (2.7)$$

or, in discrete form,

$$\lambda_{DV}(dv) = \sum_{dm} \sum_{edp} \sum_{im} P[DV > dv | DM = dm] P[DM = dm | EDP = edp] P[EDP = edp | IM = im] \Delta \lambda_{IM}(im) \quad (2.8)$$

These equations show how the various hazard terms within the PEER framework— λ_{IM} , λ_{EDP} , and λ_{DM} —all serially contribute to λ_{DV} . However, in the final form only λ_{IM} is required in combination with a series of conditional probability distributions.

2.2.3 An alternate form of the framing equation

In their paper describing the differences and similarities between deterministic and probabilistic seismic hazard analyses, Hanks and Cornell [43] formulate λ_{EDP} differently than Equation (2.4):

$$\lambda_{EDP}(edp) = \int \lambda_{IM}(im) \frac{dP[EDP > edp | IM = im]}{dIM} dIM$$

This is similar to the PEER form but uses the derivative of the probability term instead of the λ_{IM} term. It can be shown that the two forms are related through integration by parts ($\int u dv = uv - \int v du$). Starting with the PEER form in Equation (2.4),

$$\begin{aligned} \lambda_{EDP}(edp) &= \int_0^{\infty} P[EDP > edp | IM = im] \frac{d\lambda_{IM}(im)}{dIM} dIM \\ &= P[EDP > edp | IM = im] \lambda_{IM}(im) \Big|_0^{\infty} - \\ &\quad \int_0^{\infty} \lambda_{IM}(im) \frac{dP[EDP > edp | IM = im]}{dIM} dIM \end{aligned}$$

At the integration limits of $IM = 0$ and ∞ , the conditional probability term evaluates to 0 and 1, respectively, and λ_{IM} evaluates to the maximum value of ν_i for all source zones and 0, respectively. Thus, at the integration limits the term outside of the integral (uv) equals zero, and

$$\begin{aligned} \lambda_{EDP}(edp) &= \int_0^{\infty} P[EDP > edp | IM = im] \frac{d\lambda_{IM}(im)}{dIM} dIM \\ &= \int_0^{\infty} \lambda_{IM}(im) \frac{dP[EDP > edp | IM = im]}{dIM} dIM \end{aligned}$$

In discrete form, Hanks and Cornell's equation is not quite as tidy as the PEER equation:

$$\lambda_{EDP}(edp) = \sum_{im} \lambda_{IM}(im) \Delta P[EDP > edp | IM = im] \quad (2.9)$$

Because the derivative of the conditional probability is taken with respect to IM instead of EDP , the inequality cannot simply be converted to an equality. Extending this form to include DM ,

$$\begin{aligned} \lambda_{DM}(dm) &= \sum_{edp} \lambda_{EDP}(edp) \Delta P[DM > dm | EDP = edp] \\ &= \sum_{edp} \sum_{im} \lambda_{IM}(im) \Delta P[EDP > edp | IM = im] \Delta P[DM > dm | EDP = edp] \end{aligned}$$

and finally to DV ,

$$\begin{aligned} \lambda_{DV}(dv) &= \sum_{dm} \sum_{edp} \sum_{im} \lambda_{IM}(im) \Delta P[EDP > edp | IM = im] \times \\ &\quad \Delta P[DM > dm | EDP = edp] \Delta P[DV > dv | DM = dm] \end{aligned}$$

This can be expressed in continuous form as

$$\begin{aligned} \lambda_{DV}(dv) &= \iiint \lambda_{IM}(im) \frac{dP[EDP > edp | IM = im]}{dIM} \times \\ &\quad \frac{dP[DM > dm | EDP = edp]}{dEDP} \frac{dP[DV > dv | DM = dm]}{dDM} dIM dEDP dDM \end{aligned}$$

Although the Hanks and Cornell formulation is equivalent to the PEER framing equation and, in some cases may be computationally less expensive, the PEER framing equation is more widely used in current literature and is the form that will be considered in the remainder of this work.

2.2.4 A graphical interpretation

The hazard functions and conditional probability distributions in the PEER framework are often represented graphically as hazard and fragility curves, respectively. An IM hazard curve represents the relationship between the IM and its mean annual rate of exceedance; Figure 2.2a illustrates an example of an Arias intensity hazard curve. The fragility curves

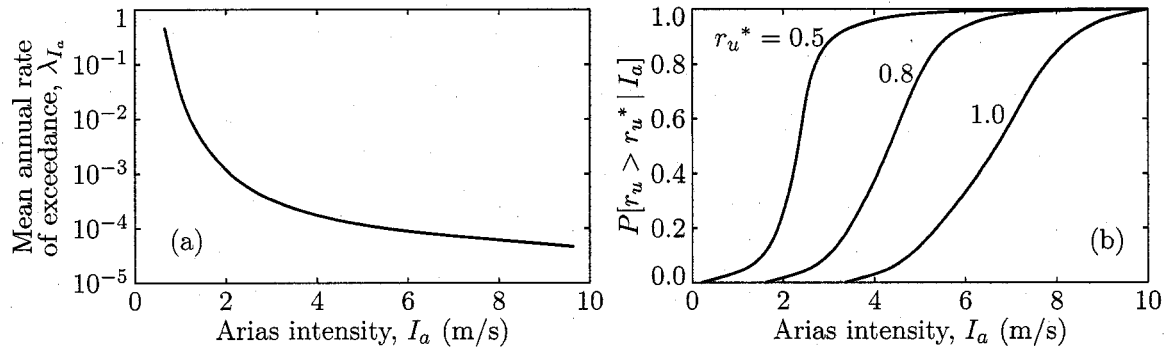


Figure 2.2: Examples of (a) *IM* hazard and (b) *IM-EDP* fragility curves for an intensity measure of Arias intensity, I_a , and an engineering demand parameter of pore pressure ratio, r_u . Note that these curves are only for illustration and are not from actual cases.

are conditional probability distributions that describe the relationship between two adjacent levels in the PEER framing equation; in Figure 2.2b, Arias intensity is the *IM*, pore pressure ratio, r_u , is the *EDP*, and the fragility curves describe the probability that various levels of r_u (0.5, 0.8, and 1.0) will be exceeded by particular Arias intensities. Each fragility curve spans the range of interest of the *EDP*, and results in a single point on the newly constructed *EDP* hazard curve. For example, the arrangement in Figure 2.2 would result in the mean annual rate of exceedance of $r_u = 0.5, 0.8$, and 1.0.

Figure 2.3 illustrates how the *IM* hazard curve and the *IM-EDP* fragility curves are integrated in the PEER framing equation to form the *EDP* hazard curve. Values of $\Delta\lambda_{IM_i}$ and $P[EDP > edp_j | IM = im_i]$ are read from the hazard curve and one of the fragility curves, respectively, at the particular value of $IM = im_i$ and multiplied together. This product is summed with the next product formed from the hazard curve and the same fragility curve at the next value of $IM = im_{i+1}$. The sum that results after traversing the entire range of *IM* for the hazard curve and a single fragility curve is the *y*-coordinate of one point on the *EDP* hazard curve (λ_{EDP_j} at $EDP = edp_j$). Since each fragility curve results in only a single point on the *EDP* hazard curve, there must be enough fragility curves to adequately define the new hazard curve.

This integration process is repeated at each level of the PEER framework to develop the hazard curve for the following level. To calculate λ_{DV} , therefore, it is necessary to have as

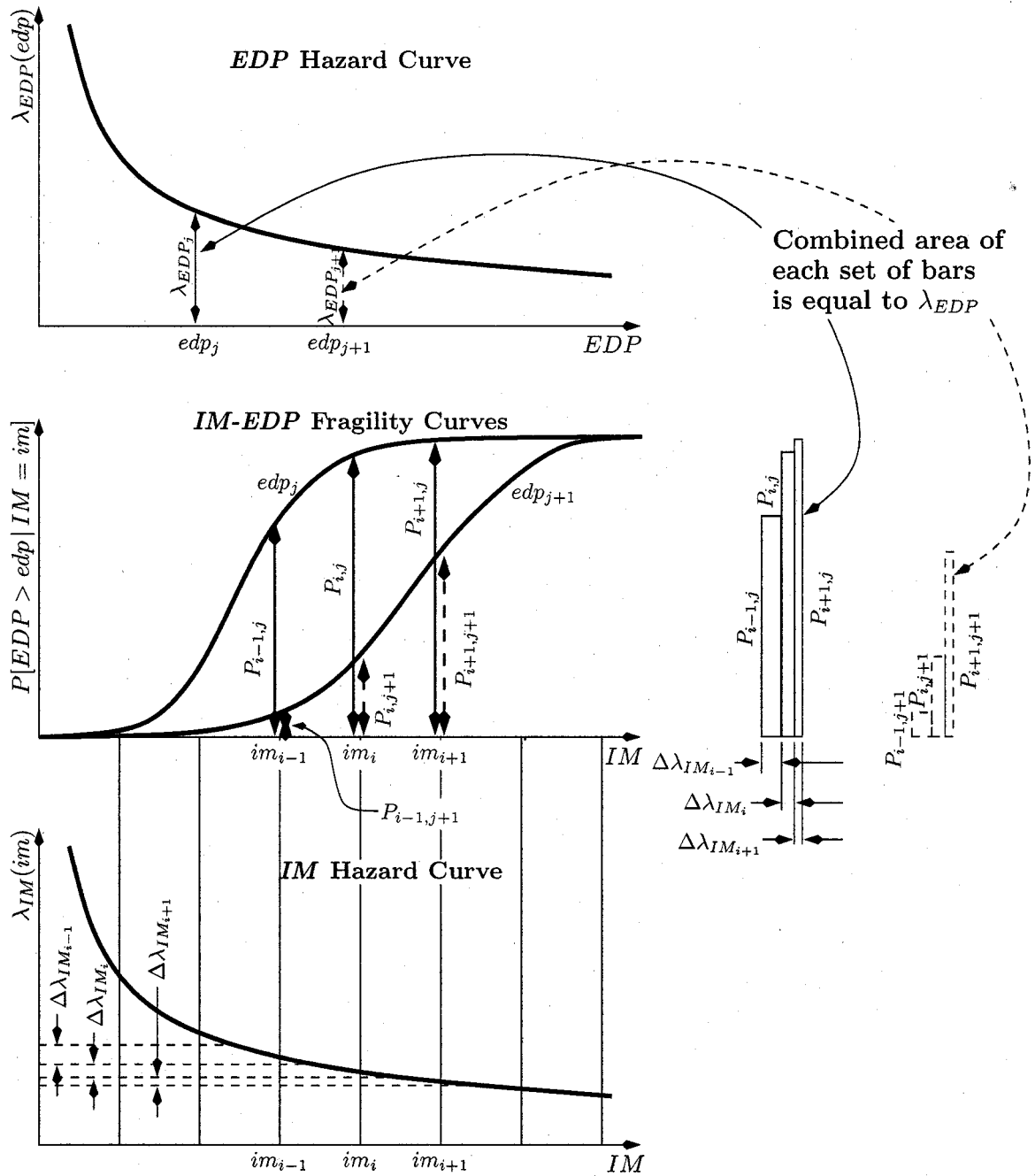


Figure 2.3: Integration of IM hazard and IM-EDP fragility curves to yield an EDP hazard curve. $\Delta\lambda_{IM}$ and $P[EDP > edp | IM]$ are multiplied to form the bar areas on the right, which are summed to produce a single point on the EDP hazard curve.

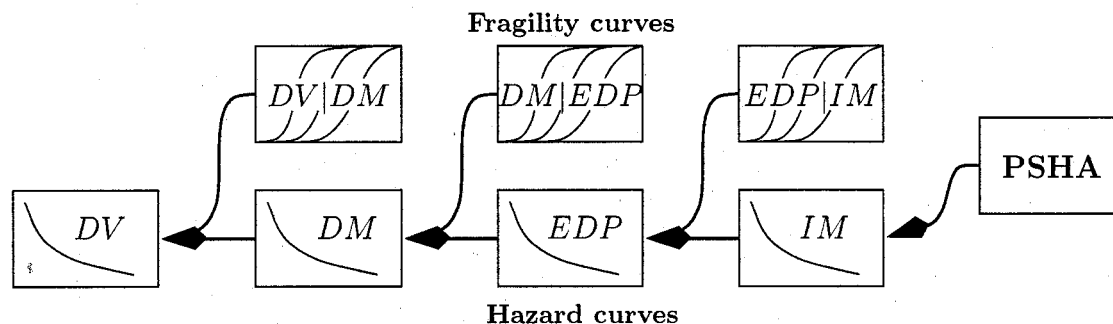


Figure 2.4: Graphical representation of PEER framework.

input only the IM hazard curve from a PSHA and a set of fragility curves for each level of the framework. Figure 2.4 illustrates the entire process.

2.3 Uncertainty within the PEER framework

The previous sections have described how the hazard from a lower level in the PEER framework is propagated to a higher level through combination with a set of fragility curves. The fragility curves are simply conditional probability distributions that quantify the uncertainty in estimations of the hazard in one level of the PEER framework from the hazard in the previous level.

The purpose of separating the analysis into different levels is to improve the overall confidence in the estimate. Even though there is uncertainty associated with each level, the overall uncertainty should be smaller because the hazard estimations at each level are understood better and can be made with less total variability than a single large step from IM to DV .

The three steps in the PEER framework— IM to EDP , EDP to DM , and DM to DV —will not be appropriate for all systems. In some, fewer steps will suffice; in others, more will be required. The total probability theorem can be used to compare the options and determine whether or not subdivision of the system into smaller steps is warranted on the basis of the overall uncertainty:

$$\sum_{im} P[DM > dm | IM = im] > \sum_{edp} \sum_{im} P[DM > dm | EDP = edp] P[EDP = edp | IM = im] P[IM = im]$$

If the inequality is true then the additional subdivision will lower the overall uncertainty. If it is false, the additional subdivision will increase the overall uncertainty but, in some cases, may still be desirable because of the additional detail it provides about the contribution to the final hazard or risk.

With the many sources of uncertainty added into the analysis at each step, it is reasonable to wonder about the accuracy of the final result. This can only be answered definitively with the benefit of hindsight, which requires a long history of use when long return period events are included in the analysis. The PEER framework has not yet been used enough to provide this hindsight. However, in the 30 years since the introduction of PSHA, which uses a similar application of the total probability theorem, no serious difficulties have surfaced except perhaps philosophical differences between the deterministic and probabilistic approaches [43]. The probabilistic performance-based method has the benefit of treating uncertainty in an open, consistent, and objective manner that can be adjusted to accommodate new conditions or changes in our understanding of the underlying physical processes. This is in contrast to the deterministic method, which relies upon subjective interpretation by one or more experts and is often difficult to communicate to non-technical stakeholders. Even if the final result of the performance-based analysis is inaccurate in an absolute sense, consistent treatment of the hazard associated with the separate components of a facility helps to identify which ones contribute most to the overall risk, thus providing a rational basis for allocating resources for design, maintenance, upgrading, and insurance where they will yield the greatest benefit.

2.3.1 *The effect of uncertainty on hazard estimates*

Jalayer and Cornell [63] performed a performance-based analysis of a steel-frame building near Los Angeles, California. Using the spectral acceleration at the building's fundamental

period, S_a , as the *IM* and interstory drift, D , as the *EDP*, they developed an explicit expression for the interstory drift hazard curve having the following form:

$$\lambda_D(d) = \lambda_{S_a}(S_a^d) \cdot e^{f(D, S_a, \beta)}$$

in which S_a^d is the spectral acceleration corresponding to drift, d , and the function in the exponential term,

$$f(D, S_a, \beta) = \frac{1}{2} \left(\frac{k\beta}{b} \right)^2$$

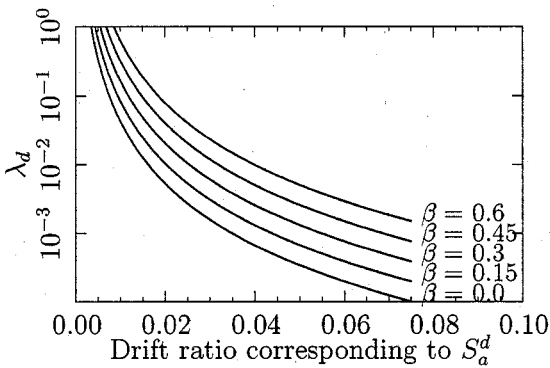


Figure 2.5: Effect of varying uncertainty levels (described by β) on the drift ratio hazard. After Jalayer and Cornell [63].

in which k is a parameter describing the shape of the S_a hazard curve, b is the slope of the relationship between S_a and D in log-log space, and β describes the dispersion of this relationship. In this formulation, the *EDP* hazard curve is simply the product of the *IM* hazard curve and an uncertainty factor that is based on log-normally distributed fragility curves. Jalayer and Cornell suggested that the *IM* hazard curve was a first-order approximation of the *EDP* hazard curve, the accuracy of which depended on the uncertainty described by the fragility

curves: if the uncertainty was zero, the approximation would be exact; if the uncertainty was large, the approximation would be poor. Because the exponential term is always greater than or equal to 1, the *EDP* hazard will always be greater than or equal to the *IM* hazard; as the uncertainty factor increases, so does the amount by which λ_{EDP} exceeds λ_{IM} . Thus, uncertainty increases the apparent *EDP* hazard level.

Jalayer and Cornell provide a numerical example that illustrates how uncertainty amplifies the *EDP* hazard. They found that $\lambda_{S_a}(S_a^d) = 0.00124(30.77d)^{-k/b}$ for the Los Angeles building, in which $k = 3.0$, $b = 1.0$, and $\beta = 0.3$. Figure 2.5 presents a series of drift ratio hazard curves for these parameters with varying β values. The upward shift of the curves as

β increases illustrates uncertainty's amplifying effect on hazard: a change in β of 0.3 alters the exceedance rate by a half order of magnitude.

2.3.2 Predictability, efficiency, and sufficiency

This section describes several terms for considering uncertainty in the hazard and fragility curves and then presents another example of its effect on the results from the PEER framing equation.

In a PSHA (Equation 2.1), the conditional probability distribution is usually determined from an attenuation relationship, which predicts the level of IM at a site given earthquake magnitude, distance, faulting characteristics, etc. Many different attenuation relationships exist in many different forms [13, 66, 120] but all of the modern ones include a term that indicates the dispersion of the predicted quantity. Usually this dispersion is represented by the standard deviation or coefficient of variance that results from the uncertainty of the attenuation model and the variability of the data considered, and describes the variability of the IM prediction. Some attenuation relationships for the same IM have lower dispersions than others, and some IM s are more predictable than others. In this dissertation, the term, *predictability*, will refer to accuracy of the IM hazard curve estimation.

The uncertainty described by the fragility curves is termed *efficiency* [113]. An efficient IM is one that can be used to estimate the EDP with little variability. Since the fragility curves that are involved in this estimation are conditional probability distributions, the degree of variability is indicated by their steepness—an efficient IM with little variability will have steep fragility curves and a tight confidence interval.

The concept of *sufficiency* was introduced by Shome and Cornell [113] and further discussed by Luco and Cornell [84]. An IM is sufficient if the EDP estimated from that IM is conditionally independent of earthquake source parameters such as magnitude or source-to-site distance. Without this independence, the fragility curves, which are usually developed empirically using the IM and an earthquake database, may vary with the specific earthquake records included in the database. Peak horizontal ground acceleration, a_{max} , is an example of an insufficient IM . It is often used in liquefaction or other seismic damage

assessments. By itself, however, a_{max} is not an efficient predictor of many $EDPs$ so it is often combined with earthquake magnitude, which acts as a proxy for the duration and frequency content of the shaking. With an insufficient IM like a_{max} , the uncertainty for both a_{max} and magnitude have to be propagated through to the EDP . This can be done in some cases by developing a 2-dimensional fragility surface—one dimension for a_{max} , the second for magnitude. Also, instead of a single a_{max} hazard curve, a suite of hazard curves is required, one for each magnitude. The complexities associated with an insufficient IM will be explored further in Chapter 4.

Kramer and Mitchell [77] presented an example to illustrate the effect of varying degrees of predictability and efficiency on results from the PEER framing equation. Reproduced in Figure 2.6, their example considered a hypothetical site located near one end of a linear fault. Using the attenuation relationship from Boore et al. [13] with a_{max} coefficients and the generic fragility curves shown in Figure 2.6b, they computed the EDP hazard curve labeled “Base” in Figure 2.6c from Equation (2.3). They then repeated the calculations with the uncertainty in the attenuation relationship and fragility curves increased and decreased by 20%, producing the four additional curves shown in Figure 2.6c. The sensitivity of λ_{EDP} to uncertainty is apparent. For $\lambda_{EDP} = 0.0021$ (475-yr return period), the Base case EDP is about 16. With a 20% decrease in the uncertainty of the hazard and fragility curves (a 20% increase in predictability and efficiency), EDP drops to 8; with a 20% increase in uncertainty (a 20% decrease in predictability and efficiency), EDP nearly doubles to 30. Figure 2.6d shows an equally dramatic change to the shapes of the distribution functions.

Like the example from Jalayer and Cornell [63], Kramer and Mitchell’s work illustrates how increased uncertainty increases the apparent hazard level. This can be seen in Figure 2.6c by the higher hazard curves (greater λ_{EDP}) which indicate more frequent exceedance of larger levels of EDP . It can also be seen in Figure 2.6d from the wider probability distributions, which indicate that larger values of EDP had to be included in the analysis.

In the PEER framework, increased EDP hazard estimates are propagated up through the DM to the DV , resulting in increasingly costly decisions. These simple examples demonstrate the importance of identifying IMs with the highest possible predictability, efficiency, and sufficiency, a task that will be described in the next chapter as it pertains to assessing soil liquefaction potential in a performance-based framework.

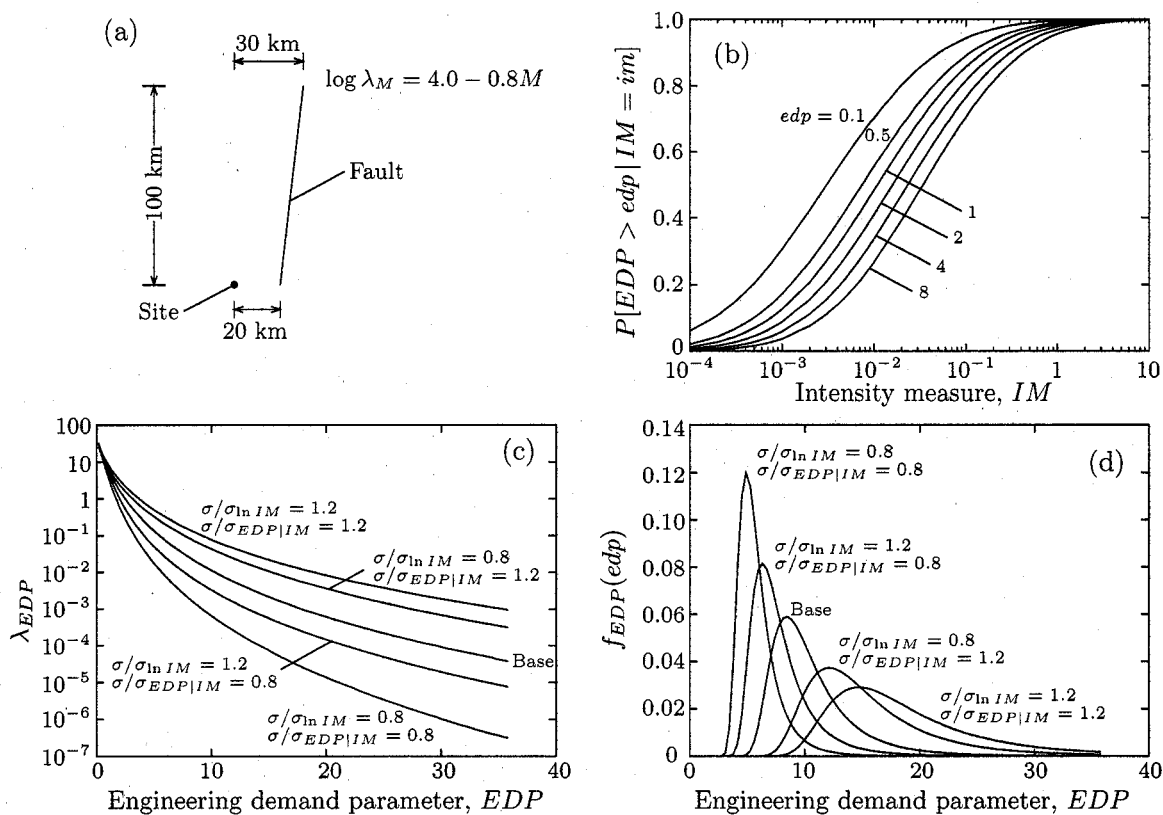


Figure 2.6: The effect of uncertainty in site characterization on EDP . (a) Schematic illustration of hypothetical site, (b) fragility curves for $EDP|IM$, (c) effects of various combinations of uncertainty in attenuation relationship (predictability) and fragility relationship (efficiency) on EDP hazard curve, and (d) probability distributions for 50-yr EDP values. After Kramer and Mitchell [77].

Chapter 3

INTENSITY MEASURES FOR LIQUEFACTION ASSESSMENT

The preceding chapter illustrated how uncertainty in the performance-based method leads to increased design loads, and suggested that a careful choice of Intensity Measure, *IM*, could lower the uncertainty included in the analysis. To prepare for the development of a performance-based method for assessing soil liquefaction potential later in the dissertation, this chapter briefly reviews the basic concepts of liquefaction and examines the current methods of assessing liquefaction potential. The *IMs* used in each method are considered with respect to the concepts introduced in the last chapter: predictability for generation of the *IM* hazard curve, and efficiency and sufficiency for generation of the *IM-EDP* fragility curves.

3.1 Soil liquefaction

Soil liquefaction is the loss of strength and stiffness that can occur due to excess pore water pressure generated when loose, saturated sand or non-plastic silt is shaken or sheared. In slow-draining soil, the tendency of loosely packed particles to move into a denser configuration causes a portion of the total confining pressure to be transferred from the soil skeleton to the pore water, decreasing the effective (interparticle) stress and reducing the stiffness and shear strength of the soil. In extreme cases, the effective stress is reduced to zero and the soil can deform like a viscous fluid; this condition is called liquefaction.

The tendency of a soil to densify depends primarily on its relative density and confining stress: loose soil under a high confining stress tends to densify more than dense soil under a low confining stress. Actual densification occurs only when soil particles move relative to one another into a closer arrangement; thus, pore pressure generation is related to the level of shear strain that occurs within the soil [31, 32, 87, 108, 126]. Under seismic shaking, the strain amplitude depends upon the response of the soil deposit to the input motion, which

is a complicated interaction between the thickness, stiffness, and damping characteristics of the individual soil layers and the amplitude, frequency content, and duration of the ground motion [73, 105].

There are two main approaches to assessing liquefaction potential. The first attempts to model this complicated interaction explicitly in a nonlinear site response analysis with an appropriate constitutive model. An example is the computer program, WAVE [50], with the UWsand constitutive model [74, 75]. In nonlinear site response analyses, the equation of motion is directly integrated in the time domain; with sufficiently small time steps, the shear strain and excess pore water pressure can be estimated from the constitutive model [73]. The accuracy of the result depends upon the suitability of the constitutive model and upon a substantial field and laboratory testing program to determine the parameters for the nonlinear soil model. Consequently, this approach is used mainly for research or projects having a large budget and a long lead time; it is not the primary focus of this dissertation.

The second approach is based upon empirical correlations between seismic loading (demand) and soil resistance to liquefaction (capacity); when demand equals or exceeds capacity, liquefaction is expected. This type of assessment has much wider usage than explicit models, primarily because it is easier and less costly to implement. However, developing a method of assessment using this approach is difficult because there are few *IMs* that describe the rich nature of earthquake shaking.

In this second approach, the methods for assessing liquefaction potential fall into three main groups: cyclic stress, cyclic strain, and energy methods. The cyclic stress method, by far the most common, was developed 35 years ago and persists today with only minor modifications to its original form. The cyclic strain method and the energy method were developed subsequently but have seen relatively little use despite their conceptual advantages over the cyclic stress method. Each of the three methods is described in the remainder of this chapter and their *IMs* are considered for use in the performance-based approach.

3.2 Cyclic shear stress method

The most widely used method for evaluating liquefaction potential describes both loading and resistance in terms of cyclic shear stress, τ_{cyc} , or, after normalizing by the initial vertical

effective stress at the depth of interest within the soil profile, the cyclic stress ratio [103],

$$CSR = \frac{\tau_{cyc}}{\sigma'_{vo}} \quad (3.1)$$

In recent years, it has become common to refer to the cyclic stress ratio that describes a soil's resistance to liquefaction as the cyclic resistance ratio, CRR [128]. With these terms, the potential for liquefaction can be expressed deterministically as a factor of safety against liquefaction,

$$FS_L = \frac{CRR}{CSR} \quad \left(= \frac{\text{resistance}}{\text{loading}} = \frac{\text{capacity}}{\text{demand}} \right) \quad (3.2)$$

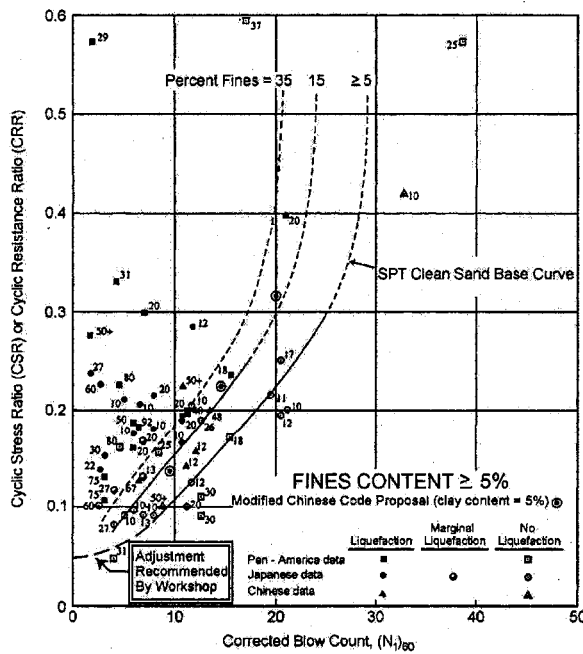


Figure 3.1: Correlation between cyclic resistance ratio and corrected penetration resistance [128].

The resistance term, CRR , is generally determined from correlations with results from field tests on the soil profile such as the cone penetration test, Becker penetration test, shear wave velocity test, or, most commonly, the standard penetration test (SPT). Figure 3.1 shows the correlation between CRR and corrected SPT blow count from Youd et al. [128].

The loading term in the cyclic stress method, CSR , is generally determined from a site-specific ground response analysis like WAVE [50], SHAKE [58, 100], or ProShake [33]; or by using the “simplified” method introduced by Seed and Idriss in 1971 [103].

The first method requires significant effort to provide accurate results: detailed characterizations of shear wave velocity profiles, modulus reduction and damping curves, and other site-specific parameters must be developed for use in multiple site response analyses with a range of carefully selected input motions. This effort is rewarded, however, with information concerning the effects that a particular soil profile has on CSR . In the simplified method, site-specific details are buried in a depth reduction factor, r_d , that approximates the average response of many soil profiles to many

ground motions. Despite this loss of detail, the simplified method is much more commonly used in engineering practice because it is so much easier to implement. A review of the development history of the simplified method provides insight about its strengths and suggests areas where improvement may be possible.

3.2.1 The simplified method

Seed and Idriss are generally credited with introducing the simplified method in 1971 [103]. Although numerous improvements have been suggested, they have been relatively minor and the original method remains largely intact. This is remarkable given the significant advances in our understanding of earthquake shaking and the mechanics of liquefaction that have taken place over the last 35 years.

Cyclic stress ratio

Most early work on liquefaction potential in the U. S. was based on laboratory testing, particularly the stress-controlled cyclic triaxial and cyclic simple shear tests [20, 107], in which cyclic shear stress was a natural measure of loading. Noting that shear stresses in a soil mass caused by earthquake shaking are primarily due to the upward propagation of shear waves, Seed and Idriss [103] related cyclic shear stress, τ_{cyc} and earthquake acceleration at the depth of interest within the soil profile, a , through Newton's second law:

$$\tau_{cyc} = \frac{\gamma h}{g} a$$

in which γ is the total unit weight of the soil above the point of interest, h is the depth of the point of interest below the ground surface, and g is gravitational acceleration in the same units as a . Because the investigative focus was on laboratory testing, the irregular amplitude of earthquake time histories was converted to an equivalent uniform amplitude for harmonic cycles that were more easily applied with the pneumatic loading equipment available at that time. This conversion involved applying a representative ratio of the peak acceleration: Whitman [124] assumed 2/3, Seed and Idriss [103] estimated 0.65. Both investigators based these ratios largely on judgment guided by preliminary statistical evaluations related to

laboratory testing; Seed et al. [106] investigated this relationship more completely and their choice of 0.65 remains in use today.

With these terms, the cyclic shear stress could be written as

$$\tau_{cyc} \approx 0.65 \frac{a}{g} \sigma_{vo}$$

and the cyclic stress ratio as

$$CSR = \frac{\tau_{cyc}}{\sigma'_{vo}} \approx 0.65 \frac{a}{g} \frac{\sigma_{vo}}{\sigma'_{vo}}$$

in which σ_{vo} is the initial vertical total stress at the depth of interest in the soil profile ($\sigma_{vo} = \gamma h$). These relationships are appropriate for cases in which the acceleration time history is available at the depth of interest within the soil profile from, say, ground response analysis. In many cases, though, there is insufficient information about the site for such an analysis, and the acceleration at the depth of interest must be estimated from a time history recorded at the ground surface. The depth reduction coefficient, r_d , presented by Seed and Idriss [103] makes this possible.

In developing r_d , the equivalent linear ground response program, SHAKE, that was under development at the University of California's Berkeley campus [100] was used to compute the ground response for a wide range of soil profiles from a wide range of seismograms. These responses were then averaged to form r_d , relating τ_{cyc} at the ground surface to τ_{cyc} at the point of interest within a soil profile (Figure 3.2). Perhaps more than any other contribution, this led to the widespread use of the Seed-Idriss simplified method within the geotechnical community. More details about the development and later refinement of r_d are in Chapter 5.

With this term, the cyclic stress ratio could be expressed as

$$CSR = \frac{\tau_{cyc}}{\sigma'_{vo}} \approx 0.65 \frac{a_{max}}{g} \frac{\sigma_{vo}}{\sigma'_{vo}} r_d \quad (3.3)$$

in which a_{max} is the peak horizontal acceleration at the ground surface. This form is equivalent to the one presented in 1971 by Seed and Idriss [103], and is still in use.

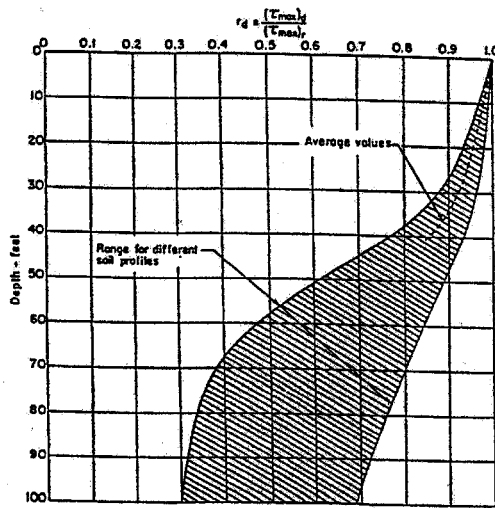


Figure 3.2: Depth reduction coefficient after Seed and Idriss [103].

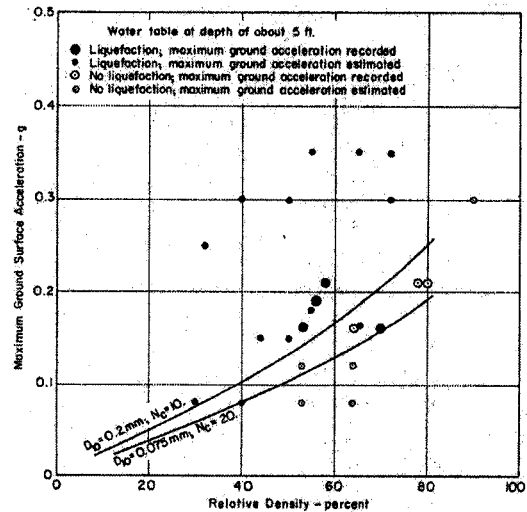


Figure 3.3: Correlation between peak ground acceleration causing liquefaction in the field and relative density of sand [103].

Cyclic resistance ratio

The resistance term of the cyclic stress method has undergone more adjustment than the loading term. This is primarily due to the limited number of case histories that were originally available: as more earthquakes have occurred and caused liquefaction, more sites encompassing varied conditions have been investigated according to the rational framework of the cyclic stress method.

Although FS_L in the cyclic stress method has always been expressed in terms of the cyclic stress ratio, Seed and Idriss's original liquefaction resistance correlation [103] was presented in terms of a_{max} and soil relative density, D_r (Figure 3.3). This was a great step forward in making the assessment of liquefaction potential available to geotechnical engineers, but presentation in these terms was limiting. The use of a_{max} instead of CSR required assumptions about the depth, groundwater level, and associated vertical stresses. The use of D_r required an assumption about its relationship with SPT penetration resistance since that was the method used to characterize the soil profile in the case histories available

at that time. Whitman [124] suggested plotting CRR versus penetration resistance, and later updates of the CRR correlation by Seed and his coworkers [105, 109] and Youd et al. [128] adopted this now-familiar format.

Over the years, several factors have been developed to expand the applicability of the CRR plot beyond the cases that were originally considered; these improvements are described in the following sections.

Magnitude scaling factor

Seed and Idriss [103] recognized that a_{max} was an incomplete measure of earthquake shaking because it contained no information about the duration or frequency content. To account for duration, they suggested that there were approximately 10, 20, and 30 significant stress cycles, N_C , for Magnitude 7, 7.5, and 8 earthquakes, respectively, and adjusted their correlations between a_{max} and D_r accordingly. These assumptions about magnitude and significant cycles were refined by Seed et al. [106] and again by Seed and Idriss [104, 105] into a magnitude scaling factor, MSF , that serves as a proxy for the duration of shaking. Since then, it has received minor adjustments from Ambraseys [1], Arango [5], Andrus and Stokoe [2], Youd and Noble [129], Idriss [54], Liu et al. [83], Çetin [21, 24] and Idriss and Boulanger [57].

The need for two parameters, a_{max} and magnitude, to describe the loading in the cyclic stress method has important consequences for statistical uncertainty that will be discussed later.

SPT corrections

In the original presentation of the simplified method, the use of relative density as a measure of the soil's resistance to liquefaction allowed data from laboratory and field testing to be used in the CRR correlation. Most laboratory testing was done on specimens reconstituted to a specific void ratio or relative density, and correlations such as the one by Gibbs and Holtz [38] were used to convert field penetration resistance to relative density. It was recognized, however, that penetration resistance was influenced by factors such as

aging, cementation, and horizontal effective stress in addition to relative density, and that these factors also influenced liquefaction resistance in laboratory testing. It is practically impossible to replicate these in situ characteristics in laboratory specimens, and even the most careful soil sampling methods alter these characteristics to some degree. Thus, the use of laboratory testing to determine CRR became limited to special soils outside the database of field case histories.

For field testing, Whitman [124] suggested that the apparent relative density from penetration resistance should be used even when actual measurements of relative density were available. Christian and Swiger [26] concurred, noting that liquefiable soils were often stratified and that laboratory determinations of minimum and maximum densities often involved mixed samples. They suggested that relative density as correlated from penetration resistance and overburden pressure per Gibbs and Holtz [38] should be considered as an index of the soil's resistance to liquefaction. By 1975 when Seed et al. [102] first updated the CRR curves, penetration resistance had supplanted D_r , and the standard penetration test came under scrutiny.

It had long been known that the penetration resistance of soil was affected by the effective overburden pressure, σ'_{vo} . In 1971, Seed and Idriss [103] used data from Gibbs and Holtz [38] to develop an overburden correction factor, C_N , to normalize the sand penetration resistances to an equivalent σ'_{vo} of 1 atm, N_1 (Figure 3.4a). Studies at the Waterways Experimental Station [12, 85] provided updated information that allowed Seed and Idriss to improve C_N [104] so that it was applicable for relative densities of 40 to 60% and 60 to 80% (Figure 3.4b). In 1986, Liao and Whitman [82] presented the simple and still widely used relationship:

$$C_N = \left(\frac{p_a}{\sigma'_{vo}} \right)^{0.5} \leq 1.7 \quad (3.4)$$

When C_N was applied to energy-corrected blow counts, N_{60} , the result was termed $N_{1,60}$.

Kayen et al. [68] suggested an alternative form for C_N that inherently included the upper limit and, according to Youd et al. [128] fits the Seed et al. curves slightly better:

$$C_N = \frac{2.2}{1.2 + \sigma'_{vo}/p_a} \quad (3.5)$$

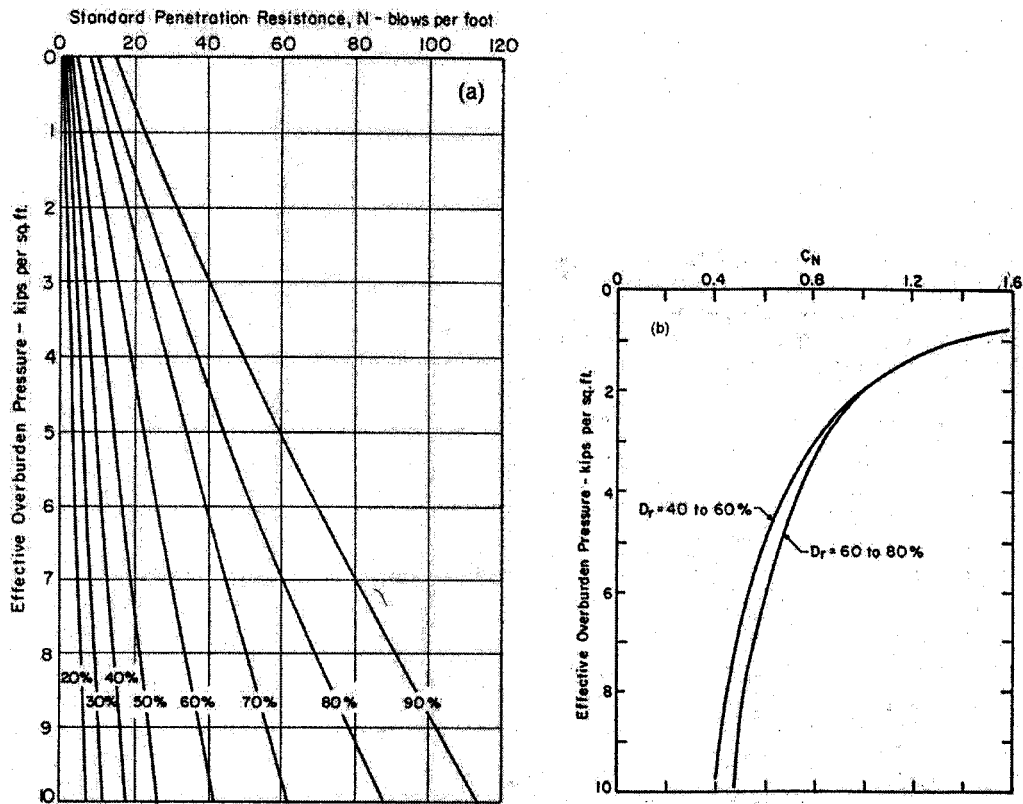


Figure 3.4: Overburden stress corrections for penetration resistance from (a) Seed and Idriss [103] and (b) Seed et al. [109].

Boulanger [15] reconsidered the WES data and determined that the relationship for C_N could be improved if the exponent in Liao and Whitman's equation was a function of relative density. Boulanger and Idriss [17] proposed the following:

$$C_N = \left(\frac{p_a}{\sigma'_{vo}} \right)^\alpha \leq 1.7, \quad \alpha = 0.784 - 0.0768\sqrt{N_{1,60}} \quad (3.6)$$

in which C_N and $N_{1,60}$ are solved iteratively.

Even though the American Society for Testing and Materials had a standard for the SPT since the early 1960s (ASTM D1568), reviews by Kovacs et al. [71, 72] and Schmertmann [99] showed that the actual energy applied to the SPT sampler from the falling hammer on typical drill rigs ranged from about 30% to about 80% of the theoretical maximum. This wide range naturally caused a large variation in the SPT blow count. Seed et al. [109, 110]

and Skempton [114] proposed a set of standards for drilling method, bore hole diameter, drilling fluid, drill rod diameter and length, hammer type, and sampler configuration that would result in a hammer efficiency of approximately 60% of theoretical. For testing conditions that varied from these standards, a series of coefficients was introduced to correct the blow counts to an equivalent N_{60} .

Although the focus thus far has been on correlating the soil's liquefaction resistance to the standard penetration test, it is important to note that there also are correlations with cone penetration resistance [96], Becker penetration resistance [46], and shear wave velocity [2, 3]. Each of these has certain advantages but they are not likely to entirely supplant the SPT because none of them allows collection of a soil sample. Since not all soil types are susceptible to liquefaction (clays, for example), the ability to classify and test a soil sample is an important part of liquefaction assessment.

Fines content

The laboratory testing that formed part of the basis for the simplified method indicated that CRR was affected by mean particle size: finer soils have lower CRR [103]. However, SPT data collected by Tokimatsu and Yoshimi [117] after the 1978 Miyagi-ken Oki earthquake in Japan showed that silty sand sites with the same penetration resistance as clean sand were less vulnerable to liquefaction. The same conclusion was reached by Zhou [131] from his work in Tangshan, China, after the devastating 1976 earthquake. It is not clear if fines somehow increase the liquefaction resistance of soil or if they reduce its penetration resistance. To account for this effect, Seed and Idriss [104] presented a CRR plot with a curve for soil with mean particle diameter, D_{50} , larger than 0.25 mm and a second curve above and to the left of the first for soil with D_{50} smaller than 0.15 mm. The modified penetration resistance, N_1 , of the new curve was 7.5 blows per foot (bpf) less than that of the original line. In 1985, Seed et al. [109] refined this correction slightly by presenting curves for three fines contents on the CRR plot: less than five percent, fifteen percent, and thirty-five percent (Figure 3.5). Relative to the clean sand (< 5% fines) curve, $N_{1,60}$ for the 15% fines curve is about 3.5 bpf less at $CRR = 0.1$ and about 5 bpf less at $CRR = 0.5$;

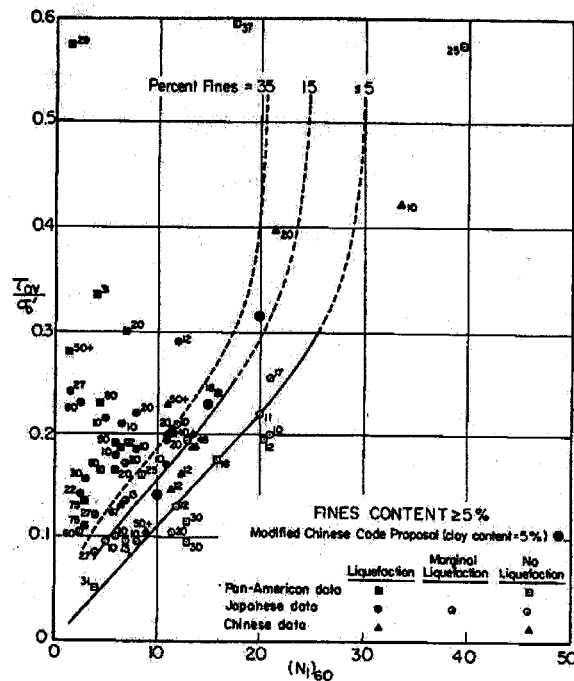


Figure 3.5: Correlation between stress ratio causing liquefaction in the field and penetration resistance of sand [109].

the 35% fines curve is about 5.5 and 8.5 bpf less at $CRR = 0.1$ and 0.5 , respectively. This version of the fines correction remains in current use, although Çetin [21, 24] proposed a slightly different version for his probabilistic model.

3.2.2 Overburden stress correction

Early laboratory testing by Castro [20] and Casagrande [19] found that the liquefaction potential of sand increases nonlinearly with effective confining stress. Thus, of two elements having the same soil type, relative density, particle size, and other characteristics, the one under greater confining stress has greater liquefaction potential. Most of the case histories in Seed and Idriss's database were for depths less than 10 m and vertical effective stresses less than about one atmosphere, so not accounting for varying overburden stress was not a significant source of error. As usage of the simplified method expanded to include cases with greater depths, Seed [101] introduced the correction factor, K_σ .

The overburden stress correction serves a different purpose than the C_N correction factor applied to penetration resistance: the latter factor allows prediction of the apparent relative density under different effective stresses, while the former allows prediction of the liquefaction potential at the same apparent relative density under different effective stresses.

Additional site data compiled by Harder [44, 112], Harder and Boulanger [45], and Hynes and Olsen [52] resulted in modifications to K_σ . Çetin [21, 24] used an expanded case history database to reassess the effect of overburden pressure on liquefaction potential, and Boulanger and Idriss [15, 16, 17, 57] used critical state soil mechanics to assemble a revised functional form for K_σ . This critical state formulation has led to a new approach for including the effects of overburden pressure: K_σ typically has been applied as a correction factor to CRR , but Boulanger and Idriss have presented a rationale for applying it to the normalized penetration resistance.

3.2.3 Static shear stress correction

For the first dozen years of its existence, the simplified CSR method was appropriate only for level ground sites without a significant static shear stress. In 1983, Seed [101] used data from isotropically consolidated triaxial tests performed under a range of confining pressures and initial shear stresses to develop the factor, K_α , to correct the CRR curves for the presence of initial shear stress. Harder and Boulanger [45] and Hynes and Olsen [52] noted that several investigators had added to and modified Seed's original work, resulting in a wide range of recommendations that sometimes conflicted. Youd et al. [128] suggested that K_α should be used only by specialists in geotechnical earthquake engineering. Recent work by Boulanger [16, 55, 56] made use of critical state soil mechanics to resolve some of the confusion about K_α and to describe the parameter's variation in terms of relative density and confining stress.

3.2.4 Current form of CSR method equations

With the addition of the correction coefficients, the factor of safety against liquefaction in the CSR method is expressed in the following form [128]:

$$FS_L = \frac{CRR}{CSR} MSF \cdot K_\sigma \cdot K_\alpha \quad (3.7)$$

where CRR is determined from Figure 3.1 and CSR is calculated according to Equation (3.3). This arrangement is awkward, in part because the IM is a combination of a ground motion parameter at the site (a_{max}) and a source parameter (M_w). More important, though, is the relationship between a_{max} and MSF . Originally the cyclic stress method was used deterministically; that is, engineers selected design earthquakes with specific magnitudes at specific locations and, for each event, calculated the expected a_{max} at the site of interest from an attenuation relationship. Thus, each value of a_{max} at the site was associated with a specific magnitude and corresponding MSF at the source. More recently, however, a probabilistic seismic hazard analysis [27, 90] is usually used to calculate a_{max} by integrating contributions from all possible magnitudes and source-to-site distances according to their probabilities of occurrence. Thus, the basis for choosing a magnitude for MSF is no longer clear. Most often, the mean magnitude (the average of all magnitudes weighted by their contribution to a_{max}) or the modal magnitude (the magnitude occurring most often in the calculation of a_{max}) is used, but in some seismic environments this is not an easy decision. In Seattle, for example, the large subduction source zone along Washington's west coast and the closer Seattle fault result in two strong magnitude modes; the mean magnitude usually falls between these two modes, thus representing a condition that is unlikely to occur.

However the choice is made, representing the frequency content and duration of an entire range of magnitudes with a single value of MSF is a notable departure from the original method. Nonetheless, the use of PSHA has become very popular because of the information it provides about the average rate at which a particular level of IM will occur: describing an a_{max} as having a mean annual rate of exceedance of 10% in 50 years is more informative than trying to describe an a_{max} that, in the judgement of a particular engineer, is most appropriate. It is common geotechnical practice [88] to require FS_L to be at least 1.1 to 1.3 given an a_{max} with an average annual rate of exceedance of 10% in 50 years.

3.2.5 Probabilistic interpretations of CRR

As the use of probabilistic estimation of CSR from the results of a PSHA was developing, researchers were also considering probabilistic representations of CRR . Seed and his collaborators located the boundary between cases where liquefaction had and had not occurred through a combination of statistical regression and manual adjustment to provide a conservative deterministic result of CRR and, thus, FS_L [103, 128]. This sharp boundary included no information about the uncertainty of the $CRR-N_{1,60}$ relationship. To overcome this deficiency, several investigators developed representations of the boundary between liquefaction and non-liquefaction cases as a probabilistic distribution rather than as a single curve. This approach led to a probability of liquefaction, P_L , instead of FS_L , for a_{max} with a chosen return period and M_w .

Liao et al. [81] presented the first probabilistic representation of CRR in 1988 based on modern statistical methods. Earlier researchers [26, 30, 41, 125] had used ad hoc combinations of error minimization, discriminant analysis, and other classification methods to estimate liquefaction probability, but Liao et al. applied logistic regression to develop a probabilistic boundary between the liquefaction and non-liquefaction cases.

At the time, the case history database compiled by Seed et al. [110] was too sparse to reliably estimate a probability distribution. Liao et al. added considerably to the database but to achieve this, they were less severe in their screening for data quality [24]. Their probability distribution between liquefaction and non-liquefaction cases is shown in Figure 3.6a. Perhaps as a result of the lower quality data, they were not able to find a significant effect of fines content on the relationship, so they limited the use of their curves to soils with a fines content less than 12 percent.

Youd and Noble [129] used an approach similar to that of Liao et al. but they pruned the case history database of the most questionable data and added cases from earthquakes that had recently occurred. Rather than look for an effect of fines from the results of the regression, they applied the fines correction deterministically to the data before the regression. As can be seen from the relatively wide spacing of the probability contours in Figure 3.6b, the resulting variance was high.

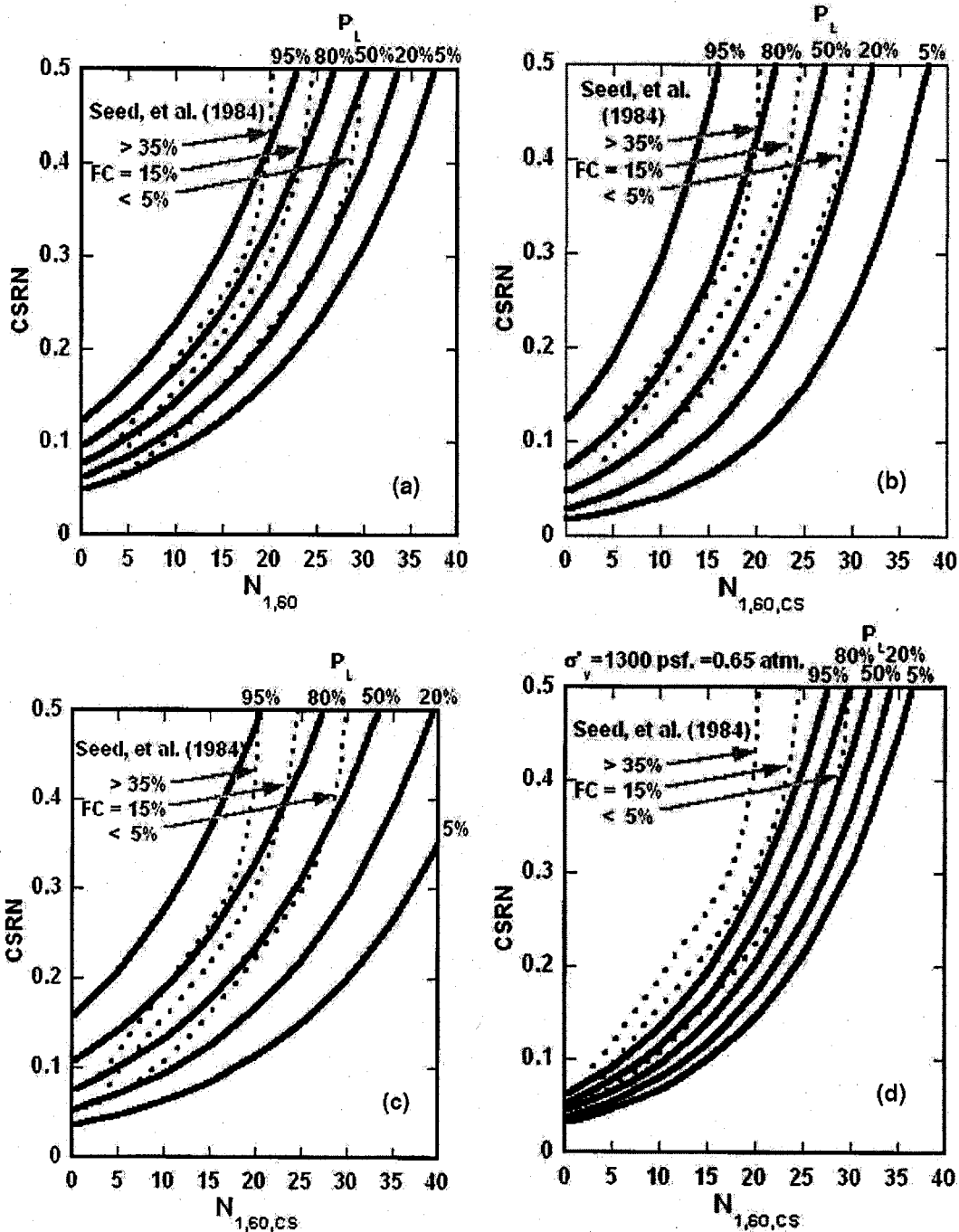


Figure 3.6: Probabilistic *CRR* curves from (a) Liao et al. [81], (b) Youd and Noble [129], (c) Toprak et al. [118], and (d) Çetin et al. [24]. *CSR_N* is *CRR* corrected for earthquake magnitude and fines content. After Seed et al. [111].

The main difference between the work by Toprak et al. [118] and Youd and Noble is the addition of more cases from recent earthquakes to the database. They continued applying the fines correction deterministically before performing the logistic regression. It is interesting to note from Figure 3.6c that the variance increased even though additional data was available.

The three methods described so far made no effort to separate parameter (aleatory) variability from model (epistemic) uncertainty. Thus, unless a practitioner used investigative methods that involved the same degree of variability as those used to produce the case history data, the probability distributions in Figure 3.6 would not be applicable. In addition to updating the database to include cases from recent earthquakes, Çetin [21] went to the extra effort of estimating the variability of each parameter (e.g., a_{max} , σ_{vo} , σ'_{vo} , r_d , fines content, and $N_{1,60}$). This parameter variability was then included in the regression as a separate independent variable so the resulting probability distribution included only the model uncertainty. Excluding parameter variability is the main reason why Çetin's distribution in Figure 3.6d is tighter than the others.

Çetin's work differed from the rest in other ways. Not only was the fines content determined from the regression, but so were C_N , MSF , and K_σ . In addition, Çetin developed a new formulation for r_d that was related to a_{max} , magnitude, and the average shear wave velocity in the upper 12 m of the soil profile. Instead of logistic regression, Bayesian updating was used with a non-informative prior distribution. Further discussion about this approach is in Chapter 6.

3.2.6 Summary of the CSR method

The shift from deterministic to probabilistic estimations of *CSR* and *CRR* has allowed the results from the cyclic stress method to be communicated in a manner that is better suited to risk-based (but not performance-based) assessments. However, the basic form and underlying assumptions remain, as do the inherent deficiencies:

1. It is well known that the development of excess pore water pressure in soil is more closely related to shear strain amplitude than shear stress amplitude [31, 32, 108, 126].

2. The entire time history is represented by a single point corresponding to a_{max} . Using this logic, all ground motions with the same a_{max} resulting from earthquakes with the same magnitude would be expected to produce the same increase in pore water pressure in a given soil deposit. This is clearly not the case, so the *CSR* method results in a high record-to-record variability.
3. With the use of a_{max} , there is no way to know if liquefaction will occur near the beginning of the ground motion or near the end. A very low FS_L or very high P_L may suggest that liquefaction will occur early in a strong ground motion, but it could also result from a ground motion with one very large acceleration pulse late in the record. As a result, the cyclic stress approach offers limited insight into the potential effects of liquefaction.
4. A ground motion parameter, a_{max} , and a source parameter, M_w , are required to predict the loading term, each contributing its uncertainty to the resulting *CSR*, FS_L , and P_L . This uncertainty is increased when a_{max} comes from a PSHA and there is no individual value of M_w that is specifically associated with it.

Despite these deficiencies, the cyclic stress method remains in widespread usage because it is easy to implement and it has proven to be comfortably conservative; that is, there are many cases in which liquefaction has not occurred even though the method has predicted liquefaction, but relatively few cases where liquefaction has occurred when the method predicted it would not occur (Figure 3.1).

Even though loading and resistance in the cyclic stress method are cast in terms of *CSR*, the *IM* is generally considered to be a_{max} since it can be used to compute *CSR* in a simple and direct manner. Because FS_L also depends on magnitude via the magnitude scaling factor, though, a_{max} is insufficient according to the definitions presented in the preceding chapter. The fragility surfaces can be computed using one of the probabilistic representations of *CRR* described above. However, the fact that pore pressure generation is more closely related to shear strain than shear stress suggests that the *IM* efficiency will not be especially high. The final characteristic, predictability, should be quite good

for a_{max} because attenuation relationships for a_{max} have been carefully studied for over a half century and the modern ones include many factors that account for near- versus far-field motions, soil type, fault type, etc. However, there is also uncertainty associated with magnitude, which will reduce the predictability of CSR from that of a_{max} . A comparison of the CSR method's efficiency, sufficiency, and predictability with those for other IM s will be presented at the end of this chapter.

3.3 Cyclic strain method

In many ways, the implementation of the cyclic strain method is similar to the cyclic stress method. The liquefaction potential is expressed as a factor of safety against liquefaction, which is the ratio of resistance to loading, and the loading term is the cyclic shear stress divided by the shear strain modulus:

$$\gamma_c = 0.65 \frac{a_{max}}{g} \frac{\sigma_{vo} r_d}{G_c} \quad (3.8)$$

in which γ_c is the shear strain caused by earthquake shaking and G_c is the shear modulus at the strain, γ_c .

The cyclic strain method offers several advantages for determining liquefaction resistance. As described earlier in the chapter, excess pore water pressure is generated as a result of the tendency of loose soils to densify under cyclic loading. Since densification requires the development of permanent strain from the movement of particles relative to one another, it is reasonable that the generation of excess pore water pressure should be closely related to shear strain. This has been confirmed in laboratory testing, which showed that pore pressure generation is affected much more by shear strain than stress history or cyclic stress [31, 32, 87, 108, 126].

There are two primary benefits to the cyclic strain approach. First, there is a threshold shear strain below which no permanent relative movement of soil particles takes place; Dobry et al. [32] found this to be approximately 0.01 percent for clean sand (Figure 3.7a). At strains below this threshold the soil skeleton deforms elastically. The cyclic strain approach accounts for this aspect of soil behavior by predicting no excess pore water pressure for ground motions that do not cause strains exceeding this threshold. Second, laboratory test

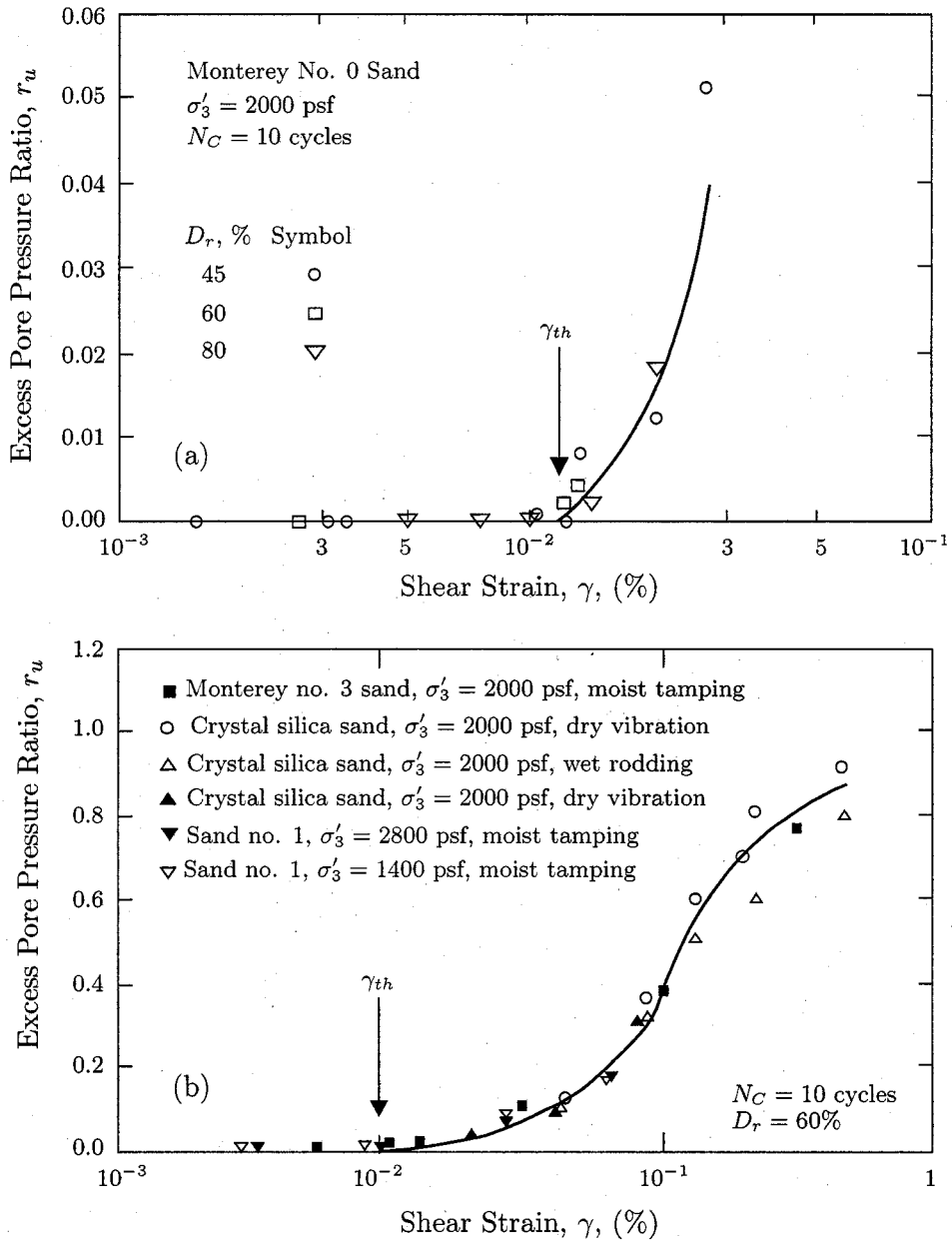


Figure 3.7: Pore pressure generation from (a) small and (b) large strains during triaxial testing. γ_{th} is the threshold strain below which permanent strain does not occur. After Dobry et al. [32].

specimens prepared by different methods and subjected to different stress histories all show very similar relationships between generated pore water pressure and cyclic shear strain [32, 108] (Figure 3.7b). This implies that liquefaction resistance could be determined from strain-controlled laboratory tests as an alternative to empirical field-based methods.

Unfortunately, there is a huge disadvantage to the cyclic strain approach on the loading side of the equation. In the current state of practice it is not possible to accurately predict γ_c due to earthquake loading. If dynamic equilibrium is satisfied, the prediction of stresses cannot be too much in error; however, there is no corresponding constraint on strain. The severity of this problem is such that the cyclic strain method is very rarely used in engineering practice. Using the definitions from the preceding chapter, γ_c is an efficient *IM* for estimating pore pressure generation but it has very poor predictability.

The difficulty in predicting cyclic strain stems from way that G_c in Equation (3.8) is determined. Dobry et al. [32] suggested the use of modulus reduction (G/G_{max}) curves:

$$G_c = G_{max} \frac{G_c}{G_{max}}$$

Thus, G_c is determined from the modulus reduction curves at the strain, γ_c , which is unknown. If the curves remained constant, G_c and γ_c could be found by iteration; however, as pore pressures increase, the soil softens and the modulus reduction curves change. With our current level of understanding of the mechanics of soil behavior, predicting this change with a reasonable degree of accuracy is not possible. Because of this, the suitability of the cyclic strain method is similar to that for the program SHAKE: it works well for situations in which there is no appreciable pore pressure buildup. Unfortunately, this is rather a severe limitation for assessing liquefaction, which results from large pore pressures.

The *IM* for the cyclic strain method is cyclic strain, γ_c . Since it depends on a_{max} and magnitude, it is an insufficient parameter. As noted above, the efficiency of liquefaction prediction appears to be considerably better than for the cyclic stress method, but the predictability of γ_c is very poor even though the predictability of a_{max} is relatively high. No probabilistic relationships exist that would allow calculation of fragility curves.

3.4 Energy approach

The most recent method for characterizing liquefaction potential is based on dissipated energy. This approach originated in the work of Nemat-Nasser and Shokooh [92], who showed that the permanent volumetric strain of an assemblage of particles sheared cyclically under drained conditions could be related to the hysteretic energy dissipated by the assemblage. They then showed how this would relate to pore water pressure generation under undrained conditions. The fact that dissipated energy, which is proportional to the area of a hysteresis loop, depends on both stress and strain puts this approach somewhere in the middle of the cyclic stress and cyclic strain approaches described above.

There have been several proposals for estimating dissipated energy, both directly from the earthquake source parameters, magnitude and distance [11, 30, 79, 121], and from site *IMs* like peak ground velocity and duration [121], spectral acceleration or velocity [121], and Arias intensity [66, 98]. Green [40] presented a comparative review of these methods and found most of them lacking in fundamental ways. For example, he noted that Running's Arias intensity method [98] predicts a decrease in FS_L with increased $N_{1,60}$, which is contrary to the cyclic shear stress and strain methods and to common sense. He noted that Kayen and Mitchell's Arias intensity method is the most promising even though it is insensitive to changes in groundwater depth.

3.4.1 Arias intensity method

Arias intensity is related to the energy dissipated by a population of single-degree-of-freedom oscillators [8], and is defined as

$$I_a = \frac{\pi}{2g} \int_0^{t_0} a_x^2(t) dt + \frac{\pi}{2g} \int_0^{t_0} a_y^2(t) dt \quad (3.9)$$

In this equation, g is gravitational acceleration, t_0 is the duration of earthquake shaking, and a_x and a_y are the two perpendicular components of horizontal ground acceleration. This relationship has some very attractive characteristics. First, I_a is an integral parameter—it is based on a time integral of the ground motion—so it considers all amplitude peaks, not just the highest one. Figure 3.8 illustrates the importance of this characteristic. Even though the

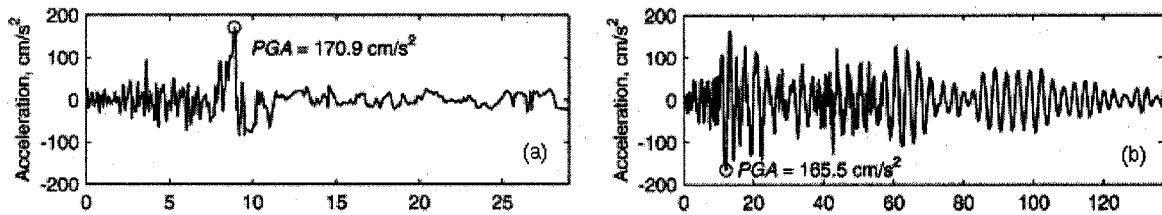


Figure 3.8: Acceleration time history of (a) Kawagishi-cho EW component 1964 Niigata earthquake (M7.5) and (b) Hachirogata NS component 1983 Nihonkai-Chubu earthquake (M7.7). After Kostadinov and Towhata [69].

Hachirogata time history has a slightly smaller a_{max} (PGA) than the Kawagishi-cho record, its overall motion is more severe because it has more strong pulses over a longer duration. In the cyclic stress method, these two records would have about the same CSR (at the same depth and with the same unit weights) because a_{max} and magnitude are about the same. However, $I_a = 0.82$ m/s for the Kawagishi-cho record and 4.47 m/s for the Hachirogata record.

Another benefit of an integral parameter is its sensitivity to duration. Pore pressures build up through the duration of the shaking, not all at once when the a_{max} spike occurs. This is evident from the pore pressures recorded at the Wildlife site during the 1987 Superstition Hills earthquake (Figure 3.9). At the time a_{max} occurred, the pore pressure ratio was less than 10%; most of the pore pressures were generated after the end of the strong shaking. Because integral IM s increase with time similar to the pore pressure ratio, they hold out the possibility of estimating the time and the value of IM at which liquefaction is initiated—something that is clearly impossible with a peak IM like a_{max} . This concept is further explored in Chapter 6.

Several researchers have noted a correlation between Arias intensity and damage. Harp and Wilson [49] found that I_a correlates well with distributions of earthquake-induced landslides. Cabañas et al. [18] found that damage to rural structures and adobe and clay houses can be correlated to I_a . Borja et al. [14] used I_a as a criterion for comparing the results from two seismic response analysis codes. Travararou et al. [120] described a study of correlations between different intensity measures and seismically induced permanent slope

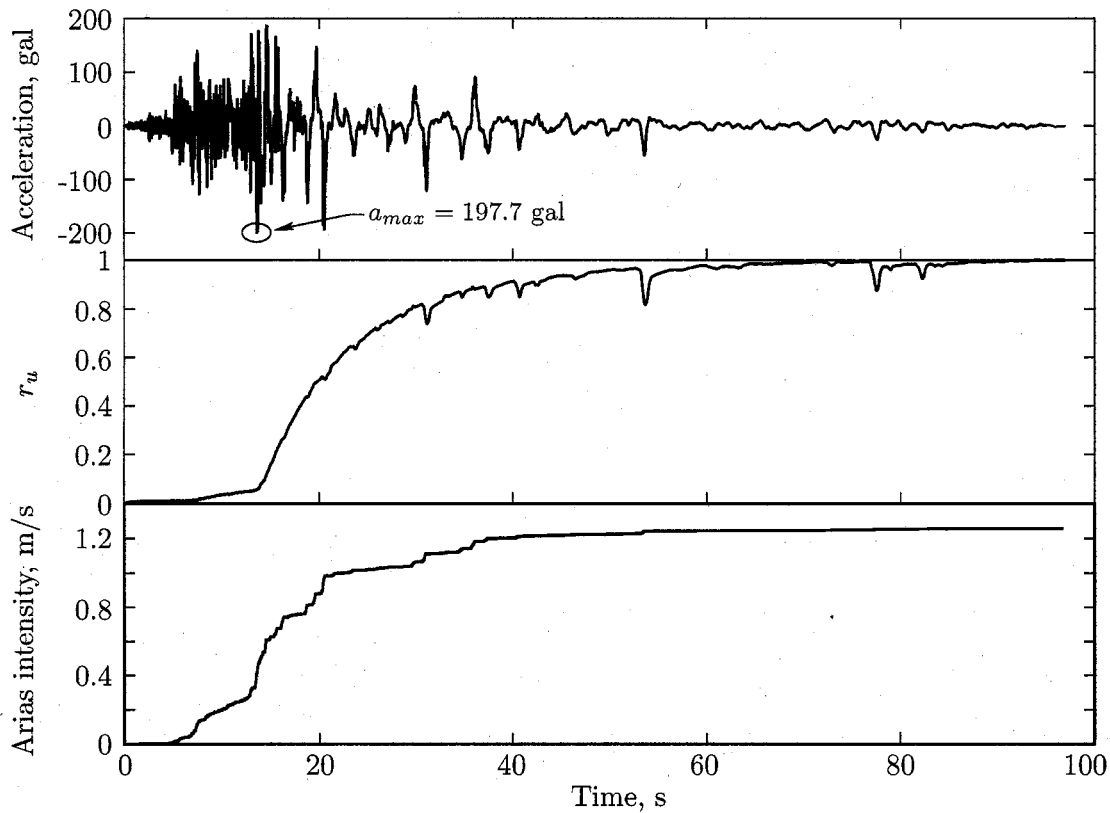


Figure 3.9: Time history of acceleration; pore pressure ratio, r_u ; and Arias intensity from the Wildlife site, 1987 Superstition Hills earthquake.

displacements which found that I_a performed better than more common parameters such as a_{max} and v_{max}^2 in correlating with damage in stiff systems (slopes with fundamental periods less than 1 s). Results for slopes with longer fundamental periods indicated that a velocity-based parameter or a period-dependent intensity measure was more appropriate.

Kayen and Mitchell [66] presented a method to estimate soil liquefaction potential using Arias intensity as the IM . Their method is a refinement of the work in Kayen's dissertation [65], which extended the work of Egan and Rosidi [34]. Its form is similar to that of the simplified cyclic stress method: liquefaction potential is expressed as a factor of safety, both loading and resistance are characterized by Arias intensity at the depth of interest within the soil profile, the loading is calculated at the ground surface and corrected by a depth reduction factor, r_b , (Figure 3.10a) to be representative at the depth of interest, and the

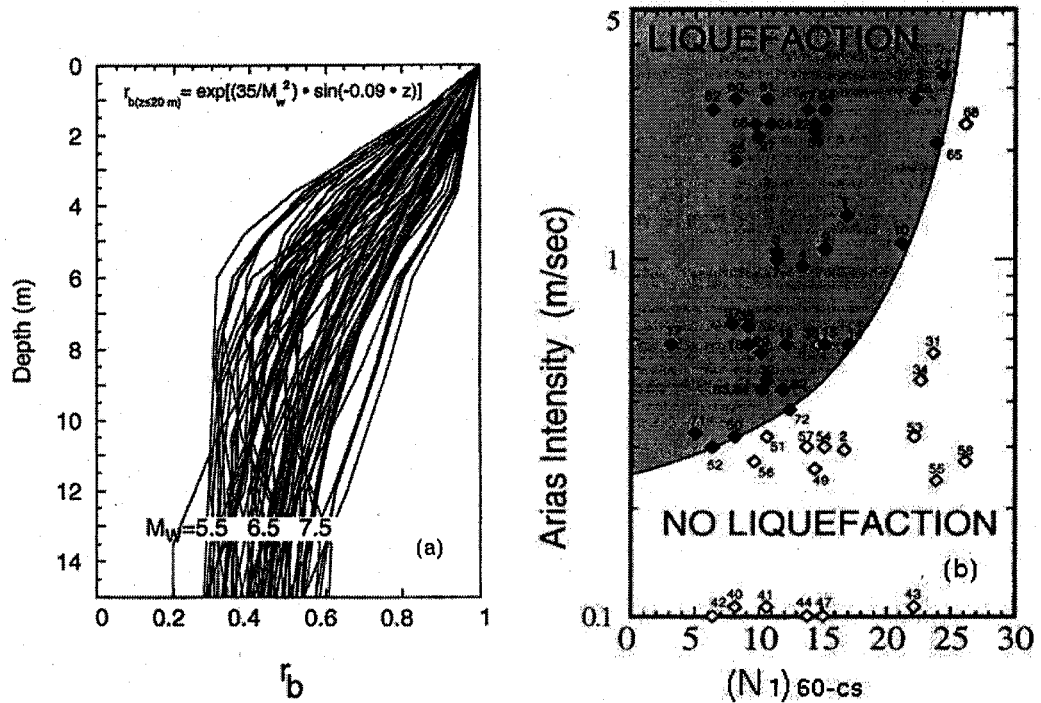


Figure 3.10: Depth reduction factor (a) and liquefaction plot (b) for the Arias intensity method. The heavier lines in (a) illustrate the mean and ± 1 standard deviation. In (b), the solid symbols represent cases in which liquefaction was observed; the open symbols represent cases in which no liquefaction was observed. After Kayen and Mitchell [66, 67].

soil resistance is correlated with penetration resistance (Figure 3.10b). The ability of Arias intensity to classify liquefaction and non-liquefaction cases as shown in Figure 3.10b appears to be better (more efficient) than *CRR* in Figure 3.1, although there are fewer cases in the Arias intensity database. There is no probabilistic representation for the Arias intensity method, so quantitative comparison of the efficiencies of the two methods is not possible. Since the Arias intensity method does not depend on magnitude or distance, I_a is considered a sufficient parameter; however, Kramer and Mitchell [77] found that correlations between I_a and pore pressure generation had a slight dependence on magnitude. Although these *IM* properties are attractive, the lack of a probabilistic representation means that no equation exists to compute fragility curves.

Kayen developed a simple attenuation relationship for I_a based on magnitude and distance for 66 records from rock, alluvium, and soft soil sites in California:

$$\begin{aligned}\log I_a &= M - 4.0 - 2 \log r^* + 0.63P && \text{Rock} \\ &= M - 3.8 - 2 \log r^* + 0.61P && \text{Alluvium} \\ &= M - 3.4 - 2 \log r^* && \text{Soft soil}\end{aligned}$$

in which M is the earthquake magnitude, r^* is the closest Pythagorean distance in kilometers between the site and the fault rupture plane at the focal depth, and P is the probit term describing the exceedance probability of Arias intensity in terms of the standard deviation about the mean ($P = \pm 1$ for $\pm 1\sigma$). Kayen did not have enough soft soil sites to develop a satisfactory estimate of uncertainty for the P term for that site class.

Travasarou et al. [120] used a greatly expanded dataset (1208 records) so were able to incorporate differences due to fault mechanisms as well as soil types (site classes).

$$\begin{aligned}\ln(I_a) &= 2.800 - 1.981(M - 6) + 20.72 \ln(M/6) - 1.703 \ln(R^2 + 8.78^2) \\ &+ (0.454 + 0.101(M - 6))S_C + (0.479 + 0.334(M - 6))S_D \\ &- 0.166F_N + 0.512F_R\end{aligned}$$

in which M is moment magnitude, R is the closest distance to the rupture plane in km, S_C and S_D are indicator variables for the materials constituting the profile (both 0 for hard rock, 1 and 0 for soft rock, and 0 and 1 for stiff clay and medium dense sand), and F_N and F_R are indicator variables for the fault types (both 0 for strike slip faults, 1 and 0 for normal faults and 0 and 1 for reverse or reverse-oblique faults). The larger dataset also allowed them to better characterize the total uncertainty, $\sigma_{tot}(M, I_a, \text{site})$, which they were able to separate into an inter-event component, $\tau(M)$, and an intra-event component, $\sigma(I_a, \text{site})$:

$$\tau(M) = 0.611 - 0.047(M - 4.7) \text{ for } 4.7 \leq M \leq 7.6$$

$$\sigma(I_a, \text{site}) = \begin{cases} \sigma_1 & \text{for } I_a \leq 0.013 \text{ m/s} \\ \sigma_1 - 0.106(\ln(I_a) - \ln(0.0132)) & \text{for } 0.013 < I_a < 0.125 \text{ m/s} \\ \sigma_2 & \text{for } I_a \geq 0.125 \text{ m/s} \end{cases}$$

$$\sigma_{tot}(M, I_a, \text{site}) = \sqrt{\tau(M)^2 + \sigma(I_a, \text{site})^2}$$

in which $\sigma_1 = 1.18$ and $\sigma_2 = 0.94$ for hard rock, $\sigma_1 = 1.17$ and $\sigma_2 = 0.93$ for soft rock, and $\sigma_1 = 0.96$, and $\sigma_2 = 0.73$ for stiff clay and medium dense sand. As an example, for strike slip earthquake of $M_w = 7.0$ at $R = 30$ km at a site comprising stiff clay, $\tau = 0.50$, $\sigma = 0.73$, and $\sigma_{tot} = 0.88$.

This example identifies the primary technical disadvantage of Arias intensity as an *IM*: the accuracy with which it can be predicted. Travasarou et al. [120] compared the uncertainty in predicting $\ln(I_a)$ ($\sigma_{tot} = 0.88$) with that for other *IMs* including $\ln(a_{max})$ (0.43), $\ln(S_a(0.5 \text{ s}))$ (0.54), and $\ln(T_P)$ (0.56). Thus, the uncertainty in predicting I_a is more than 50% greater than in predicting a_{max} . Even though there may be a better correlation between Arias intensity and liquefaction, this is at least partially offset by the high uncertainty in predicting Arias intensity.

3.4.2 CAV_5

Investigations by Kramer and Mitchell [77] identified an *IM* similar to Arias intensity that could improve the estimation of liquefaction by the energy approach. The modified form of cumulative absolute velocity, referred to as CAV_5 , is an integral parameter like Arias intensity and has all the associated benefits described earlier. In addition, though, pulses of an acceleration time history with an absolute amplitude less than 5 cm/s^2 do not contribute to CAV_5 . Thus, CAV_5 incorporates a threshold that is conceptually similar to the threshold strain below which no pore water pressure was generated in the cyclic strain approach. Other benefits of this *IM* will be discussed after its background is presented.

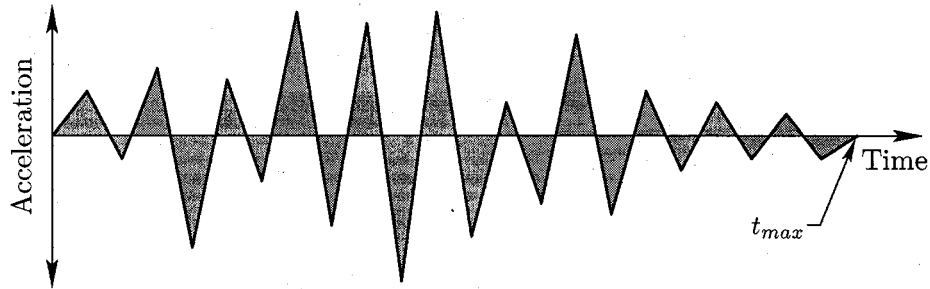


Figure 3.11: Cumulative absolute velocity (*CAV*) from acceleration time history. *CAV* is the sum of the shaded areas above and below the acceleration axis.

Development of CAV

Until the late 1980's, nuclear power plants used an a_{max} criterion to determine if shutdown was required to check for damage following an earthquake. After several small but nearby earthquakes exceeded the a_{max} threshold and caused plants to shutdown unnecessarily, the Electrical Power Research Institute (EPRI) commissioned a study in 1988 to determine which *IM* was most appropriate for use in a shutdown criterion [35]. It was in this study that Robert Kennedy, one of the authors, introduced cumulative absolute velocity (*CAV*), describing it as the area under the absolute accelerogram and defining it as

$$CAV = \int_0^{t_{max}} |a(t)| dt \quad (3.10)$$

in which $a(t)$ is the acceleration time history and t_{max} is the duration of the record. The shaded area in Figure 3.11 represents *CAV* for the given acceleration time history.

The EPRI study used Modified Mercalli Intensity (MMI) as the measure of an earthquake motion's damage potential, selecting MMI level VI as a conservative estimate of the upper limit for which there was reasonable engineering assurance that no damage would occur to nuclear power plant structures or equipment. A suite of 263 earthquake records was selected from sites where MMI of VI or less was either observed or estimated and the following *IMs* were investigated for correlation with MMI: a_{max} ; Arias intensity; *CAV*; peak spectral acceleration in the range of 0 to 10 Hz with 2, 5, and 7 percent damping; and average spectral acceleration over the range of 2 to 10 Hz with 2, 5, and 7 percent

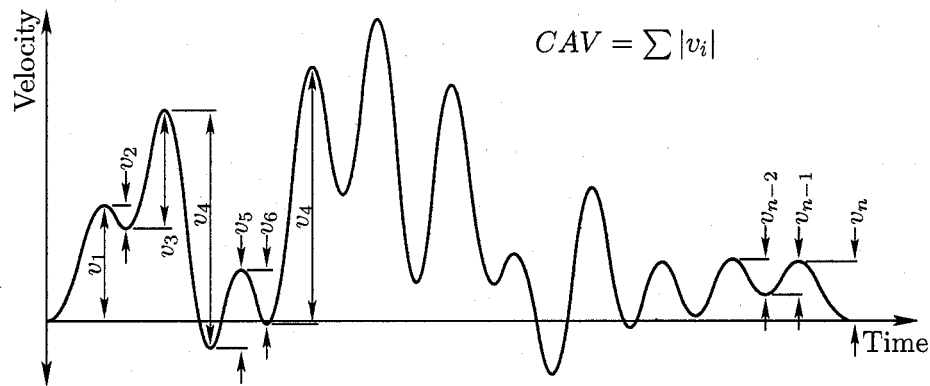


Figure 3.12: CAV from velocity time history. After EPRI [35].

damping. The first three IMs were investigated with and without the time histories filtered to remove frequencies greater than 10 Hz; the final two were investigated only with unfiltered response. The poorest predictor of MMI levels II through VI was found to be a_{max} , with filtering slightly improving its performance. Average and peak spectral accelerations were slightly better, with greater damping decreasing their predictive ability. Arias intensity was significantly better than all of the acceleration parameters, with filtering slightly improving its performance. Best of all, though, was CAV , with filtering having little effect. Based on their results, EPRI concluded that CAV 's relative insensitivity to high frequency motion made it a good predictor of structural damage. They recommended replacing the a_{max} shutdown criterion with one in which $CAV = 2.94$ m/s (0.3 g-s).

As noted earlier, CAV is the area under the absolute accelerogram. EPRI [35] also described it as the sum of the absolute value of the peak-to-peak heights of a velocity time history (Figure 3.12). Recalling that velocity is the time integral of acceleration, each peak-to-peak height equals the area under the acceleration time history between zero crossings. Thus, summing the peak-to-peak velocities is the same as summing the individual areas under the absolute accelerogram. The EPRI report also provided a third representation of CAV , one that is less apparent than the first two. As shown in Figure 3.13, CAV is the area under a plot of absolute acceleration versus duration. Each point on this plot represents the total duration over which the absolute value of a particular acceleration, a^* , is exceeded.

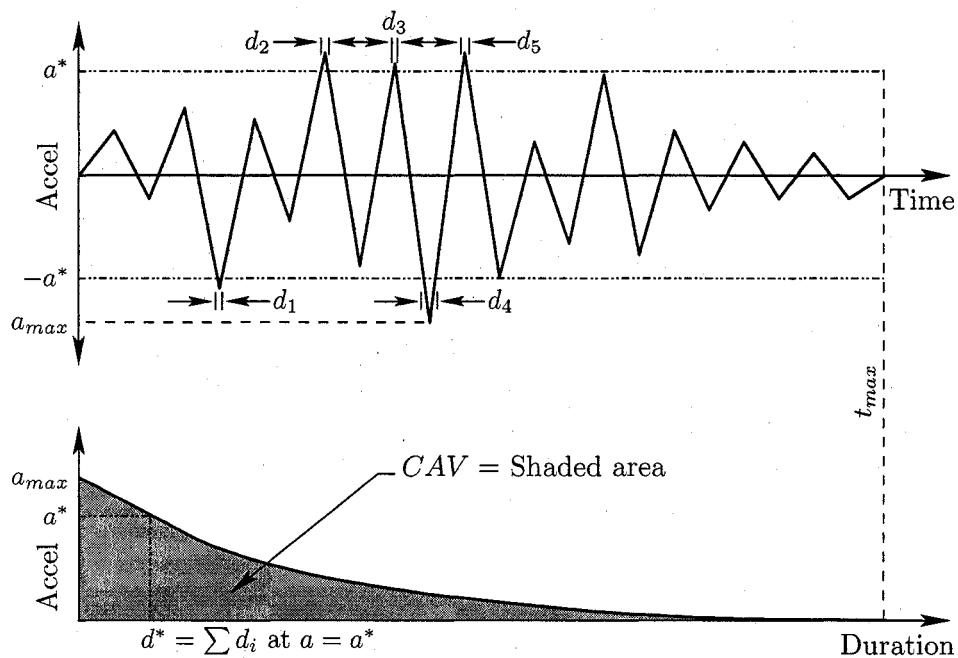


Figure 3.13: *CAV* from acceleration vs duration curve. After EPRI [35].

Since a_{max} occurs only instantaneously, its duration, $d = 0$; since the acceleration in the time history eventually diminishes to zero, the acceleration-duration curve also diminishes to zero at the end of the earthquake record. The shape of this curve indicates the relative contribution to *CAV* of large and small accelerations.

In 1991, EPRI released another study on *CAV* [36]. While implementing the recommendations from their 1988 report, they noted that earthquake records of long duration having low-amplitude, non-damaging codas could result in unreasonably high values of *CAV*. After considering several different versions of bracketed durations for use with *CAV*, they decided to break the acceleration time history into one-second segments and include in the summation of *CAV* only those segments with at least one peak exceeding an absolute acceleration of 0.025 g. The difference made by this reinterpretation was significant: the shutdown criterion was reduced to $CAV = 1.57$ m/s (0.16 g-s) from 2.94 m/s (0.3 g-s) according to their new definition.

CAV has been found to be an effective predictor of geotechnical damage as well as structural damage. Hardy [47] noted that *CAV* was a better predictor of earthquake-

induced settlement than Arias intensity and other integrated time histories of squared and absolute-valued acceleration, velocity, or displacement. He further noted that Arias intensity was not significantly better than a_{max} at predicting settlement.

Archuleta [7] studied ground response due to earthquake shaking using data from the Yokohama seismic array for earthquakes of magnitude 4.0 to 7.3 and depths from 3 to 430 km. As part of his work, he looked at the correlation between the average shear wave velocity of the upper 30 m of the soil profile and several *IMs* describing ground response. He found that the strongest correlation was with spectral intensity and duration, and that the weakest was with a_{max} and Arias intensity; the correlation with *CAV* was only slightly less than that of spectral intensity and duration.

Development of CAV_5

Kramer and Mitchell [77] examined the correlation between seismically-induced pore pressures in soil and a wide range of input motion *IMs* using the 1-dimensional, non-linear, effective-stress ground response program, WAVE, with the UWsand model for liquefaction behavior [50, 74, 75]. For each of the nine permutations of $N_{1,60,cs}$ and upper soil layer thickness for the profile shown in Figure 3.14, they applied 450 input motions to the base of the dense soil layer and calculated the average pore pressure ratio, \bar{r}_u , for the upper soil layer. They then correlated \bar{r}_u with each of nearly 300 *IMs* computed from the input motions.

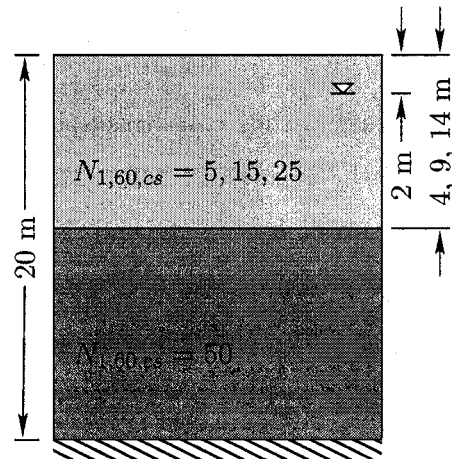


Figure 3.14: Mitchell's generic soil profile [77].

In addition to the better-known parameters described earlier, they investigated a series of transitional variations. For example, Arias intensity is proportional to the integral of the squared acceleration time history and *CAV* is the integral of the absolute value of the acceleration time history. In addition to raising the absolute acceleration time history to

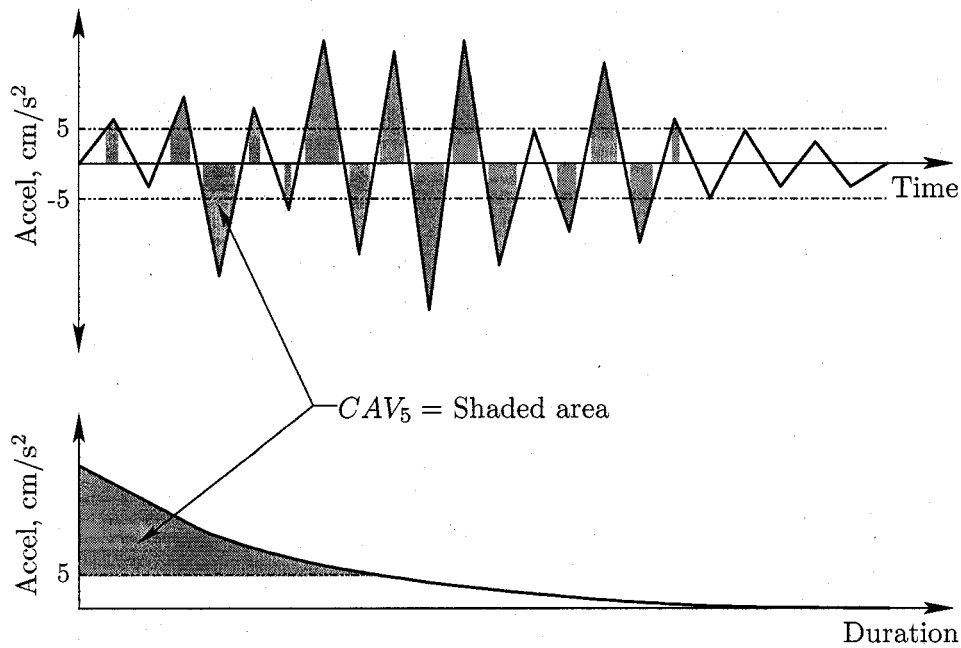


Figure 3.15: CAV_5 from acceleration time history and acceleration vs duration curve.

powers of 2 and 1, they considered powers of 0.1 up to 3. Also, recognizing that a strain threshold must be exceeded before pore pressures are generated, they studied a range of acceleration thresholds. In the end, Kramer and Mitchell found that the best predictor of modeled pore pressures was CAV with an acceleration threshold of 5 cm/s^2 ; they called this parameter CAV_5 and defined it as follows:

$$CAV_5 = \int_0^{\infty} \chi |a(t)| dt \quad \text{where } \chi = \begin{cases} 0 & \text{if } |a| < 5 \text{ cm/s}^2, \\ 1 & \text{if } |a| \geq 5 \text{ cm/s}^2. \end{cases} \quad (3.11)$$

Figure 3.15 illustrates the calculation of CAV_5 from an acceleration time history and from an acceleration-duration plot; the area below the 5 cm/s^2 line in the acceleration-duration curve, which is due primarily to the low-amplitude tail of the record, is excluded from CAV_5 .

CAV_5 has several attractive properties. As noted earlier, it is an integral parameter, thus strongly influenced by the amplitude and duration. It is affected by nearly all of the earthquake record, unlike a_{max} , which is characterized by only a single point. The only portion of the record not included in CAV_5 is the low amplitude portion, which is unlikely

to generate permanent strain or excess pore pressure in the soil. Like Arias intensity (and pore pressure), it builds up over time, thus offering the possibility of predicting the point in the time history when liquefaction is initiated. This could be an important advance in geotechnical earthquake engineering because the effects of liquefaction—permanent deformation associated with lateral spreading, settlement, etc.—develop primarily after the initiation of liquefaction and are therefore expected to be greater when liquefaction occurs early in the earthquake and the liquefied soil is subjected to strong shaking.

CAV₅ as an IM for liquefaction potential

There is no existing method for estimating liquefaction potential using *CAV₅* as an *IM*, so its efficiency, sufficiency, and predictability regarding liquefaction potential cannot be directly compared with Arias intensity and *CSR*. There are, however, several *IM* comparisons for properties closely related to liquefaction that provide indirect evidence about how *CAV₅* might perform in liquefaction assessment. These are described in the following paragraphs.

Frequency content Kramer [73] described three important characteristics of earthquake shaking: amplitude, duration, and frequency content. Earlier descriptions of Arias intensity and *CAV₅* noted that, as integral *IMs*, they were strongly affected by amplitude and duration, but there has been little mention of the influence of frequency content. This is an important consideration for studies of liquefaction because strain amplitude and, thus, pore pressure generation are sensitive to the frequency content of the ground motion.

This sensitivity can be illustrated by the relationship between shear strain amplitude, γ_s , and particle velocity, \dot{u} , for shear waves passing through an elastic medium:

$$\gamma_s = \frac{\partial u}{\partial z} = \frac{\partial u / \partial t}{\partial z / \partial t} = \frac{\dot{u}}{V_s} \quad (3.12)$$

in which V_s is the shear wave velocity of the medium. From the 1-dimensional equation of motion due to harmonic shear waves passing through an elastic medium,

$$\frac{\partial^2 u}{\partial t^2} = V_s^2 \frac{\partial^2 u}{\partial z^2}$$

the resulting horizontal displacement is

$$u(z, t) = 2A \cos(kz) e^{i\omega t}$$

in which A and ω are the amplitude and circular frequency of the input motion and k is the wave number ($k = \omega/V_s$). By differentiating the displacement once to obtain the particle velocity (\dot{u}) and again to obtain acceleration (\ddot{u}), the frequency dependence of these parameters can be seen:

$$\dot{u} = i\omega u; \quad \ddot{u} = -\omega^2 u$$

Because of the squared term, particle acceleration is influenced more by higher frequencies than particle velocity, which in turn is related to higher frequencies than particle displacement. This suggests that a good IM for liquefaction should correlate well to the amplitude of motion at frequencies that are most closely related to strain amplitude and thus velocity. These frequencies should be lower than those that are most closely related to acceleration and a_{max} .

To investigate this premise, Upsall [122] computed a_{max} , I_a , and CAV_5 for the two horizontal components of each of 455 acceleration records from more than 60 earthquakes spanning a wide range of magnitudes, source-to-site distances, and site classes. She also computed the response spectrum for 5% damping for each of these 910 time histories and correlated the resulting spectral acceleration for periods ranging from 0.001 s to 10 s with each of the three IM s; the coefficient of determination, R^2 , was used to describe the strength of the correlation [123]. The results in Figure 3.16 confirm that a_{max} correlates best with high frequency (short period) motion. This result is expected since the spectral acceleration for period, $T = 0$, equals a_{max} by definition, thus the perfect correlation at that period. As the period increases, R^2 for a_{max} rapidly diminishes, indicating that a_{max} is only weakly related to longer period (shorter frequency) components of the earthquake motions. For the integral parameters, R^2 is relatively low at short periods but it increases to a maximum at a period of about one second. At longer periods, R^2 for I_a drops off rapidly to match that of a_{max} while R^2 for CAV_5 remains relatively high.

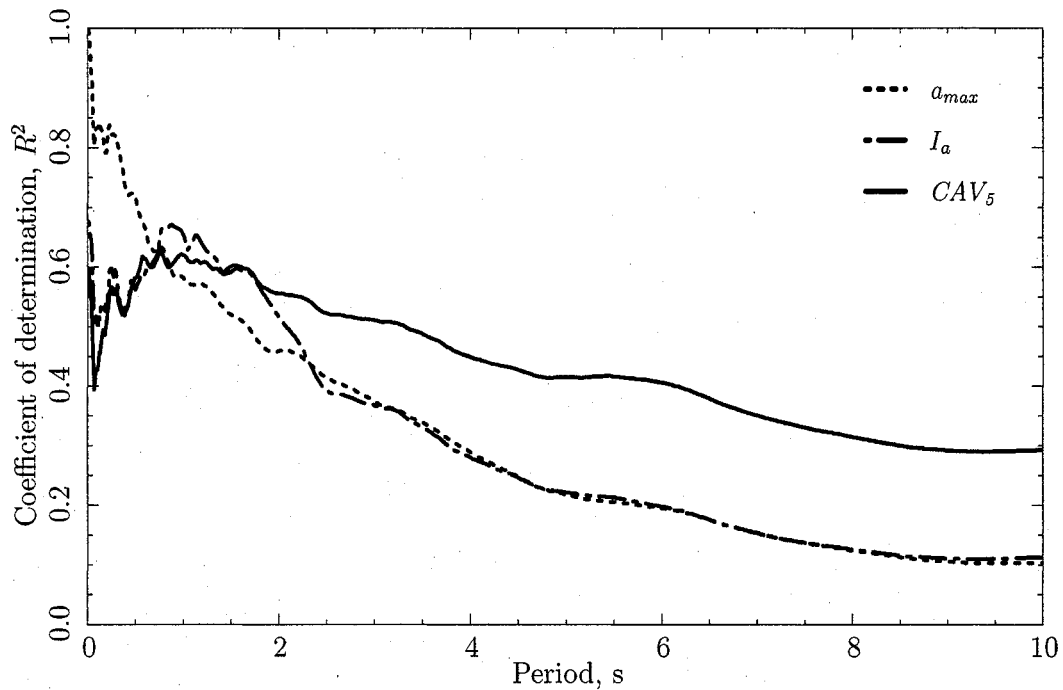


Figure 3.16: Correlation between spectral acceleration and a_{max} , I_a , and CAV_5 .

It is interesting to apply the earlier relationship for shear waves passing through an elastic medium (Equation (3.12)) to shear stress:

$$\tau = G\gamma_s \quad (3.13)$$

in which τ is shear stress and G is the shear modulus of the soil. Expanding these terms,

$$\begin{aligned} \tau &= \rho V_s^2 \frac{\partial u}{\partial z} \\ &= \rho V_s^2 \frac{\partial u / \partial t}{\partial z / \partial t} \\ &= \rho V_s \dot{u} \end{aligned}$$

Thus, shear stress is proportional to particle velocity within the profile, again supporting the use of a velocity-related IM for predicting liquefaction potential.

Pore pressure generation—efficiency and sufficiency From their correlations between *IM*s at the bedrock surface and \bar{r}_u calculated from WAVE, Kramer and Mitchell [77] compared the efficiency and sufficiency of a_{max} , I_a , and CAV_5 . Figure 3.17 illustrates the superior efficiency and sufficiency of CAV_5 in predicting pore pressures modeled from earthquake shaking. In the top row, the efficiency of a_{max} , I_a , and CAV_5 in predicting \bar{r}_u are compared. Less scatter, as described by a lower value of σ , indicates a more efficient parameter: CAV_5 is somewhat better than I_a and clearly superior to a_{max} in this respect. *IM* sufficiency—that is, the predictive ability of an *IM* on its own without additional information about magnitude or source-to-site distance—is compared by plotting the residuals from the top row against earthquake magnitude (middle row) and source-site distance (bottom row). For a perfectly sufficient parameter, the residuals would show no trend with respect to M_w or R ; a notable trend indicates that the predictive ability of the *IM* could be improved by including information about M_w or R . The thick trend lines in the bottom two rows of Figure 3.17 show that a_{max} is clearly insufficient, especially with respect to M_w . This has long been known and is the reason why the magnitude scaling factor is included in the *CSR* method. I_a is more sufficient than a_{max} but still shows some dependence on magnitude and distance, while CAV_5 is almost perfectly sufficient. The combination of high efficiency and sufficiency for CAV_5 suggests that it should be a good predictor of seismically-generated pore pressures, and that adding information about M_w and R is not necessary to improve its predictive ability.

Kramer and Mitchell's pore pressure correlations were with *IM*s calculated at the bedrock surface. In a series of unpublished investigations at the University of Washington, Ho used Kramer and Mitchell's soil profiles (Figure 3.14) and 56 of their bedrock motions to compute time histories at the ground surface using the equivalent linear ground response program, ProShake [33]. From these results, he computed the three *IM*s and compared them with the WAVE-computed pore pressures from Kramer and Mitchell (Figure 3.18). Ho's findings were consistent with those of Kramer and Mitchell— CAV_5 predicted \bar{r}_u with less scatter than I_a and much less scatter than a_{max} .

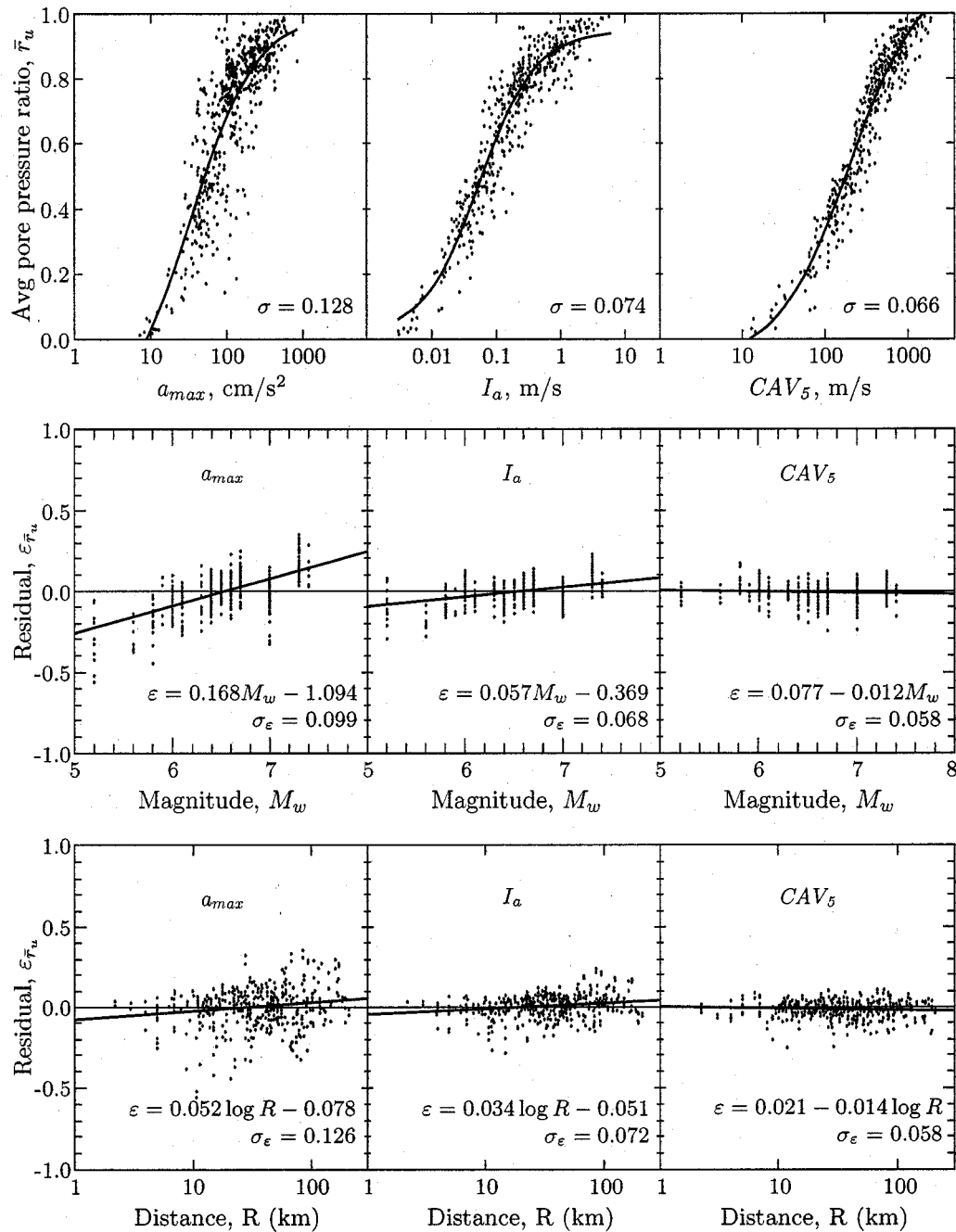


Figure 3.17: Efficiency (top row) and sufficiency (bottom two rows) of a_{max} , I_a , and CAV_5 in predicting pore pressures generated due to seismic loading for the soil profile in Figure 3.14. The equations for ε in the bottom two rows describe the trend line through the residuals. After Kramer and Mitchell [77].

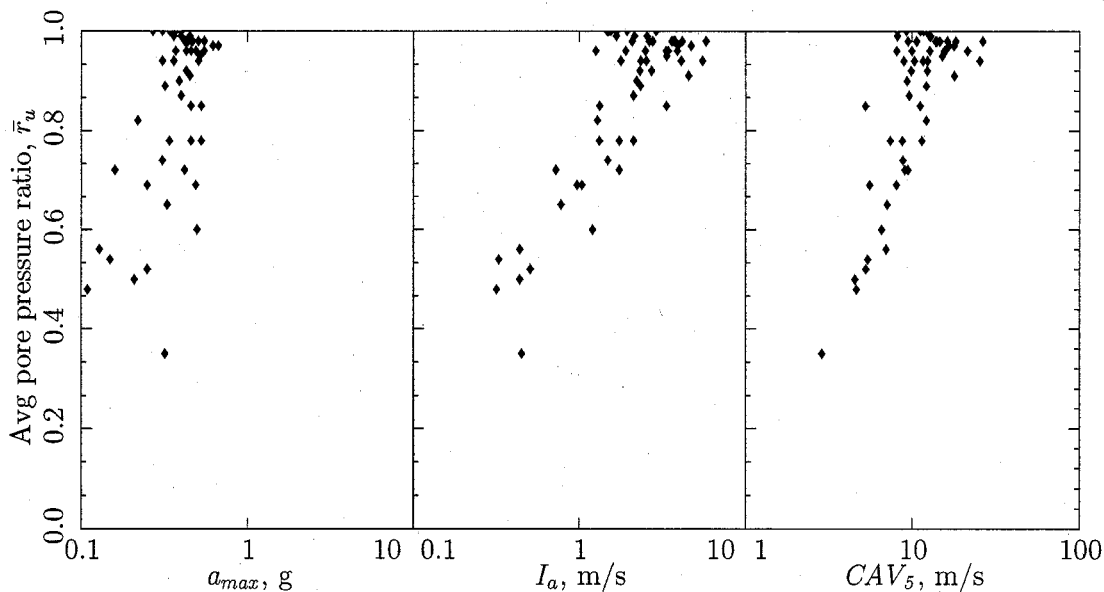


Figure 3.18: Correlation between average pore pressure ratio and a_{max} , I_a , and CAV_5 at the ground surface.

Predictability The final property, predictability, has been the weak point of other proposed estimators of liquefaction potential. As noted earlier in this chapter, the cyclic strain method is infrequently used despite its fundamental attractiveness because cyclic strain amplitudes cannot be accurately predicted.

To investigate the predictability of CAV_5 , Kramer and Mitchell [77] selected 282 records from 40 earthquakes in PEER's strong motion database and used the functional form of the I_a attenuation relationship from Travararou et al. [120] to develop an attenuation relationship for CAV_5 . To compare the predictability of a_{max} and I_a independent of model uncertainty, Mitchell used the same data set and functional form to develop attenuation relationships for those IMs as well. The resulting standard errors for $\ln a_{max}$, $\ln I_a$, and $\ln CAV_5$ were 0.620, 1.070, and 0.708, respectively, indicating that a_{max} is most predictable, I_a is least predictable, and CAV_5 's predictability is close to that of a_{max} . This high predictability of a_{max} is misleading, though, because the magnitude scaling factor must also be used

Table 3.1: Relative ranking of *IMs*' efficiency, sufficiency, and predictability discussed in this chapter. The third and fourth columns refer to the existence of an attenuation relationship for predicting the *IM* hazard curve and of a probabilistic relationship between the *IM* and liquefaction. In the last three columns, a ranking of 1 is highest and a ranking of 3 is lowest.

Method	<i>IM</i>	Haz. curve	Frag. curve	Eff.	Suff.	Pred.
Cyclic stress	a_{max} , M	Y	Y	3	3	1
Cyclic strain	a_{max} , M	Y	N	1	1	3
Arias intensity	I_a	Y	N	2	2	2
CAV_5	CAV_5	Y	N	1	1	1

to calculate *CSR*. Youd et al. [128] showed that there is significant uncertainty in the relationship for *MSF*, and this uncertainty decreases the overall predictability of *CSR* even though the predictability of a_{max} is high.

3.5 Intensity measures for performance-based liquefaction assessment

This chapter has reviewed several methods and *IMs* in the context of their efficiency, sufficiency, and predictability for estimating soil liquefaction potential. Table 3.1 summarizes these characteristics for each *IM* and notes which ones have existing attenuation relationships for computing the *IM* hazard curve and probabilistic relationships between the *IM* and liquefaction for computing the fragility curves. Using this information to select *IMs* for implementation in a performance-based framework, it seems clear that CAV_5 is a candidate because of its superior efficiency, sufficiency, and predictability. To effect this, though, a probabilistic relationship will have to be developed for calculating the fragility curves. The cyclic strain and Arias intensity methods do not appear as attractive in this comparison because they both have poorer efficiency, sufficiency, and predictability than CAV_5 and both require probabilistic *IM-EDP* relationships. Although the cyclic stress method is not as efficient or sufficient as CAV_5 , there are several attenuation *IM-EDP* relationships in existence for it so a performance-based implementation should be relatively easy. Also, because of its widespread use, it is the standard of comparison for any new method of assessing liquefaction potential.

The remainder of this dissertation describes the development of performance-based cyclic stress and CAV_5 methods. Chapter 4 covers the cyclic stress implementation and compares the resulting performance-based approach with the current CSR probabilistic and deterministic procedures, Chapters 5 and 6 document the development of the CAV_5 probabilistic $IM-EDP$ relationship, and Chapter 7 implements the new CAV_5 performance-based method.

Chapter 4

PERFORMANCE-BASED CYCLIC STRESS METHOD

The two preceding chapters have described the performance-based framework and proposed earthquake intensity measures for assessing liquefaction potential. In this chapter, these two topics are combined in the development of a performance-based method for assessing liquefaction potential using cyclic stress ratio as the *IM*.

The roots of performance-based liquefaction assessment go back to work presented by Yegian and Whitman in 1978 [125], although earthquake loading was described as a combination of earthquake magnitude and source-to-site distance rather than *CSR* or even peak ground acceleration and magnitude. Atkinson et al. [9] incorporated *CSR* in a procedure for estimating the mean annual probability of liquefaction using linearized approximations of the CRR curves of Seed and Idriss [104] in a deterministic manner. More recently, Marone et al. [86] described a liquefaction assessment method that incorporated probabilistic CRR curves and the full range of magnitudes and peak accelerations in a manner similar to the PEER framework described herein. Hwang et al. [51] described an approach based on Monte Carlo simulations that appears to produce similar results.

The remainder of this chapter implements the cyclic stress ratio *IM* into the PEER performance-based framework. The work begins with the development of *IM* hazard curves and a series of *IM-EDP* fragility curves. Liquefaction potential from the resulting framework is then compared with that from conventional analyses.

4.1 *IM* hazard curve

The intensity measure in the *CSR* method consists of two parts: the peak horizontal ground acceleration, a_{max} , and the magnitude, M_w , which is used to calculate the magnitude scaling factor, *MSF*. Since magnitude is one of the source parameters used in probabilistic seismic hazard analyses to compute a_{max} , all the necessary information about the two-part *IM*

is available from the deaggregation of a_{max} from a PSHA. The following two subsections describe how the *IM* hazard curve for the *CSR* method is developed from this information.

4.1.1 Peak ground acceleration

In the continental U. S., assembling data for the *IM* hazard curve is relatively easy because deaggregated a_{max} PSHAs are available on line from the US Geological Survey¹ for six hazard levels: 50 percent probability of exceedance in 75 years and 20, 10, 5, 2, and 1 percent probability of exceedance in 50 years. Assuming a Poisson distribution, these hazard levels correspond to return periods, T_R , of 108, 224, 475, 975, 2475, and 4975 years, respectively. These six return periods and the corresponding values of a_{max} form the basis for constructing the a_{max} hazard curve in this dissertation.

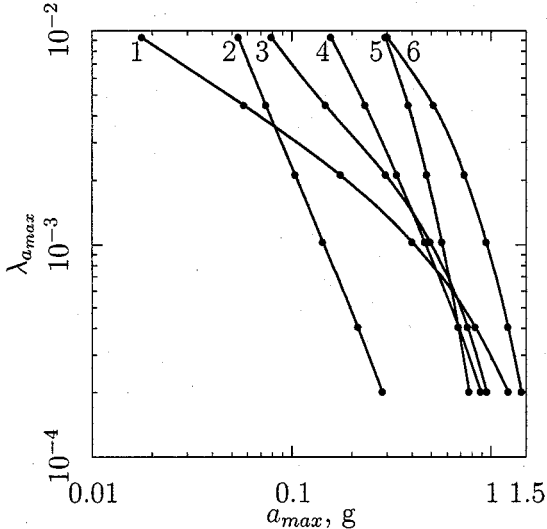


Figure 4.1: Hazard curves for a_{max} for: (1) Charleston, SC, (2) Butte, MT, (3) Salt Lake City, UT, (4) Seattle, WA, (5) San Jose, CA, and (6) Eureka, CA. Data for these curves are from the USGS Interactive Deaggregations (2002) website.

Although return periods of 100 to 5000 years span the range of interest to most engineers, there is some contribution to liquefaction hazard from events with lesser and greater return periods. To account for this in the performance-based *CSR* method, the a_{max} hazard curve is extrapolated at both ends. It is common to assume that the a_{max} hazard curve can be approximated by a power-law relationship (e.g. [84]); however, as Figure 4.1 shows, this assumption is not always appropriate. Curves 2 (Butte), 4 (Seattle), and 5 (San Jose) on the log-log plot are relatively straight, indicating that a power-law relationship reasonably approximates the a_{max} hazard curve. Curves 1 (Charleston), 3 (Salt Lake City), and 6 (Eureka), have considerable curvature, suggesting that the power-law assumption is not reasonable.

imates the a_{max} hazard curve. Curves 1 (Charleston), 3 (Salt Lake City), and 6 (Eureka), have considerable curvature, suggesting that the power-law assumption is not reasonable.

¹<http://eqint.cr.usgs.gov/eq-men/html/deaggint2002-06.html>

In order to accommodate a wide range of hazard curve shapes, the extrapolation is done in two parts. For return periods less than 108 years, a return period of 0 is assumed to correspond to $a_{max} = 0$. For return periods greater than 4975 years, the USGS points for return periods of 975, 2475, and 4975 years are used to construct a parabola in log-log space, which is used to estimate a_{max} at $T_R = 10,000$ years. The upper limit on the return period is due to the available USGS data; the methodology described here can accommodate any range of T_R .

The values of a_{max} provided by the USGS are for profiles comprising stiff soil or soft rock outcroppings with an average shear wave velocity in the upper 30 m of 750 m/s. This is not reasonable for sites with a significant potential for liquefaction, so an amplification factor, F_A , described by Stewart et al. [115] is used to estimate a_{max} for soil, a_{max_s} , from the USGS values of a_{max} for rock, a_{max_r} :

$$\ln F_A = a + b \ln a_{max_r}$$

in which a and b are coefficients that Stewart et al. determined using statistical regression for various soil types. The amplification factor,

$$F_A = \frac{a_{max_s}}{a_{max_r}} = e^a \cdot a_{max_r}^b$$

$$a_{max_s} = e^a \cdot a_{max_r} \cdot a_{max_r}^b = e^a \cdot a_{max_r}^{(b+1)}$$

For Quaternary alluvium, which is typical for liquefiable soil, Stewart et al. suggested $a = -0.15$ and $b = -0.13$. Using these values, the eight points on the hazard curve—six from USGS and two from extrapolation—are adjusted to produce a_{max_s} . A mathematical cubic spline through the eight points is used for interpolating between the eight points at intervals of 0.01 g. Figure 4.2 illustrates this procedure for the site in Seattle. For the remainder of this dissertation, references to a_{max} imply a_{max_s} unless specifically stated otherwise.

4.1.2 Magnitude

As noted earlier in this section, the a_{max} and magnitude components of the *CSR IM* can be derived from PSHA deaggregations like those provided by the USGS website. Figure 4.3

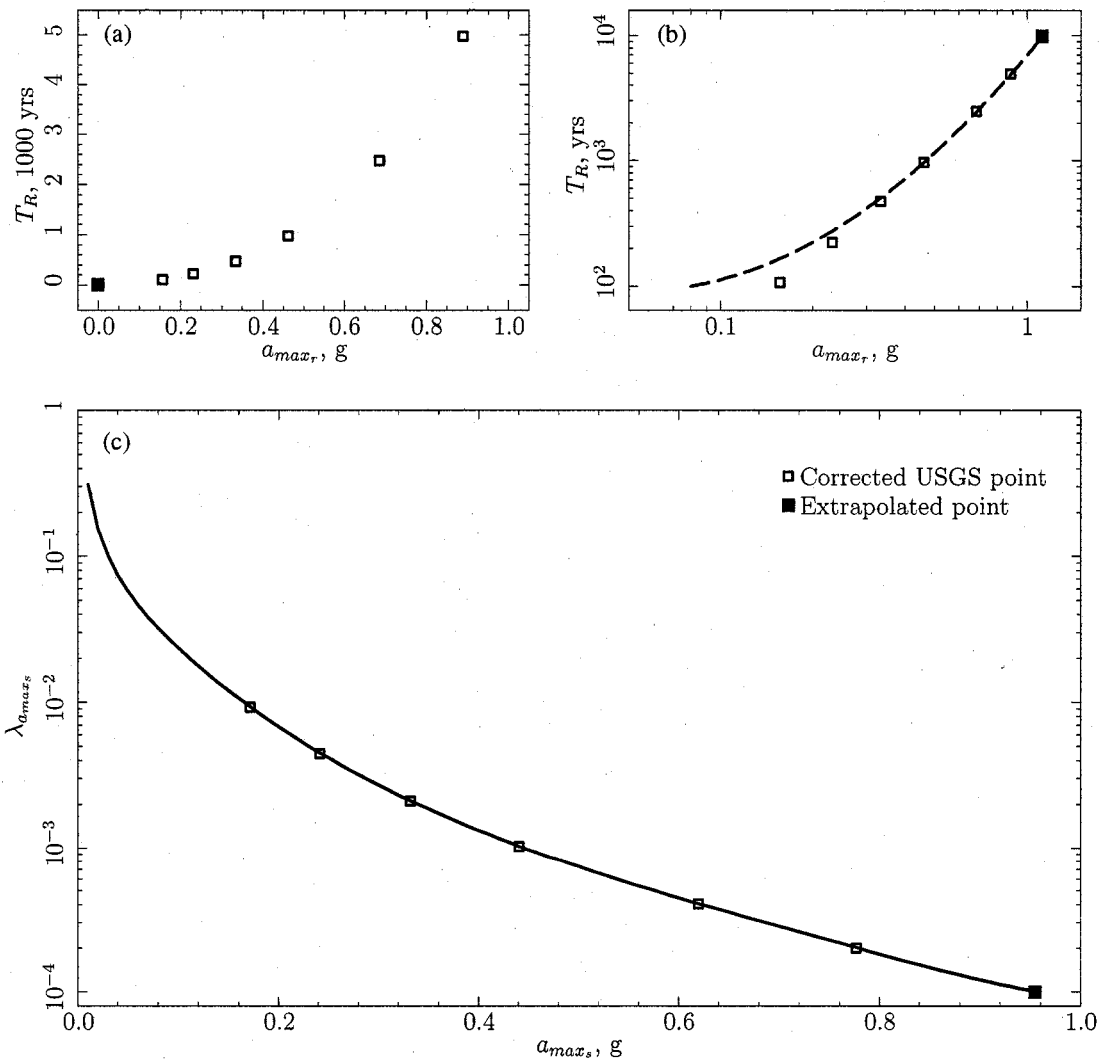


Figure 4.2: Extrapolation of the a_{max} hazard curve for Seattle: (a) addition of a point at $a_{max} = 0$ and $T_R = 0$; (b) construction of a parabola using the USGS points at $T_R = 975$, 2475, and 4975 years to extrapolate to $T_R = 10,000$ yrs; (c) the extrapolated hazard curve. The correction referred to in the legend of (c) is the soil amplification factor, which converts a_{max_r} to a_{max_s} .

illustrates the deaggregation of the 475-yr a_{max} for Seattle. Each 3-dimensional bar describes the contribution (vertical axis) to the total mean annual rate of exceedance of the 475-yr a_{max} for the interval of magnitude (end axis) and source-to-site distance (side axis) of the

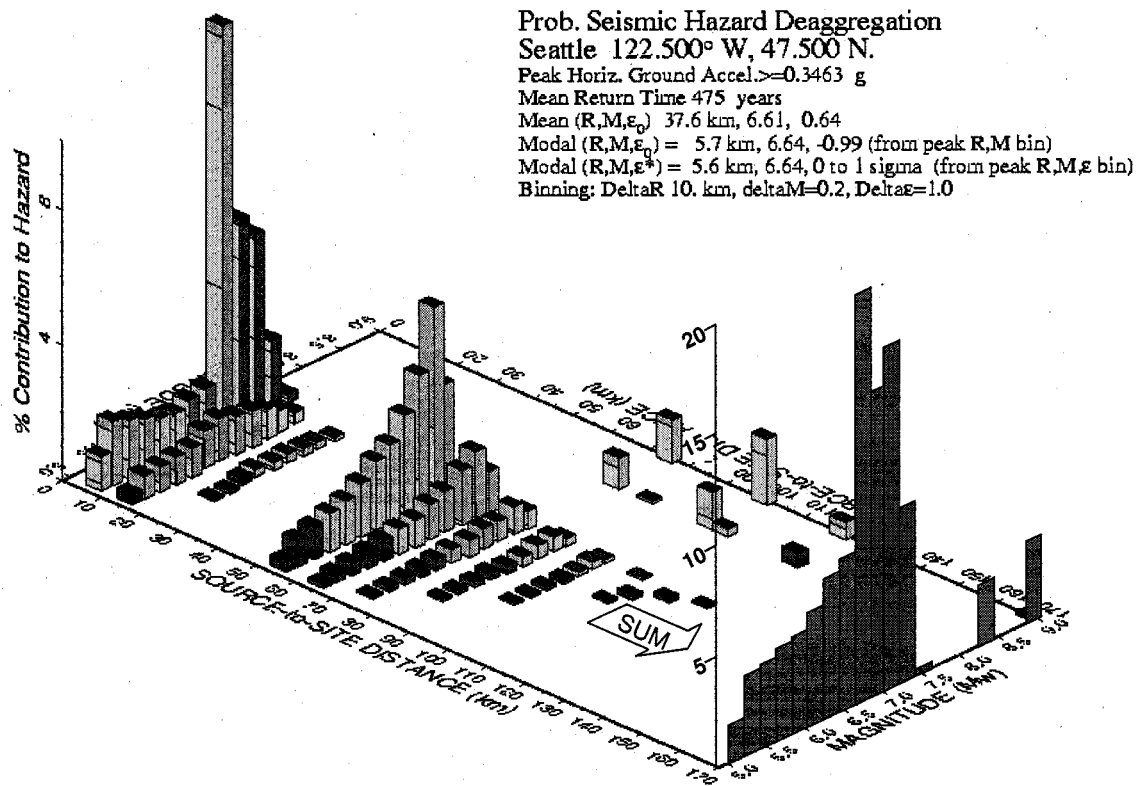


Figure 4.3: PSHA deaggregation of the 475-yr a_{max} for Seattle. The marginal magnitude distribution at the right end of the plot was superimposed on the figure provided by the USGS deaggregation website.

bar. The largest contribution in this example, about 7.5%, is from an event with magnitude 6.8–7.0 occurring at a distance of 0–10 km. The bar heights total 100% and thus the surface defined by the tops of the bars is a three-dimensional joint probability distribution.

The source-to-site distance is not used in the *CSR* method, so the 3-D joint distribution can be collapsed into the 2-D marginal magnitude distribution illustrated along the right end of the plot in Figure 4.3. The height of each bar of the marginal distribution represents its relative contribution to the total a_{max} hazard at that return period and equals the sum of the heights of the bars in the joint distribution for all distances in the same magnitude bin. Note that the vertical scales of the joint and marginal distributions are different.

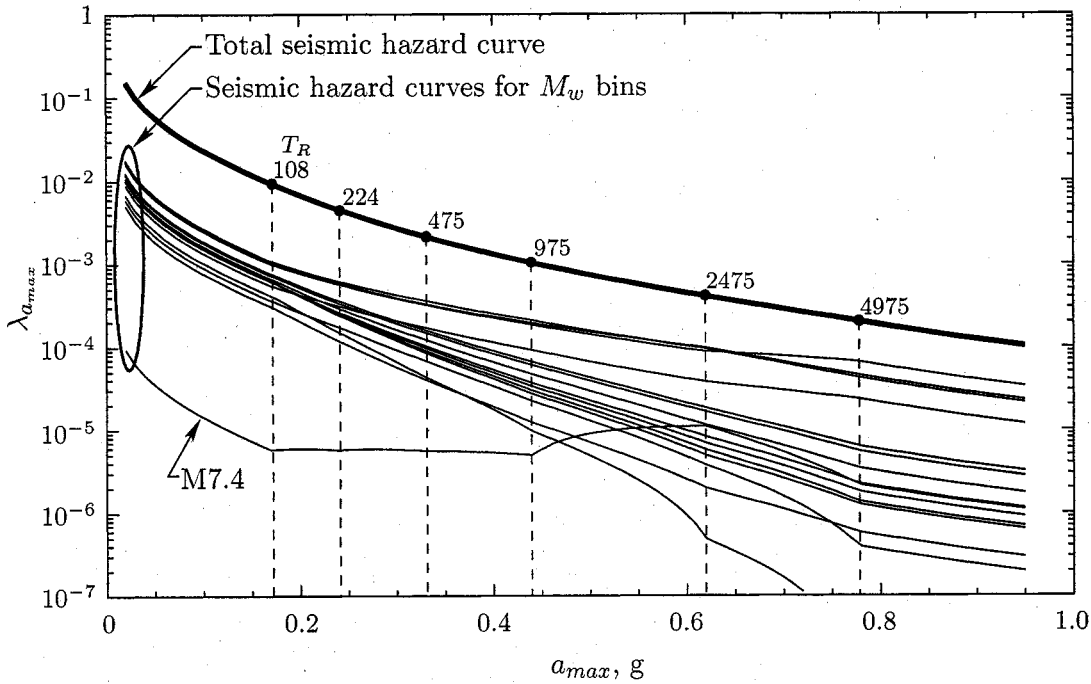


Figure 4.4: Hazard curves for Seattle. The upper curve is the total a_{max} hazard and each of the lower curves is the hazard conditional upon a particular magnitude bin.

The value of $\lambda_{a_{max}}$ for each point along the total a_{max} hazard curve illustrated in Figure 4.2(c) represents the sum of the contributions from each magnitude bin in its own marginal magnitude distribution. Using the marginal magnitude distributions from deaggregations at the each of the six USGS points, the Seattle total a_{max} hazard curve in Figure 4.2c is decomposed into a series of hazard curves, each corresponding to a magnitude bin of the marginal distribution (Figure 4.4). These curves are produced by multiplying the total mean annual rate of exceedance at each of the six USGS points by each of the probabilities in the marginal magnitude distribution from the deaggregation at that point. Between the six USGS points, the probabilities of each magnitude bin are estimated by linear interpolation. Beyond the six points, the marginal magnitude distribution at the last point is used.

Note that the marginal magnitude distribution in Figure 4.3 is irregularly shaped and that some of the magnitude bins make no contribution to the total IM hazard. Applying

these irregularly shaped distributions to the generally smooth total hazard curve results in some individual magnitude curves that stand out from the rest. In Figure 4.4, for example, the M7.4 curve in the lower left corner is the result of a very low contribution from magnitude 7.4 events to the 108-yr total hazard. At the 975-yr and 2475-yr return periods, the increased contribution from this magnitude bin causes the curve to cut across the others. This is simply the result of the changing levels of hazard contributions for the various magnitude bins across the range of return periods. The importance of these changes are illustrated later in this chapter.

Several of the magnitude curves in Figure 4.4 have noticeably curved segments between return periods; the segment of the M7.4 curve between the 975- and 2475-yr return periods is an example. The shape is a result of the linear interpretation between return periods described above that is then plotted in semi-log space. In an arithmetic plot, the segments are linear.

The curves for the magnitude bins in Figure 4.4 are the *IM* hazard curves from which $\Delta\lambda_{IM}$ in the PEER framing equation (Equation (2.3) and Figure 2.3) is calculated. The information needed for the remaining part of the framing equation is considered in the following section.

4.2 *IM-EDP fragility curves*

Chapter 2 described how *IM-EDP* fragility curves define the relationship between a value of *IM* and the probability of exceeding a specified value of *EDP* conditional upon the value of *IM*. This relationship can be determined from a probabilistic interpretation of *CRR* such as those proposed by Liao et al. [81], Youd and Noble [129], Toprak et al. [118], and Çetin et al. [24]. For this chapter, the relationship by Çetin et al. has been selected because of its expanded database of liquefaction versus non-liquefaction sites and its partitioning of model and parameter uncertainty.

Çetin et al. described the probability of liquefaction as

$$P_L = \Phi \left[\frac{N_{1,60}(1 + 0.004FC) - 13.32 \ln CSR_{eq} - 29.53 \ln M_w - 3.70 \ln \frac{\sigma'_{vo}}{p_a} + 0.05FC + 16.85}{2.70} \right] \quad (4.1)$$

in which Φ is the standard normal cumulative probability operator, $N_{1,60}$ is the SPT blow-count corrected for energy and overburden stress, FC is the fines content in percent, CSR_{eq} is the cyclic stress ratio not corrected for magnitude, M_w is the earthquake magnitude, σ'_{vo} is the vertical effective stress at the point of interest in the soil profile, and p_a is the atmospheric pressure in the same units as σ'_{vo} . This rather complicated form can be more easily understood by comparing it with the relationship between CSR and CRR described in Chapter 3.

The factor of safety against liquefaction was defined as

$$FS_L = \frac{CRR}{CSR} = \frac{CRR_{7.5,1}}{CSR} \cdot MSF \cdot K_\sigma$$

in which $CRR_{7.5,1}$ is the CRR equivalent for $M_w = 7.5$ and 1 atm of overburden pressure, MSF is the magnitude scaling factor, and K_σ is the overburden correction factor. At the boundary between liquefaction and non-liquefaction cases, $FS_L = 1.0$, $CSR = CRR$, and

$$CRR_{7.5,1} = \frac{CRR}{MSF \cdot K_\sigma} = f(N_{1,60,cs}) = f(N_{1,60}, FC)$$

The relationship between CRR and $N_{1,60,cs}$ was illustrated in Figure 3.1. Continuing,

$$CRR = f(N_{1,60}, FC) \cdot MSF \cdot K_\sigma$$

$$\ln CRR = f(N_{1,60}, FC) + \ln MSF + \ln K_\sigma$$

Equation (4.1) can be rearranged to form an expression for CRR :

$$\ln CRR = \ln CSR_{eq} = \frac{N_{1,60}(1 + 0.004FC) + 0.05FC - 29.53 \ln M_w - 3.70 \ln \frac{\sigma'_{vo}}{p_a} + 16.85 + 2.70\Phi^{-1}(P_L)}{13.32}$$

From this, it is clear that $N_{1,60,cs} = N_{1,60}(1 + 0.004FC) + 0.05FC$. Also, at the boundary between liquefaction and non-liquefaction, $P_L = 0.5$ and $\Phi^{-1}(P_L) = 0$, so

$$\ln CRR = \frac{N_{1,60,cs} - 29.53 \ln M_w - 3.70 \ln \frac{\sigma'_{vo}}{p_a} + 16.85}{13.32}$$

Çetin et al. [24] and Youd et al. [128] describe the overburden stress correction as

$$K_{\sigma} = \left(\frac{\sigma'_{vo}}{p_a} \right)^{(f-1)} \quad \text{or}$$

$$\ln K_{\sigma} = (f - 1) \ln \frac{\sigma'_{vo}}{p_a}$$

From the form of $\ln CRR$, $(f - 1) = -3.70/13.32 = -0.278$, thus $f = 0.722$. This is near the middle of the range of 0.6–0.8 suggested by Çetin et al. and Youd et al. Using this simplification,

$$\ln CRR = \frac{N_{1,60,cs} - 29.53 \ln M_w + 16.85}{13.32} + \ln K_{\sigma}$$

From Youd et al., $MSF = 10^{2.24} M_w^{-2.56}$, which can be written more generally as $\ln MSF = \ln a + b \ln M_w$. From the form of $\ln CRR$, $b = -29.53/13.32 = -2.217$. At $M_w = 7.5$, $MSF = 1$ by definition, and $\ln MSF = 0$, thus

$$\ln a = 2.217 \ln 7.5 = 4.467 = \frac{59.5}{13.32} \quad \text{and}$$

$$\ln CRR = \frac{N_{1,60,cs} - 42.65}{13.32} + \ln MSF + \ln K_{\sigma}$$

Using this information, Equation (4.1) can be written as

$$P_L = \Phi \left[-\frac{N_{1,60,cs} - 13.32 \ln \frac{CSR_{eq}}{MSF \cdot K_{\sigma}} - 42.65}{2.70} \right] \quad (4.2)$$

in which $MSF = e^{4.467} M_w^{-2.217}$ and $K_{\sigma} = (\sigma'_{vo}/p_a)^{(0.722-1)}$.

Note that Çetin's P_L equation contains no terms for static shear stress or K_{α} . He states clearly that this relationship is applicable only to free-field, level-ground cases, and that situations involving static shear stress are not considered. Since his equation is used to compute the *IM-EDP* fragility curves for this implementation of the performance-based method, the restriction to free-field, level-ground cases is also imposed herein.

4.2.1 Uncertainty terms in Çetin's probability of liquefaction

One of the attractions of Çetin's relationship between *CSR* and soil penetration resistance is the separation of uncertainty due to the model parameters from uncertainty due to the

form of the model itself. This explicit apportionment of uncertainty, described in detail by Çetin et al. [22], is an improvement on many of the past probabilistic assessments of liquefaction, but since all of the parameters in Equation (4.1)—especially the penetration resistance—have some uncertainty or variability associated with them, users must be careful to add the parameter uncertainty back into the equation to get a usable result. This section expands on the description by Çetin et al. [22] of computing the parameter uncertainty and adding it to Equation (4.1) before calculating the return period of liquefaction.

Çetin et al. [22] pointed out that Equation (4.1) is based on the form of the standard normal probability distribution:

$$P = \Phi \left(\frac{x - \mu_x}{\sigma_x} \right)$$

in which P is the probability, x is the probabilistic variable of interest, and μ_x and σ_x are the mean value and standard deviation of the probabilistic variable, respectively. Probabilistic representations of liquefaction potential generally use case histories to estimate the location of the limit state between liquefaction and non-liquefaction, and the uncertainty in the location of the limit state is described by the dispersion in the probability distribution. In structural reliability, the limit state is given a value of zero, states of failure—liquefaction in this case—have values less than zero, and states of non-failure have values greater than zero. Thus, the probability of liquefaction can be written as

$$P_L = \Phi \left(-\frac{x - \mu_x}{\sigma_x} \right) = \Phi \left(-\frac{x}{\sigma_x} \right)$$

The negative sign in the fraction is necessary because the state of liquefaction is represented by negative values, and the simplified second form occurs because the errors in the limit state due to uncertainty are assumed to be normally distributed with zero mean.

In the simplified *CSR* method, the case history database is presented on a plot of *CSR* and $N_{1,60}$ (Figures 3.1 and 3.6) in which

$$f(CSR) = f(N_{1,60}, FC, M_w, \sigma'_{vo})$$

This equation can be rearranged to define a liquefaction limit state variable, \hat{g} , that has a value of zero at the limit state, is negative for liquefaction cases, and is positive for non-liquefaction cases:

$$\hat{g} = f(N_{1,60}, FC, M_w, \sigma'_{vo}) - f(CSR)$$

In this form, there is no provision for model or parameter uncertainty. To allow for uncertainty

$$g = \hat{g} + \varepsilon = f(N_{1,60}, FC, M_w, \sigma'_{vo}) - f(CSR) + \varepsilon$$

By assuming that ε is normally distributed with a mean of zero, Çetin et al. defined the probability of liquefaction as

$$\begin{aligned} P_L &= \Phi \left(-\frac{\hat{g}}{\sigma_\varepsilon} \right) \\ &= \Phi \left(-\frac{f(N_{1,60}, FC, M_w, \sigma'_{vo}) - f(CSR)}{\sigma_\varepsilon} \right) \end{aligned}$$

which is the general form of Equations (4.1) and (4.2). Note that all of the uncertainty is described by the term in the denominator; thus, when the parameter uncertainty is added back into Equation (4.1), only the term in the denominator changes.

Çetin et al. defined σ_ε as follows:

$$\begin{aligned} \sigma_\varepsilon^2 &= (1 + 0.004FC)^2 \sigma_{N_{1,60}}^2 + (-13.32)^2 \sigma_{\ln CSR_{eq}}^2 + (-29.53)^2 \sigma_{\ln M_w}^2 + \\ &\quad (-3.70)^2 \sigma_{\ln \sigma'_{vo}}^2 + (0.004N_{1,60} + 0.05)^2 \sigma_{FC}^2 + 2.70^2 \end{aligned} \quad (4.3)$$

in which σ_i^2 represents the variance of parameter i . This same result can be achieved by using the first-order second moment method assuming all the parameters are uncorrelated. Appendix A presents the derivation of the parameter variances for an example element of soil with the following characteristics: depth = 6 m, depth to the ground water table = 2 m, soil specific gravity = 2.67, soil void ratio = 0.67, fines content = 10 percent, and $N_{1,60} = 15$ blows per ft. The estimates were made for relatively large and small levels of uncertainty that were intended to correspond to site investigations for preliminary and final design stages. Table 4.1 summarizes the results from Appendix A. A value for $\sigma_{\ln M_w}^2$ is not included because the performance-based method explicitly integrates across the entire marginal magnitude distribution. The lower value of σ_ε (4.41) is very close to the value of 4.21 listed by Çetin et al. [22] which represents the overall parameter uncertainty from their

Table 4.1: Estimates of parameter variances for high and low levels of uncertainty for example soil element.

Parameter	High	Low
$\sigma_{N_{1,60}}^2$	20.3	9.01
$\sigma_{\ln CSR_{eq}}^2$	0.0193	0.0134
$\sigma_{\ln \sigma'_{vo}}^2$	0.0332	0.00772
σ_{FC}^2	4.84×10^{-6}	4.84×10^{-6}
σ_{ε}	33.1	19.5
σ_{ε}	5.75	4.41

case history database. To include parameter uncertainty in Çetin's probabilistic equation, therefore, the value of 2.70 in the denominator of Equation (4.1) should be replaced with 4.21 for cases involving a detailed site investigation has taken place and 5.75 for cases in which only a preliminary investigation has been done.

4.2.2 Useful EDPs

Soil liquefaction is a binary state: liquefaction has occurred if the effective confining stress of the soil has dropped to zero; otherwise liquefaction has not occurred. However, liquefaction potential in the performance-based framework is best described by a continuous variable that can be represented by a set of fragility curves, which in turn can be used to produce a new *EDP* hazard curve. An obvious choice is factor of safety against liquefaction, FS_L , since this is the metric used in the current methods of assessing liquefaction potential. FS_L can be implemented in the second term of Equation (4.1) as

$$P_L = \Phi \left[\frac{N_{1,60}(1 + 0.004FC) - 13.32 \ln(FS_L \cdot CSR_{eq}) - 29.53 \ln M_w - 3.70 \ln \frac{\sigma'_{vo}}{p_a} + 0.05FC + 16.85}{4.21} \right] \quad (4.4)$$

and fragility curves can be constructed for each specified level of FS_L and IM (a_{max} and M_w) by substituting the appropriate values into Equation (4.4) and computing the conditional probability. Note that the denominator in Equation (4.4) includes parameter uncertainty corresponding to a detailed site investigation.

The use of FS_L as the EDP is awkward for two reasons. First, factor of safety is typically regarded as a deterministic parameter; developing a relationship for the probability of a factor of safety is a combination of two incompatible descriptions of uncertainty. Second, the probability of failure increases with the loading magnitude, but FS_L decreases. If FS_L is used as the measure of liquefaction potential, it will not have a mean annual rate of exceedance, λ_{FS_L} , but a mean annual rate of *non-exceedance*, which Kramer and Mayfield [76] denote as Λ_{FS_L} . These are not insurmountable issues but they are awkward.

As an alternative to FS_L , liquefaction potential can be described by the degree of resistance to liquefaction that a soil must have. In terms of penetration resistance, liquefaction potential can be described as the SPT blowcount required to prevent liquefaction, N_{req} . This parameter increases with loading magnitude, so a mean annual rate of exceedance can be determined within the PEER framework. Also, N_{req} can be directly compared with the results of a site investigation: if the site blowcount is greater than N_{req} , the potential for liquefaction is small; if it is less than N_{req} , the difference indicates how much ground improvement is required to reduce the liquefaction risk. The first term of Equation (4.1) can be modified as follows to compute the fragility curves for this EDP :

$$P_L = \Phi \left[\frac{N_{req}(1 + 0.004FC) - 13.32 \ln(CSR_{eq}) - 29.53 \ln M_w - 3.70 \ln \frac{\sigma'_{v2}}{p_a} + 0.05FC + 16.85}{4.21} \right] \quad (4.5)$$

4.2.3 Relating FS_L and N_{req}

It is interesting to consider the relationship between FS_L and N_{req} . Rearranging Equation (4.1) yields an expression for the cyclic resistance ratio, CRR , which is the value of cyclic stress ratio, CSR_{eq} , required to resist liquefaction with probability, P_L :

$$CRR = \exp \left[\frac{N_{1,60}(1 + 0.004FC) - 29.53 \ln M_w - 3.70 \ln \frac{\sigma'_{v2}}{p_a} + 0.05FC + 16.85 + \sigma_\epsilon \cdot \Phi^{-1}(P_L)}{13.32} \right] \quad (4.6)$$

Figure 4.5a illustrates the case in which an element of soil has penetration resistance, N_{site} , at a location and depth where the penetration resistance required to resist liquefaction

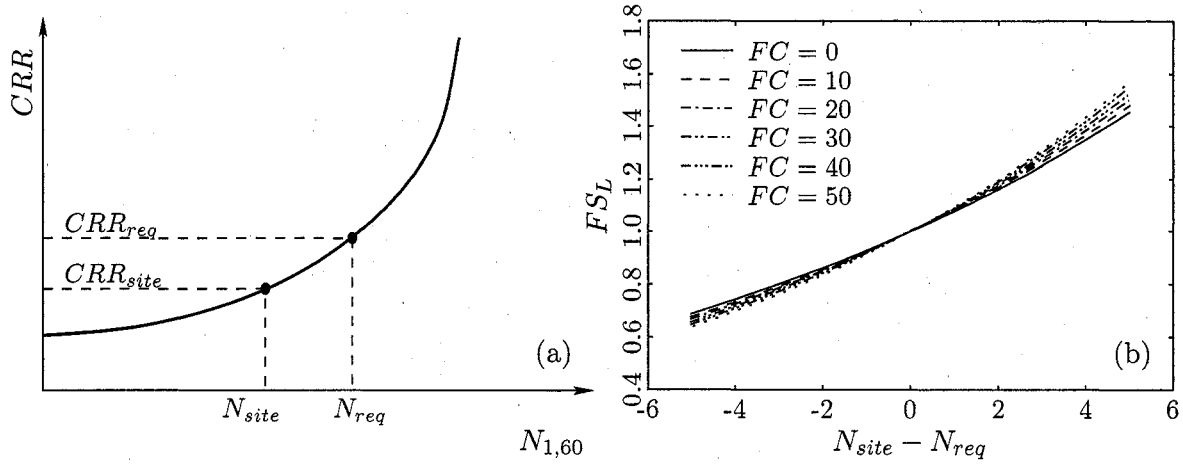


Figure 4.5: (a) Illustration of the relationship between CRR and penetration resistance, and (b) the effect of fines content on the factor of safety against liquefaction.

at some chosen return period is N_{req} . Comparing capacity and demand, the factor of safety against liquefaction is expressed as

$$FS_L = \frac{CRR_{site}}{CRR_{req}}$$

Substituting the appropriate values of penetration resistance into Equation (4.6)

$$\begin{aligned}
 FS_L &= \frac{\exp \left[\frac{N_{site}(1 + 0.004FC) - 29.53 \ln M_w - 3.70 \ln \frac{\sigma'_{vo}}{p_a} + 0.05FC + 16.85 + \sigma_\varepsilon \cdot \Phi^{-1}(P_L)}{13.32} \right]}{\exp \left[\frac{N_{req}(1 + 0.004FC) - 29.53 \ln M_w - 3.70 \ln \frac{\sigma'_{vo}}{p_a} + 0.05FC + 16.85 + \sigma_\varepsilon \cdot \Phi^{-1}(P_L)}{13.32} \right]} \\
 &= \exp \left[\frac{(N_{site} - N_{req})(1 + 0.004FC)}{13.32} \right] \\
 &= 1.078^{[(N_{site} - N_{req})(1 + 0.004FC)]} \tag{4.7}
 \end{aligned}$$

For clean sand ($FC = 0$),

$$FS_L = 1.078^{(N_{site} - N_{req})} \quad (4.8)$$

$$(4.9)$$

Thus, FS_L or N_{req} can be calculated if the other is known.

Figure 4.5b illustrates the effect of fines content on FS_L . Within about ± 5 bpf of N_{req} , the fines content has a relatively small effect and can be ignored. For greater differences in penetration resistance, the fines content should be considered.

4.2.4 Magnitude dependence

The dependence of the *CSR* method upon magnitude also plays a part in the *IM-EDP* fragility curves. The presence of the magnitude term in Equation (4.1), which forms the basis for constructing the fragility curves, requires each hazard curve that is conditional upon a magnitude bin to correspond to a fragility curve that is conditional upon the same range of magnitudes. Thus, the family of fragility curves—one for each level of *EDP*—implied by the general form of $P[EDP > edp | IM = im]$ in the performance-based approach is actually a family of sets of curves for the *CSR* method—one set for every magnitude bin at each level of *EDP* as defined by $P[N_{req} > n | a_{max} = a, M_w = m]$.

The two-part *IM* in the *CSR* method complicates the performance-based approach somewhat and increases the necessary computational effort. However, the mechanics of the integration remain the same as the illustration in Figure 2.3: each a_{max} hazard curve that is conditional upon a magnitude is integrated across the full range of a_{max} with the family of fragility curves that is conditional upon the same magnitude. This process is implemented in the next section for a site in Seattle, Washington.

4.3 The return period of soil liquefaction in Seattle

The first example of performance-based liquefaction assessment in this dissertation is for an idealized ground profile at a site near the Seattle-Tacoma International Airport (47.53N latitude, 122.3W longitude). The profile, shown in Figure 4.6, consists of clean sand with

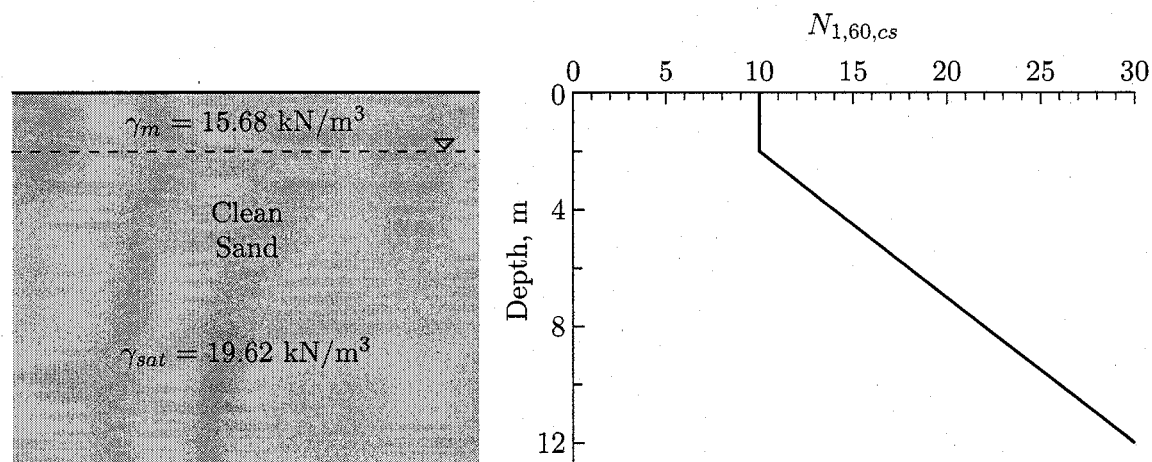


Figure 4.6: Subsurface profile used in assessing the return period of liquefaction in Seattle.

relatively low penetration resistance near the surface increasing to high penetration resistance at 12 m. The soil closer to the surface would be expected to liquefy during modest ground shaking, while the deeper soil would only be expected to liquefy during severe ground shaking. The a_{max} hazard curves from Figure 4.4 and the fragility curves computed from Equations (4.4) and (4.5) were integrated according to the PEER framework, producing the FS_L and N_{req} hazard curves in Figure 4.7. The vertical axis for the FS_L hazard curve is denoted by Λ_{FS_L} ; $\lambda_{N_{req}}$ is used for the N_{req} hazard curve.

The overall trends in the performance-based results are reasonable: liquefaction is much more likely (smaller FS_L and greater N_{req}) at shallow depths than in the deeper zones of the idealized profile, and stronger shaking at longer return periods (smaller Λ and λ) results in smaller FS_L and larger N_{req} .

In Figure 4.8, the results have been rearranged to describe the variation of liquefaction potential with depth in the soil profile. The heavy dashed line in the N_{req}^{pb} plot is the $N_{1,60}$ profile from Figure 4.6. Portions of the N_{req} curves to the left of the $N_{1,60}$ line have FS_L less than 1.0. Again, the overall trends seem reasonable: FS_L decreases and N_{req} increases with increasing IM return period, N_{req} is relatively low at the ground surface, and FS_L is relatively low at the ground surface where $N_{1,60}$ is low.

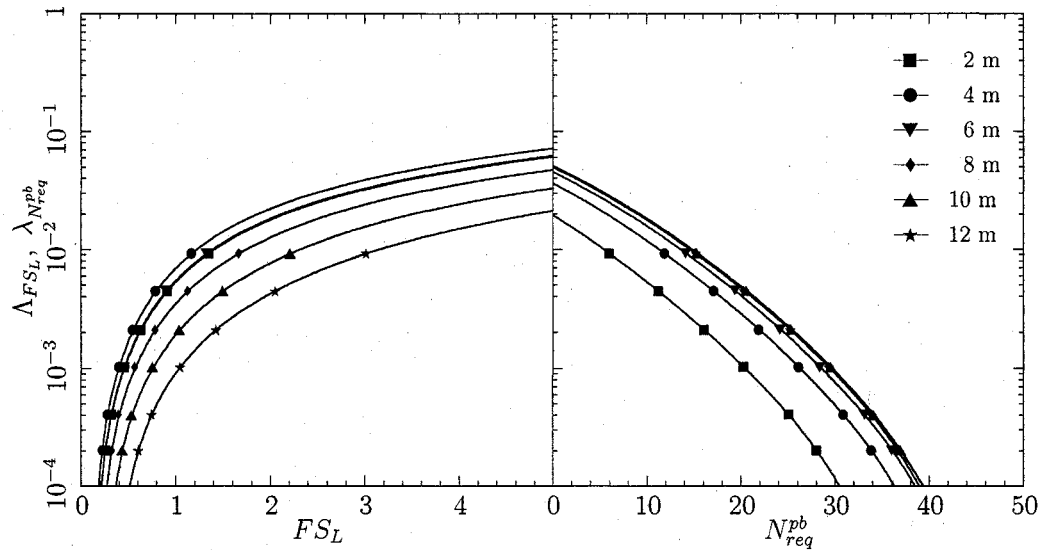


Figure 4.7: *EDP hazard curves for FS_L and N_{req} at the Seattle site.*

4.3.1 Comparison with conventional liquefaction analyses

There are several versions of the simplified *CSR* method that are in current use. In each one, the *IM* for a single return period is selected deterministically to assess the liquefaction potential, and the results are conditional upon that level of loading. In contrast, the performance-based approach considers all levels of *IM*, which should provide a more complete and consistent representation of the liquefaction potential.

In this section, results from two versions of conventional liquefaction assessment are compared with those presented above from the performance-based method. The first is the most recent development of the Seed and Idriss method as summarized in a 1996 workshop sponsored by the National Center for Earthquake Engineering Research (NCEER) and described by Youd et al. [128]. This is generally considered to represent the state of practice in geotechnical engineering and is in widespread usage; it was described in Chapter 3. In the NCEER method, the limit state between liquefaction and non-liquefaction cases is represented by a single deterministically-located curve (Figure 3.1).

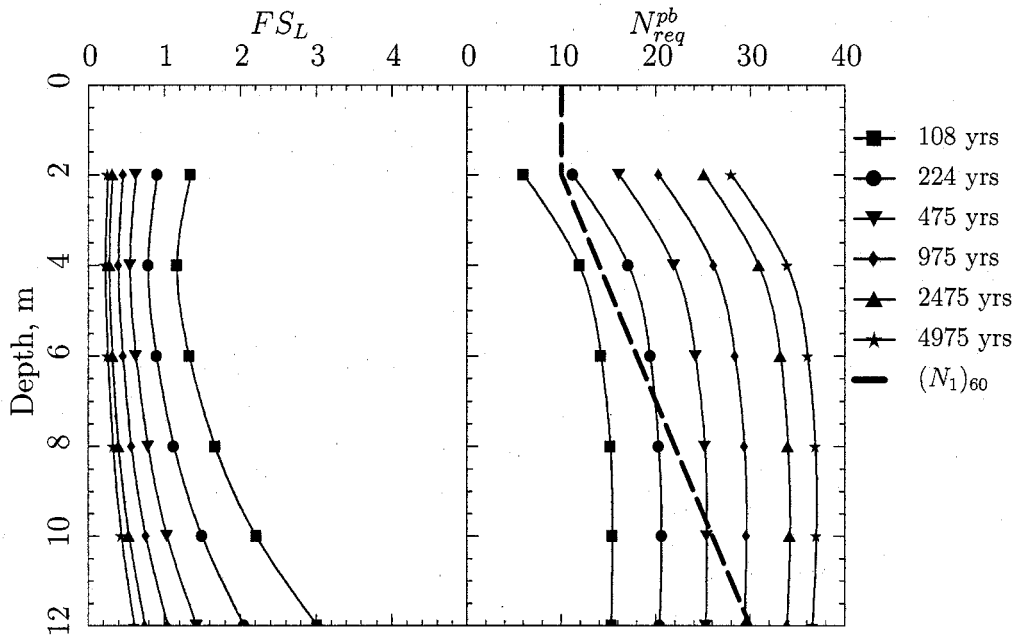


Figure 4.8: Performance-based FS_L and N_{req} depth profiles at the Seattle site.

Comparisons of FS_L from the NCEER and performance-based methods are straightforward: both are the ratio between the available liquefaction resistance and the demand and can be used directly without consideration of performance level. Comparisons of N_{req} are less clear because N_{req} implicitly involves a performance level. In conventional liquefaction assessments, a minimum FS_L of 1.1 to 1.3 is generally required [88]. This margin of safety combined with the conservative placement of the limit state line provide a performance level for liquefaction potential *conditional upon a single IM hazard level* that is generally considered to be appropriate for design.

The performance-based method has not been used widely enough for development of a consensus among professionals regarding the appropriate level of performance for design. However, the availability of the entire liquefaction hazard curve allows margins of safety to be represented by a liquefaction return period rather than by a factor of safety. This subtle change will increase the consistency of hazard assessments because the magnitude of

the hazard reduction due to a constant factor of safety depends on the slope of the hazard curve. This point will be discussed in more detail later in this chapter.

For the purposes of this dissertation, N_{req} was calculated for $FS_L = 1.2$ in conventional analyses and denoted as N_{req}^{det} ; in performance-based analyses, N_{req} was calculated for $FS_L = 1.0$ and denoted as N_{req}^{pb} . While the use of different factors of safety for the performance level may be criticized as an attempt to make the performance-based results appear more attractive (lower N_{req} for the same level of safety) than conventional results, the intent is to compare results from state-of-the-practice methods with those from a performance-based method that are stripped of hidden conservatism.

The second version of conventional analysis uses Equation (4.6) from Çetin et al. [24] with the slight modifications to include FS_L and N_{req} as described for Equations (4.4) and (4.5). Although Çetin et al. [24] stated that $P_L = 15$ percent in Equation (4.6) is approximately equivalent to the intent of the NCEER method, a simple parametric study for the Seattle site showed that $P_L = 0.60$ was more appropriate. This compares well with a similar study by Arango et al. [6] for a site in San Francisco where they found that $P_L = 0.65$ gave comparable results. In calculations for this dissertation, $P_L = 0.60$ was used.

The NCEER and Çetin versions of the simplified *CSR* method as described above are applied to the same Seattle site with the seismic parameters listed in Table 4.2. The values of a_{max} are the same as those for total a_{max} hazard curve in Figure 4.4 and the values of mean M_w are from the USGS deaggregations. FS_L for the assumed blowcount profile and N_{req}^{det} to achieve $FS_L = 1.2$ from these conventional analyses are presented as dashed lines in Figure 4.9. For comparison, the performance-based results from Figure 4.8 are included as solid lines.

Table 4.2: Peak horizontal ground accelerations and mean magnitudes for deterministic analyses at Seattle site.

T_R , yrs	a_{max} , g	Mean M_w
108	0.1718	6.44
224	0.2420	6.51
475	0.3323	6.57
975	0.4406	6.64
2475	0.6205	6.74
4975	0.7774	6.80

The performance-based and conventional results are generally consistent except at high values of N_{req} from the NCEER method. This discrepancy occurs because the NCEER method

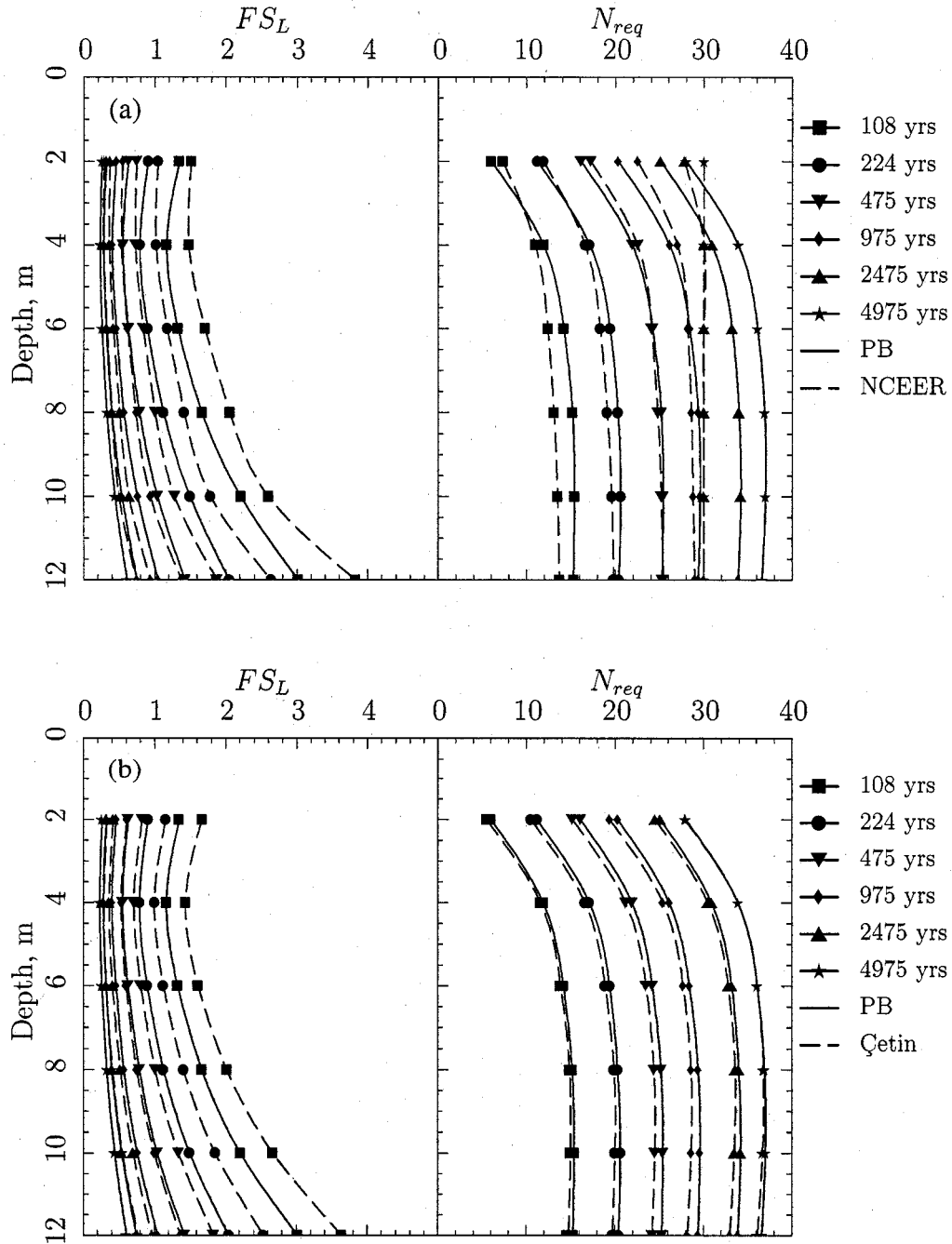


Figure 4.9: Deterministic FS_L and N_{req} depth profiles at Seattle from the (a) NCEER and (b) Çetin methods.

considers soil with $N_{1,60}$ greater than about 30 to be nonliquefiable under even the largest seismic loading; thus, N_{req}^{det} from the NCEER method can never exceed 30. In contrast, the Çetin equation, which is used for the performance-based calculations, does not have an upper blowcount limit. The other notable difference is in the FS_L plots: FS_L from the conventional analyses is somewhat higher than from the performance-based analysis. This highlights the important fact that the liquefaction potential conditional upon the IM from a single return period is not the same as the liquefaction at that same return period when all levels of IM are considered. At the Seattle site, the conditional liquefaction potential is slightly less (higher FS_L and lower N_{req}) from the conventional analysis than the total liquefaction potential from the performance-based analysis. The generality of this statement is investigated later in this chapter.

4.3.2 Equivalent return periods of liquefaction

The performance-based hazard curves can be used to calculate the equivalent return period of liquefaction implied by the results of conventional analyses. At the Seattle site, the equivalent return period is the inverse of $\lambda_{N_{req}^{pb}}$ from the righthand plot of Figure 4.7 that corresponds to N_{req}^{det} using the appropriate depth curve. Figure 4.10 illustrates the results of this exercise for the NCEER and Çetin results for the Seattle site. The pronounced curvature of the long return period lines from the NCEER analysis result from the 30-bpf maximum that is inherent in that method; the equivalent return periods for the upper portions of the profile are higher than T_R from the performance-based analysis, but they quickly drop to T_R lower than from the performance-based method at greater depths when the 30-bpf limit is reached. Below about 4 m, all of the equivalent return periods are slightly less than those from the performance-based analysis. This is consistent with the slightly higher FS_L of the conventional methods in Figure 4.9.

The equivalent return period curves for N_{req}^{det} from the Çetin analyses are nearly vertical. This is because the Çetin equation does not impose a blowcount limit; also it was used in both the conventional and performance-based analyses so the two results are more consistent. Despite this, the varying amounts of deviance from verticality and the offsets from the

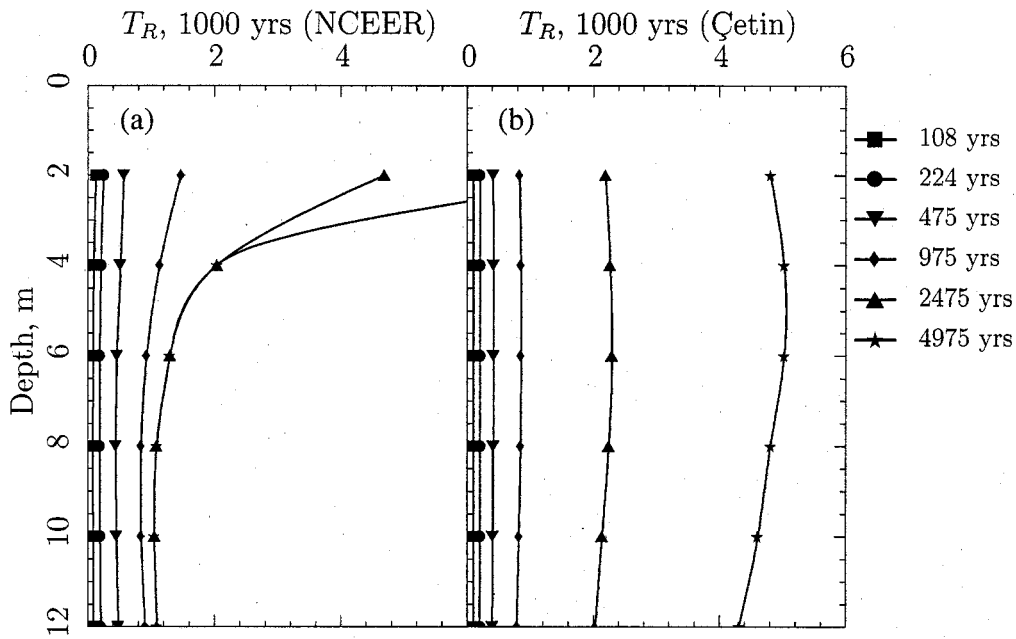


Figure 4.10: Equivalent performance-based return periods of N_{req}^{det} at the Seattle site from the (a) NCEER and (b) Çetin methods.

performance-based return periods indicate that the conventional analysis does not entirely capture the effects of the full a_{max} hazard curve and marginal magnitude distribution.

4.3.3 Deaggregation of liquefaction hazard

One of the useful characteristics of the performance-based approach is the ability to examine the contribution of each level of IM hazard to the total liquefaction hazard. Analogous to the PSHA deaggregation discussed earlier in this chapter, the liquefaction hazard can be deaggregated to illustrate the distribution of a_{max} and M_w and to allow computation of the mean and modal values of these IM components.

Figure 4.11 presents deaggregations of the liquefaction hazard for return periods of 475 and 2475 years for a soil element 6 m below the ground surface at the Seattle site. These plots are similar to the deaggregations (joint probability distributions) shown in Figure 4.3 but the view is from directly over the bars. The height of the bars in Figure 4.11 is denoted by the

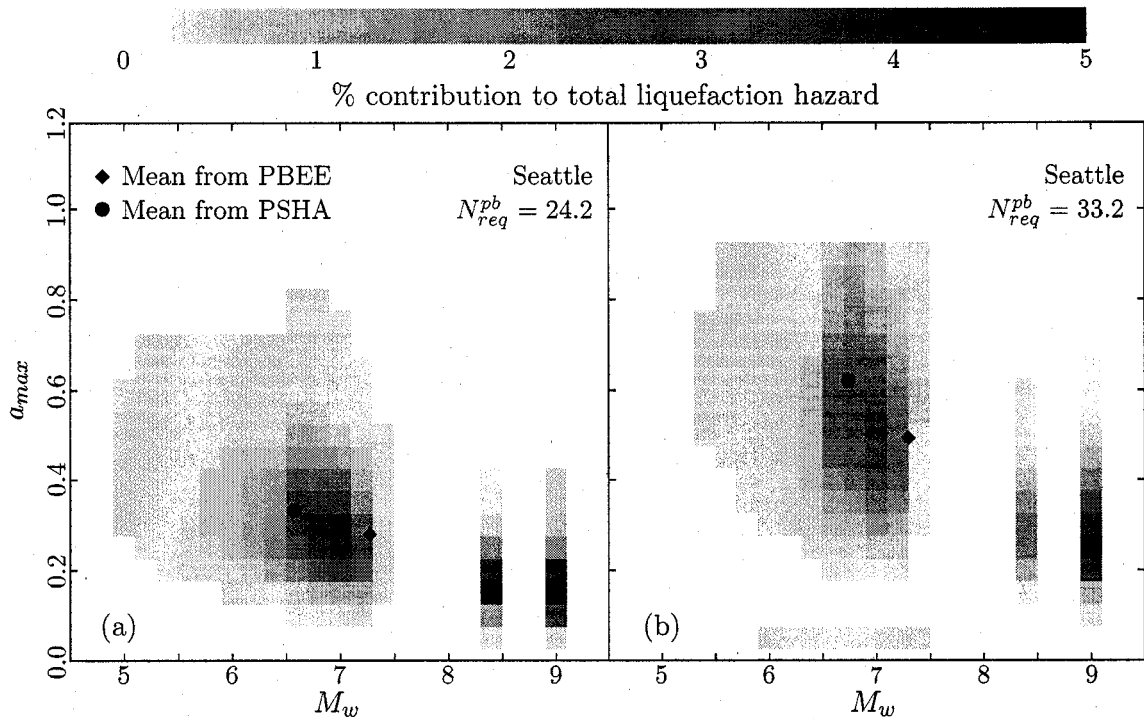


Figure 4.11: Deaggregation of (a) 475-yr and (b) 2475-yr return period liquefaction hazard for 6-m depth at Seattle. Round bullets mark the mean a_{max} and M_w from the PSHA used in the conventional approach, diamond bullets mark mean a_{max} and M_w from the performance-based approach.

shading: a black patch represents a 4.75% to 5% contribution to the liquefaction hazard, a white patch represents 0 to 0.25% contribution, and there are 20 shades of gray representing evenly spaced intervals between these two limits. The darkest patches in Figure 4.11 show that the modal magnitude for the liquefaction hazard at both return periods is 9.0 but diamonds mark the mean magnitude at about 7.3. The modal and mean a_{max} are about 0.15g and 0.28g, respectively, for the 475-yr return period and 0.25g and 0.5g, respectively, for the 2475-yr return period. For comparison, the PSHA values of mean magnitude and a_{max} in Table 4.2—shown as round bullets in Figure 4.11—are at lower M_w and higher a_{max} at both return periods but by differing amounts.

This result is relevant to a topic of debate in the geotechnical profession about the conventional *CSR* method: should the mean or modal earthquake magnitude be used to

Table 4.3: Peak accelerations for 10 U. S. cities from the USGS deaggregation web site. Accelerations are ratios of gravity.

Location	N. Lat.	W. Long.	475-yr a_{max}	2475-yr a_{max}
Butte, MT	46.003	112.533	0.120	0.225
Charleston, SC	32.776	79.931	0.189	0.734
Eureka, CA	40.802	124.162	0.658	1.023
Memphis, TN	35.149	90.048	0.214	0.655
Portland, OR	45.523	122.675	0.204	0.398
Salt Lake City, UT	40.755	111.898	0.298	0.679
San Francisco, CA	37.775	122.418	0.468	0.675
San Jose, CA	37.339	121.893	0.449	0.618
Santa Monica, CA	34.015	118.492	0.432	0.710
Seattle, WA	47.530	122.300	0.332	0.620

compute the magnitude scaling factor? Figure 4.11 suggests that neither will consistently capture the liquefaction hazard because each is only a single point in the magnitude distribution. The combination of the entire magnitude distribution and the shape and position of the entire a_{max} hazard curves are needed to consistently calculate the liquefaction hazard. This point is illustrated in more detail in the next section.

4.4 The return period of soil liquefaction across the U. S.

Comparisons of liquefaction potential from the performance-based and conventional methods for the Seattle site identified several differences. However, if those differences are consistent across different seismic environments, it may be possible to calibrate the conventional approaches to include the additional information from the performance-based approach.

To investigate this possibility, the soil profile from the Seattle site is assumed to be located in nine additional cities across the U. S., and the liquefaction potential at these locations is calculated using the performance-based and conventional methods. Table 4.3 lists the locations of these cities as well as the 475-yr and 2475-yr a_{max} from the USGS deaggregation web site. These cities are chosen to represent a wide range of seismic environments: Butte and Salt Lake City are seismically active but with relatively modest magnitudes; Charleston and Memphis are in areas of low recent seismicity with very large

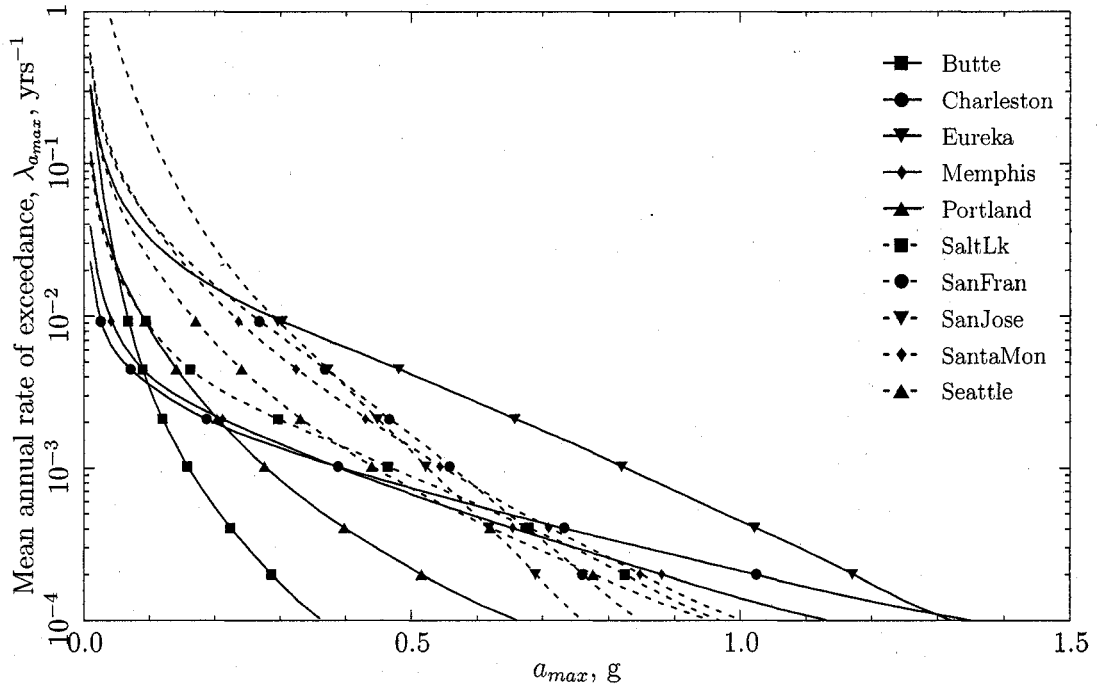


Figure 4.12: Total a_{max} hazard curves for ten cities across the U. S. The values of a_{max} have been modified by the rock-soil amplification factor per Stewart et al. [115].

historical earthquakes; Eureka, Portland, and Seattle are in areas subject to large-magnitude subduction earthquakes; and San Francisco, San Jose, and Santa Monica are in very active seismic environments. The seismicity levels vary widely, with 475-yr a_{max} values ranging from 0.12g in Butte to 0.66g in Eureka.

Figure 4.12 illustrates the a_{max} total hazard curves for the ten cities. Each is based on six data points from the USGS deaggregation web site, extrapolated and modified with Stewart's amplification factor as described for the Seattle site. The curves show that the differences in the cities' seismicity extend well beyond just a_{max} amplitude. While the amplitude is described by the position of the curves, the different slopes indicate that the rate of change of amplitude with mean annual rate of exceedance varies significantly, as does the different curvatures of the lines.

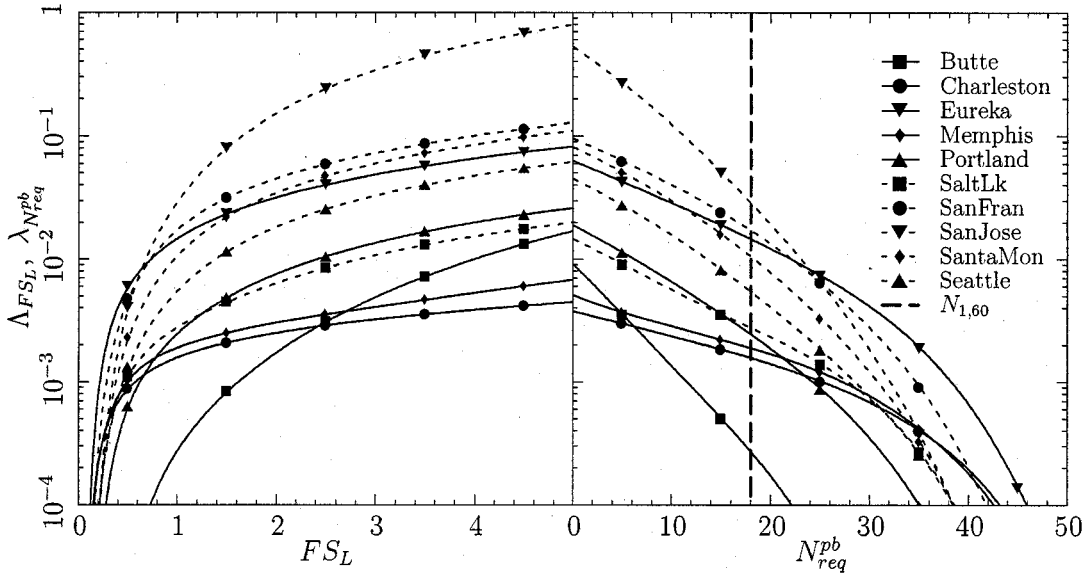


Figure 4.13: EDP hazard curves for FS_L and N_{req} at 6-m depth for ten U. S. cities.

The performance-based liquefaction hazard curves for a soil element 6 m below the ground surface of the idealized profile are presented in Figure 4.13. The vertical line in the N_{req}^{pb} plot illustrates the actual blowcount at 6 m in the profile; this line crosses the individual N_{req}^{pb} hazard curves at the mean annual rate of exceedance corresponding to $FS_L = 1.0$ for the performance-based method. The variety of shapes that was evident in the a_{max} hazard curves persists in the liquefaction hazard curves.

4.4.1 Deaggregation of liquefaction hazard

Other effects of different seismic environments can be seen from deaggregations of the liquefaction as illustrated in Figure 4.14. The relative positions of the modal and mean values of a_{max} and M_w vary considerably for the different cities, as do the relative positions of the mean values for liquefaction potential, designated as “Mean from PBEE” in Figure 4.14, and for the PSHA. In general, sites with lower PSHA a_{max} have lower PBEE a_{max} but by varying amounts. The greatest discrepancies is for M_w : in Salt Lake City, the mean M_w for

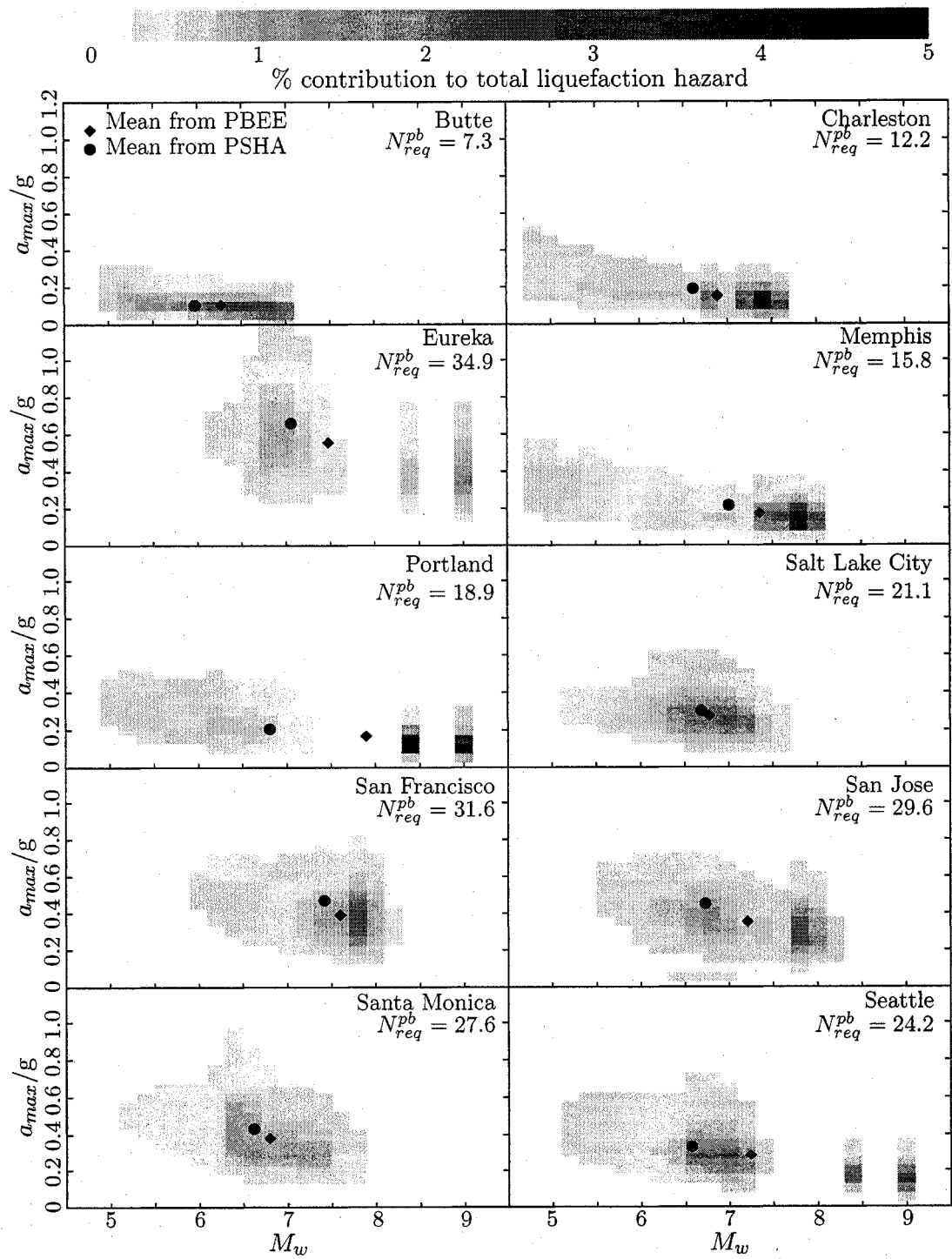


Figure 4.14: Deaggregation of 475-yr return period liquefaction hazard for 6-m depth at ten U. S. cities.

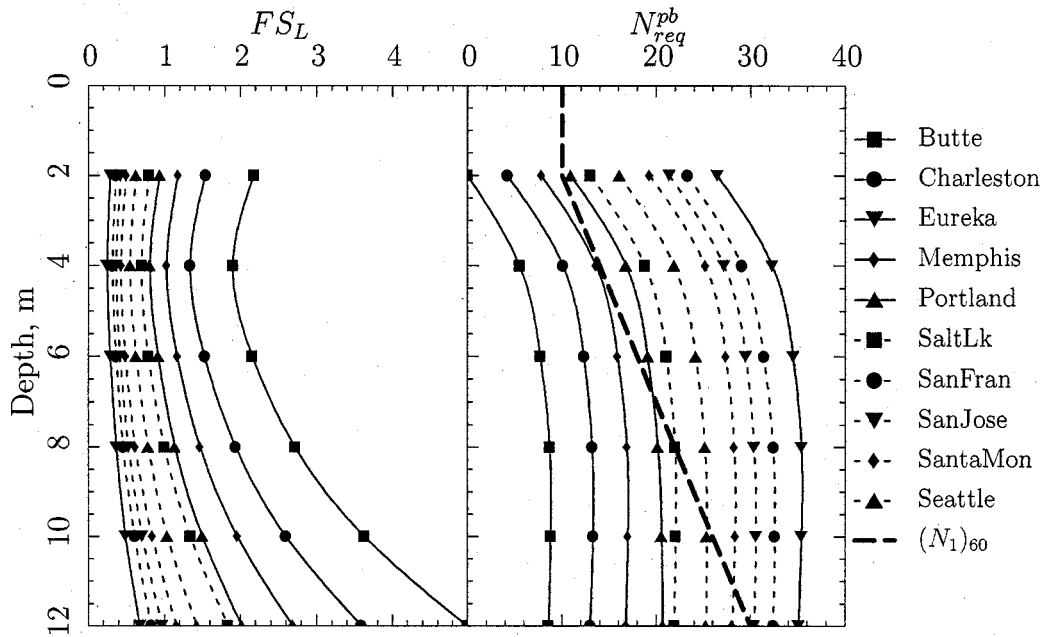


Figure 4.15: Performance-based FS_L and N_{req}^{pb} depth profiles at ten U. S. cities for the 475-yr return period.

the PBEE and PSHA analyses are nearly the same, but in Portland the difference is greater than one full magnitude interval. The shape of the deaggregated contributions suggests why this occurs—the distribution is unimodal in Salt Lake City but bimodal in Portland—but there is no apparent pattern to allow prediction of this difference.

4.4.2 Comparison with conventional liquefaction analyses

The FS_L and N_{req}^{pb} results from Figure 4.13 are replotted in the form of depth profiles in Figure 4.15, and the corresponding depth profiles from the two deterministic methods are in Figure 4.16. The performance-based results are not overlaid here for the sake of clarity, but a comparison of three results for the 475-yr return period is listed in columns (b) through (d) of Table 4.4. For the NCEER method, the difference between N_{req}^{det} and N_{req}^{pb} ranges from -4.5 bpf for Eureka to +3.6 bpf for Memphis, and for the Çetin method, the difference ranges from -1.2 bpf for Portland to +3.7 bpf for Charleston. The relatively large negative

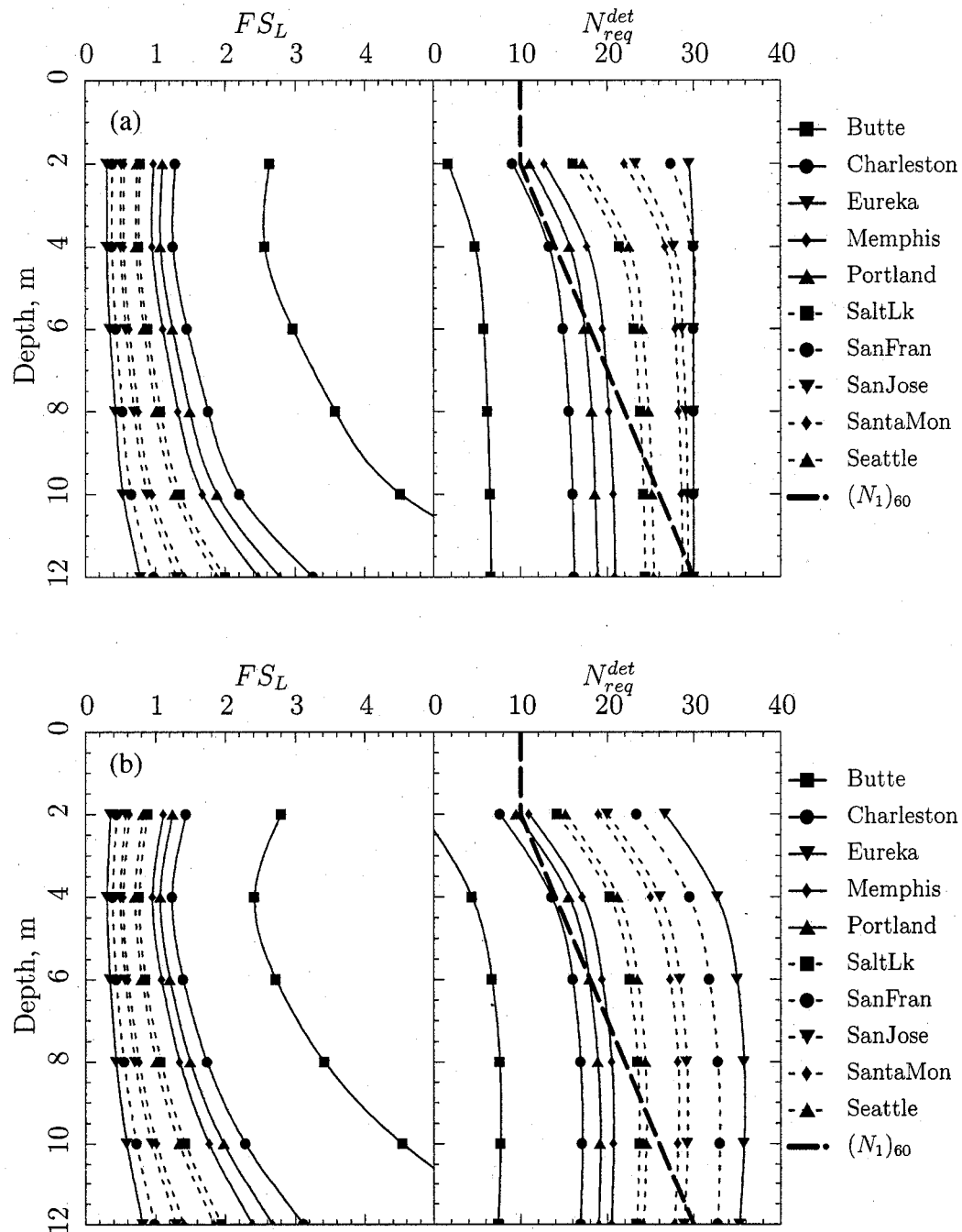


Figure 4.16: Deterministic FS_L and N_{req} depth profiles at ten U. S. cities for the 475-yr return period a_{max} from the (a) NCEER and (b) Çetin methods.

Table 4.4: Required penetration resistances and ratios of equivalent factors of safety for 475-yr liquefaction hazard at 6-m depth in the idealized site at ten U. S. cities.

(a) Location	(b) NCEER N_{req}^{det}	(c) Çetin N_{req}^{det}	(d) 475-yr N_{req}^{pb}	(e) NCEER FS_L	(f) Çetin FS_L
Butte	5.8	6.7	7.7	0.87	0.93
Charleston	14.9	16.0	12.3	1.22	1.32
Eureka	30.0	35.0	34.5	N/A*	1.04
Memphis	19.5	19.4	15.9	1.31	1.30
Portland	17.4	17.9	19.1	0.88	0.91
Salt Lake City	23.1	22.6	21.1	1.16	1.12
San Francisco	30.0	31.8	31.4	N/A*	1.03
San Jose	28.7	28.4	29.5	0.94	0.93
Santa Monica	27.9	27.3	27.4	1.04	0.99
Seattle	24.1	23.5	24.2	0.99	0.95

* Factors of safety are not applicable for cases in which the upper limit of $N_{1,60} = 30$ implied by NCEER procedure is reached.

differences from the NCEER method for Eureka and San Francisco results from the limit of 30 bpf implicit in that method.

The inherent variability of the Standard Penetration Test may make these differences appear to be insignificant. However, the factors of safety in columns (e) and (f) illustrate the relatively large effect made by even small differences in N . These values were computed using Equation (4.8) and the difference between the conventional and performance-based values of N_{req} (columns (b) - (d) and columns (c) - (d)).

The factors of safety in Table 4.4 point out an important issue: *consistent use of the conventional methods in different seismic environments produces inconsistent estimates of liquefaction potential*. For example, the relatively high factors of safety for Charleston and Memphis indicate that designs based on conventional liquefaction assessment in these areas are required to achieve a higher level of safety—with higher commensurate costs—than designs in Portland or San Jose. As noted earlier, this inconsistency occurs because the results from conventional methods are conditional upon only one point from the a_{max} hazard curve and one magnitude from the marginal magnitude distribution. Results from

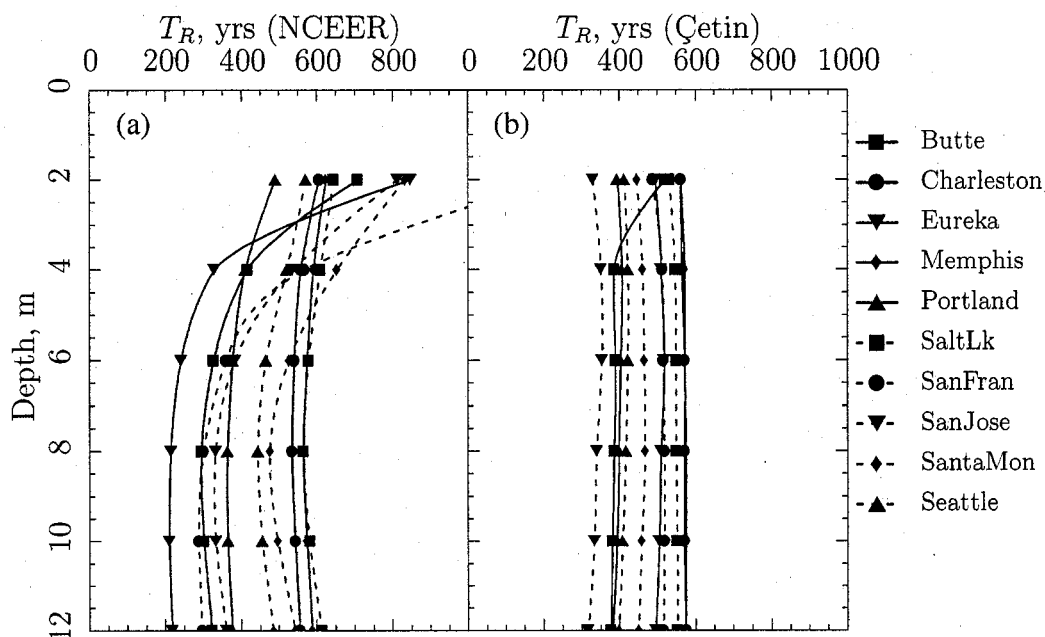


Figure 4.17: Equivalent liquefaction return periods of 475-yr N_{req}^{det} for 6-m depth at ten U. S. cities from the (a) NCEER and (b) Çetin methods.

the performance-based analyses are more consistent because they are based on the entire range of a_{max} and all combinations of a_{max} and M_w are explicitly accounted for with their contributions weighted by their relative likelihoods of occurrence.

4.4.3 Equivalent return periods of liquefaction

A similar conclusion can be reached by considering the equivalent return periods implied by the conventional analyses. As described for the Seattle site, N_{req}^{det} from the conventional analyses (Table 4.4) can be used with the N_{req}^{pb} hazard curves from the performance-based analyses (Figure 4.13) to determine the equivalent mean annual rate and, thus, the return period of liquefaction. Figure 4.17 and Table 4.5 present the results. The most extreme differences between the equivalent liquefaction return period and the a_{max} return period selected for the conventional analyses are for cities at which the 30-bpf limit is reached in the NCEER method; the equivalent return periods from the 2475-yr a_{max} at Eureka and San

Table 4.5: Equivalent liquefaction return periods of 475-yr and 2475-yr N_{req}^{det} for 6-m depth at ten U. S. cities.

Location	475-yr motions		2475-yr motions	
	NCEER	Çetin/NCEER	NCEER	Çetin/NCEER
Butte	348	418	1592	2304
Charleston	532	571	1433*	2725
Eureka	236*	483	236*	1590
Memphis	565	575	1277*	2532
Portland	376	422	1675	1508
Salt Lake City	552	543	1316*	2674
San Francisco	355*	503	355*	1736
San Jose	360	341	532*	1021
Santa Monica	483	457	794*	1901
Seattle	448	427	1280*	2155

*affected by upper limit of $N_{l,60} = 30$ bpf implied by NCEER procedure.

Francisco are particularly striking—236 and 355 years, respectively. Even for cities that did not reach the NCEER blowcount limit, the equivalent liquefaction return periods vary significantly from the a_{max} return periods used in the conventional analyses.

The results for Portland and Charleston provide an interesting comparison of the conventional and performance-based methods. Figure 4.12 shows that the 475-yr a_{max} for these two cities are nearly identical at about 0.2g, suggesting that the results from the conventional analysis should be similar. Figure 4.16 and Table 4.4 confirm this, although $N_{req}^{det} = 17.4$ bpf for Portland is about 2.5 bpf higher than for Charleston's 14.9 bpf; the difference is due to differences in the mean earthquake magnitudes used to compute MSF . The difference in N_{req}^{pb} from the performance-based analysis is much greater: 19.1 bpf for Portland and 12.3 bpf for Charleston. Table 4.5 shows that this difference of nearly 7 bpf results in equivalent liquefaction return periods of 376 and 532 years for Portland and Charleston—a significant departure from the 475-yr a_{max} that was used in the conventional analyses.

These inconsistent return periods highlight the importance of considering the entire a_{max} hazard curve and magnitude distribution in assessing liquefaction potential: unless this is done, the results generally will not provide a consistent representation of the liquefaction

hazard across differing seismic environments. Some areas, like Portland in this example, are unknowingly accepting a lower standard of safety while others, like Charleston, are paying for a higher standard. By considering the entire a_{max} hazard curve and magnitude distribution, the performance-based approach incorporates the hazard from all possible combinations of a_{max} and magnitude, and provides a more complete and consistent estimate of liquefaction potential for all seismic environments.

4.5 Development of a performance-based liquefaction criterion

One of the goals of building codes and standards is to produce designs with a uniform risk across the regions of their application. The previous sections have shown that conventional procedures for liquefaction assessment have significant limitations in this respect, and that performance-based procedures can overcome those limitations. Before the performance-based approach can be widely adopted by the geotechnical profession, though, there are two questions that need to be addressed:

1. What return period from a performance-based analysis should be adopted to provide an overall level of safety and cost that is similar to the intent of conventional analyses using the ground motion from a single return period?
2. Which liquefaction evaluation procedure should be used in the performance-based analysis?

These are complex issues that cannot be settled in a dissertation; they require broad discussion within the profession to develop a consensus. The following sections describe some of the considerations underlying these two questions.

4.5.1 An appropriate liquefaction return period

In conventional liquefaction assessments, FS_L of 1.1 to 1.3 is often adopted for a “safe” design [88]. In addition to this explicit level of conservatism, the NCEER method is based on a limit state boundary between liquefaction and non-liquefaction cases that is conservatively located to reduce the likelihood of a site being classified as non-liquefiable when it is really

liquefiable. In the performance-based approach described in this dissertation, N_{req} has been determined for $FS_L = 1.0$ and the limit state boundary from the Çetin et al. equation is located where the probability of liquefaction is 50%, thus imposing no additional conservatism. An earlier section suggested that conservatism in the performance-based method should be invoked by choosing results with an appropriate return period of liquefaction rather than by adding a factor of safety, but there was no suggestion of how to decide which return period is appropriate.

This issue is complicated by the inconsistent results from the conventional analyses. If the results were consistent, a return period could be chosen to yield the same result as the conventional method. The average equivalent return period in Table 4.5 based on the 475-yr a_{max} is 426 yrs from the NCEER method and 474 yrs from the Çetin method; based on the 2475-yr a_{max} , the NCEER average is 1049 yrs and the Çetin average is 2015 yrs. It appears, therefore, that some overall averaging process may provide guidance for choosing the performance-based return period but the results will vary with the method of analysis, the return period being considered, and the locations used in the averaging process. As noted above, this issue will require careful discussion within the geotechnical profession.

4.5.2 A suitable liquefaction evaluation procedure

In this dissertation, the performance-based analyses using the *CSR* method have used the relationship between *CRR* and $N_{1,60}$ described by Çetin et al. [24]. It was chosen for calculating the *IM-EDP* fragility curves because of the reassessment of and addition to the liquefaction case history database and the separation of model and parameter uncertainty that were part of its development. However, other probabilistic capacity-demand models for liquefaction exist ([81, 118, 129] for example) and could have been used. Key considerations for selecting a model include the following:

1. The model must be probabilistic. In a deterministic model like the one in the NCEER method, the limit state boundary between liquefaction and non-liquefaction cases is separated by a single line and there is no explicit consideration of the uncertainty associated with the location of that boundary. Probabilistic models like those by

Çetin et al. describe the limit state boundary as a probability distribution rather than a line, and this distribution allows computation of the *IM-EDP* fragility curves.

2. The combination of model and parameter uncertainty should be as low as possible. Greater uncertainty results in flatter fragility curves, which result in increased liquefaction hazard (higher mean annual rates and lower return periods of liquefaction). As the quality of the case history database improves and parameter uncertainty decreases, updated models should produce more accurate estimates of liquefaction potential.

The use of a different liquefaction model in the performance-based method would require reassessment of the relationship between FS_L and N_{req} presented in Equation (4.8) as well as the characterization of the uncertainty and development of the site-specific correction factor described in Appendices A and B.

4.6 Liquefaction hazard maps for Washington State

Most liquefaction assessment is done for individual sites as described earlier in this chapter for the ten U. S. cities. However, the consistency of the performance-based results across varying seismic environments suggests that it can be used to produce directly comparable estimates of liquefaction hazard over large areas.

In this research project, the performance-based *CSR* method is applied to the standard reference profile in Figure 4.18 at a grid of locations covering Washington State, and the resulting values of N_{req} at return periods of 475 and 2475 yrs are contoured in Figure 4.19. The grid of points subjected to the liquefaction assessment is spaced at 0.3 degrees of latitude and 0.5 degrees of longitude, for a total of 247 locations; the individual points are marked with faint crosses on the maps.

The shape of the N_{req} contours is in general agreement with our understanding of the geometry of the Juan de Fuca plate: the hazard is greatest along the west coast closest to the offshore subduction zone, and it decreases to the east, especially east of the Cascade Mountains. The eastward bulge of the contours at latitude 47.5, especially for the 475-yr return period, shows the influence of the deep, intraplate events like the 1949, 1965, and Nisqually earthquakes.

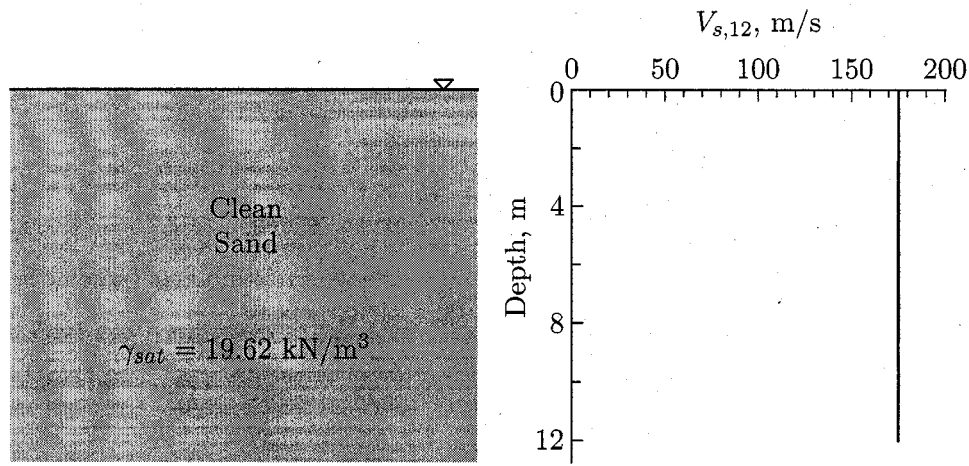


Figure 4.18: Reference soil profile for performance-based analysis across Washington State. $V_{s,12}$ is related to the penetration resistance of the soil and is used to calculate Çetin's depth reduction coefficient, r_d .

For Seattle, the 475-yr map indicates that N_{req} is about 25.7 bpf compared to 24.2 bpf in Table 4.4. This discrepancy occurs because the shear wave velocity, V_s , for the example profile in Figure 4.6 is slightly higher than for the profile used to produce the maps. There is also a small apparent error as a result of the contour interpolation.

The maps allow a user to take advantage of performance-based liquefaction assessment without having to go through the lengthy computations. For a location of interest, the user can match the fines-corrected SPT results from a site investigation, $N_{1,60,cs}$, with the N_{req} value from the map, subject to the site-specific adjustments described in the following section. If site value is higher, the return period of liquefaction is greater than the map return period. If the site value is lower, the user has an immediate indication of how much site improvement is required to increase the return period of liquefaction to the map return period.

4.7 Adjustment of mapped N_{req} values for site-specific conditions

The N_{req} maps in Figure 4.19 are based on a simple standard reference profile. In this section, a procedure is developed to adjust N_{req} from the mapped values to account for site-specific conditions that are different from those of the reference profile. The adjustment,

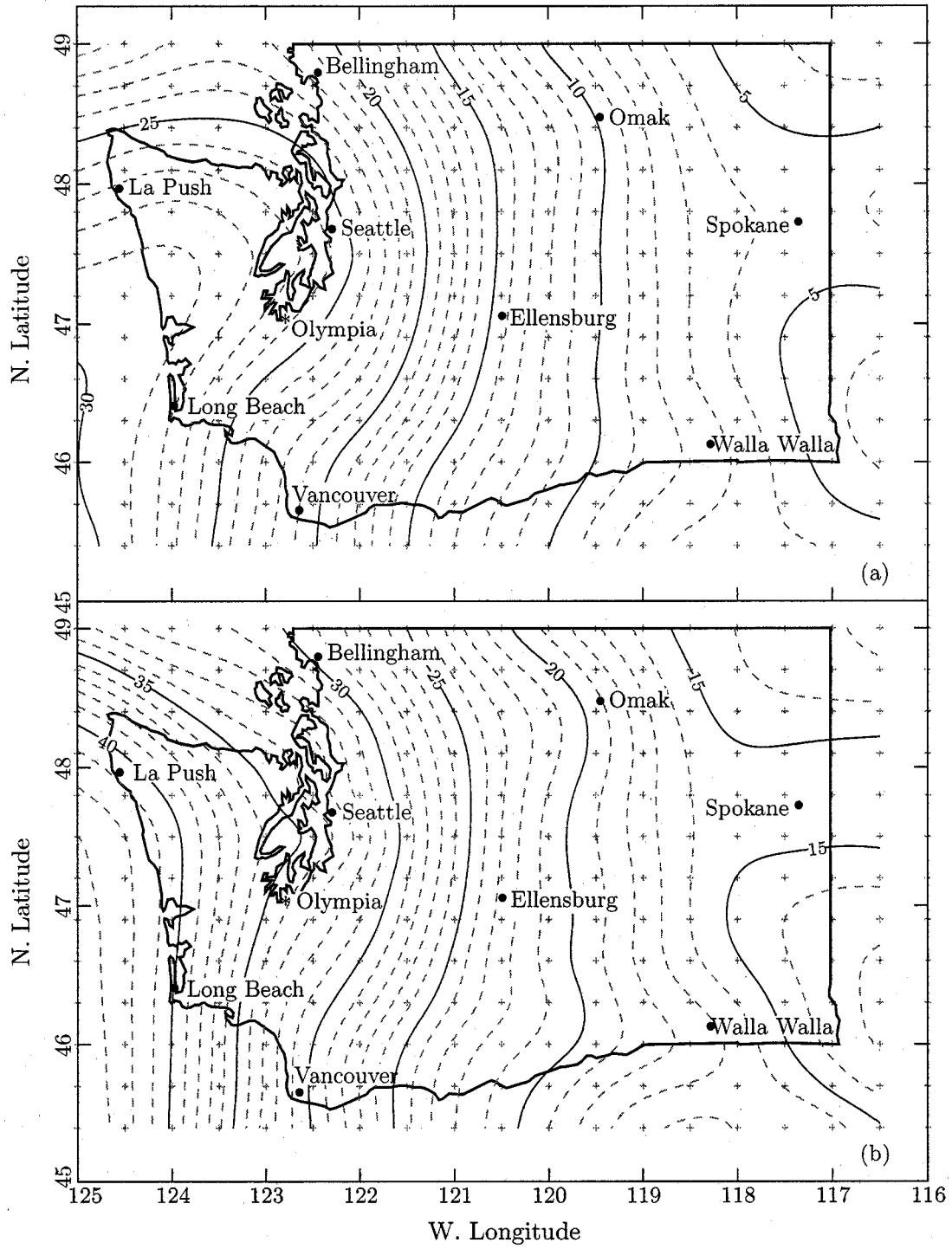


Figure 4.19: (a) 475-yr and (b) 2475-yr N_{req} at 6-m depth in reference profile for Washington State.

ΔN_{req} , is an additive value that is based on Equation (4.1) modified from Çetin et al. [24]. Rearranging Equation (4.1),

$$\begin{aligned} N_{req} &= N_{1,60,cs} = N_{1,60}(1 + 0.004FC) + 0.05FC \\ &= 13.32 \ln CSR + 29.53 \ln M_w + 3.70 \ln \frac{\sigma'_{vo}}{p_a} - 16.85 - \sigma_\varepsilon \Phi^{-1}(P_L) \end{aligned}$$

Note that σ_ε has a value of 2.70 when no parametric uncertainty exists, and higher values when parametric uncertainty is accounted for. For the production of the maps in Figure 4.19, $\sigma_\varepsilon = 4.21$, which is appropriate for cases in which the results from a detailed site investigation are available.

If the site-specific constituents of this equation are evaluated in terms of the reference profile (denoted by the subscript, *ref*), an expression for the required clean sand SPT resistance for the reference soil profile can be written as

$$N_{1,60,cs,ref} = 13.32 \ln \left(0.65 a_{max} \frac{\sigma_{vo,ref}}{\sigma'_{vo,ref}} r_{d,ref} \right) + 29.53 \ln M_w + 3.70 \ln \frac{\sigma'_{vo,ref}}{p_a} - 16.85 - \sigma_\varepsilon \Phi^{-1}(P_L)$$

Recalling the a_{max} soil amplification factor from Stewart et al. [115] that was described earlier in this chapter,

$$F_A = \frac{a_{max}}{a_{max,rock}} = \exp(a + b \ln a_{max,rock}) \quad (4.10)$$

in which $a = -0.15$ and $b = -0.13$ for quaternary alluvium. Now,

$$\begin{aligned} N_{1,60,cs} &= 13.32 \ln \left(0.65 F_A a_{max,rock} \frac{\sigma_{vo}}{\sigma'_{vo}} r_d \right) + \\ &\quad 29.53 \ln M_w + 3.70 \ln \frac{\sigma'_{vo}}{p_a} - 16.85 - \sigma_E \Phi^{-1}(P_L) \end{aligned}$$

The required clean sand SPT resistance for a soil profile other than the reference profile can be expressed as the sum of the required clean sand SPT resistance for the reference profile and the site-specific adjustment value, ΔN_{req} ,

$$N_{1,60,cs} = N_{1,60,cs,ref} + \Delta N_{req}$$

Therefore,

$$\begin{aligned}
\Delta N_{req} &= N_{1,60,cs} - N_{1,60,cs_{ref}} \\
&= 13.32 \ln \left(0.65 F_a a_{max_{rock}} \frac{\sigma_{vo}}{\sigma'_{vo}} r_d \right) + 29.53 \ln M_w + 3.70 \ln \frac{\sigma'_{vo}}{p_a} - 16.85 - \sigma_\epsilon \Phi^{-1}(P_L) - \\
&\quad \left[13.32 \ln \left(0.65 F_{A_{ref}} a_{max_{rock}} \frac{\sigma_{vo_{ref}}}{\sigma'_{vo_{ref}}} r_{d_{ref}} \right) + 29.53 \ln M_w + \right. \\
&\quad \left. 3.70 \ln \frac{\sigma'_{vo_{ref}}}{p_a} - 16.85 - \sigma_\epsilon \Phi^{-1}(P_L) \right] \\
&= 13.32 \ln \left(\frac{F_a}{F_{A_{ref}}} \frac{\sigma_{vo}/\sigma'_{vo}}{\sigma_{vo_{ref}}/\sigma'_{vo_{ref}}} \frac{r_d}{r_{d_{ref}}} \right) + 3.70 \ln \frac{\sigma'_{vo}}{\sigma'_{vo_{ref}}} \\
&= \left[13.32 \ln \frac{\sigma_{vo}/\sigma'_{vo}}{\sigma_{vo_{ref}}/\sigma'_{vo_{ref}}} + 3.70 \ln \frac{\sigma'_{vo}}{\sigma'_{vo_{ref}}} \right] + 13.32 \ln \frac{F_a}{F_{A_{ref}}} + 13.32 \ln \frac{r_d}{r_{d_{ref}}} \\
&= \Delta N_\sigma + \Delta N_F + \Delta N_{r_d}
\end{aligned}$$

In this form, there are three components of the site-specific N_{req} adjustment: one based on the initial vertical stress profile, one based on the amplification of a_{max} up through the soil column, and one based on the r_d profile. Appendix B describes the development of ΔN_{req} in more detail. Figure 4.20 presents the charts for ΔN_σ and ΔN_{r_d} ; ΔN_F can be calculated as follows:

$$\Delta N_F = 13.32 [(a + 0.15) + (b + 0.13) \ln a_{max_{rock}}] \quad (4.11)$$

in which a and b are soil type coefficients described by Stewart et al. [115].

4.7.1 Comparison with conventional liquefaction analyses

The mapped N_{req} values can be compared with the results from conventional liquefaction analyses using the procedures described for the ten U. S. cities. Figure 4.21 presents the contoured values of Çetin's N_{req}^{det} for 475-yr and 2475-yr a_{max} and mean magnitude, and Figure 4.22 presents the equivalent liquefaction return periods for N_{req}^{det} when compared to the performance-based N_{req} hazard curves. If the performance-based and conventional methods for assessing liquefaction potential produced the consistent results, every point

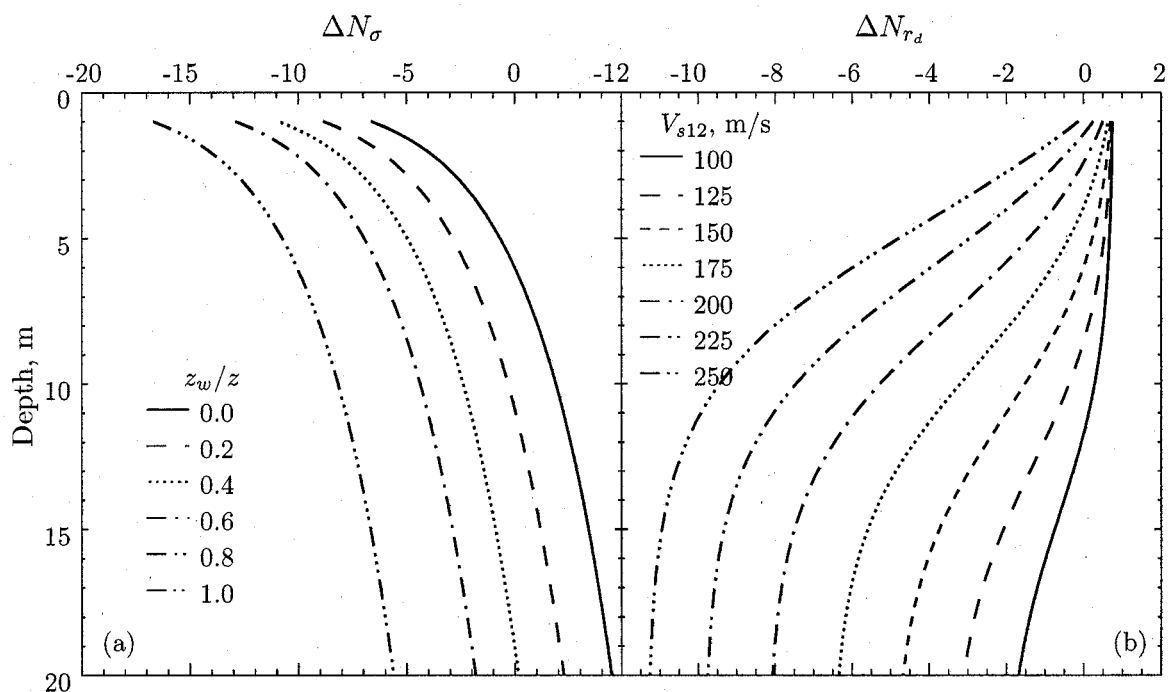


Figure 4.20: Correction factors for N_{req} maps. Correction factor for changes in (a) depth and groundwater level, ΔN_{σ} , and (b) correction factor for changes in depth and shear wave velocity, ΔN_{r_d} .

on each map in Figure 4.22 would have the same return period—475 yrs on the upper map and 2475 yrs on the lower map. However, the contours on Figure 4.22 show that the conventional method produces inconsistent results across varying seismic environments. The longer return periods in the western part of the state, especially along the Pacific coast, indicate that the conventional method imposes a higher level of safety and cost in this area than in the eastern part of the state.

The inconsistency of the conventional method can be also be illustrated by comparing N_{req}^{det} across the state to N_{req}^{pb} at a predetermined return period. For example, if Seattle were chosen as the reference location for the entire state, then the maps in Figure 4.22 would indicate that the 400-yr and 1700-yr values of N_{req}^{pb} could be used in place of N_{req}^{det} from the conventional analyses using the 475-yr and 2475-yr return period loading. As Figure 4.23 illustrates, however, the actual values of N_{req}^{det} across the state vary considerably from N_{req}^{pb}

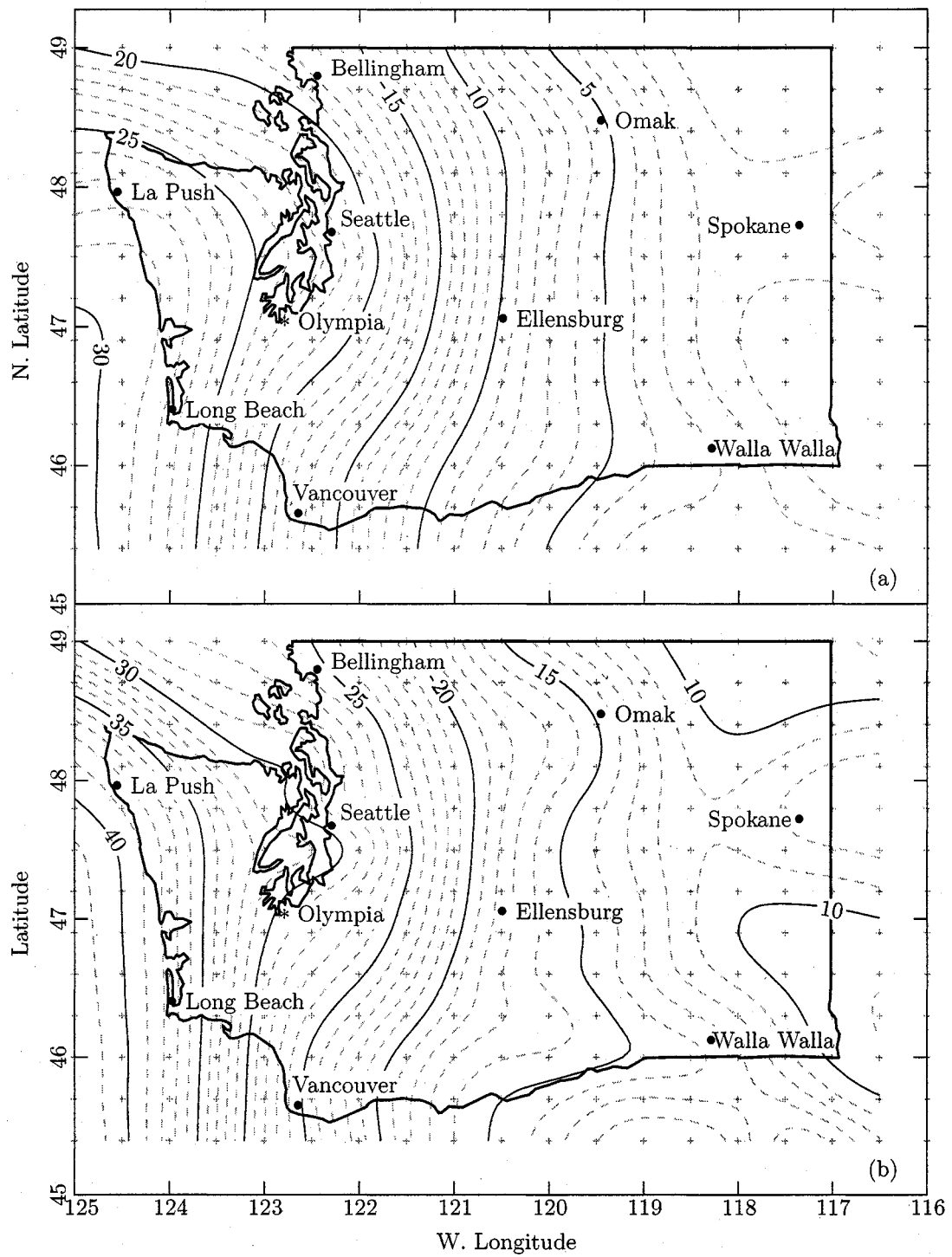


Figure 4.21: (a) 475-yr and (b) 2475-yr N_{req} at 6-m depth in reference profile for Washington State from conventional analyses using Çetin's method [24].

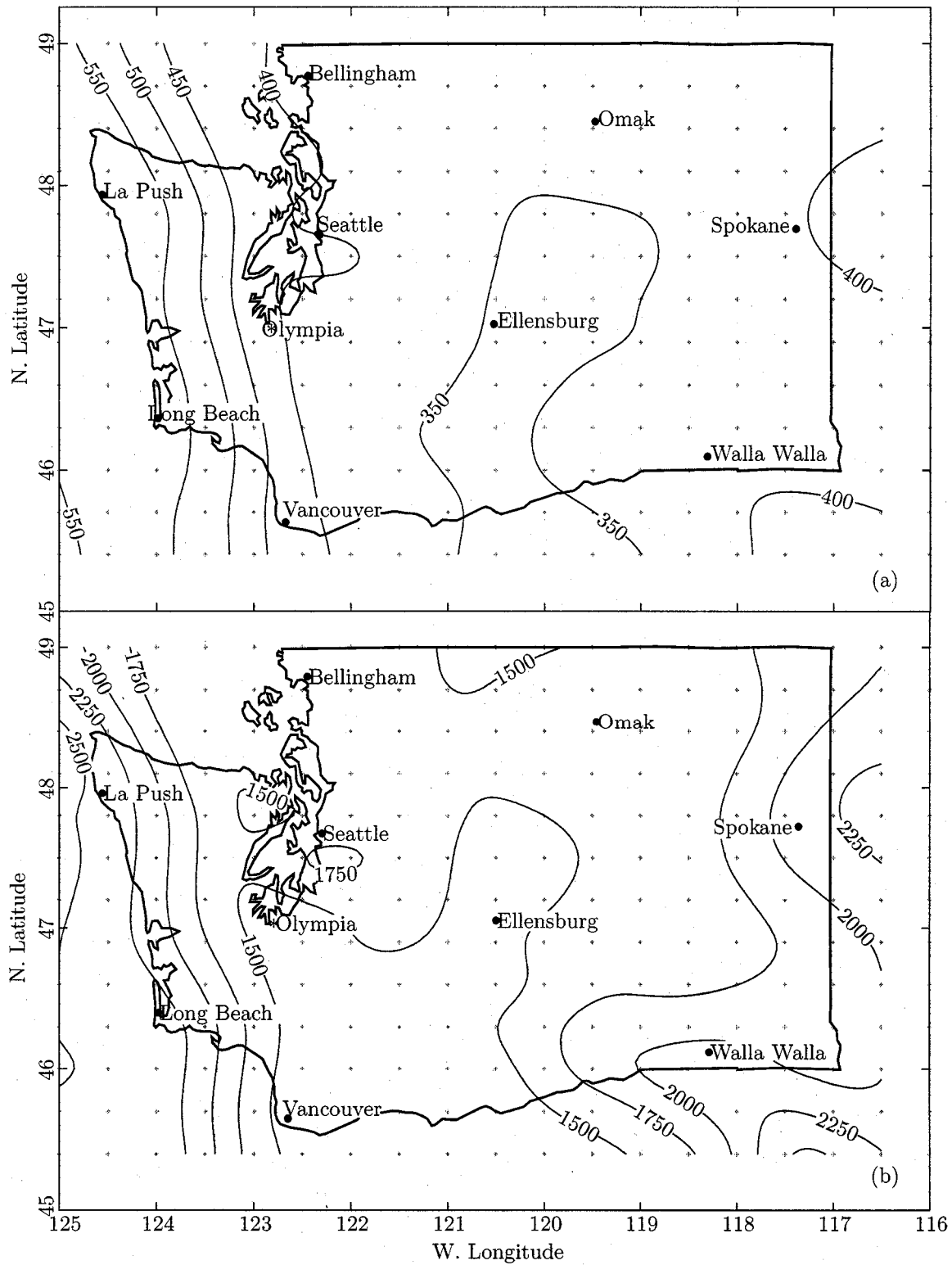


Figure 4.22: Equivalent liquefaction return period of (a) 475-yr and (b) 2475-yr (N_{req}) from conventional analyses at 6-m depth in reference profile for Washington State.

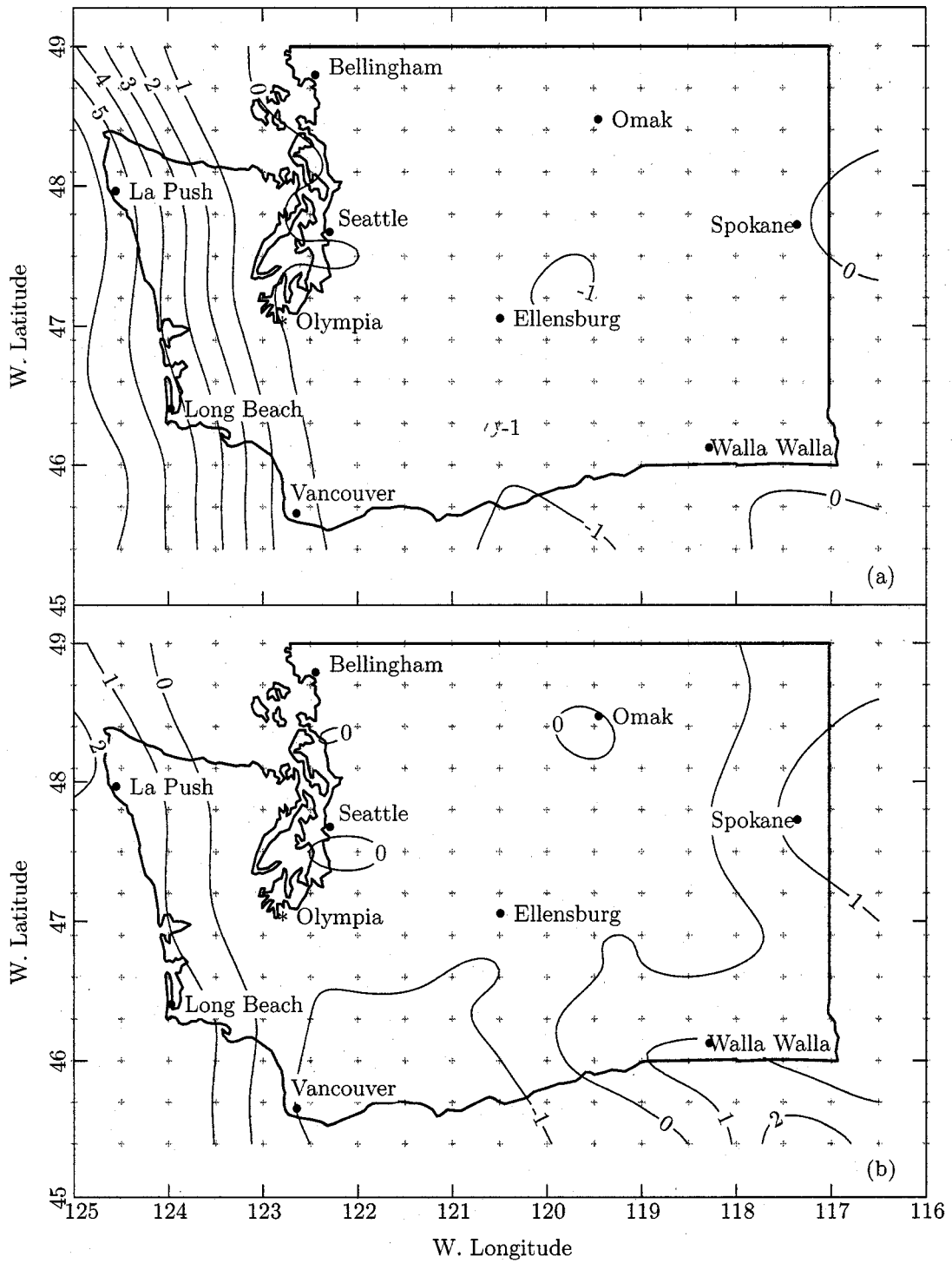


Figure 4.23: Difference between (a) 475-yr and (b) 2475-yr N_{req} from conventional analyses and 400-yr and 1700-yr N_{req} from performance-based analyses at 6-m depth in reference profile for Washington State.

at these predetermined return periods. The maps show that N_{req}^{det} and N_{req}^{pb} are equal in Seattle, since that is where the comparison is based, but along the west coast N_{req}^{det} is as much as 6 bpf greater than N_{req}^{pb} . Using Equation (4.8), an equivalent factor of safety can be computed from this blowcount difference, (Figure 4.24) indicating the degree of conservatism imposed by conventional analyses relative to performance-based analyses.

It is important to note that these illustrations are not meant to endorse any particular standard for applying the performance-based results in geotechnical engineering practice. They are meant only to show the inconsistency of the results from conventional liquefaction assessments and to show the benefits of the performance-based approach. As noted earlier in this chapter, determination of a performance-based liquefaction criterion requires broad discussion within the geotechnical community.

4.8 Summary of the performance-based CSR approach

This chapter has described the implementation of the cyclic stress ratio method for assessing liquefaction potential into PEER's performance-based framework. The computational effort required for performance-based analysis is considerably greater than for conventional analysis, but the level of complexity is not significantly greater. In fact, the performance-based method involves many iterations of conventional analyses and weighting the results according to the likelihood of their input parameters. This additional effort yields several significant rewards.

Results from conventional analyses are inconsistent across different seismic environments because they are based on only a single level of loading without consideration for the overall shape and position of the *IM* hazard curve. Because performance-based analyses incorporate the entire *IM* hazard curve at each site of interest, estimates of liquefaction hazard at different sites are more comparable. Also, by using the entire hazard curve, the performance-based method avoids the common question from the conventional method: should the mean or modal magnitude be used?

Deaggregation of the performance-based result allows a level of understanding about the liquefaction hazard at a particular site that is not possible with the conventional method. Knowing the contribution to the overall hazard from the various combinations of a_{max}

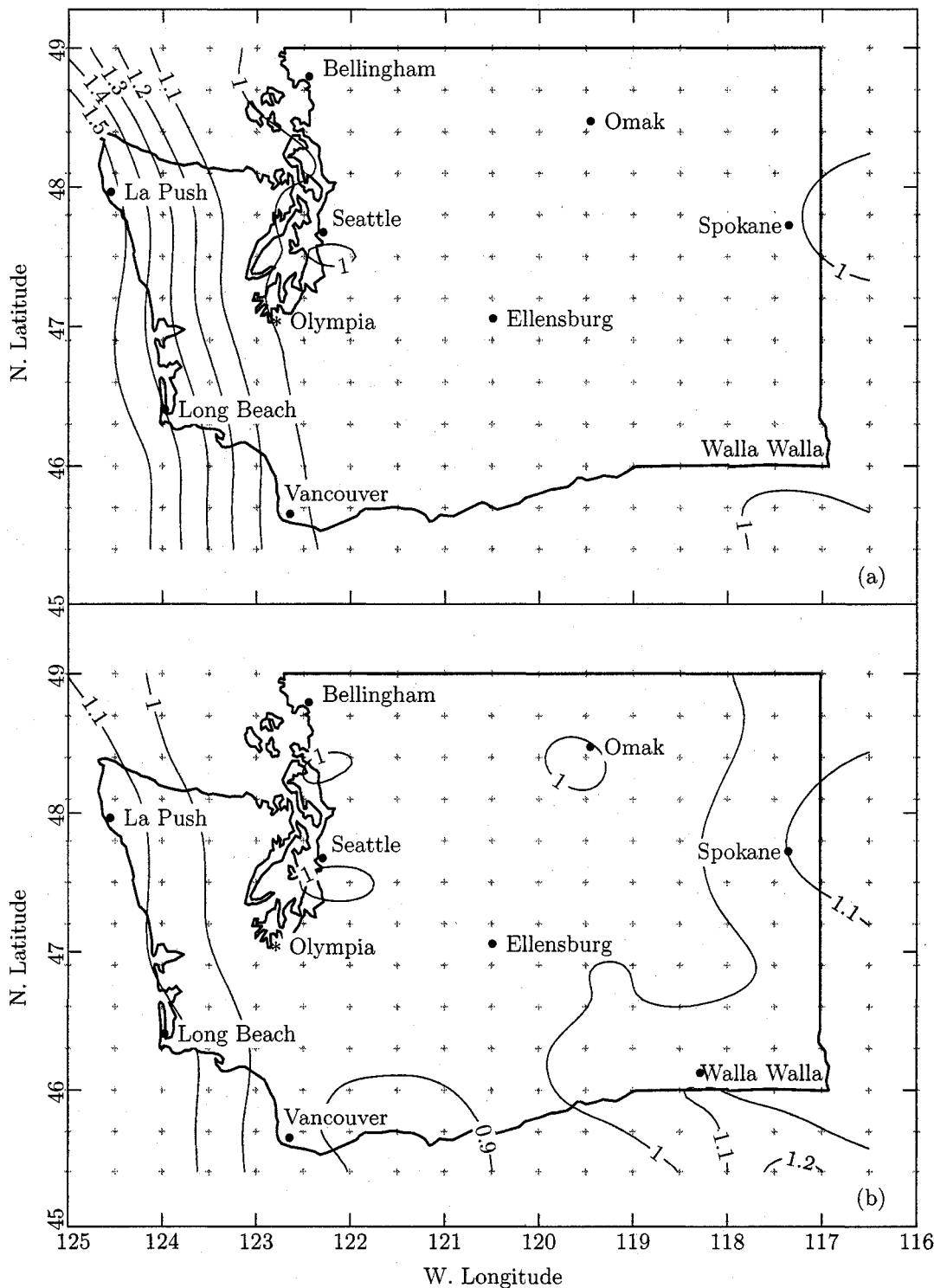


Figure 4.24: Factors of safety implied by N_{req} difference in Figure 4.23 at (a) 475-yr and (b) 2475-yr return periods.

and M_w provides valuable insight about the sensitivity of design assumptions relating to liquefaction.

In conventional analyses, the exceedance rate of the result is implied only indirectly from the exceedance rate of the loading parameter. A conventional analysis using the 475-yr a_{max} is often assumed to produce an estimate of the 475-yr liquefaction potential but, as this chapter has repeatedly shown, this is not necessarily true. Performance-based liquefaction analyses explicitly determine the exceedance rate of liquefaction and, thus, provide one of the key pieces of information for estimating damage hazard and risk from other performance-based analyses.

In conclusion, the performance-based approach to liquefaction assessment provides several important advantages over the conventional approach and merits further study. To that end, the next three chapters consider performance-based liquefaction assessment using the ground motion intensity measure, CAV_5 , which was identified in Chapter 3 as having several potential advantages over CSR .

Chapter 5

CAV₅ REDUCTION COEFFICIENT

In the great majority of cases in which liquefaction is a concern, the ground motion due to an earthquake is measured or estimated at the ground surface but the zone of the soil profile most susceptible to liquefaction is at some depth below the surface. The soil's variable nature and compliant behavior can cause a wide range of ground motions throughout the soil profile even for a single earthquake. Predicting this ground motion from earthquakes having different magnitudes with different rupture mechanisms in different seismic source zones is a complex task.

Ground response analyses are the usual means for predicting ground motions. Kramer [73] notes that an ideal analysis would model the rupture mechanism at the earthquake source, the propagation of energy through the earth to the bedrock surface below the site of interest, and then up through the soil profile to the ground surface. As with most processes in the real world, our analytical capabilities fall far short of the ideal: the mechanism of fault rupture is poorly understood and the nature of the materials between the rupture source and the site of interest is, in a practical sense, impossible to measure.

Ground response analyses normally begin with an assumed ground motion at some point in the soil profile, usually the surface of either the ground or the bedrock, then estimate the propagation of ground motions throughout the profile from linear or nonlinear approximations of soil behavior. In almost all cases, the soil profile and ground motions are assumed to be uniform in lateral extent, which allows the problem to be treated as one-dimensional with vertically-propagating shear waves. SHAKE, SHAKE91, [58] and ProSHAKE [33] are examples of computer programs that implement 1-D linear-equivalent ground response analyses; DESRA [80], TESS [93], and WAVE with the UWsand constitutive model [75] are examples of nonlinear implementation.

Golesorkhi [39] studied the relative merits of linear and nonlinear methods of ground response analysis and found that comparable results were obtained in cases that did not involve large strains or significant soil softening due to pore pressure rise. This conclusion has important practical consequences because the data requirements for nonlinear methods are difficult to satisfy except for projects with large budgets and lead times.

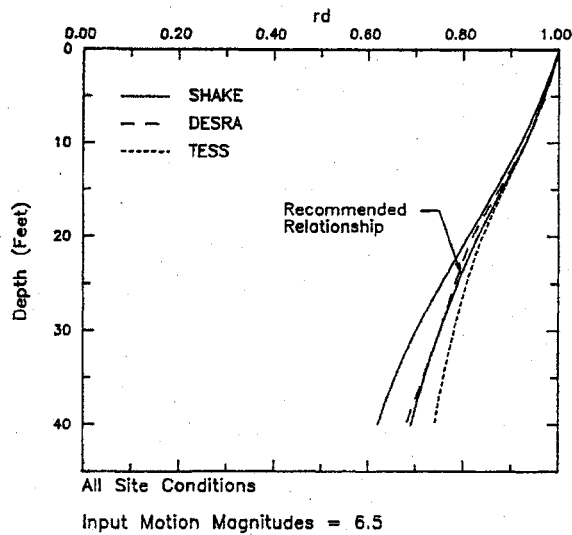


Figure 5.1: Comparison of average r_d from linear and nonlinear methods. After Golesorkhi [39].

results of ground response analyses using a wide range of soil profiles and earthquake motions, thus, much of the richness and detail from an individual ground response analysis is lost by their use.

Nonetheless, the most common approaches for predicting liquefaction potential (using cyclic stress and Arias intensity, for example) include a simplified method involving some form of depth reduction coefficient, and one for use with CAV_5 is desirable to enable comparison with these other methods.

5.1 Previous work

The approaches for developing a predictive model for depth reduction coefficients range between two extremes. The purely statistical approach focuses on finding a model that

Many engineering practitioners consider even linear equivalent analyses as too burdensome. This belief has been encouraged by the widespread use of depth reduction coefficients in simplified methods and the observation that these simplified methods produce satisfactory results in most cases.

Depth reduction coefficients are defined as the ratio of the ground motion intensity measure at the some depth in the soil profile to the intensity measure at the ground surface (e.g. $r_d = PGA(z)/PGA(z = 0)$ or, for this study $r_c = CAV_5(z)/CAV_5(z = 0)$). They are typically averaged from the

minimizes the uncertainty (dispersion) in model predictions for a particular dataset. Parameters and combinations of parameters are included or rejected without considering the physical basis of the relationship. In contrast, a theoretical model considers only the physical aspects of the relationship. There is little regard for the relative effect of an individual parameter or for the practicalities of data gathering.

In practice, both extremes are usually unsatisfactory. The purely statistical approach is relevant only to the dataset used in its derivation, and extending the model beyond the range of the dataset cannot be done with confidence. On the other hand, the theoretical approach is usually impractical because our understanding of physical processes is incomplete or incorrect. Further, it is often difficult to obtain data for all of the properties required to describe the physical problem and satisfy a theoretical model.

The most effective approaches use theory to identify the basic form of the model and statistical analysis to refine the details and determine parameter coefficients. Previous investigators have generally used this hybrid approach for developing the reduction coefficients reviewed below.

5.1.1 *Cyclic stress and strain approaches*

Although the key predictive parameter, a_{max} , in the cyclic stress and strain approaches is different than CAV_5 , both are derived from acceleration time histories. It is relevant, therefore, to review the development of cyclic stress and strain depth reduction coefficients before addressing one for CAV_5 . The depth reduction coefficients for cyclic stress and cyclic strain approaches are treated together here because in Chapter 3, the demand in the cyclic strain approach was shown to differ from the cyclic stress demand only by the inclusion of the shear modulus. The depth reduction coefficient in both approaches is the same.

Seed & Idriss (1971)

Chapter 3 described Seed & Idriss's development of the simplified cyclic stress method for predicting liquefaction potential and their definition of r_d :

$$r_d = \frac{(\tau_{max})_d}{(\tau_{max})_r}$$

in which τ_{max} is the maximum cyclic shear stress at the point of interest within the soil profile, and the subscripts d and r denote conditions for deformable (actual) and rigid soil profiles, respectively, above the point of interest. Because $(\tau_{max})_r$ is defined as the product of the total vertical stress at the point of interest and the peak acceleration (a_{max}) in g's, r_d is often treated as the ratio of the peak acceleration at the depth of interest to the peak acceleration at the ground surface, a_{max} . This is possible be-

cause the total vertical stress at the point of interest is the same for both $(\tau_{max})_d$ and $(\tau_{max})_r$. Figure 5.2 illustrates the range and mean values of r_d for depths less than 100 ft.

As discussed below, many studies have proposed other forms for r_d , but the plot shown in Figure 5.2 persists as the most commonly used by the geotechnical profession. Liao & Whitman [82] proposed a bilinear closed-form solution for Seed & Idriss's r_d plot:

$$r_d = 1.0 - 0.00765z \text{ for } z \leq 9.15 \text{ m}$$

$$r_d = 1.174 - 0.0267z \text{ for } z = 9.15\text{--}23 \text{ m}$$

Ishihara (1977)

Ishihara's work on the liquefaction potential of sandy soils [60] included a derivation of r_d from a solution of the wave equation for a uniform soil subjected to harmonic motion with an angular frequency, ω , and a horizontal displacement, u_o . The horizontal displacement at depth, z , below the ground surface is

$$u = u_o \cos\left(\frac{\omega z}{V_s}\right) e^{i\omega t}$$

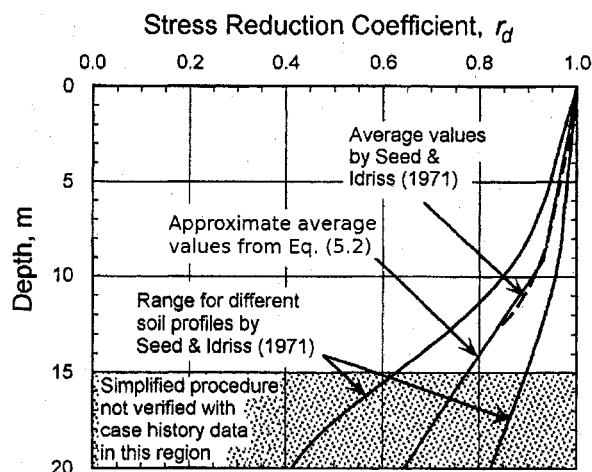


Figure 5.2: Depth reduction factor, r_d , vs depth. After Youd et al. [128].

in which V_s is the shear wave velocity of the soil and t is the time. The shear stress is then

$$\tau = G \frac{\partial u}{\partial z} = -\frac{u_o G \omega}{V_s} \sin\left(\frac{\omega z}{V_s}\right) e^{i\omega t}$$

in which G is the shear modulus of the soil. The ground surface ($z = 0$) acceleration, which Ishihara designated as a_{max} , is

$$a_{max} = \frac{\partial^2 u}{\partial t^2} = -\omega^2 u_o e^{i\omega t}$$

For a rigid soil column, the shear stress at depth z is

$$\tau_r = \rho z a_{max} = -\omega^2 u_o \rho z e^{i\omega t}$$

in which ρ is the mass density of the soil deposit. Finally, Ishihara described the depth reduction factor as the ratio of the shear stress at depth z in a deformable soil to the shear stress at the same depth in a rigid soil:

$$r_d = \frac{\tau}{\tau_r} = \frac{V_s}{\omega z} \sin\left(\frac{\omega z}{V_s}\right)$$

This is the earliest known case of including the shear wave velocity and the frequency content of the input motion in an expression for the depth reduction coefficient. Figure 5.3 shows r_d vs depth for different soil thicknesses. The input motion frequency, ω_o , equals the site frequency corresponding to the first mode of vibration.

$$\omega_o = \frac{\pi V_s}{2H}$$

Iwasaki et al. (1978)

Iwasaki studied the depth reduction factor for cyclic shear stresses by analyzing two alluvial deposits subjected to six earthquake motions [62]. The simple linear form of his correlation between r_d and depth,

$$r_d = 1 - 0.015z$$

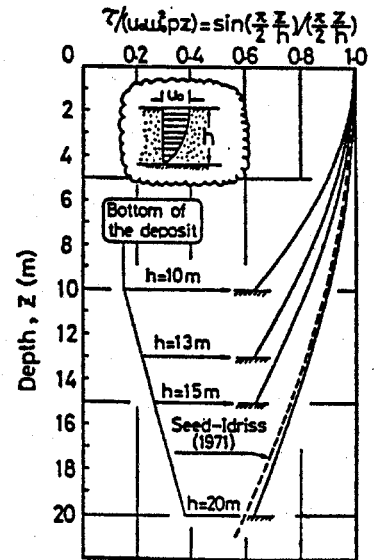


Figure 5.3: Depth reduction factor, r_d , vs depth. After Ishihara [60].

believes the large variation in his results and the parameters that he considered to affect r_d . Figure 5.4 illustrates the soil profiles and the resulting r_d , and Figure 5.5 compares his mean relationship for r_d with the range suggested by Seed and Idriss. A comparison of the two figures shows that Iwasaki's results were more variable than those from Seed and Idriss, and Iwasaki suggested that soil deposits with larger natural periods and earthquake motions with shorter predominant periods resulted in smaller values of r_d . He also suggested a possible dependence of r_d on earthquake magnitude and distance since those parameters influence the frequency content of the input motion.

Imai et al. (1981)

Imai et al. [59] began their investigations of r_d with Ishihara's model [60] and modified the amplitude term by replacing z/V_s with the travel time, T , of the shear waves from depth z to the ground surface:

$$r_d = \frac{1}{\omega T} \sin \left(\frac{\omega z}{V_s} \right)$$

Figure 5.6 shows the results of their 143 ground response analyses for different site conditions and five earthquake motions.

Imai et al. noted that different earthquake motions often produce different r_d curves and suggested using time-dependent r_d curves on this basis. The complexity and level of effort to achieve this, however, makes the simplified method not so simple, and Imai's approach has not been widely used.

Golesorkhi (1989)

The 1989 work by Golesorkhi [39] was a significant advance in the development of depth reduction factors. He considered the effect on r_d of earthquake magnitude, frequency content of the input motion and soil stiffness using linear equivalent (SHAKE), lumped-mass nonlinear (DESRA), and finite difference nonlinear (TESS) ground response analyses. As noted earlier in this chapter, Golesorkhi found that the differences between these methods was relatively small and none of the methods produced results that were consistently higher or lower than the others.

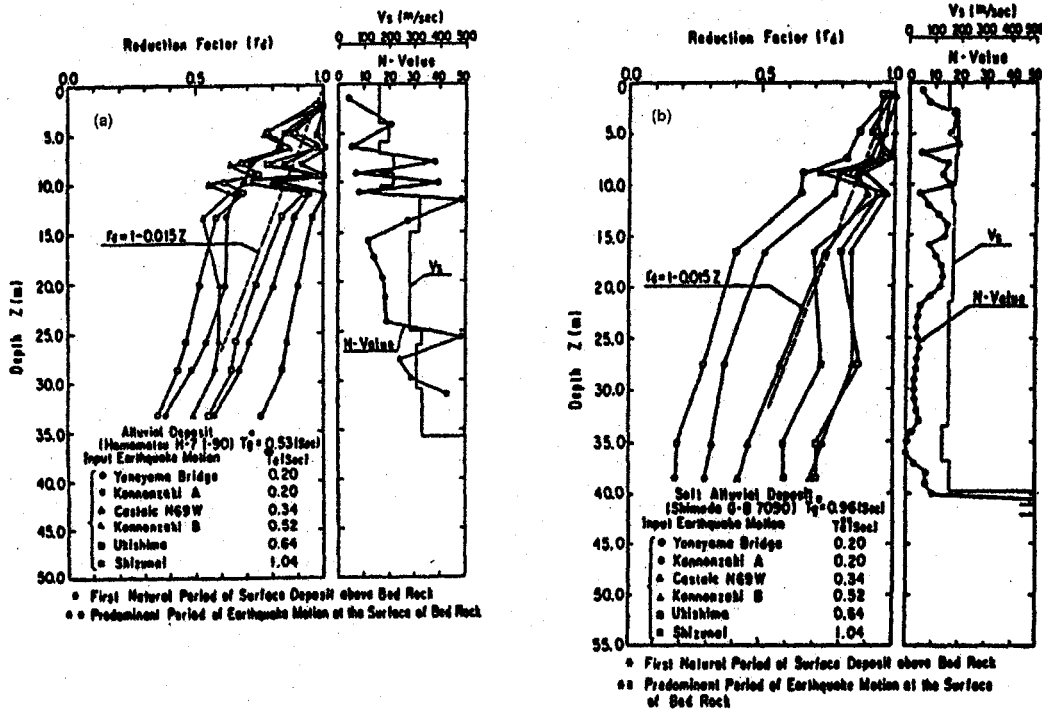


Figure 5.4: Depth reduction coefficients based on ground response analyses and soil profiles vs depth. (a) Earthquake response analysis of alluvial deposit at Hamamatsu City. (b) Earthquake response analysis of alluvial deposit at Shimoda City. After Iwasaki et al. [62] and Iwasaki [61].

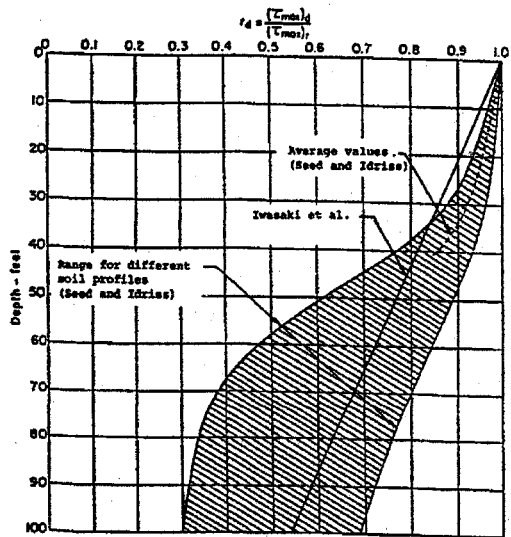


Figure 5.5: Comparison of Iwasaki's average r_d and the range of results from Seed and Idriss [103]. After Iwasaki [62].

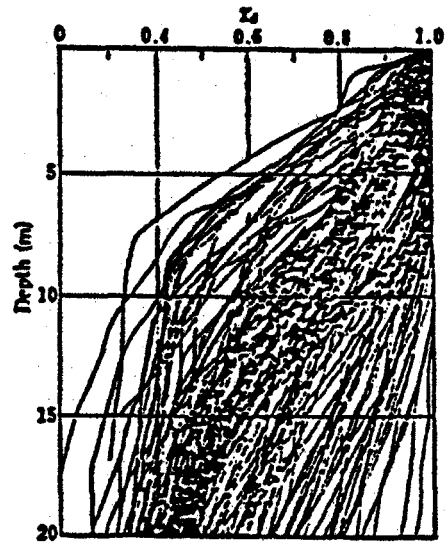


Figure 5.6: Depth reduction factor, r_d , vs depth after Imai et al. [59].

Golesorkhi included 35 ground motions with a_{max} from 0.04g to 0.81g and magnitudes greater than 5.0 for three idealized soil profiles: 100-ft deep uniform sand with 75% relative density, 100-ft deep uniform sand with 40% relative density, and 350-ft deep uniform sand with 75% relative density. He assumed that these uniform soils were directly over very hard bedrock ($V_s \approx 2500$ m/s) with no transitional layers, creating a very high impedance contrast. Figures 5.7 and 5.8 present Golesorkhi's r_d results for a range of ground motions and magnitudes using linear equivalent analyses.

Golesorkhi's results are limited by the use of only linear regression methods in estimating their variability. Also, he did not develop a closed-form relationship for r_d . Nonetheless, the systematic study of the magnitude and spectral content of the input motion and the stiffness and thickness of the soil profile with linear and nonlinear methods was a significant achievement.

Idriss (1999)

Idriss [54] extended Golesorkhi's work on r_d , primarily by performing additional SHAKE analyses and developing a closed-form correlation between depth, magnitude, and r_d :

$$\begin{aligned}\ln(r_d) &= \alpha(z) + \beta(z) M_w \\ \alpha(z) &= -1.012 - 1.126 \sin\left(\frac{z}{38.5} + 5.133\right) \\ \beta(z) &= 0.106 + 0.118 \sin\left(\frac{z}{37.0} + 5.142\right)\end{aligned}$$

in which z is the depth in feet and M_w is the moment magnitude. Figure 5.9 illustrates this relationship for different magnitudes. Idriss noted that these equations are appropriate for $z \leq 100$ ft, and that for $z > 100$ ft, the following equation is more appropriate:

$$r_d = 0.12e^{0.22M_w}$$

He also noted that the uncertainty in r_d increases with depth and recommended that these equations be used only for depths less than about 65 ft; greater depths merit ground response analyses.

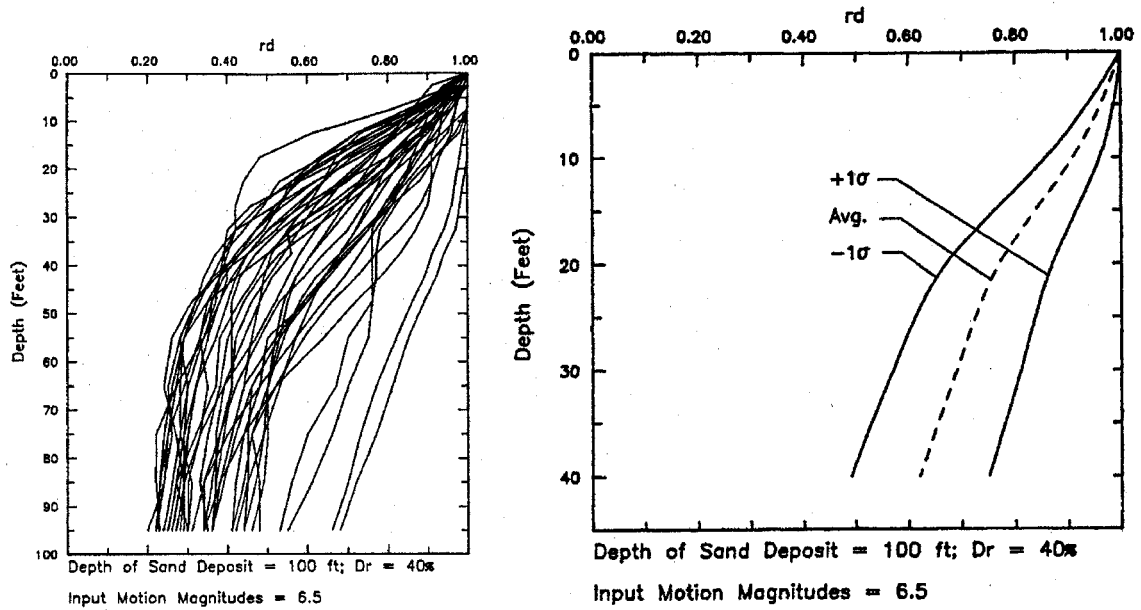


Figure 5.7: Depth reduction coefficients based on linear equivalent (SHAKE) ground response analyses. The left plot shows the actual r_d profiles; the right plot shows the mean of the results and $\pm 1\sigma$. Note the different depth scales. After Golesorkhi [39].

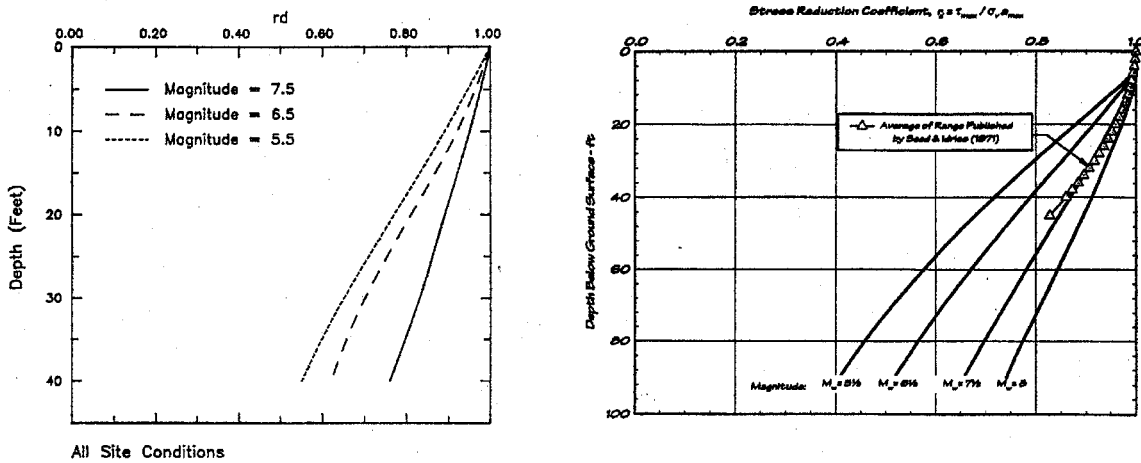


Figure 5.8: The effect of magnitude on r_d . After Golesorkhi [39].

Figure 5.9: Depth reduction factor, r_d , vs depth for Magnitudes 5.5 to 8.0. After Idriss [54].

Çetin (2000)

The goal of Çetin's r_d development [21, 23, 24] was to advance the strong points of Golesorkhi's work by using more realistic soil profiles. He assembled 50 profiles based on test

hole logs; 42 near-, medium-, and far-field ground motion records representing strike-slip, normal, and reverse faulting with a wide range of a_{max} ; a more realistic transition from soil to bedrock; nonlinear regression for determining the variability of the results; and he developed a closed-form solution for r_d dependent upon shear wave velocity, magnitude, a_{max} , and depth. Çetin also considered closest distance to fault rupture, predominant period of the input motion, initial site period, final site period, and soil profile thickness but found that several of these were highly correlated with others and could be omitted. For the sake of simplicity, he excluded parameters with low statistical significance.

Çetin's equation for r_d [23, 24] is

$$r_d = \frac{\left[1 + \frac{-23.013 - 2.949a_{max} + 0.999M_w + 0.0525\bar{V}_{s,12}}{16.258 + 0.201 \exp[0.341(-z + 0.0785\bar{V}_{s,12} + 7.586)]} \right]}{\left[1 + \frac{-23.013 - 2.949a_{max} + 0.999M_w + 0.0525\bar{V}_{s,12}}{16.258 + 0.201 \exp[0.341(0.0785\bar{V}_{s,12} + 7.586)]} \right]} \pm \hat{\sigma}_{r_d} \quad (5.1)$$

in which a_{max} is expressed as a fraction of gravity, $\bar{V}_{s,12}$ is the ratio of 12 m of soil profile thickness to the shear wave travel time through the upper 12 m of the profile (m/s), and z is the depth in meters, which is not to exceed 20 m. For cases in which $z > 20$ m, $z = 20$ m is used in Equation (5.1). The final term is standard error of the relationship for the chosen dataset, defined as

$$\hat{\sigma}_{r_d} = 0.0198 z^{0.85} \quad (5.2)$$

in which $z \leq 12$ m. For cases in which $z > 12$ m, $z = 12$ m is used in Equation (5.2). Note that these forms of r_d and $\hat{\sigma}_{r_d}$ are from Çetin et al. [24] and differ slightly from those published in Çetin's dissertation [21]. Figure 5.10 shows the mean and mean \pm one standard deviation of this model overlying the results from the SHAKE analyses. This relationship appears to contain the key parameters for describing the dynamic characteristics of the soil profile (z , $\bar{V}_{s,12}$) and the input motion (a_{max} , M_w); with the larger dataset Çetin's r_d relationship should yield satisfactory results over a wider range of conditions than the earlier work.

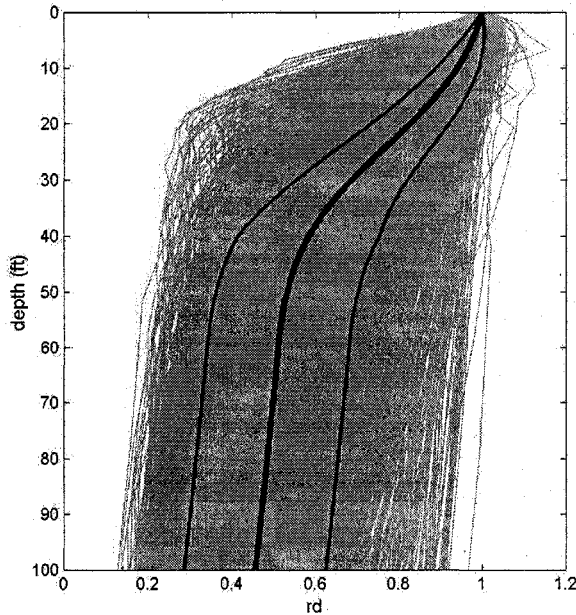


Figure 5.10: Depth reduction factor, r_d , vs depth. After Çetin et al. [24].

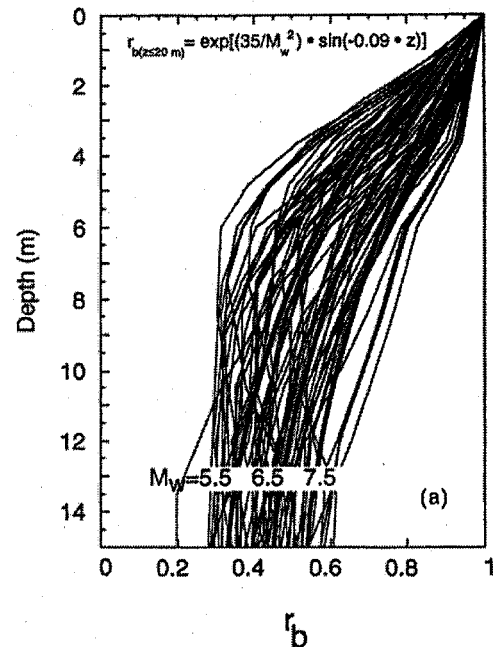


Figure 5.11: Arias intensity depth reduction factor, r_b , vs depth. After Kayen and Mitchell [67].

Idriss and Boulanger [57] suggest that Çetin's model for r_d is overly complex and that including a_{max} and $\bar{V}_{s,12}$ does little to reduce the model uncertainty. There have been other unpublished criticisms that, while the variables included in the model have a sound theoretical basis, the actual form of the model is generic and was chosen only to fit the data. Neither of these comments is damning and the fact that one argues for less complexity while the other argues for more suggests that Çetin may have found a reasonable middle ground given the current state of knowledge.

5.1.2 Energy approach

Chapter 3 noted that the energy approach can be thought of as a hybrid of the cyclic strain and cyclic stress approaches, and that it also can be implemented in a simplified form. The following paragraphs summarize the key developments of depth reduction coefficients for the energy approach.

Kayen (1993)

Kayen [65] and Kayen & Mitchell [66, 67] describe the development of a depth reduction factor for Arias intensity, r_b , using an approach similar to those used in the development of r_d for cyclic shear stress. Kayen studied eight synthetic soil profiles 30 to 90 m deep comprising uniform sand with relative densities of 45 and 75 percent. To these he applied eight acceleration time histories from strike-slip, normal, and shallow reverse earthquakes with source distances ranging from 7 to 122 km and magnitudes ranging from 5.2 to 7.6. Using SHAKE, he computed acceleration time histories, Arias intensities, and r_b at a series of depths to about 30 m. The results, shown in Figure 5.11, appear similar in shape and magnitude to those from the *CSR* method. In the earlier work [65, 66] Kayen did not develop a closed-form relationship for r_b but in 1998, he published the following [67]:

$$r_b = \frac{I_a(z)}{I_a(z=0)} = \exp\left(\frac{35}{M_w^2} \sin(-0.09z)\right)$$

Kayen's model does not seem to fit the SHAKE results in Figure 5.11 particularly well, especially at depths of 3 to 12 m. This, combined with the limited number of cases included in the analysis, suggest that the depth reduction coefficient for Arias intensity may not represent a wide range of ground conditions.

Kayen addressed an important issue regarding the shape of the shear wave velocity profile. He noted that cases in which there is a stiff layer overlying soft layers—which he termed an impedance inversion—can result in amplification of ground motion at the base of the stiff layer. This is different from the general behavior shown in Figure 5.11, in which the ground motion monotonically decreases from the ground surface. Kayen suggested that the use of a depth reduction coefficient, both for Arias intensity and cyclic stress ratio, is not appropriate where there are impedance inversions and that ground response analyses should be used for those cases.

Others

Several of the energy methods described in Chapter 3 forego the use of a depth reduction factor. These usually rely on some measure of stress—vertical or mean, total or effective—

to act as a replacement for the depth reduction coefficient. Examples include Davis and Berrill [30], Berrill and Davis [11], Trifunac [121], and Running [98]. The simplicity of relying entirely on shear stress is attractive, and is comparable to the early formulations of r_d for the cyclic stress method that were dependent only upon depth. As noted by Çetin and Seed [23] and Idriss & Boulanger [57], however, there are other parameters of the soil profile and ground motion that can be reasonably expected to influence ground response.

5.2 Theoretical considerations for a CAV_5 depth reduction coefficient

For the initial form of the r_c relationship, consider the one-dimensional equation of motion due to shear waves:

$$\frac{\partial^2 u}{\partial t^2} = V_s^2 \frac{\partial^2 u}{\partial z^2}$$

in which u is horizontal displacement, t is time, V_s is the shear wave velocity of the soil, and z is the depth below the ground surface. In a simple profile of isotropic, linear-elastic soil overlying rigid bedrock, horizontal harmonic motion in the bedrock produces vertically propagating shear waves through the soil. The resulting horizontal displacement in the soil is

$$u(z, t) = 2A \cos(kz) e^{i\omega t}$$

in which A and ω are the amplitude and circular frequency of the bedrock motion, respectively, and k is the wave number ($k = \omega/V_s$). Differentiating this displacement twice with respect to time yields the horizontal acceleration within the soil profile,

$$a(z, t) = -2A\omega^2 \cos(kz) e^{i\omega t}$$

The cumulative absolute velocity, CAV (not CAV_5), is

$$\begin{aligned} CAV(z) &= \int_0^{T_d} |a(z, t)| dt \\ &= |2A\omega^2 \cos(kz)| \int_0^{T_d} |e^{i\omega t}| dt \end{aligned} \quad (5.3)$$

in which T_d is the total duration of the harmonic motion. By definition, $|e^{i\omega t}| = 1$ for an integral number of cycles, so,

$$CAV(z) = |2A\omega^2 \cos(kz)| T_d$$

At the ground surface ($z = 0$),

$$CAV(0) = |2A\omega^2|T_d$$

and the ratio of these two values of CAV is

$$r_c = \frac{CAV(z)}{CAV(z=0)} = |\cos(kz)| = \left| \cos\left(\frac{\omega z}{V_s}\right) \right| \quad (5.4)$$

This simple result is for an unrealistically simple soil profile subjected to steady-state motion with only a single frequency and amplitude so cannot be expected to capture the complexities of a real transient earthquake motion applied to a multi-layered soil profile. Nonetheless, it suggests that r_c should contain a harmonic term that is dependent upon the inverse of the soil's shear wave velocity.

There are theoretical and empirical arguments for including properties other than shear wave velocity. As noted earlier, the solution above is for a linear-elastic soil. Real soil is nonlinear, especially at larger strains, which suggests that the ground response should depend on the intensity of the ground motion. Idriss [53] illustrated this with case histories from the 1985 Mexico City and 1989 Loma Prieta earthquakes.

Kramer [73] noted that the amplitude of the ground motion in a layered soil profile depends upon the impedance ratio at soil layer boundaries. This is consistent with Kayen's work described earlier. At the boundary between soil layers m and $m + 1$, the impedance ratio is

$$\alpha_m = \frac{\rho_m V_{s_m}}{\rho_{m+1} V_{s_{m+1}}}$$

in which ρ_m is the total stress density of the soil in layer m and V_{s_m} is the shear wave velocity of the soil in layer m . In natural soil deposits, the density and shear wave velocity generally increase with depth resulting in impedance ratios less than one. In developed areas, however, soft soils are often capped with a layer of dense, stiff, structural fill, which results in an impedance ratio greater than one. As noted by Kayen, this "reverse" behavior can have a significant effect on the ground response and potentially on r_c .

As a simplified proxy for impedance ratio at each soil boundary, this work uses the slope of the shear wave velocity profile averaged over the upper 12 m of soil profile, dV_s ; Figure 5.12 illustrates this calculation. Positive values of dV_s correspond to positive impedance

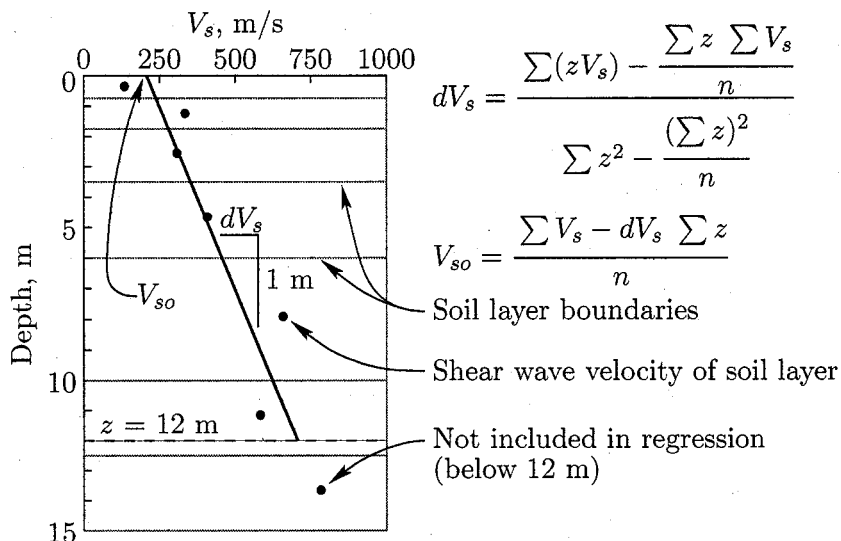


Figure 5.12: Illustration of the shear wave velocity parameters, V_{s0} and dV_s , for shear wave velocity measurements in the upper 12 m of a soil deposit.

ratios and indicate generally increasing soil stiffness and shear wave velocity with depth. Negative values correspond to negative impedance ratios and indicate the impedance inversions that Kayen discussed. The intercept of this linear regression at the ground surface, V_{s0} , is used for the shear wave velocity term in the harmonic term described earlier. The limit of 12 m for calculating V_{s0} and dV_s is based on analyses by Çetin [21, 24] that showed there was a relatively small variation in ground response below this depth.

It is important to note that V_{s0} and dV_s as defined here are used as a simple representation of the actual shear wave velocity profile. Attempts to determine V_{s0} by measuring the shear wave velocity at shallow depths will not generally produce a comparable result. For cohesionless soils like those generally considered in a liquefaction analysis, the shear wave velocity at any point in the soil is partially dependent upon the confining pressure at that point. Because of this, the shear wave velocity at the ground surface generally will approach zero. The values of V_{s0} used in this study are considerably greater than zero and, thus, can be considered to include information about the average shear wave velocity of the soil profile and the slope of the shear wave velocity profile. This matter will be discussed further with the results of the r_c regression analysis.

In summary, the key parameters chosen as predictors of r_c are depth (z), the intercept of the shear wave velocity profile at the ground surface (V_{s0}), the average slope of the shear wave velocity profile over the upper 12 m (dV_s), and the ground motion intensity measure, CAV_5 . The next section establishes the general form of the r_c predictive model in the regression analyses.

5.3 Form of the predictive model

In the preceding section, a theoretical form for r_c was derived from the equation of motion using an idealized soil profile and a ground motion with single frequency and amplitude. This section considers how r_c is affected by soil profiles and ground motions of varying complexity.

The theoretical model in Equation (5.4) described r_c as the absolute value of a harmonic wave, which results in values from 0 to 1 with an average of $\pi/8$. Actual ground motions are much more complex. However, using Fourier analyses, ground motions can be decomposed into a suite of harmonic waves across a spectrum of frequencies, each component with its own amplitude.

In addition to the motion input at the bedrock surface, the ground surface motion is also influenced by the composition of the soil profile. Unlike the theoretical model, which consisted of a uniform elastic material with a constant shear wave velocity, real soil profiles are composed of inelastic layers with different V_s .

Thus, r_c is likely to be influenced by the frequency content and amplitude of the ground motion and by the shape of the shear wave velocity profile at the site of interest. Figure 5.13 illustrates the resulting r_c profiles from a series of simple soil profiles subjected to the East-West component of the Gilroy 1 ground motion from the Loma Prieta earthquake. This motion was scaled to produce the values of CAV_5 shown in the top right panel and applied at the bedrock level in SHAKE91 analyses. The r_c profiles start at 1.0 at the ground surface, by definition, and decay to a depth of about 5 m, below which they remain relatively constant. There is some oscillation about this overall pattern, remnant of the harmonic term, but it decreases with depth, especially for the stiffer (higher V_s) soils and more uniform (smaller dV_s) profiles.

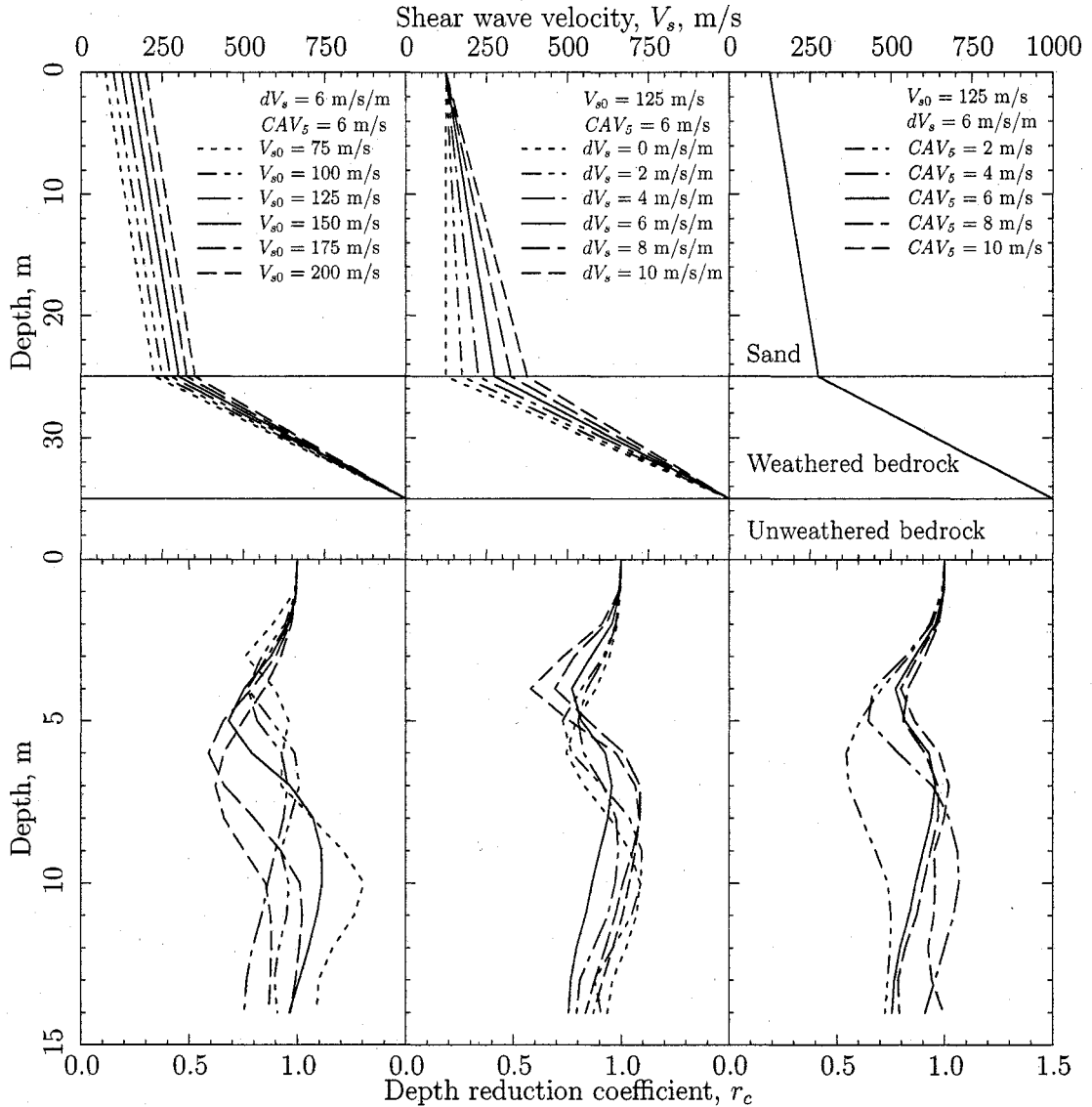


Figure 5.13: Shear wave velocity (top row) and CAV_5 depth reduction coefficient (bottom row) profiles from SHAKE91 analyses using simple soil profiles.

To model the anticipated behavior of r_c described at the start of this section, a general form with three terms is studied. An offset term, $\alpha(z) = \theta_1 + (1 + \theta_2 z)^{-z}$, is used to describe the overall shape of the r_c profile ($r_c = 1$ at $z = 0$, decays until $z \approx 5$ m, relatively constant

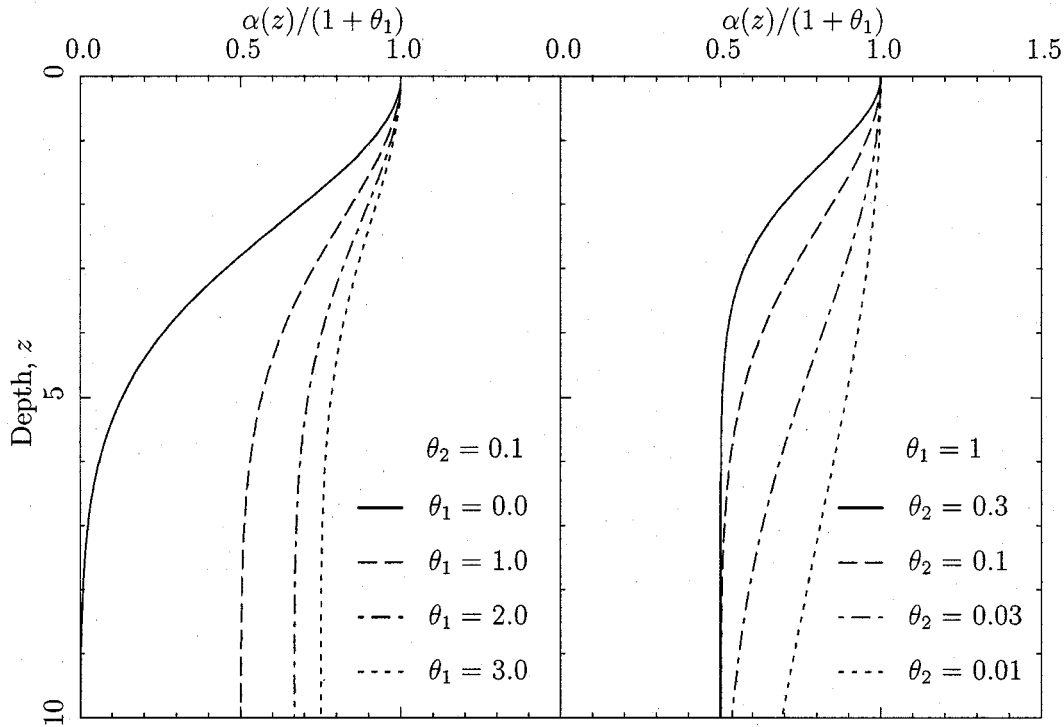


Figure 5.14: Illustration of the general form of the normalized r_c offset term.

below); its behavior is illustrated in Figure 5.14. The lower limit and inflection points of the offset term are controlled by θ_1 and θ_2 , respectively, and the upper limit of 1.0 at $z = 0$ is maintained by the normalizing factor, $1 + \theta_1$.

A harmonic term, $\beta(z) = \cos(\theta_3 z)$, modified by a decaying amplitude term, $\gamma(z) = (1 + \theta_4 z)^{-z}$ was added to the offset term. The functional form of the offset term was also adopted for the decay term. These three terms were normalized to ensure $r_c = 1$ at the ground surface:

$$\begin{aligned}
 r_c &= \frac{\alpha(z) + \beta(z) \gamma(z)}{2 + \theta_1} \\
 &= \frac{\theta_1 + (1 + \theta_2 z)^{-z} + \cos(\theta_3 z) (1 + \theta_4 z)^{-z}}{2 + \theta_1}
 \end{aligned} \tag{5.5}$$

In this model, θ_1 through θ_4 can be functions of V_{s0} , dV_s , and CAV_5 as determined by regression analysis.

5.4 Dataset

A key part of using statistical regression to develop a model for r_c is assembling a representative set of data. The dataset must include a range of cases broad enough to encompass the conditions likely to be encountered by users of the model, yet not so broad as to include special cases that will distort the general result. This determination cannot be made with certainty until after the regression analysis because the regression itself provides the measure of what is a general result and what is a special case. Thus, preparing a dataset can be a lengthy and iterative task.

Fortunately, cases already have been assembled and screened for developing models of depth reduction coefficients for the cyclic stress method. One of the most extensive is from Çetin [21]: it includes 35 California sites where soil liquefaction has been observed and is supplemented by another 11 soil profiles that are depth-truncated versions of the original sites. In these truncated profiles, Çetin retained the upper portion of the profile while assuming shallower bedrock depths. Table 5.1 summarizes the key depth and shear wave velocity parameters for these sites; plots of the individual profiles are in Çetin's dissertation [21].

To calculate the ground response using SHAKE91, each soil layer in these profiles was assigned one of the 21 modulus reduction and damping curves shown in Table 5.2. Most of these result from Roblee and Chiou's recent interpretation [97] of Darendeli's work on dynamic soil behavior [29]. They are a significant improvement over the curves used by Çetin because they account for the dependence of a soil's nonlinear stress-strain properties on confining pressure.

Çetin studied the response of these soil profiles by exciting them with 36 earthquake records spanning a wide range of magnitudes, distances, and amplitudes (see Table 5.3). The record component with the largest peak horizontal ground acceleration was chosen for inclusion in the study. As can be seen by the eighth and tenth columns, Çetin scaled the peak ground accelerations to better cover the range of amplitudes. The values of CAV_5 in the ninth and eleventh columns are for the unscaled and scaled records, respectively.

Table 5.1: Soft soil sites used to develop r_c .

Profile	Depth to bedrock, m	V_{s0} m/s	dV_s m/s/m	$\bar{V}_{s,12}$ m/s
Balboa Boulevard	90	131	10.9	185
Farris Farm	180	127	13.5	195
Heber Road A1	275	132	14.2	200
Heber Road A2	270	130	15.2	205
Heber Road A3	275	136	17.0	225
Kornbloom Site	270	110	10.9	165
Malden Street	90	119	9.7	160
Marine Lab B1	180	157	2.1	170
Marine Lab B2	180	127	5.6	155
MBARI N° 3 EB-1	180	184	0.9	190
MBARI N° 3 EB-5	180	137	3.5	155
MBARI N° 3 UC-B10	180	127	8.0	170
McKim Ranch A	265	159	3.5	180
Miller Farm CMF-3	180	123	8.6	170
Miller Farm CMF-5	180	136	9.5	185
Miller Farm CMF-8	180	104	11.0	160
Miller Farm CMF-10	180	134	8.0	175
Miller Farm	180	138	8.8	180
Moss Landing UC-B1	180	125	6.7	160
Moss Landing UC-B2	180	157	4.0	180
Port of Oakland 7-2	135	125	9.2	175
Port of Oakland 7-3	170	156	-2.2	155
Port of Richmond POR-2	30	74	12.5	135
Port of Richmond POR-3	30	54	18.2	140
Port of Richmond POR-4	30	45	18.9	130
Radio Tower B1	270	121	9.3	170
Radio Tower B2	270	134	8.5	180
Richmond City Hall	35	46	17.7	130
River Park A & C	270	130	11.3	190
San Francisco-Oakland Bay Bridge 1	160	120	6.3	155
San Francisco-Oakland Bay Bridge 2	155	161	-1.0	170
Treasure Island	105	147	2.1	160
Wildlife Site	270	80	9.4	130
Woodward Marine UC-B4	180	119	11.4	175
Wynne Avenue	90	118	10.6	170
Truncated profiles				
Farris Farm	45	127	13.5	195
Heber Road A2	70	130	15.2	205
Kornbloom	50	110	10.9	165
Marine Lab B1	75	157	2.1	170
MBARI N° 3 UCB-10	50	127	8.0	170
Miller Farm CMF-10	35	134	8.0	175
Miller Farm	35	138	8.8	180
Moss Landing UC-B1	55	125	6.7	160
Radio Tower B1	55	121	9.3	170
River Park A & C	50	130	11.3	190
Woodward Marine UC-B4	70	119	11.4	175

Table 5.2: Soil types used in SHAKE91 analyses to develop r_c .

Material	Description	Depth	Reference
1	PCA ^a	0–10 m	Roblee and Chiou [97]
2	PCA ^a	10–20 m	Roblee and Chiou [97]
3	PCA ^a	20–40 m	Roblee and Chiou [97]
4	PCA ^a	40–80 m	Roblee and Chiou [97]
5	PCA ^a	80–160 m	Roblee and Chiou [97]
6	PCA ^a	> 160 m	Roblee and Chiou [97]
7	FML ^b	0–10 m	Roblee and Chiou [97]
8	FML ^b	10–20 m	Roblee and Chiou [97]
9	FML ^b	20–40 m	Roblee and Chiou [97]
10	FML ^b	40–80 m	Roblee and Chiou [97]
11	FML ^b	80–160 m	Roblee and Chiou [97]
12	FML ^b	> 160 m	Roblee and Chiou [97]
13	FMH ^c	0–10 m	Roblee and Chiou [97]
14	FMH ^c	10–20 m	Roblee and Chiou [97]
15	FMH ^c	20–40 m	Roblee and Chiou [97]
16	FMH ^c	40–80 m	Roblee and Chiou [97]
17	FMH ^c	80–160 m	Roblee and Chiou [97]
18	FMH ^c	> 160 m	Roblee and Chiou [97]
19	Gravel	All	Seed et al. [110]
20	Bay mud	All	Sun et al. [116]
21	Rock	All	Schnabel et al. [100]

^aPrimarily coarse, $\leq 30\%$ -#200, all plasticities

^bFine-grained matrix, lower plasticity, $> 30\%$ -#200, $PI \leq 15\%$

^cFine-grained matrix, higher plasticity, $> 30\%$ -#200, $PI > 15\%$

With this combination of soil profiles and earthquake records, a series of ground response analyses was performed using SHAKE91 with each earthquake record applied to the surface of unweathered bedrock in each soil profile. Acceleration time histories were computed at the surface of each soil profile layer within about 30 m of the ground surface and were used to calculate CAV_5 and r_c profiles. This resulted in a dataset containing 30,005 time histories from 1643 successful SHAKE91 runs.

The careful reader will note that 46 soil profiles and 36 earthquake records should produce 1656 runs. Thirteen runs were discarded because strain larger than three percent was predicted in at least one soil layer, and the accuracy of the results using SHAKE91's linear equivalent algorithm was questioned at large strain.

Table 5.3: Input motions used to develop r_c .

Year	Earthquake	Station	Dir deg	Mechanism	M_w	R km	PGA g	CAV_5 m/s	Scaled PGA	CAV_5 m/s	Field Motion ^a
1985	Michoacan	Ocotito	270	Reverse	8.1	337.0 ^b	0.05	2.77	0.10	6.85	f
1978	Tabas	Dayhook	TR	Reverse	7.4	17.0 ^b	0.36	8.75	0.30	7.27	n
1992	Landers	Lucerne Valley	000	Strike slip	7.3	1.1	0.76	23.41	0.40	12.15	n
1992	Landers	Silent Valley	000	Strike slip	7.3	51.3	0.045	2.49	0.09	5.83	f
1979	St Elias	Munday Creek	000	Reverse	7.3	72.0	0.05	2.23	0.10	5.53	f
1994	Eureka	Cape Mendocino	090	Strike slip	7.2	126.0 ^b	0.03	0.23	0.05	0.66	f
1999	Hector Mines	LA City Terrace	090	Strike slip	7.1	184.0 ^b	0.04	1.43	0.08	4.18	f
1971	Adak	Adak Naval Base	090	?	7.1	66.2 ^b	0.15	4.10	0.15	4.10	m
1992	Cape Mendocino	Cape Mendocino	000	Reverse	7.0	3.8 ^b	1.25	13.88	0.55	5.86	n
1989	Loma Prieta	Gilroy Array #1	090	Strike slip	7.0	10.0	0.44	6.40	0.30	4.26	n
1989	Loma Prieta	UCSC Lick Observatory	000	Strike slip	7.0	18.0	0.42	12.19	0.30	8.59	n
1989	Loma Prieta	Piedmont Jr High	045	Strike slip	7.0	16.0	0.20	1.24	0.15	3.42	n
1985	Nahanni	Site 1	280	Reverse	6.8	6.0	1.04	12.48	0.55	6.52	n
1985	Nahanni	Site 3	270	Reverse	6.8	16.0	0.20	3.86	0.15	2.86	m
1976	Gazli	Karakyr	EW	Reverse	6.8	3.0	0.66	13.50	0.35	7.15	n
1994	Northridge	Lake Hughes #9	090	Reverse	6.7	28.9	0.18	2.68	0.15	2.16	f
1994	Northridge	Vasquez Rocks	360	Reverse	6.7	24.0	0.14	3.93	0.15	4.24	f
1971	San Fernando	Carbon Canyon	220	Reverse	6.6	66.4	0.07	2.84	0.12	5.32	f
1971	San Fernando	Lake Hughes #4	069	Reverse	6.6	38.4	0.05	2.81	0.08	4.33	m
1971	San Fernando	Cedar Springs	126	Reverse	6.6	86.6	0.03	0.57	0.05	1.13	f
1983	Coalinga	Parkfield Cholame 3E	090	Reverse	6.6	38.4	0.05	1.85	0.08	3.38	f
1979	Imperial Valley	Cerro Prieto	147	Strike slip	6.5	23.5	0.163	13.59	0.25	21.10	m
1979	Imperial Valley	Superstition Mountain	135	Strike slip	6.5	26.0	0.146	2.50	0.23	4.17	m
1986	Chalfant Valley	Paradise Lodge	070	Strike slip	6.2	23.0 ^b	0.163	1.74	0.25	2.93	m
1986	Chalfant Valley	Tinemaha	090	Strike slip	6.2	40.6	0.037	1.06	0.06	2.13	f
1984	Morgan Hill	Gilroy Array #1	320	Strike slip	6.2	16.2	0.082	1.31	0.13	2.23	f
1984	Morgan Hill	UCSC Lick Observatory	320	Strike slip	6.2	44.1	0.054	1.76	0.09	3.18	f
1986	N Palm Springs	Silent Valley	090	Reverse	6.0	25.8	0.125	1.05	0.13	1.10	m
1986	N Palm Springs	Murrieta Hot Springs	090	Reverse	6.0	63.3	0.051	1.06	0.09	2.31	f
1987	Whittier Narrows	Mount Wilson	090	Reverse	6.0	28.0 ^b	0.15	2.75	0.25	4.83	m
1980	Victoria	Cerro Prieto	045	Strike slip	5.9	34.8 ^b	0.604	9.53	0.40	6.24	n
1981	Westmorland	Superstition Mountain	135	Strike slip	5.8	23.9	0.09	1.61	0.10	1.81	m
1983	Coalinga ^c	Transmitter Hill	360	Reverse	5.8	9.2	0.95	6.57	0.40	2.58	n
1983	Coalinga ^c	Skunk Hollow	270	Reverse	5.8	10.9	0.20	3.74	0.25	3.07	n
1983	Coalinga ^c	Oil Fields Fire Station	270	Reverse	5.8	28.0 ^b	0.15	3.51	0.25	4.43	n
1979	Coyote Lake	Gilroy Array #1	320	Strike slip	5.7	9.1	0.116	1.39	0.12	1.45	m

^an = near field motion, m = mid field motion, f = far field motion^bEpicentral distance^c8 July 22 0239 UTC aftershock

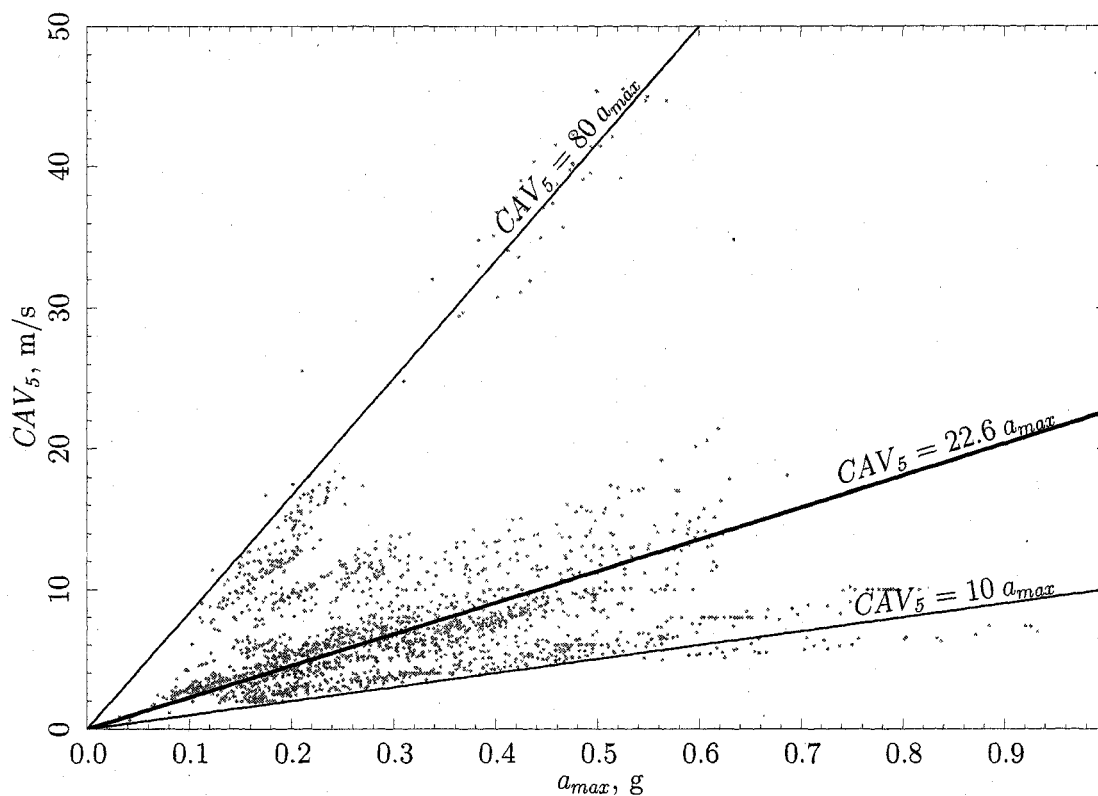


Figure 5.15: CAV_5 vs a_{max} from dataset produced by SHAKE91 runs. The heavy line illustrates the mean relationship; the light lines envelope the majority of the data.

An interesting byproduct made available from the time histories is the CAV_5 versus a_{max} correlation illustrated in Figure 5.15. For these data, a 1-g peak acceleration corresponds to CAV_5 ranging from 10 to 80 m/s with an average of 22.6 m/s. This wide range indicates that the two IMs are affected by different characteristics of the ground motion and suggests the potential for different behavior in the r_c relationship in this chapter as well as the in the correlation with liquefaction potential that will be addressed in Chapter 6.

Returning to the r_c development, Figure 5.16 shows r_c vs depth from the resulting dataset. In general, the data follow the shape of the offset term described earlier. From a value of 1 at the ground surface, r_c decays to an average of about 0.7 at 5 m depth. Below that point, the decrease in r_c is much slower.

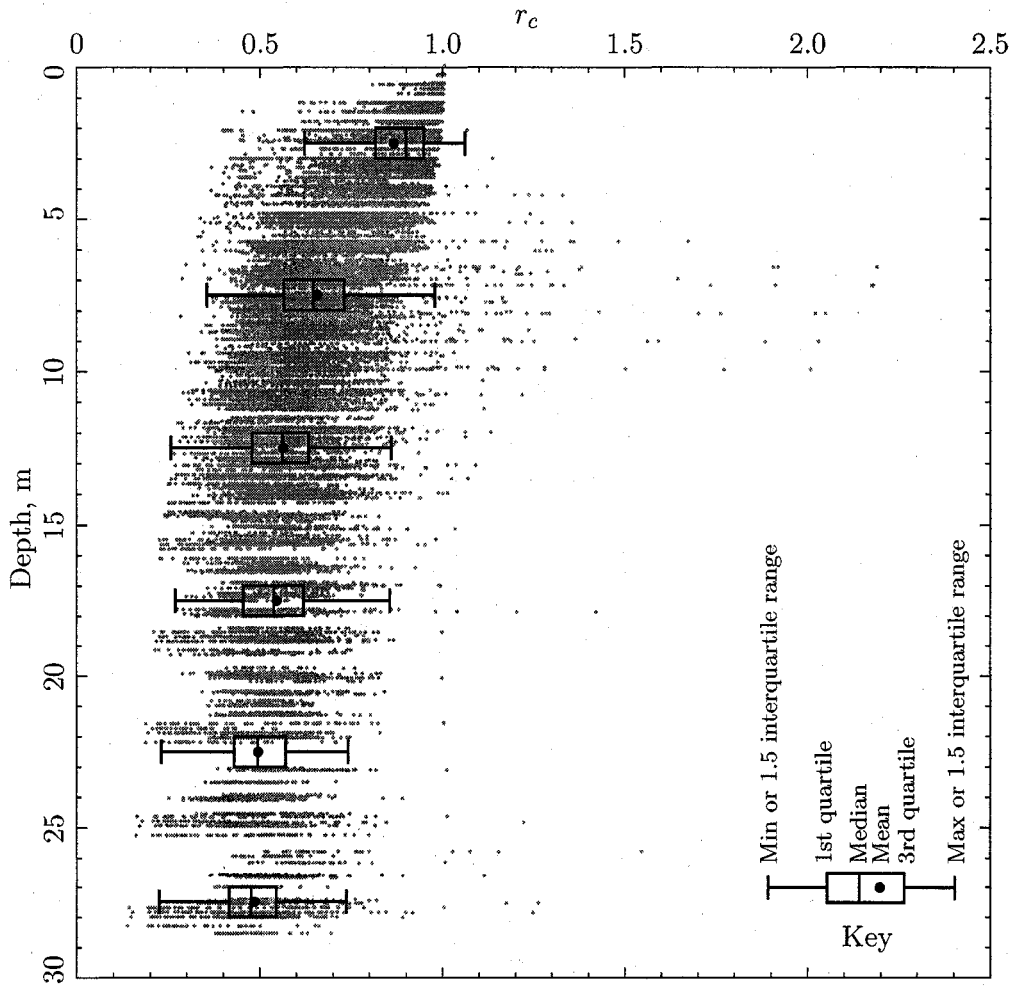


Figure 5.16: r_c vs depth from the dataset produced by SHAKE91 runs.

The points with high values of r_c between 5 and 10 m depth are from truncated soil profiles with large inverse impedance contrasts (stiff soil over soft) near the ground surface. These are the type of profiles on which Kayen and Mitchell [66] suggested performing actual ground response analyses rather than using a depth reduction coefficient. It is apparent from Figure 5.16 that the use of r_c can result in a significant degree of unconservatism (predicted CAV_5 lower than actual values) for soil profiles with inverse impedance contrasts.

Table 5.4: Statistical parameters of variables in dataset used to develop r_c .

Parameter	Min	1st quartile	Median	Mean	3rd quartile	Max	Std dev
r_c	0.133	0.535	0.665	0.695	0.873	2.186	0.202
z , m	0.0	3.05	7.88	9.32	13.85	30.94	7.42
CAV_5 , m/s	1.89	4.68	6.52	8.09	9.82	45.55	6.15
V_{s0} , m/s	44.8	119.2	127.0	124.0	136.5	183.7	28.2
dV_s , m/s/m	-2.17	6.72	9.29	9.20	11.39	18.94	4.72

Table 5.5: Correlation matrix for variables in dataset used to develop r_c .

Variable	r_c	z	V_{s0}	dV_s
z , m	-0.73			
V_{s0} , m/s	0.22	-0.02		
dV_s , m/s/m	-0.15	-0.03	-0.74	
CAV_5 , m/s	0.01	0.01	-0.08	0.03

5.4.1 1- and 2-d data exploration

Before starting the regression analysis for the r_c model, the dataset is subjected to a series of data exploration tests. Table 5.4 lists several common statistical parameters for each of the dataset variables. In a normal distribution, the median and mean are the same, the first and third quartiles are balanced about the mean, and 99.7% of the data points are within three standard deviations of the mean. From Table 5.4, r_c and dV_s meet all of these criteria, V_{s0} does not have balanced quartiles, z does not have balanced quartiles and the mean and median are notably different, and CAV_5 does not meet any of these criteria. Meeting all these criteria does not ensure a normal distribution but rather is an indication of the suitability of common statistical measures. The fact that some of the variables do not meet these criteria does not render the analysis invalid, but establishes the need for careful review of the results.

Table 5.5 lists the correlation between pairs of variables in the dataset. The strongest correlation is between V_{s0} and dV_s , which is not surprising since these two parameters together represent the shear wave velocity profile of the soil. The strong correlation suggests that it may be possible to describe one of these parameters in terms of the other. Since

there is a stronger correlation between r_c and V_{s0} than between r_c and dV_s , using V_{s0} in the r_c model and expressing dV_s in terms of V_{s0} is the more reasonable approach. The next strongest correlation is between r_c and depth; this is not surprising since the early relationships for cyclic stress r_d were based solely on depth.

The lack of correlation between r_c and CAV_5 is of particular note. Recent models for cyclic stress r_d include magnitude [57] or magnitude and amplitude (a_{max}) [21, 24]. As noted earlier in this chapter, the nonlinear behavior of soil suggests that ground response should be dependent on ground motion intensity. This issue is discussed further with the results of the regression analysis.

The final exercise in exploring the dataset is shown in Figure 5.17. The *coplot* function in the statistical analysis program, R [94], subdivides a pair of secondary variables— V_{s0} and CAV_5 in this case—into bins with approximately the same number of data points in each bin. The horizontal bars above and to the right of the scatter plots indicate the bin ranges. The primary variables— r_c and z in this case—are then plotted for each bin of the secondary variables to show the effect of the secondary variables on the primary variables. The coplots show that V_{s0} has a notable effect on r_c , especially at greater depth, but that the effect of CAV_5 is not readily apparent. This behavior is different than that noted in Figure 5.13, where CAV_5 affected r_c at depth almost as much as V_{s0} . The reasons for this are discussed later in the chapter.

5.5 Regression

The predictive model for r_c is developed using nonlinear regression of the dataset, specifically, the *nlm* routine in the statistical analysis program, R [94]. For a model with p unknown coefficients, this routine fits a p -dimensional nonlinear surface through the sample space, adjusting the coefficients to minimize the sum of the squared residuals from the fitted surface.

Equation (5.5) is used as the starting point for the r_c model, with V_{s0} added to the denominator of the harmonic term in accordance with the earlier theoretical derivation:

$$r_c = \frac{\theta_1 + (1 + \theta_2 z)^{-z} + \cos\left(\frac{\theta_3 z}{V_{s0}}\right) (1 + \theta_4 z)^{-z}}{2 + \theta_1} \quad (5.6)$$

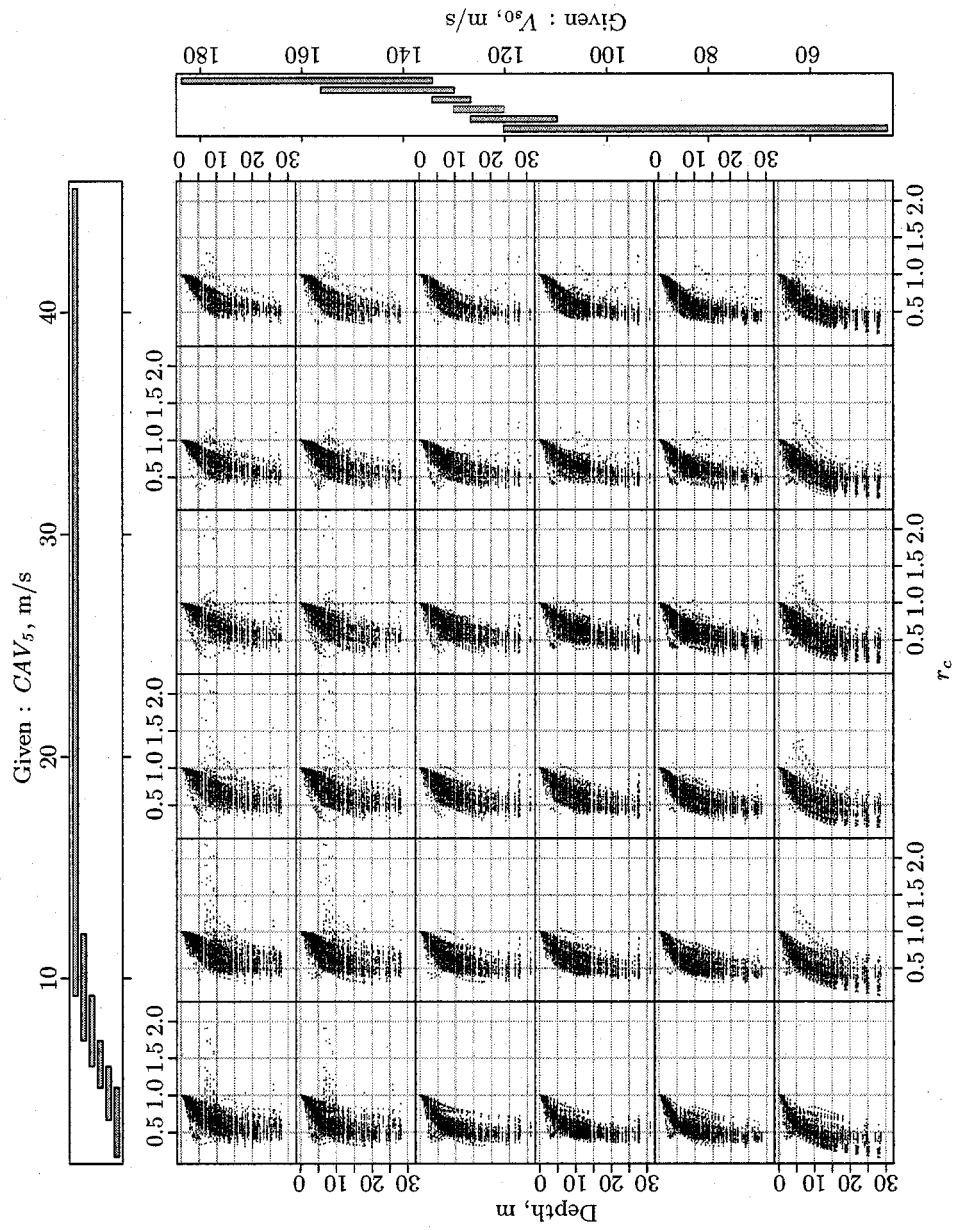


Figure 5.17: Plots of r_c vs depth for bins of V_{s0} and CAV_5 in the dataset.

V_{s0} is then added to each of the θ terms (one at a time) in various linear and exponential forms and the changes are checked for statistical significance. Then dV_s and CAV_5 are added in turn, each time checking for statistical significance. Consideration is also given to the complexity of the model: changes that marginally reduce the standard error but added to the model complexity are discarded. In this way, the following model is eventually developed:

$$r_c = \frac{0.87 + 0.0091V_{s0} + \left(1 + \frac{1.38z}{\sqrt{V_{s0}}}\right)^{-z} + \cos\left(\frac{5.00z}{V_{s0}}\right) \left(1 + \frac{0.077z}{\sqrt{V_{s0}}}\right)^{-z}}{2.87 + 0.0091V_{s0}} \pm \hat{\sigma}_{r_c} \quad (5.7)$$

The standard error, $\hat{\sigma}_{r_c}$, for this model is 0.11. However, it is apparent from Figure 5.16 that the dispersion of the data increases from zero at the ground surface (according to the definition of r_c) to a maximum value at a depth of about 5 m and then is approximately constant. Thus, instead of using a constant value of 0.11 for the entire depth, a taper function is introduced to produce a revised standard error as a function of depth:

$$\hat{\sigma}_{r_c}(z) = 0.11(1 - 1.5^{-z}) \quad (5.8)$$

Figure 5.18 compares the performance of the model with the dataset and shows its behavior across a range of V_{s0} . The bulge in the curve for $V_{s0} = 25$ m/s indicates that the model behavior at very low values of V_{s0} (less than about 50 m/s) becomes unstable. This is a fault of the model form rather than the regression analysis; as can be seen in Table 5.4, the lower range of V_{s0} in the dataset is about 45 m/s. It is suggested that the model is not appropriate for cases in which V_{s0} is less than about 40 m/s. At the upper end of the V_{s0} range, the model seems to behave in a stable and reasonable manner, even for values of V_{s0} that are beyond the limits of the dataset (about 185 m/s).

Figure 5.19 illustrates the level of bias of the model. The r_c residuals are defined as $r_{ci} - r_{c_{model}}$, in which r_{ci} is the value of r_c at a particular point in the dataset and $r_{c_{model}}$ is the value of r_c calculated using the model given the values of z and V_{s0} at that point. If the model were completely free of bias for each of the plotted variables, the residuals would all be evenly distributed about the zero axis. The heavy dashed lines in Figure 5.19 are from linear regression of the residuals, and their deviation from the zero residual axis indicates

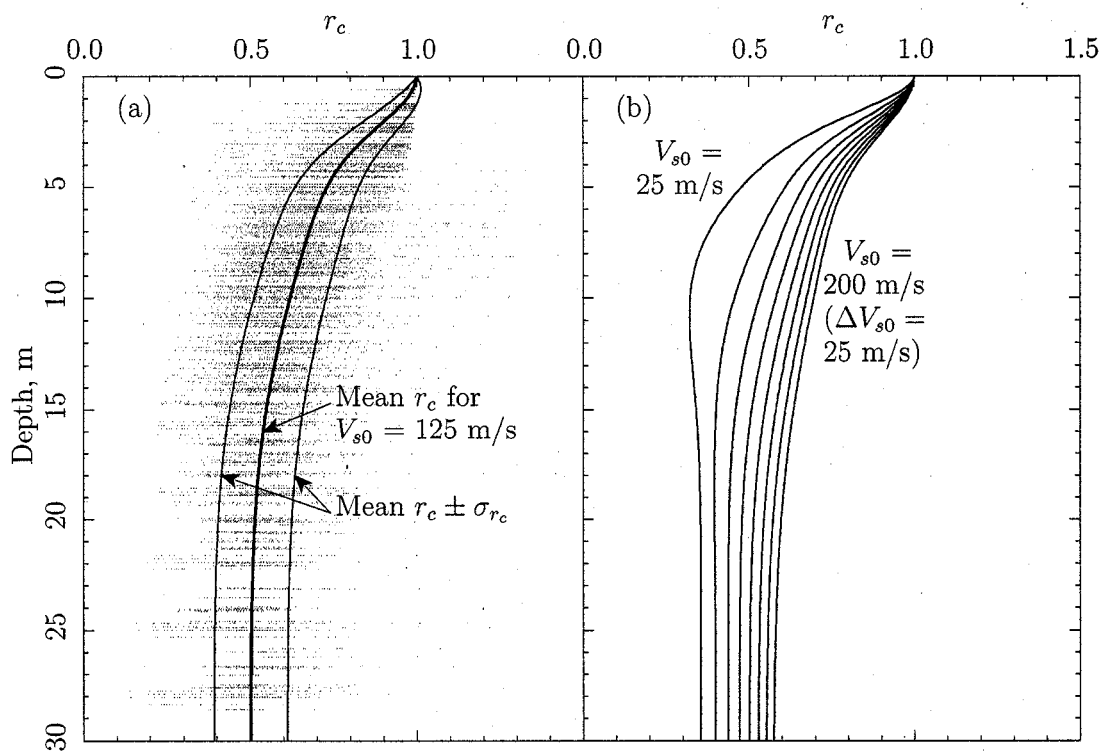


Figure 5.18: Plot of r_c model. (a) Mean r_c and mean $r_c \pm \sigma$ for $V_{s0} = 125$ m/s overlaying the entire regression dataset; (b) Mean r_c for $V_{s0} = 25$ m/s to 200 m/s in increments of V_{s0} 25 m/s. Note how model starts to deteriorate at $V_{s0} = 25$ m/s.

the level of bias that exists in the model with respect to the variable of interest. The close agreement between the dashed lines and the zero axis indicates that there is little bias in the model for any of the variables considered in this study.

As a check on the model performance, the calculated r_c is compared with four instances of r_c based on measurements at the downhole seismic array at the Wildlife site in southern California. In 1987, the Elmore Ranch and Superstition Hills earthquakes, magnitudes 6.2 and 6.6, respectively, occurred at the south end of the Salton Sea near the Wildlife recording site. The downhole seismic array recorded acceleration time histories of both of these earthquakes on seismographs at the ground surface and at a depth of 7.5 m below the surface. From these time histories, CAV_5 and r_c are calculated and compared to the results

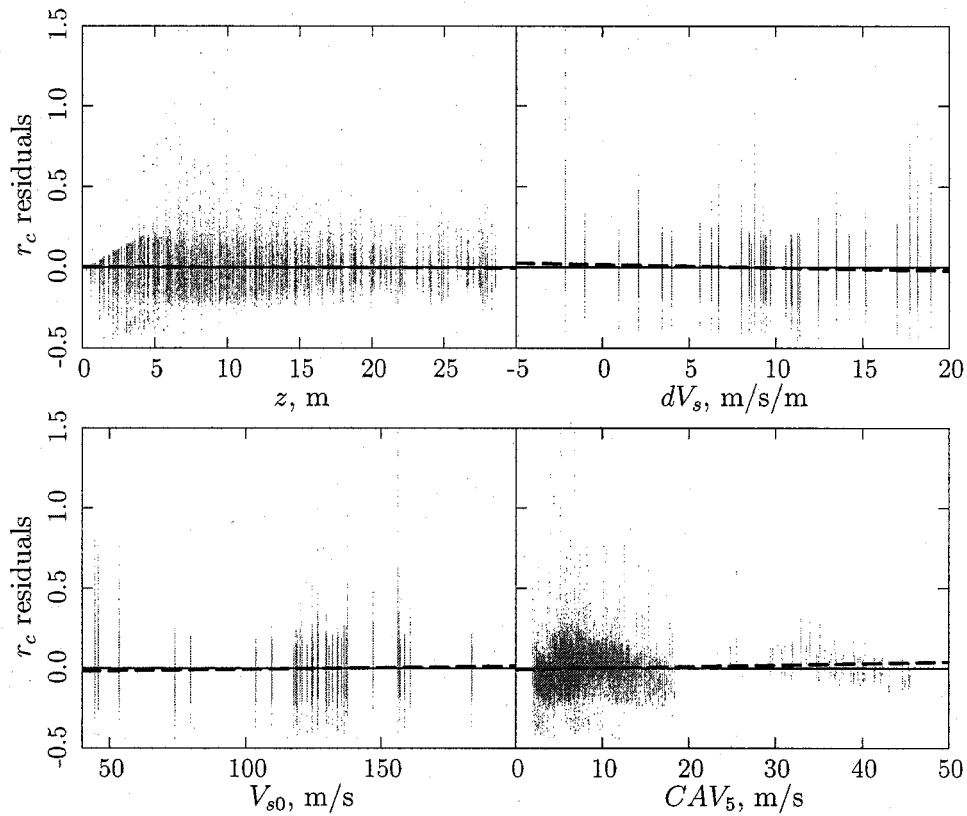


Figure 5.19: Plot of r_c residuals vs depth, V_{s0} , dV_s , and CAV_5 . The fine solid horizontal line is the zero residual axis; the thicker dashed lines are fitted through the residuals using linear regression and indicate the degree of bias in the model with respect to the x-axis variable.

of the model described in this section using $V_{s0} = 79.9$ m/s for the soil profile. The results, summarized in Table 5.6, indicate that model predictions are approximately centered in the range of measured values and within the standard error for the model.

Figure 5.20 compares the results from the r_c model with Çetin's model for r_d [23, 24]. Note that the data points in Çetin's plot are connected by lines, which add to the apparent density of the data in that plot; in the r_c plot, the data points are not connected. From the general range of the data as well as from the separation of the $\pm\sigma$ lines on either side of the means, it is apparent that there is less scatter in the r_c dataset. The tighter r_c distribution

Table 5.6: Comparison of r_c calculated using model with r_c measured at the Wildlife seismic array.

Earthquake	Component	CAV_5 at		r_c
		$z = 0$	$z = 7.5$ m	
Elmore Ranch	360	3.87	2.24	0.58
	090	4.17	2.21	0.53
Superstition Hills	360	13.01	8.63	0.66
	090	10.33	7.13	0.61
Model ($V_{s0} = 79.9$ m/s)				0.60

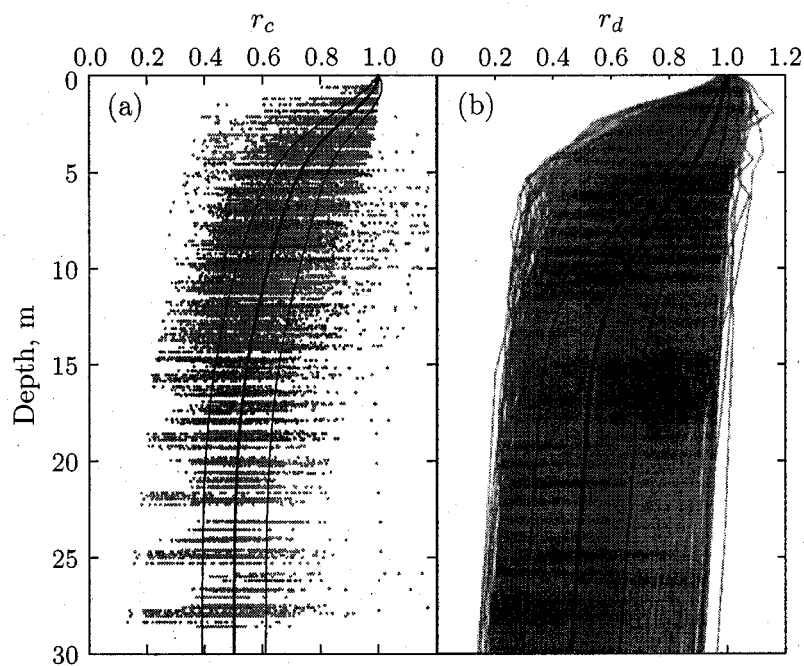


Figure 5.20: Comparison of datasets and models for (a) r_c from this study for $V_{s0} = 125$ m/s and (b) r_d from Çetin [23, 24] for $a_{max} = 0.2$ g, $M_w = 6.7$, and $\bar{V}_{s,12} = 160$ m/s. The thick line illustrates the model means; the thinner lines illustrate the means $\pm \hat{\sigma}$.

is also evident from a comparison of the model standard errors: Çetin's is

$$\hat{\sigma}_{r_d} = 0.0198 z^{0.85} \quad (5.9)$$

or 0.164 at a depth of 12 m. At the same depth the standard error for r_c from Equation (5.8) is 0.109, a significant reduction in variability.

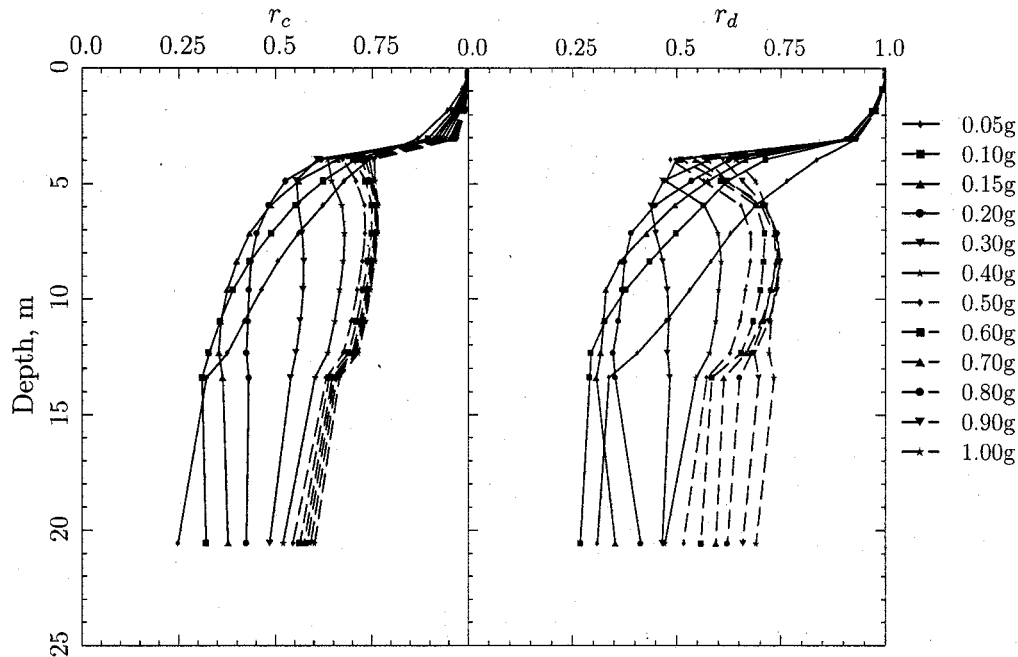


Figure 5.21: Comparison of r_c and r_d profiles investigating the sensitivity of CAV_5 and a_{max} to nonlinear soil behavior. The legend indicates the a_{max} to which the input motions were scaled.

The lack of correlation between r_c and CAV_5 that was noted earlier is confirmed by the regression analysis: CAV_5 is not found to be statistically significant in any of the model terms. This is further confirmed by the relatively minor degree of bias in the CAV_5 -residual plot in Figure 5.19 even though CAV_5 is not a part of the model. The insensitivity of r_c to CAV_5 may be due in part to the soil profiles and earthquake motions that were used to develop the dataset, but there is also an indication that this insensitivity is due to the nature of CAV_5 itself.

To investigate this, twelve SHAKE91 analyses are performed on the Radio Tower B-1 soil profile using the East-West component of the Loma Prieta earthquake recorded at the Gilroy 1 station scaled to $a_{max} = 0.05, 0.1, 0.15, 0.2, 0.3, 0.4, 0.5, 0.6, 0.7, 0.8, 0.9,$ and 1.0 g. The resulting acceleration time histories at 15 soil layer surfaces in the upper 20.6 m of the profile are used to calculate the r_d and r_c profiles shown in Figure 5.21. The difference

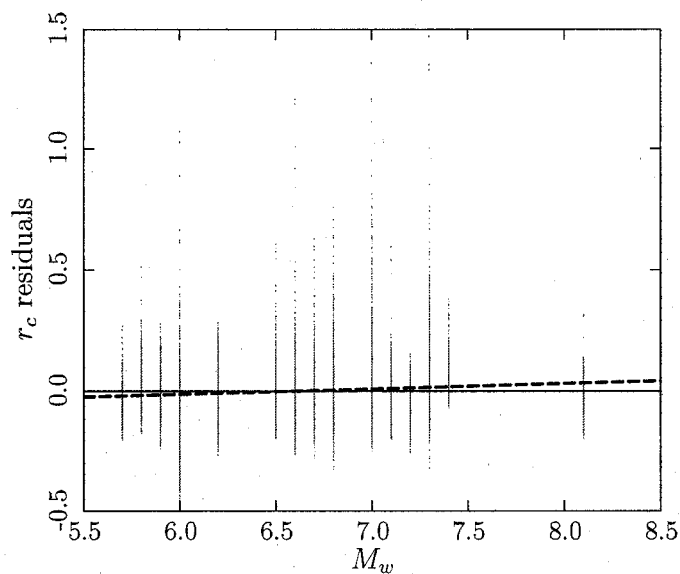


Figure 5.22: Plot of r_c residuals vs earthquake magnitude.

in r_c from the strongest and weakest motions is less than in r_d , indicating that CAV_5 has less influence on r_c than does a_{max} on r_d . This behavior is even more pronounced for the strongest 6 ground motions: the profiles for r_c change much less than those for r_d .

Kayen's r_b model and several of the cyclic stress r_d models listed at the beginning of this chapter included earthquake magnitude as an input variable. As a check on the effect of magnitude on r_c , Figure 5.22 plots the residuals from the r_c regression against the magnitude of the earthquakes that generated the input motions. The bias is relatively small—about the same as the bias for CAV_5 itself (Figure 5.19)—indicating that adding magnitude to the model would not significantly reduce the standard error.

In summary, the combination of theoretical and statistical methods produced a model for the CAV_5 depth reduction coefficient, r_c , that behaves reasonable well, has about one-third less variability than comparable models for the cyclic stress depth reduction coefficient, r_d , and that is not overly complex in its form or data requirements. In the next chapter, this model is used to develop a relationship between CAV_5 and standard penetration resistance at the threshold of seismic soil liquefaction.

Chapter 6

ESTIMATING LIQUEFACTION POTENTIAL USING CAV_5

The key component in assessing liquefaction potential is the relationship between seismic loading imparted to a site, described by an intensity measure, IM , and the site soil's resistance to liquefaction. This relationship is used in conventional liquefaction assessments to provide estimates of the factor of safety against liquefaction, FS_L , in deterministic analyses or the probability of liquefaction, P_L , in probabilistic analyses. In the performance-based method, the relationship is used to compute IM - EDP fragility curves, which, when combined with IM hazard curves from a probabilistic seismic hazard analysis, allow calculation of an EDP hazard curve.

This chapter presents the development of a relationship between the IM , CAV_5 , and the corrected penetration resistance of soil at the onset of liquefaction. In the absence of other CAV_5 liquefaction relationships, a general approach has been adopted that is similar to the one used for developing the CSR method described in Chapter 3 and, more specifically, the method used by Çetin [21, 22, 24]:

- develop a general form for the relationship based on soil mechanics theory and accepted practice;
- assemble a database of liquefaction and non-liquefaction case histories;
- use statistical methods to determine the parameter coefficients for the relationship.

This chapter presents the details and results of this three-step process.

6.1 Model parameters

Chapter 3 described how liquefaction results from the increased pore water pressure in soil that is shaken or sheared. This change in pressure occurs because of the soil's tendency for

volume change. This is termed dilatant behavior when the tendency is toward an increase in volume and a decrease in pore pressure, and contractive behavior when the tendency is toward a decrease in volume and an increase in pore pressure. The latter condition is necessary for the occurrence of liquefaction.

The volume change behavior of the soil is primarily a function of its *in situ* “state”. When soil can be sheared at a constant shear stress and constant effective confining pressure with no volume change, it is at the critical state. Soil that is denser than the critical state at the same effective confining pressure exhibits dilatant behavior, and soil looser than the critical state exhibits contractive behavior. Thus, to express the soil’s volume change behavior and its liquefaction potential, a liquefaction model must include parameters that characterize the *in situ* density and effective confining pressure of the soil.

The latter term can be approximated by the initial vertical effective stress, σ'_{vo} , which can be computed from the unit weights of the overlying soil and the depth of the ground water table. The former term is more complicated, but there is an established history of using penetration resistance—particularly from the standard penetration test (SPT) or cone penetration test (CPT)—as a proxy for relative density. In this chapter, the SPT is used to describe the penetration resistance; its background was described in Chapter 3.

With the soil’s resistance to liquefaction described by SPT penetration resistance and σ'_{vo} , and the seismic loading described by CAV_5 , the key elements of the model are in place. It is now possible to assemble a set of liquefaction and non-liquefaction case histories that include these parameters.

6.2 Case history database

The database assembled by Çetin [21, 24] for the *CSR* method provides a valuable starting point. It comprises 201 case histories: 109 where there was surface evidence of liquefaction, 89 where there was no surface evidence of liquefaction, and 3 where the surface evidence was inconclusive. Each case includes the information necessary to calculate σ'_{vo} , *CSR*, and SPT penetration resistance.

The kernel of Çetin’s database was the case history collection described by Seed et al. [109]. Çetin updated the calculation of penetration resistance and *CSR* to incorporate

advances in the understanding of liquefaction behavior, and presented the key parameters in terms of a mean and standard deviation. This estimate of the parameter uncertainty for each case history allowed Çetin to separate the overall parameter uncertainty from the liquefaction model uncertainty.

Of the 126 cases in the Seed et al. database, Çetin chose to ignore 36 cases for three main reasons: the basis for correcting penetration resistance could not be confirmed, the sites were not on approximately level ground, or the seismic shaking was not known well enough to allow a reliable calculation of *CSR*. To the remaining 90 cases, Çetin added 111 new cases primarily from the following earthquakes: 1987 Elmore Ranch and Superstition Hills, 1989 Loma Prieta, 1993 Kushiro-Oki, 1994 Northridge, and 1995 Hyogoken-Nambu.

The following sections describe the database parameters for soil liquefaction resistance and seismic loading.

6.2.1 Penetration resistance

As noted earlier, Çetin's database includes information about the SPT penetration resistance of soil at the depth of interest. To the raw blow counts from the SPT, Çetin applied corrections for applied energy and overburden pressure according to the procedures described by Youd et al. [128], but developed a new correction for fines content through logistic regression. Since Çetin's work, Idriss and Boulanger [15, 16, 17, 57] have updated the penetration resistance corrections for overburden pressure and fines content through a review of recent experimental and empirical data, and through the application of principles from critical state soil mechanics. Those corrections, which are gaining acceptance in the geotechnical profession and have been adopted for the work in this dissertation, are summarized in the following paragraphs.

Energy correction

The energy correction proposed by Idriss and Boulanger is the same as that described by Youd et al. [128] and Çetin et al. [24]: $C_E = 60/E$ in which E is the percentage of the theoretical maximum energy actually applied during the test. This correction is applied to

the measured penetration resistance (blow count): $N_{60} = N \cdot C_E$ in which N_{60} is the blow count normalized to a standard driving energy of 60% of the theoretical maximum energy.

Overburden stress correction

Idriss and Boulanger's overburden stress correction has the same form as the one used by Youd et al. and Çetin et al. ($N_{1,60} = C_N \cdot N_{60}$) but the overburden correction factor, C_N , is subtly different:

$$C_N = \left(\frac{p_a}{\sigma'_{vo}} \right)^\alpha \leq 1.7$$

in which p_a is atmospheric pressure in the same units as σ'_{vo} , and

$$\alpha = 0.784 - 0.0768\sqrt{N_{1,60}}$$

In the overburden stress correction used by Youd et al. and Çetin, α is fixed at 0.5. Idriss and Boulanger [57] showed that the inclusion of $N_{1,60}$ in the relationship for C_N is an improvement because the effect of overburden stress on the penetration resistance depends upon the relative density (and hence the penetration resistance) of the soil: soils with lower relative density and penetration resistance are affected to a greater degree by varying overburden stress than are soils with higher relative density and penetration resistance.

Fines content correction

The form of Idriss and Boulanger's fines content correction is different from that of Youd et al. but the same as that of Çetin et al.: $N_{1,60,cs} = N_{1,60} + \Delta N_{1,60}$. Idriss and Boulanger's definition of $\Delta N_{1,60}$ differs from that of Çetin et al., however:

$$\Delta N_{1,60} = \exp \left[1.63 + \frac{9.7}{FC} - \left(\frac{15.7}{FC} \right)^2 \right]$$

in which FC is the fines content in percent.

6.2.2 Effective confining pressure

Historically, the overburden stress correction, C_N , has been applied to the penetration resistance to remove the depth dependence from relationships between $N_{1,60}$ and relative

density, D_r . As noted at the start of this chapter, however, the volume change behavior of the soil, and hence its liquefaction potential *at a particular relative density*, is also affected by overburden pressure. To account for this volume change behavior, most liquefaction methods incorporate σ'_{vo} separately from its use in computing C_N . Although vertical *effective* stress, σ'_{vo} , is somewhat different than effective *confining* stress, the relationship between the two is relatively consistent in the normally-consolidated soils that are typically of interest in liquefaction assessments. As noted in Chapter 3, this second inclusion of σ'_{vo} is often referred to as the “ K_σ ” correction.

6.2.3 CAV_5

Çetin’s database was assembled for development of a *CSR* method of liquefaction assessment, hence does not include information about CAV_5 . The following paragraphs describe the estimation of CAV_5 for this chapter.

CAV₅ from on-site record

Ideally, a recorded acceleration time history would be available at each site, from which the surface value of CAV_5 , CAV_{5surf} , could be computed directly. This is relatively rare, however, occurring in only seven of the case histories. For sites at which a time history is available, CAV_{5surf} is computed for each of the two horizontal components and the geometric mean of the two values ($\sqrt{CAV_{5,surf,1} \cdot CAV_{5,surf,2}}$) is multiplied by the depth reduction factor to produce the value of CAV_5 at the depth of interest that is used in the regression:

$$CAV_5 = CAV_{5surf} \cdot r_c$$

The uncertainty of CAV_{5surf} computed from a time history is approximately the same as the uncertainty of the recorded acceleration values. As described by Çetin [21], this uncertainty can be represented by a coefficient of variation, $COV = 0.05$.

Table 6.1: Coefficients for Kramer and Mitchell's CAV_5 attenuation relationship [77].

θ_1	θ_2	θ_3	θ_4	h	f_1	f_2	$\sigma_{\ln CAV_{5surf}}$
3.495	2.764	-8.539	-1.008	6.155	-0.464	0.165	0.708

CAV_5 from attenuation relationship

For sites at which no acceleration time history is available, CAV_{5surf} is estimated using the attenuation relationship described by Kramer and Mitchell [77]:

$$\ln CAV_{5surf} = \theta_1 + \theta_2(M_w - 6) + \theta_3 \ln(M_w/6) + \theta_4 \ln \sqrt{R^2 + h^2} + f_1 F_N + f_2 F_R + \varepsilon_{\ln CAV_{5surf}} \quad (6.1)$$

in which M_w is the earthquake moment magnitude, R is the closest distance to the rupture plane (km), h is a fictitious hypocentral depth determined by regression, F_N and F_R are variables describing the fault type ($F_N = F_R = 0$ for strike slip faults, $F_N = 1$ and $F_R = 0$ for normal faults, and $F_N = 0$ and $F_R = 1$ for reverse and reverse-oblique faults), and $\varepsilon_{\ln CAV_5}$ is the error term, which is normally distributed with zero mean and standard deviation $\sigma_{\ln CAV_{5surf}}$. Table 6.1 lists the values of the coefficients, and Figure 6.1 illustrates the behavior of the attenuation relationship for reverse and reverse-oblique faulting.

Kramer and Mitchell developed their relationship using records from stations with site classes B or C according to the National Earthquake Hazards Reduction Program [37], which are stiffer than soils that are generally subject to liquefaction. To adjust these stiff ground estimates of CAV_{5surf} , a soil amplification factor, F_A , described by Stewart et al. [115] and Choi and Stewart [25] is applied:

$$\ln F_A = a + b \ln a_{max_{rock}} \quad (6.2)$$

$$IM_{surf} = IM_{rock} \cdot F_A \quad (6.3)$$

in which a and b are coefficients based on the soil conditions at the site, $a_{max_{rock}}$ is the peak horizontal acceleration (PHA) at the bedrock surface, IM_{surf} is the IM at the ground surface of the site, and IM_{rock} is the IM at the bedrock surface below the site. Although CAV_5 was not specifically considered in their studies, the amplification factor for spectral

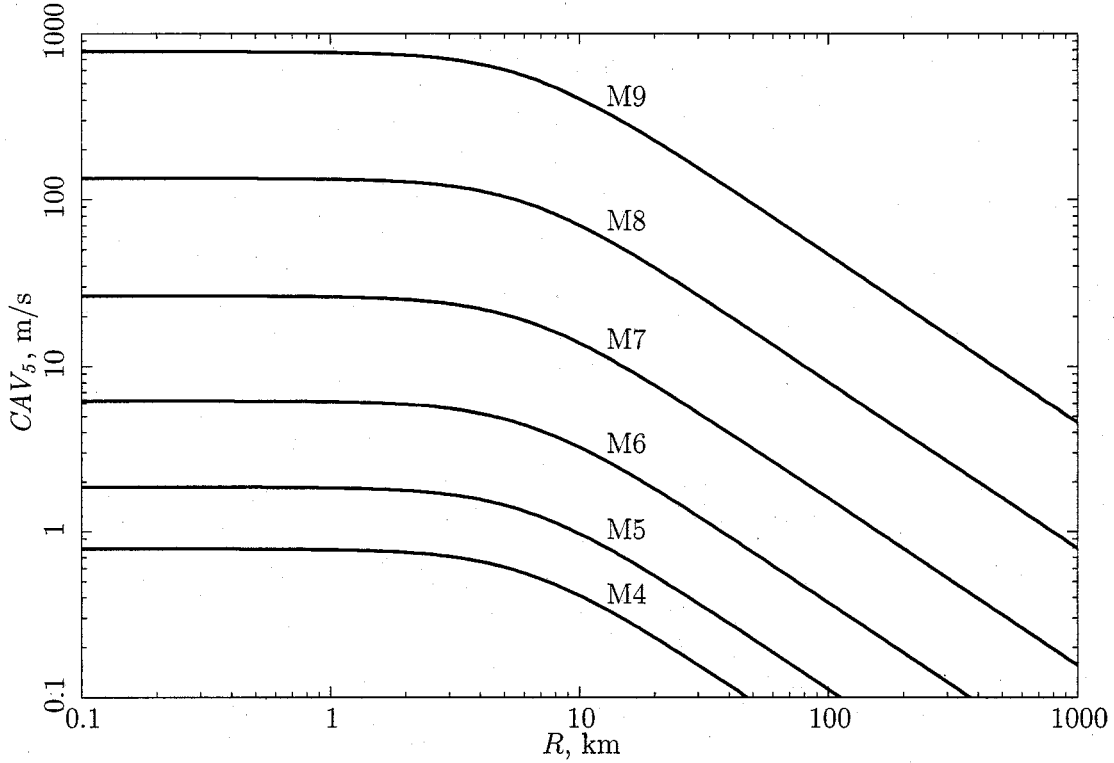


Figure 6.1: CAV_5 attenuation curves for reverse faulting from Kramer and Mitchell [77].

acceleration with a period of one second, $S_a(1.0)$ is judged to be acceptable because of the strong correlation between $S_a(1.0)$ and CAV_5 as shown in Figure 3.16.

In most cases, $a_{max_{rock}}$ is not known at a site but PHA at the ground surface, a_{max} , is available from Çetin's database. Using Equation (6.3), it is possible to relate a_{max} and $a_{max_{rock}}$ by treating PHA as the IM :

$$\ln F_{A_{PHA}} = a_{PHA} + b_{PHA} \ln a_{max_{rock}} = \ln a_{max} - \ln a_{max_{rock}}$$

in which the PHA subscript refers to coefficients for $IM = PHA$. Rearranging this,

$$\begin{aligned} \ln a_{max} &= a_{PHA} + (b_{PHA} + 1) \ln a_{max_{rock}} \\ a_{max_{rock}} &= \exp\left(\frac{\ln a_{max} - a_{PHA}}{b_{PHA} + 1}\right) \end{aligned}$$

This value of $a_{max_{rock}}$ is used to compute F_A for CAV_5 , F_{ACAV_5} , which in turn is used to compute CAV_5 at the ground surface:

$$\ln F_{ACAV_5} = a_{CAV_5} + b_{CAV_5} \ln a_{max_{rock}}$$

$$CAV_{5surf} = CAV_{5rock} \cdot F_A$$

in which CAV_{5rock} is the value of CAV_5 at the bedrock surface computed from Kramer and Mitchell's attenuation relationship.

As listed in Table 6.1, the standard deviation of $\ln CAV_{5surf}$ is 0.708. Baecher and Christian [10] describe how the standard deviation of a log-normal distribution is related to the COV of a normal distribution:

$$COV_X = \sqrt{\exp(\sigma_{\ln X}^2) - 1}$$

Thus, the COV of CAV_{5surf} computed with Kramer and Mitchell's attenuation relationship is 0.807.

CAV₅ from records with similar site conditions

For many of the cases in the database, a time history is available from a recording station in the same general area as the site, or from a recording station with soil conditions that are similar to those at the site. While it is not appropriate to use these time histories for a direct computation of CAV_{5surf} , the information contained in them can be used to improve the estimation from Kramer and Mitchell's attenuation relationship using the following procedure:

1. Compute the geometric means of CAV_{5surf} and a_{max} from the two horizontal components of the recorded time history;
2. Use the computed a_{max} to calculate F_{APHA} , $a_{max_{rock}}$, F_{ACAV_5} , and CAV_5 at the bedrock surface below the recording site, CAV_{5rock} , for the appropriate soil conditions at the recording site;
3. Use Kramer and Mitchell's attenuation relationship with CAV_{5rock} , the rupture distance to the recording station, and the fault type to compute an apparent magnitude;

4. Use Kramer and Mitchell's attenuation relationship with this apparent magnitude, the rupture distance to the case history site, and the fault type to compute CAV_{5rock} at the case history site;
5. Use a_{max} from Çetin's database and the soil conditions at the case history site to compute F_{APHA} , $a_{maxrock}$, F_{ACAV_5} , and CAV_{5surf} at the case history site.

As with the other two methods, the computed CAV_{5surf} is multiplied by r_c to yield CAV_5 at the depth of interest. This procedure, though somewhat lengthy, has the benefit of explicitly and transparently accounting for differences in rupture distance and site condition in the adjustment of CAV_5 from a nearby recording station.

The uncertainty of CAV_{5surf} computed in this manner depends on the distance between the recording station and the case history site. If the recording site is at the case history site, $COV = 0.05$ as described earlier. With increasing separation between the recording site and the case history site, the uncertainty increases due to the effects of spatial variability (*i. e.* incoherence). Harichandran and Vanmarcke [48] noted that the coherency of the 1 Hz component of earthquake shaking was nearly absent at sites in the seismic array at Lotung, Taiwan, that were more than about 1 km apart. In the absence of site-specific information, the coherence behavior observed at Lotung is used to describe the dependency of CAV_5 uncertainty on distance: where the recording station is 1 km or more from the case history site, the CAV_{5surf} uncertainty equals the intra-event component of the uncertainty term in the attenuation relationship.

Kramer and Mitchell did not separate inter- and intra-event uncertainty in their attenuation relationship. However, Harichandran and Vanmarcke noted that the coherency decay with distance was related to the frequency component of the ground motion. Since both CAV_5 and Arias Intensity are strongly correlated to the 1 Hz components of shaking, the relative proportions of the inter- and intra-event uncertainty for CAV_{5surf} are assumed to be about the same as those for the Arias Intensity attenuation relationship described by Travararou et al. [120]: $\sigma_{\ln I_a, intra} \approx 1.5 \cdot \sigma_{\ln I_a, inter}$. Applying this ratio to $\sigma_{\ln CAV_{5surf}} = 0.708$ from Kramer and Mitchell's attenuation relationship, $COV = 0.644$ for CAV_{5surf} from time

histories recorded at sites 1 km or more from the case history sites. Where the distance between the recording station and the case history site approaches zero, the *COV* of CAV_{5surf} approaches 0.05 as described above. At distances between 0 and 1 km, *COV* is linearly interpolated between these two values.

6.2.4 Database summary

It was possible to compute CAV_{5surf} for 179 of Çetin's 201 cases. For the remaining 22, it was not possible to locate either the site or the rupture surface of the earthquake accurately enough to be able to estimate the source-to-site distance required for Kramer and Mitchell's attenuation relationship. To augment the database, two cases from the 1999 Chi Chi earthquake and ten cases from Kayen's database for Arias Intensity [65] were added, providing 192 cases for determining the CAV_5 liquefaction relationship. Table 6.2 presents a statistical summary of the database; Appendix C contains a complete listing of the case history data.

6.3 Transformation of model parameters

Soil mechanics theory does not indicate which form the key parameters should take in the liquefaction model. For example, is the loading parameter, CAV_5 , best related to the resistance parameters, $N_{1,60,cs}$ and σ'_{vo} , as its logarithm, a polynomial, or untransformed? Historically, deterministic liquefaction models, like the ones described by Youd et al. [128] and Idriss and Boulanger [57] have taken polynomial forms, while probabilistic models, like the ones described by Liao et al. [81] and Çetin [21, 24] have taken logarithmic forms. These authors do not provide much detail concerning their rationale for choosing the model form, implying perhaps that any model form can be used as long as it effectively separates the liquefaction and non-liquefaction cases.

In their chapter on data classification, which includes a discussion of logistic regression, Baecher and Christian [10] suggest that parameters should be transformed so that their frequency distributions are approximately normal. Figure 6.2 presents the quantile plots of $N_{1,60,cs}$, $\ln(CAV_5)$, and $\ln(\sigma'_{vo})$ for liquefaction and non-liquefaction cases. Linear plots, especially between values of -1 and 1 for the standard normal variate, indicate that the

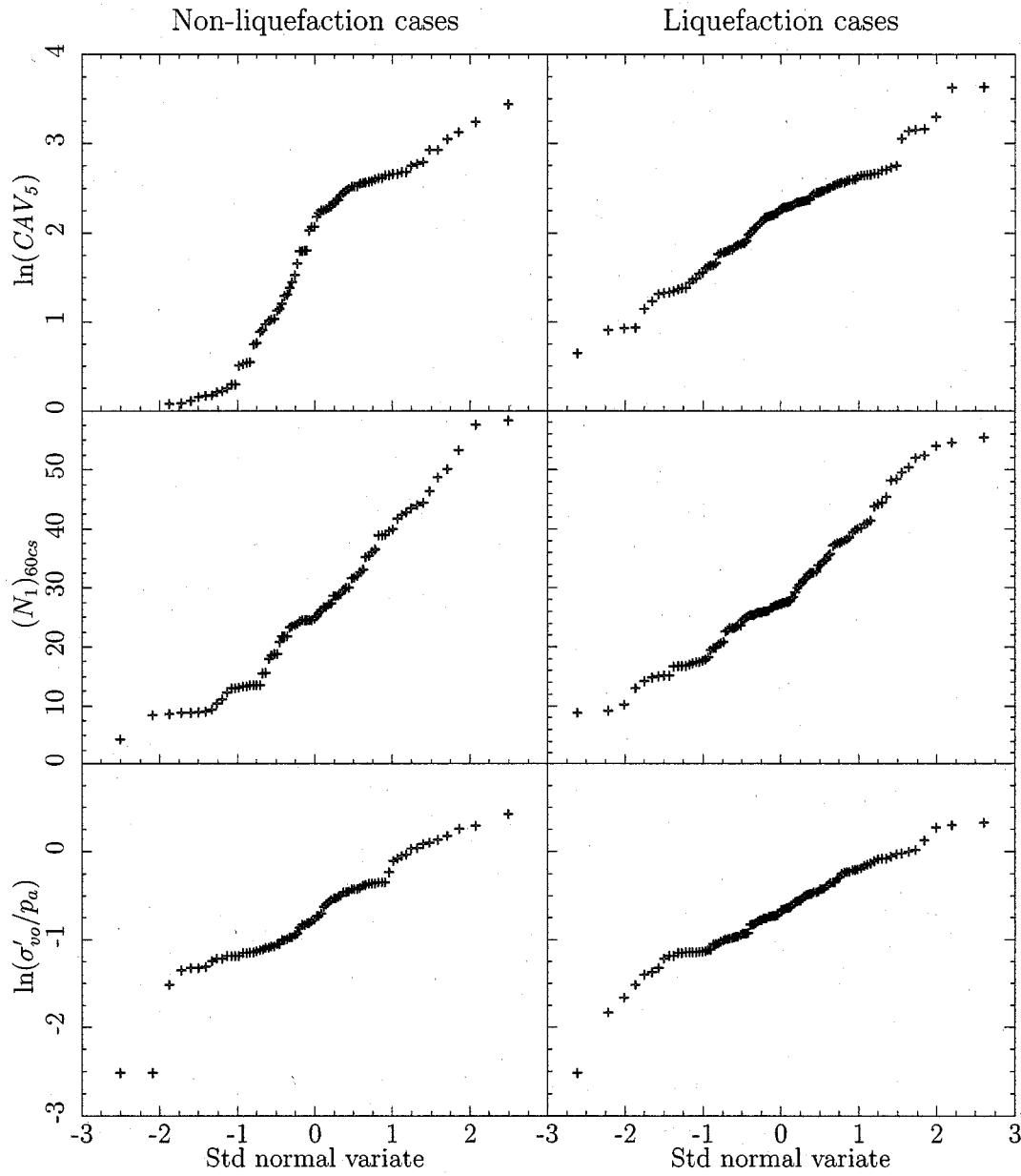


Figure 6.2: Quantile plots of non-liquefaction and liquefaction cases for key liquefaction model parameters. Linear plots, especially between standard normal variate of -1 and +1, indicate that the parameters are normally distributed.

Table 6.2: Statistical parameters of the CAV_5 case history database.

Parameter	All cases	Non-liquefaction	Liquefaction
Number of cases	191	81	110
Mean $\ln CAV_5$	1.968	1.710	2.158
Equiv CAV_5 , m/s	7.16	5.53	8.65
Mean $N_{1,60,cs}$	19.7	26.4	14.7
Mean $\ln \sigma'_{vo}$	-0.698	-0.726	-0.697
Equiv σ'_{vo} , atm	0.498	0.484	0.498
Variance $\ln CAV_5$	0.700	1.119	0.312
Std dev	0.837	1.058	0.559
Coef of variation	0.425	0.619	0.259
Variance $N_{1,60,cs}$	117.6	159.7	28.4
Std dev	10.8	12.6	5.3
Coef of variation	0.548	0.477	0.361
Variance $\ln \sigma'_{vo}$	0.251	0.298	0.218
Std dev	0.501	0.546	0.467
Coef of variation	-0.718	-0.752	-0.670
Covariance($\ln CAV_5, N_{1,60,cs}$)	2.49	8.24	0.552
Correlation coef	0.275	0.617	0.185
Covariance($\ln CAV_5, \ln \sigma'_{vo}$)	0.0865	0.208	-0.0113
Correlation coef	0.206	0.360	-0.0432
Covariance($N_{1,60,cs}, \ln \sigma'_{vo}$)	1.54	3.06	0.678
Correlation coef	0.283	0.444	0.272

form of the parameter shown in the figure is normally distributed. From Figure 6.2, it appears that $N_{1,60,cs}$ and $\ln(\sigma'_{vo})$ are approximately normally distributed except in the tails (standard normal variate less than -1 and greater than 1) for both the non-liquefaction and liquefaction cases, and that $\ln(CAV_5)$ is approximately normally distributed for the liquefaction cases but not for the non-liquefaction cases. Baecher and Christian note that of all the classification procedures, logistic regression is least sensitive to deviations from normality, thus these forms are judged to be suitable for use in the development of the CAV_5 liquefaction relationship.

6.4 Logistic regression

Logistic regression is frequently used to explore the relationship between a dichotomous response and a set of continuous or discrete explanatory variables. For the purpose of this work, the presence or absence of liquefaction is the dichotomous response and $N_{1,60,cs}$, $\ln CAV_5$, and $\ln \sigma'_{vo}$ are the continuous explanatory variables. Unlike ordinary least squares regression, logistic regression estimates the likelihood of one or the other response rather than actual value of the response. This fits with the goal of this chapter: to find a relationship that predicts the probability of liquefaction using $N_{1,60,cs}$, $\ln CAV_5$, and $\ln \sigma'_{vo}$.

As noted by Baecher and Christian [10], the key component in logistic regression is the likelihood function, which describes the likelihood of a set of parameter coefficients, θ , given a set of m observations of some process \mathbf{G} ,

$$L(\theta|\mathbf{G}) = L(\theta|g_1, g_2, \dots, g_m) = P[g_1, g_2, \dots, g_m|\theta]$$

in which g_1 through g_m are the individual observations. If the observations of \mathbf{G} , which form the distribution, $f_{\mathbf{G}}(g|\theta)$, are independent and identically distributed, the likelihood function is equal to the product of the probabilities of the individual observations given the set of parameter coefficients:

$$\begin{aligned} L(\theta|\mathbf{G}) &= f_{\mathbf{G}}[g_1, g_2, \dots, g_m|\theta] dg_1 dg_2 \dots dg_m \\ &= \prod_{i=1}^m f_{\mathbf{G}}[g_i|\theta] dg_i \end{aligned}$$

For this work, in which the probability of liquefaction, P_L , and non-liquefaction, $P_{NL} = 1 - P_L$ are of interest,

$$L(\theta|\mathbf{G}) = \prod_{i=1}^m (P_L[g_i|\theta])^{Y_i} \times (P_{NL}[g_i|\theta])^{1-Y_i}$$

in which $Y_i = 1$ if liquefaction occurred, 0 if it did not. If the k liquefaction cases are separated from the $m - k$ non-liquefaction cases, the likelihood function can be rewritten as

$$L(\theta|\mathbf{G}) = \prod_{i=1}^k (P_L[g_i|\theta]) \times \prod_{j=k+1}^m (P_{NL}[g_j|\theta]) \quad (6.4)$$

Following from the discussion of the liquefaction limit state variable, \hat{g} , in Chapter 4 and modifying the forms for CAV_5 as described above,

$$\begin{aligned}\hat{g} &= f(N_{1,60,cs}, \ln \sigma'_{vo}) - f(\ln CAV_5) \\ &= N_{1,60,cs} - \theta_1 \ln CAV_5 - \theta_2 \ln \sigma'_{vo} - \theta_3\end{aligned}\quad (6.5)$$

Then,

$$\begin{aligned}P_L &= \Phi\left(-\frac{\hat{g}}{\sigma_E}\right) \\ &= \Phi\left(-\frac{N_{1,60,cs} - \theta_1 \ln CAV_5 - \theta_2 \ln \sigma'_{vo} - \theta_3}{\sigma_E}\right)\end{aligned}\quad (6.6)$$

in which Φ is the standard normal cumulative probability operator and σ_E is the total (parameter and model) uncertainty in the relationship. Consequently,

$$\begin{aligned}P_{NL} &= 1 - P_L \\ &= \Phi\left(\frac{\hat{g}}{\sigma_E}\right) \\ &= \Phi\left(\frac{N_{1,60,cs} - \theta_1 \ln CAV_5 - \theta_2 \ln \sigma'_{vo} - \theta_3}{\sigma_E}\right)\end{aligned}\quad (6.7)$$

6.4.1 Bayesian updating

Çetin [21, 22] combined his *CSR* likelihood function with a prior distribution in a Bayesian framework to produce an updated posterior distribution:

$$f_{\Theta}(\theta|\mathbf{G}) = c \cdot f_{\Theta}(\theta) \cdot L(\theta|\mathbf{G})\quad (6.8)$$

in which $f_{\Theta}(\theta|\mathbf{G})$ is the posterior distribution, c is a normalizing constant to ensure that the area encompassed by the posterior distribution = 1, $f_{\Theta}(\theta)$ is the prior distribution, and $L(\theta|\mathbf{G})$ is the likelihood function described above.

The Bayesian framework is especially useful for combining prior information or understanding about the data distribution with the likelihood distribution. For situations in which there is no prior information or the prior information is to be ignored, a non-informative (constant-valued) prior distribution can be used. If $f_{\Theta}(\theta)$ is a constant, $c \cdot f_{\Theta}(\theta)$ is also

constant, and the resulting posterior distribution in Equation (6.8) is equal to the likelihood function.

While Çetin chose not to include any prior information about the *CSR* method in his liquefaction relationship, he explicitly included the prior distribution by assigning it a constant value then solved for the parameter coefficients, θ , within the Bayesian framework. For *CAV₅*, there is no prior information to be included. Instead of adopting a constant prior distribution and solving the Bayesian equation, the prior distribution is entirely ignored and θ is determined by maximizing the likelihood function using the *mle* routine of the statistical analysis program, *R* [94]. As noted in the previous paragraph, these two approaches are equivalent.

6.4.2 Sampling bias

Table 6.2 shows that there are significantly more liquefaction cases in the database than non-liquefaction cases: 110 versus 81. It is easy to appreciate why investigators are more interested in examining the conditions of failures than successes, but this bias is undesirable in logistic regression and can affect the result.

Çetin [21, 22] and Baecher and Christian [10] note that this bias can be addressed approximately by weighting each class of cases (liquefaction or non-liquefaction) according to the proportion of the other class's population in the total database. However, it is desirable that the overall information content should stay approximately constant, so the sum of the liquefaction and non-liquefaction weights should equal 2.0. With these two criteria, the liquefaction weights are computed as follows:

$$w_{NL} = w_L \frac{110}{81} = 1.36w_L$$

in which w_{NL} is the weight applied to non-liquefaction cases, w_L is the weight applied to liquefaction cases, and 110 and 81 are the number of liquefaction and non-liquefaction cases in the database.

$$w_{NL} + w_L = 2.36w_L = 2$$

$$w_L = 0.8, w_{NL} = 1.2$$

Table 6.3: Model coefficients from regression with model and parameter uncertainty.

	θ_1	θ_2	θ_3	σ_E
Mean	6.47	4.20	9.45	5.25
Std error	0.90	1.34	2.27	0.76
2.5% limit	4.86	1.51	4.52	4.01
97.5% limit	8.46	6.92	13.65	7.10

Table 6.4: Correlation matrix for coefficients from regression with model and parameter uncertainty.

	θ_1	θ_2	θ_3	σ_E
θ_1	1.00	-0.29	-0.86	0.32
θ_2	-0.29	1.00	0.64	0.01
θ_3	-0.86	0.64	1.00	-0.21
σ_E	0.32	0.01	-0.21	1.00

in which the weights are rounded to one decimal place. Now, the likelihood function in Equations (6.4) to (6.7) can be rewritten as

$$L[\theta|\mathbf{G}] = \prod_{i=1}^k \left[\Phi \left(\frac{N_{1,60,cs_i} - \theta_1 \ln CAV_{5i} - \theta_2 \ln \sigma'_{vo_i} - \theta_3}{\sigma_E} \right) \right]^{0.8} \times \prod_{j=k+1}^m \left[\Phi \left(\frac{N_{1,60,cs_j} - \theta_1 \ln CAV_{5j} - \theta_2 \ln \sigma'_{vo_j} - \theta_3}{\sigma_E} \right) \right]^{1.2} \quad (6.9)$$

6.5 Liquefaction relationship including parameter and modeling uncertainty

The logistic regression using the likelihood function in Equation (6.9) yields the following result:

$$P_L = \Phi \left[\frac{N_{1,60,cs} - 6.47 \ln(CAV_5) - 4.20 \ln \left(\frac{\sigma'_{vo}}{p_a} \right) - 9.45}{5.25} \right] \quad (6.10)$$

Table 6.3 lists the coefficients in Equation (6.10) as well as their standard errors and 95% confidence limits; Table 6.4 present their correlation matrix. This regression is based on using the most appropriate of the three sources of information for estimating CAV_{5surf} : records at the site, records near the site, and Kramer and Mitchell's attenuation relationship. It is important to note that CAV_5 as listed in Equation (6.10) is the value at the depth of interest in the soil profile and is equal to the product of CAV_{5surf} and r_c .

The term, σ_E , is of particular interest since it describes the efficiency of the liquefaction relationship. The regressed value of 5.25 is somewhat higher than the value of 4.21 computed by Çetin for the *CSR* method, but given that the CAV_5 attenuation relationship has seen little use and refinement in comparison to a_{max} relationships, it is encouraging that σ_E for

CAV_5 is so close to that from the *CSR* method. The similarity may be in part because the case histories, including their blow counts, fines contents, depths, and vertical stresses used in the two regressions are nearly the same.

6.5.1 Overburden stress correction

Using the procedure described in Chapter 4, it is possible to derive an expression for the overburden stress correction, K_σ , for the CAV_5 liquefaction relationship:

$$K_\sigma = \left(\frac{\sigma'_{vo}}{p_a} \right)^{f-1} \quad \text{or}$$

$$\ln K_\sigma = (f - 1) \ln \left(\frac{\sigma'_{vo}}{p_a} \right)$$

Rearranging Equation (6.10),

$$\ln(CAV_5) = \frac{N_{1,60,cs} - 4.20 \ln \left(\frac{\sigma'_{vo}}{p_a} \right) - 9.45 + \sigma_E \Phi^{-1}(P_L)}{6.47}$$

in which Φ^{-1} is the inverse standard normal cumulative distribution operator. Comparing this with the general form for K_σ , it can be seen that $f - 1 = -4.20/6.47 = -0.65$, thus $f = 0.35$ and,

$$K_\sigma = \left(\frac{\sigma'_{vo}}{p_a} \right)^{-0.65}$$

The exponent for K_σ is considerably lower than the value of -0.28 inferred from Çetin's method, the range of -0.4 to -0.2 listed by Youd et al. [128], and the blow count-dependent ranges listed by Boulanger and Idriss [17]. However, because K_σ corrects for stress and depth effects, it must be considered in combination with r_c , which also affects the value of CAV_5 with depth. Thus, the difference in K_σ for the CAV_5 relationship is not an indication of better or worse performance, but of the difference in behavior between CAV_5 and *CSR*.

6.5.2 Liquefaction curves

Figure 6.3 presents the case history data points and the liquefaction state boundaries determined from the regression. CAV_5 in the vertical axis has been corrected for overburden stress using K_σ :

$$CAV_5 \text{ at 1 atm} = \frac{CAV_{5surf} \cdot r_c}{K_\sigma} \quad (6.11)$$

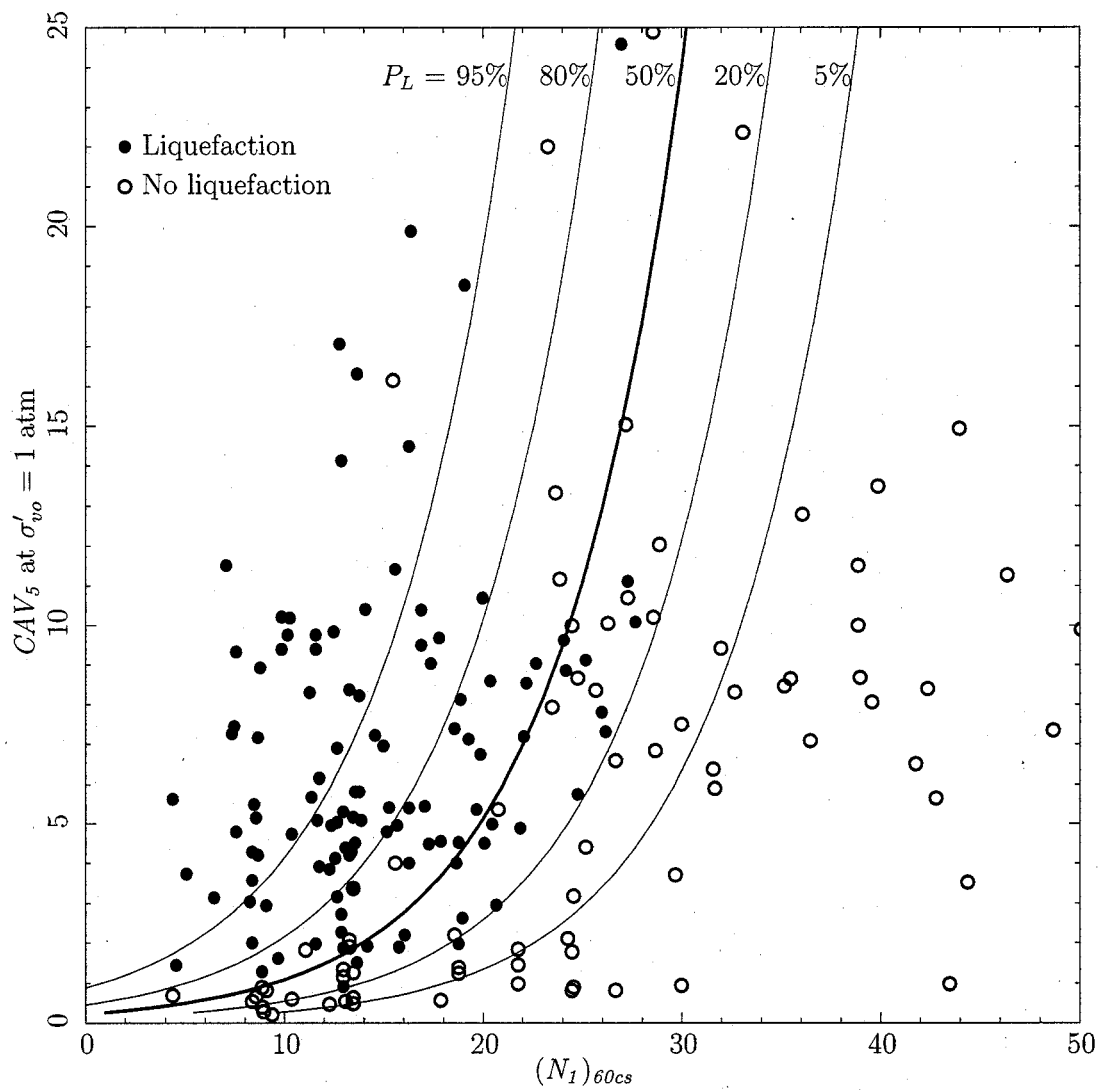


Figure 6.3: Liquefaction state boundary curves with parameter and model uncertainty included. The closed circles represent cases at which liquefaction was evident at the ground surface; the open circles represent cases where surface evidence of liquefaction was absent.

Figure 6.4 presents the same data as Figure 6.3 except the individual points are labeled with their case number instead of liquefaction or non-liquefaction symbols. These case numbers correspond to the listing in Appendix C.

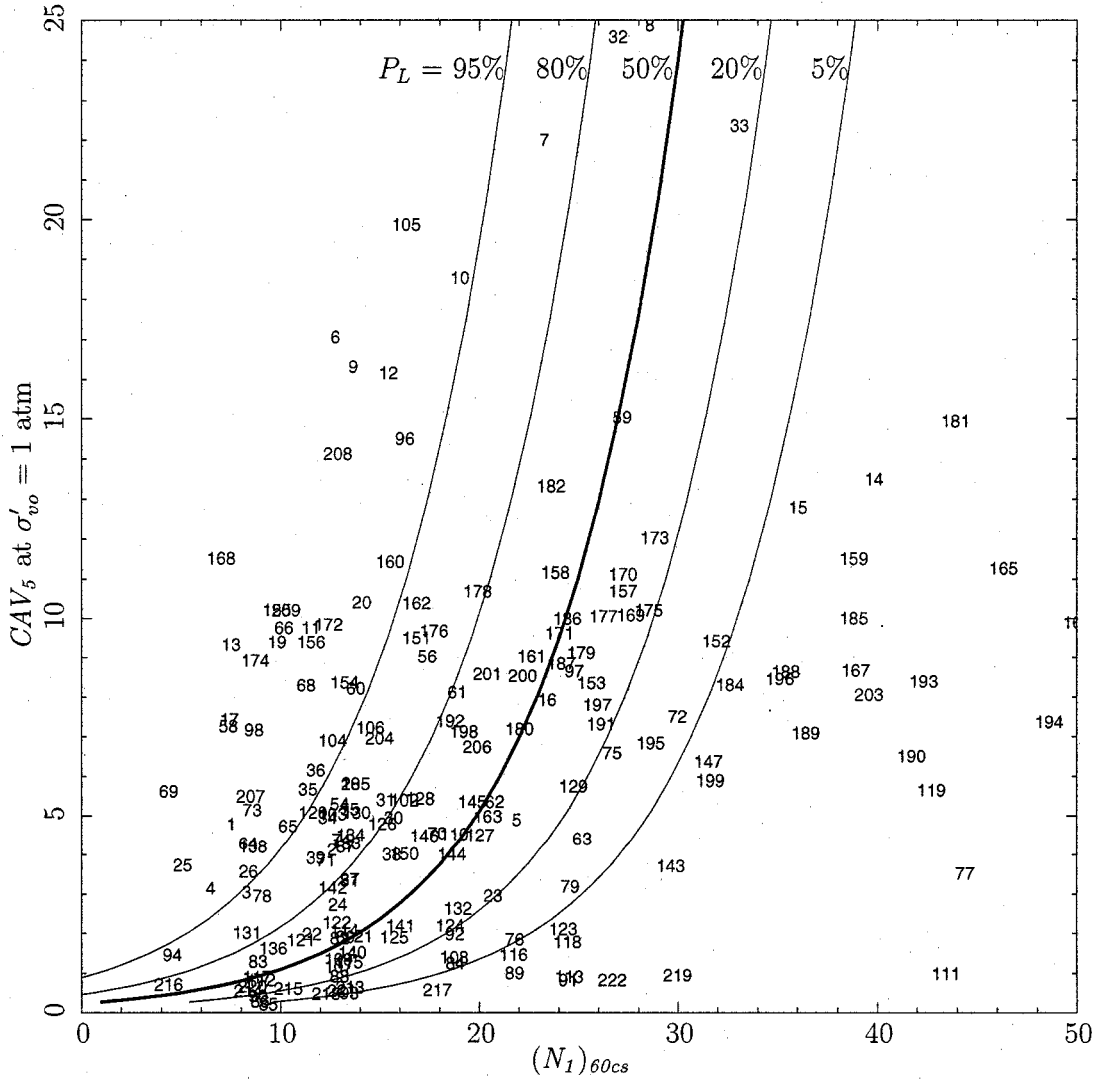


Figure 6.4: Case histories and liquefaction state boundary curves with parameter and model uncertainty included.

Figure 6.3 indicates that the liquefaction model is reasonably effective at separating the liquefaction and non-liquefaction cases. The mis-classified cases (liquefaction cases to the right of the $P_L = 50\%$ curve and non-liquefaction cases to the left) are generally contained between the $P_L = 20\%$ and 80% curves. The obvious exceptions are the two

non-liquefaction cases in the upper left portion of the figure. From Figure 6.4, we can see that these points correspond to Cases 7 and 12 from the 1964 Niigata earthquake. Çetin's relationship correctly classified Case 7 but also misclassified Case 12. However, Çetin used the time history recorded at the Kawagishi-cho apartments, where liquefaction occurred, to estimate a_{max} . To avoid the potential for underestimating CAV_5 from a liquefaction record, CAV_{5surf} for these cases was estimated from Kramer and Mitchell's attenuation relationship, which resulted in considerably higher values than from the Kawagishi-cho record. As CAV_5 is used more and a better understanding develops about the effect of liquefaction on CAV_5 calculated from a time history, it may be possible to refine the estimates of CAV_{5surf} for these cases.

The overall shape of the curve for $P_L = 50\%$ appears reasonable compared to the shape of Çetin's 50% curve (Figure 3.6d) and the deterministic curve presented by Youd et al. (Figure 3.1). For both the CAV_5 and CSR methods, liquefaction potential is relatively insensitive to $N_{1,60,cs}$ at low IM and very sensitive to $N_{1,60,cs}$ at high IM . Also, $N_{1,60,cs}$ at high IM is approximately 30 bpf for all the methods: Çetin's curve is somewhat higher than the CAV_5 curve, Youd et al.'s is somewhat lower.

One obvious difference between the CAV_5 and CSR curves is near the origin of the plot: the intercept of CSR curves is much greater than that for the CAV_5 curves. This is likely due to the threshold that is imposed in the calculation of CAV_5 . For records with very low levels of shaking, this threshold is not exceeded except by the strongest pulses, thus there is little contribution to CAV_5 . For records with stronger shaking, a relatively smaller proportion of the record is excluded from the CAV_5 accumulation.

6.5.3 Use of the CAV_5 liquefaction relationship

The relationship described by Equation (6.10) and Figure 6.3 can be used directly to estimate the conventional liquefaction potential, that is, the liquefaction potential conditional upon a single level of seismic shaking. The procedure consists of four steps:

1. Compute $N_{1,60,cs}$ for the soil layer of interest by applying corrections for energy, overburden stress, and fines content to the measured SPT penetration resistance as described earlier in this chapter and by Idriss and Boulanger [57].

2. Estimate CAV_{5surf} from an attenuation relationship, probabilistic seismic hazard analysis, or other method. If the method of estimation results in CAV_{5rock} , compute CAV_{5surf} using a site amplification factor or linear or nonlinear site response analyses like SHAKE91 or WAVE.
3. Compute CAV_5 from CAV_{5surf} by applying r_c for the depth of interest and the K_σ correction per Equation (6.11).
4. Compute P_L using Equation (6.10).

This procedure can also be rearranged to estimate CAV_{5surf} for a desired P_L given $N_{1,60,cs}$, or to estimate the parameter, N_{req} , that was introduced in Chapter 4 for a desired P_L and CAV_5 .

6.5.4 Limitations and potential sources of bias

There are several limitations inherent in this procedure for estimating liquefaction potential:

1. Cases with significant initial shear stress have been excluded from the database; thus, the relationship described above is not applicable to sites on sloping ground or in locations where adjacent facilities or past loading history has imposed an initial shear stress to the soil profile.
2. This procedure is appropriate only for soils that are susceptible to liquefaction. Specifically excluded are soils with fines having a plasticity index greater than about 7% and organic soils. Although some plastic and organic soils are subject to significant and rapid strength loss upon earthquake shaking, their behavior is different than the liquefaction behavior of non-plastic soils. Idriss and Boulanger [57] describe alternate procedures for assessing the liquefaction potential of plastic soils, although not with CAV_5 as the IM .
3. There are a few earthquakes that contribute relatively large proportions of the case history database. It is possible that the particular characteristics of these earthquakes

have influenced the overall results. A mixed effects logistic regression model might prove useful in assessing the presence and significance of intra-event correlation.

4. There are no terms in Kramer and Mitchell's attenuation relationship to account for seismic characteristics such as directivity, fling, or source location relative to the fault hanging-wall, or for site conditions such as soil type.
5. Finally, and most importantly, the use of CAV_5 for estimating liquefaction potential is untested. The conceptual advantages of CAV_5 over CSR that were described in Chapter 3 are attractive; nonetheless, without a body of experience, this method should not be relied upon exclusively. At least one of the established CSR methods described by Youd et al., Çetin et al., and Idriss and Boulanger should be used to support the result from the CAV_5 method.

6.5.5 Deterministic CAV_5 liquefaction relationship

The probabilistic liquefaction model can be adapted for use in deterministic analyses by selecting a single probability contour to represent the boundary between liquefaction and non-liquefaction states. For the original CSR model and its later modifications, Seed and Idriss [103] located the state boundary so that it encompassed all but a few of the liquefaction points. This interpretation left few mis-classified liquefaction points but a greater number of mis-classified non-liquefaction points. The authors and the geotechnical profession judged that this arrangement was reasonable because the consequences of predicting that no liquefaction would occur when it actually did are greater than the consequences of predicting that liquefaction would occur when it actually did not.

Çetin et al. [24] noted that H. B. Seed intended that the deterministic CSR curve should represent $P_L \approx 15\%$, and Baecher and Christian [10] implied that $P_L \approx 20\%$ is a reasonable level. A review of Figure 6.3 shows that the 20% contour is very close to the lower bound of the liquefaction cases, thus should perform in a manner consistent with the intent implied by Seed and Baecher & Christian.

The deterministic relationship can be derived by rearranging Equation (6.10):

$$CAV_5 = \exp \left[\frac{N_{1,60,cs} - 4.20 \ln \left(\frac{\sigma'_{vo}}{p_a} \right) - 9.45 + 5.25 \cdot \Phi^{-1}(P_L)}{6.47} \right] \quad (6.12)$$

For $P_L = 20\%$,

$$\Phi^{-1}(0.2) = -0.84$$

Substituting this into Equation (6.12) yields an expression for the deterministic CAV_5 liquefaction relationship corresponding to the $P_L = 20\%$ curve:

$$CAV_5 = \exp \left[\frac{N_{1,60,cs} - 4.20 \ln \left(\frac{\sigma'_{vo}}{p_a} \right) - 13.87}{6.47} \right] \quad (6.13)$$

All the limitations noted in the previous section apply to this relationship.

6.5.6 Relating FS_L and N_{req}

In Chapter 4, Çetin's probabilistic relationship was used to relate the factor of safety against liquefaction, FS_L , and the SPT blow count required to resist liquefaction, N_{req} . Similarly for CAV_5 ,

$$FS_L = \frac{CAV_{5\ site}}{CAV_{5\ req}}$$

in which $CAV_{5\ site}$ is the value of CAV_5 from Equation (6.12) or (6.13) that the site can withstand before liquefaction is initiated, and $CAV_{5\ req}$ is the value of CAV_5 imposed by earthquake shaking that the site has to withstand in order to prevent liquefaction. Substituting Equation (6.12) into this expression for FS_L with the appropriate values of penetration resistance,

$$\begin{aligned} FS_L &= \frac{\exp \left[\frac{N_{site} - 4.20 \ln \left(\frac{\sigma'_{vo}}{p_a} \right) - 9.45 + 5.25 \cdot \Phi^{-1}(P_L)}{6.47} \right]}{\exp \left[\frac{N_{req} - 4.20 \ln \left(\frac{\sigma'_{vo}}{p_a} \right) - 9.45 + 5.25 \cdot \Phi^{-1}(P_L)}{6.47} \right]} \\ &= \exp \left(\frac{N_{site} - N_{req}}{6.47} \right) \\ &= 1.167^{(N_{site} - N_{req})} \end{aligned} \quad (6.14)$$

The higher value of the base in Equation (6.14) relative to the base in the equivalent CSR-based expression (Equation (4.8)) indicates that the CAV_5 liquefaction relationship is slightly more sensitive to penetration resistance than Çetin's.

6.6 Parameter uncertainty

The denominator in Equations (6.9) and (6.10) represents the total statistical uncertainty in the likelihood function; that is, it includes both parameter uncertainty, σ_p , and model uncertainty, σ_ε , as follows:

$$\sigma_E^2 = \sigma_p^2 + \sigma_\varepsilon^2$$

By determining σ_p from the uncertainty of each individual parameter in each case history, it is possible to use logistic regression to estimate the model uncertainty. The contributions to σ_p from each parameter can be estimated using the first-order second-moment (FOSM) method. Baecher and Christian [10] describe how the propagation of errors through an n -variable function, $g(x_1, x_2, \dots, x_n)$, can be estimated using the Taylor series. If all the $(x_i - \mu_{x_i})$ terms are small, their squares, cubes, and higher powers will be very small and can be ignored. The remaining first order terms can then be used to describe the first two moments (mean and variance) of g :

$$\begin{aligned} \mu_g &\approx g(\mu_{X_1}, \mu_{X_2}, \dots, \mu_{X_n}) \\ \sigma_g^2 &\approx \sum_{i=1}^n \sum_{j=i}^n \text{cov}(X_i, X_j) \frac{\partial g}{\partial x_i} \frac{\partial g}{\partial x_j} \end{aligned}$$

in which cov is the covariance operator. Noting that $N_{1,60,cs} = N_{1,60} + \Delta N_F$ and $CAV_5 = CAV_{5surf} \cdot r_c$, Equation (6.5) can be written as

$$\hat{g} = N_{1,60} + \Delta N_F - \theta_1 \ln CAV_{5surf} - \theta_1 \ln r_c - \theta_2 \ln \sigma'_{vo} - \theta_3$$

Since \hat{g} contains all the parameters of the likelihood function, the parameter variance, σ_p^2 , equals the variance of \hat{g} , $\sigma_{\hat{g}}^2$, which can be expressed using the FOSM simplification as

$$\begin{aligned}\sigma_{\hat{g}}^2 \approx & \sigma_{N_{1,60}}^2 + \sigma_{\Delta N_F}^2 + \theta_1^2 \sigma_{\ln CAV_{5surf}}^2 + \theta_1^2 \sigma_{\ln r_c}^2 + \theta_2^2 \sigma_{\ln \sigma'_{vo}}^2 + 2 \text{cov}(N_{1,60}, \Delta N_F) \\ & + 2\theta_1 \text{cov}(N_{1,60}, \ln CAV_{5surf}) + 2\theta_1 \text{cov}(N_{1,60}, \ln r_c) + 2\theta_2 \text{cov}(N_{1,60}, \ln \sigma'_{vo}) \\ & + 2\theta_1 \text{cov}(\Delta N_F, \ln CAV_{5surf}) + 2\theta_1 \text{cov}(\Delta N_F, \ln r_c) + 2\theta_2 \text{cov}(\Delta N_F, \ln \sigma'_{vo}) \\ & + 2\theta_1^2 \text{cov}(\ln CAV_{5surf}, \ln r_c) + 2\theta_1\theta_2 \text{cov}(\ln CAV_{5surf}, \ln \sigma'_{vo}) + 2\theta_1\theta_2 \text{cov}(\ln r_c, \ln \sigma'_{vo})\end{aligned}$$

The following covariance pairings can be discounted because there is no physical basis for correlation: $N_{1,60}$ and CAV_{5surf} , $N_{1,60}$ and r_c , fines content and CAV_{5surf} , fines content and r_c , fines content and σ'_{vo} , CAV_{5surf} and r_c , and CAV_{5surf} and σ'_{vo} . In addition, r_c and σ'_{vo} were shown to be uncorrelated in Chapter 5. With this information, the variance of \hat{g} can be simplified to

$$\begin{aligned}\sigma_{\hat{g}}^2 \approx & \sigma_{N_{1,60}}^2 + \sigma_{\Delta N_F}^2 + \theta_1^2 \sigma_{\ln CAV_{5surf}}^2 + \theta_1^2 \sigma_{\ln r_c}^2 + \theta_2^2 \sigma_{\ln \sigma'_{vo}}^2 \\ & + 2 \text{cov}(N_{1,60}, \Delta N_F) + \theta_2 \text{cov}(N_{1,60}, \ln \sigma'_{vo})\end{aligned}$$

In the next few paragraphs, each of these components is evaluated.

Blow count variance

There are four terms relating to blow count in the relationship for $\sigma_{\hat{g}}^2$. The first, blow count variance, $\sigma_{N_{1,60}}^2$, is easily determined from the values in the last column of Table C.2 labeled as “±”. These values, most of which are from Çetin’s database, range from 0.1 to 12.2 bpf with a mean of 3.2 bpf and can be assumed to equal $\sigma_{N_{1,60}}$.

The second term, $\sigma_{\Delta N_F}^2$, is based on the fines content correction, ΔN_F , defined by Idriss and Boulanger [57]:

$$\Delta N_F = \exp \left[1.63 + \frac{9.7}{FC} - \left(\frac{15.7}{FC} \right)^2 \right]$$

in which FC is the fines content expressed as a percentage. The variance of ΔN_F can be estimated by using the FOSM method:

$$\begin{aligned}\sigma_{\Delta N_F}^2 & \approx \sigma_{FC}^2 \left(\frac{\partial \Delta N_F}{\partial FC} \right)^2 \\ & \approx \sigma_{FC}^2 \left\{ \exp \left[1.63 + \frac{9.7}{FC} - \left(\frac{15.7}{FC} \right)^2 \right] \cdot \left(\frac{2 \cdot 15.7^2}{FC^3} - \frac{9.7}{FC} \right) \right\}^2\end{aligned}$$

Values for FC and σ_{FC} are included in Table C.2. Values for σ_{FC} range from 0.0 to 23.0 percent with a mean of 2.8 percent, and values for $\sigma_{\Delta N_F}$ range from 0 to 31.5 bpf with a mean of 2.9 bpf.

The third variance term related to blow count depends on the covariance between $N_{1,60}$ and ΔN_F . This relationship has long been debated among geotechnical engineers: is the fines correction needed because fines affect the soil's penetration resistance or because fines affect the soil's liquefaction resistance at a given penetration resistance? If the former argument is true, there should be a clear correlation between $N_{1,60}$ and FC ; if the latter argument is true, the correlation will be negligible. Looking at the 191 cases in the Appendix C, the correlation coefficient for $N_{1,60}$ and FC is only -0.39—not a strong correlation. The correlation coefficient for $N_{1,60,cs}$ and FC is -0.24. This reduction suggests that fines content may have some small effect on the penetration resistance, but that the correlation (and covariance) between these two parameters is negligible.

The final variance term related to blow count depends on the covariance between $N_{1,60}$ and σ'_{vo} . Since $N_{1,60} = N_{60} \cdot C_N$ and C_N is a function of σ'_{vo} , it seems the correlation between $N_{1,60}$ and σ'_{vo} would be strong. However, the purpose of applying C_N to N_{60} in the first place is to remove the effect of overburden stress on the blow count. The effectiveness of Idriss and Boulanger's C_N correction [57] is apparent from the liquefaction database: the correlation coefficient for σ'_{vo} and $C_N = N_{1,60}/N_{60}$ is a strong -0.91, for σ'_{vo} and N_{60} it is a modest 0.39, and for σ'_{vo} and $N_{1,60}$ it is a negligible 0.19. Thus, the covariance between $N_{1,60}$ and σ'_{vo} can be ignored.

CAV₅ variance

The two variance terms related to CAV_5 are $\sigma_{\ln CAV_{5surf}}^2$ and $\sigma_{\ln r_c}^2$, both of which can be computed from values given in Table C.2. Baecher and Christian [10] describe how the variance of a log-normal distribution can be computed from the mean and variance of a normal distribution:

$$\sigma_{\ln X}^2 = \ln \left(\frac{\sigma_X^2}{\mu_X^2} + 1 \right)$$

By applying the FOSM assumption that the individual data points are reasonable approximations of the mean, $\sigma_{\ln CAV_{5surf}}^2$ can be computed from CAV_{5surf} and $\sigma_{CAV_{5surf}}$, and $\sigma_{\ln r_c}^2$ can be computed from r_c and σ_{r_c} , all of which are listed in Table C.2. Values for $\sigma_{CAV_{5surf}}$ range from 0.20 to 44.97 m/s with a mean of 8.76 m/s; values for σ_{r_c} range from 0.038 to 0.110 with a mean of 0.092.

Overburden pressure variance

The only remaining term is $\sigma_{\ln \sigma'_{vo}}^2$. Table C.2 provides data for the mean and the standard deviation of σ'_{vo} , so $\sigma_{\ln \sigma'_{vo}}^2$ can be computed as described for the CAV_5 variance terms. Values for $\sigma_{\sigma'_{vo}}$ range from 1.94 to 23.38 kPa with a mean of 5.99 kPa

6.6.1 Liquefaction relationship with parameter uncertainty removed

The evaluations in the preceding paragraphs allow the parameter variance to be stated:

$$\sigma_p^2 = \sigma_{\hat{g}}^2 \approx \sigma_{N_{1,60}}^2 + \sigma_{\Delta N_F}^2 + \theta_1^2 \sigma_{\ln CAV_{5surf}}^2 + \theta_1^2 \sigma_{\ln r_c}^2 + \theta_2^2 \sigma_{\ln \sigma'_{vo}}^2 \quad (6.15)$$

in which the individual variances have been defined above. Values of σ_p range from 0.61 to 31.5 with a mean of 5.14. This relationship is used in the denominator of the likelihood function, allowing an estimate of the model uncertainty, σ_ε , to be determined from the logistic regression along with the parameter coefficients, θ :

$$L[\theta|\mathbf{G}] = \prod_{i=1}^k \left[\Phi \left(\frac{N_{1,60,cs_i} - \theta_1 \ln CAV_{5i} - \theta_2 \ln \sigma'_{vo_i} - \theta_3}{\sqrt{\sigma_p^2 + \sigma_\varepsilon^2}} \right) \right]^{0.8} \times \prod_{j=k+1}^m \left[\Phi \left(\frac{N_{1,60,cs_j} - \theta_1 \ln CAV_{5j} - \theta_2 \ln \sigma'_{vo_j} - \theta_3}{\sqrt{\sigma_p^2 + \sigma_\varepsilon^2}} \right) \right]^{1.2} \quad (6.16)$$

Using the *mle* function in *R* to maximize Equation (6.16) yielded the coefficients listed in Tables 6.5 and 6.6, and the curves illustrated in Figures 6.5 and 6.6.

Again, the values of CAV_5 in the figures were computed as $CAV_{5surf} \cdot r_c / K_\sigma$, where the exponent for K_σ is equal to $-\theta_2/\theta_1 = -0.67$. The heavy dashed line in the figures illustrates the location of the 50% curve from Figure 6.3.

Table 6.5: Model coefficients from regression with only model uncertainty.

	θ_1	θ_2	θ_3	σ_ε
Mean	6.88	4.59	8.75	1.62
Std error	1.10	1.65	2.78	2.79
2.5% limit	4.94	1.27	2.82	-5.24
97.5% limit	9.32	7.88	13.82	5.26

Table 6.6: Correlation matrix for coefficients from regression with only model uncertainty.

	θ_1	θ_2	θ_3	σ_ε
θ_1	1.00	-0.29	-0.87	-0.32
θ_2	-0.29	1.00	0.63	0.13
θ_3	-0.87	0.63	1.00	0.33
σ_ε	-0.32	0.13	0.33	1.00

The coefficients θ_1 through θ_3 have changed by relatively small amounts from those listed in Table 6.3 but there has been a large decrease in the denominator term: from 5.25 to 1.62. This implies that most of the uncertainty in the logistic regression presented in Section 6.5 is due to parameter uncertainty and only a small amount is due to model uncertainty. This is not surprising given the relatively large uncertainties that were described for CAV_5 and $N_{1,60,cs}$. However, it is important to note that the methods for estimating parameter uncertainty, including published estimates of variance, are often very approximate. Since the model uncertainty computed in this section is simply the portion of the total uncertainty that remains after the parameter uncertainty is accounted for, the estimate of the model uncertainty can be no better than the estimates of the parameter uncertainty. A biased procedure that underestimates parameter uncertainty will result in an overestimate of model uncertainty and vice versa.

The remaining model uncertainties for the CAV_5 model and Çetin's CSR model are not directly comparable. Because of the different approaches for calculating the two IM s and their uncertainties, the model uncertainties should be considered useful only for allowing a revised estimate of total uncertainty when site data of greater or lesser quality is used for design. Newly computed values of parameter uncertainty, σ_p , can be combined with any value of model uncertainty, σ_ε , according to the procedures described in this chapter as long as σ_ε is known.

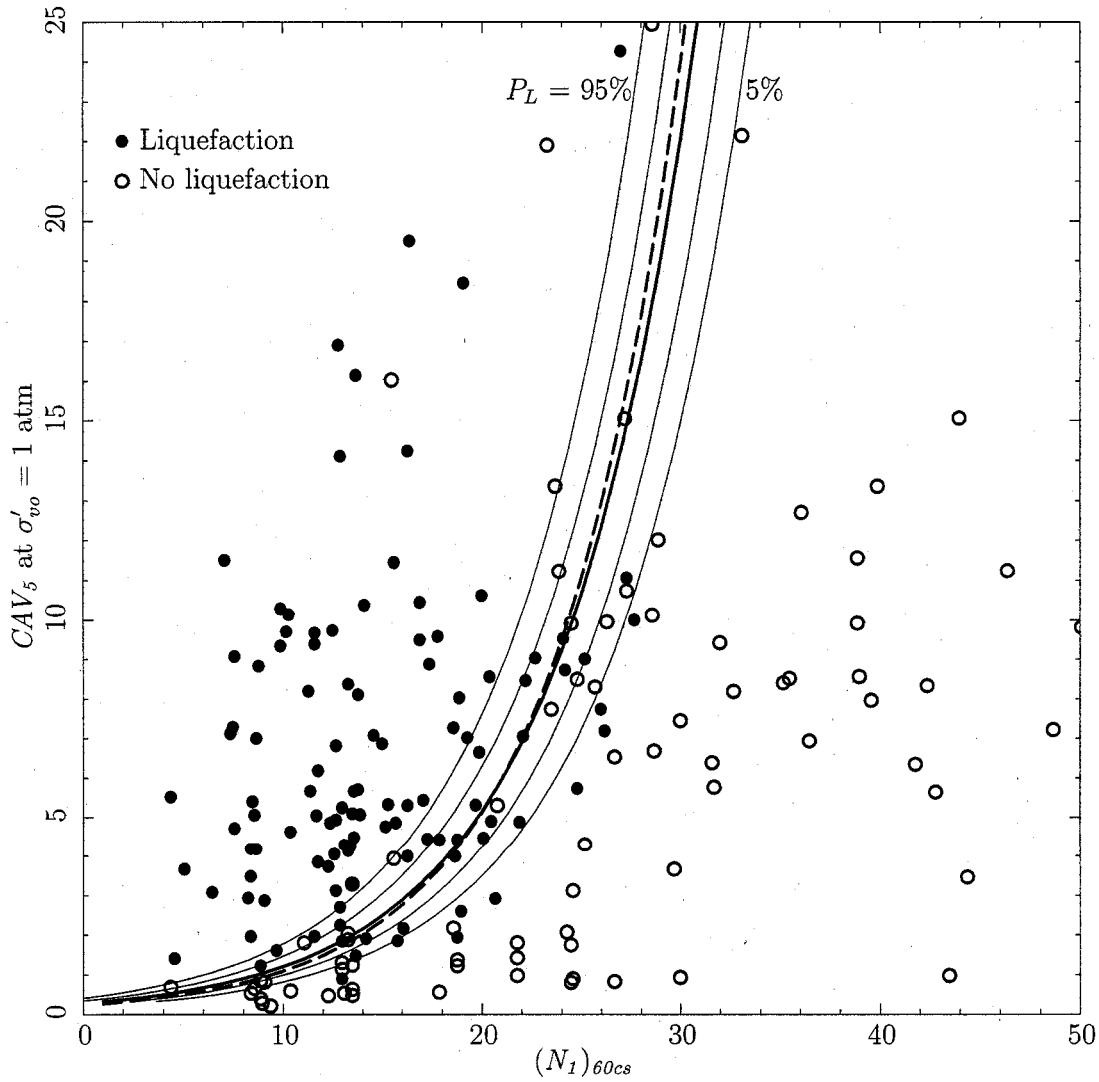


Figure 6.5: Liquefaction state boundary curves with only model uncertainty. The dashed curve is the $P_L = 50\%$ contour from Figure 6.5.

6.7 Alternative forms of the CAV_5 liquefaction model

A series of alternates to the liquefaction model presented in Equation (6.10) and Figure 6.3 were considered in an attempt to decrease the dispersion described by σ_E :

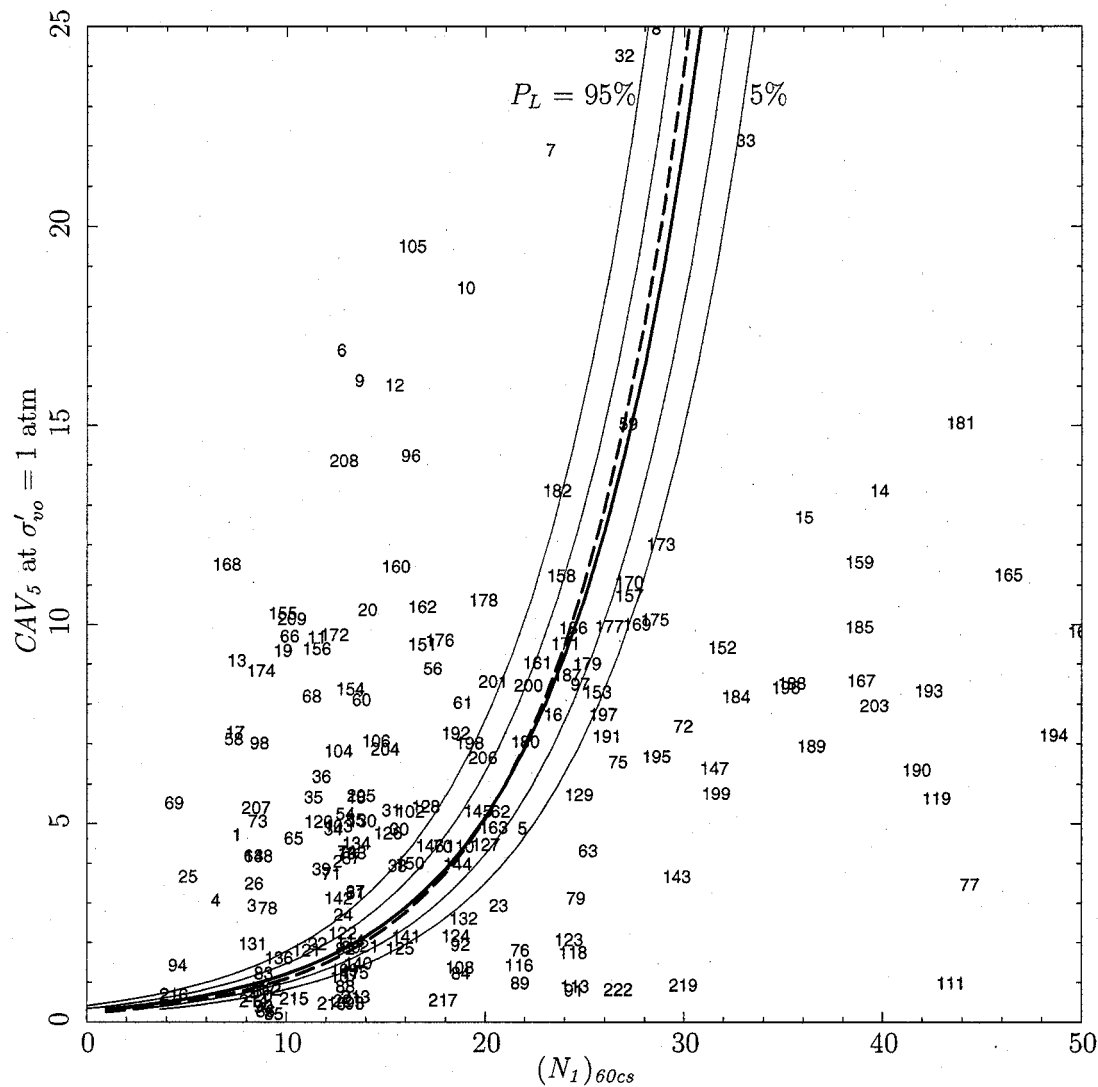


Figure 6.6: Case histories and liquefaction state boundary curves with only model uncertainty. The dashed curve is the $P_L = 50\%$ contour from Figure 6.5.

- The $N_{1,60,cs}$ and σ'_{v0} terms were replaced by Boulanger and Idriss's N_ξ , in which the K_σ correction is deterministically applied to $N_{1,60,cs}$;
- $N_{1,60}$ was included as part of the σ'_{v0} term to investigate the dependence of K_σ on relative density as described by Youd et al. and Boulanger and Idriss;

Table 6.7: Model coefficients from regression using estimates of CAV_5 only from Kramer and Mitchell's attenuation relationship.

	θ_1	θ_2	θ_3	σ_E
Mean	5.12	4.03	12.42	4.98
Std error	0.67	1.24	1.78	0.72
2.5% limit	3.88	1.56	8.66	3.80
97.5% limit	6.59	6.56	15.85	6.74

Table 6.8: Correlation matrix for coefficients from regression using estimates of CAV_5 only from Kramer and Mitchell's attenuation relationship.

	θ_1	θ_2	θ_3	σ_E
θ_1	1.00	-0.26	-0.79	0.24
θ_2	-0.26	1.00	0.69	0.04
θ_3	-0.79	0.69	1.00	-0.10
σ_E	0.24	0.04	-0.10	1.00

- $N_{1,60,cs}$ was replaced with $N_{1,60}$ and various forms of fines corrections;
- Various powers of $\ln CAV_5$ were investigated to try to improve the fit of the liquefaction state boundary.

None of these alternatives produced significantly better fits than the one described by Equation (6.9) and the coefficients in Table 6.3.

The method of estimating CAV_5 for most of the cases in the database relies on a combination of Kramer and Mitchell's attenuation relationship [77] and soil amplification factors described by Stewart et al. [115] and Choi and Stewart [25] to adjust values of CAV_{5surf} from nearby recording stations. To investigate the performance of this approach, a new logistic regression is run in which information from nearby recording stations is ignored, and values of CAV_{5rock} are all computed using Kramer and Mitchell's attenuation relationship. The result follows:

$$P_L = \Phi \left[\frac{N_{1,60,cs} - 5.12 \ln(CAV_5) - 4.03 \ln\left(\frac{\sigma'_{vo}}{pa}\right) - 12.42}{4.98} \right] \quad (6.17)$$

The equation coefficients, their standard errors, 95% confidence limits, and correlation matrix are presented in Tables 6.7 and 6.8, and the revised data points and P_L contours are illustrated in Figures 6.7 and 6.8. The exponent for K_σ is equal to $-\theta_2/\theta_1 = -0.79$.

Although the dispersion as described by σ_E is less for this data set than the original one and the standard error and correlation matrices are comparable, the maximization of

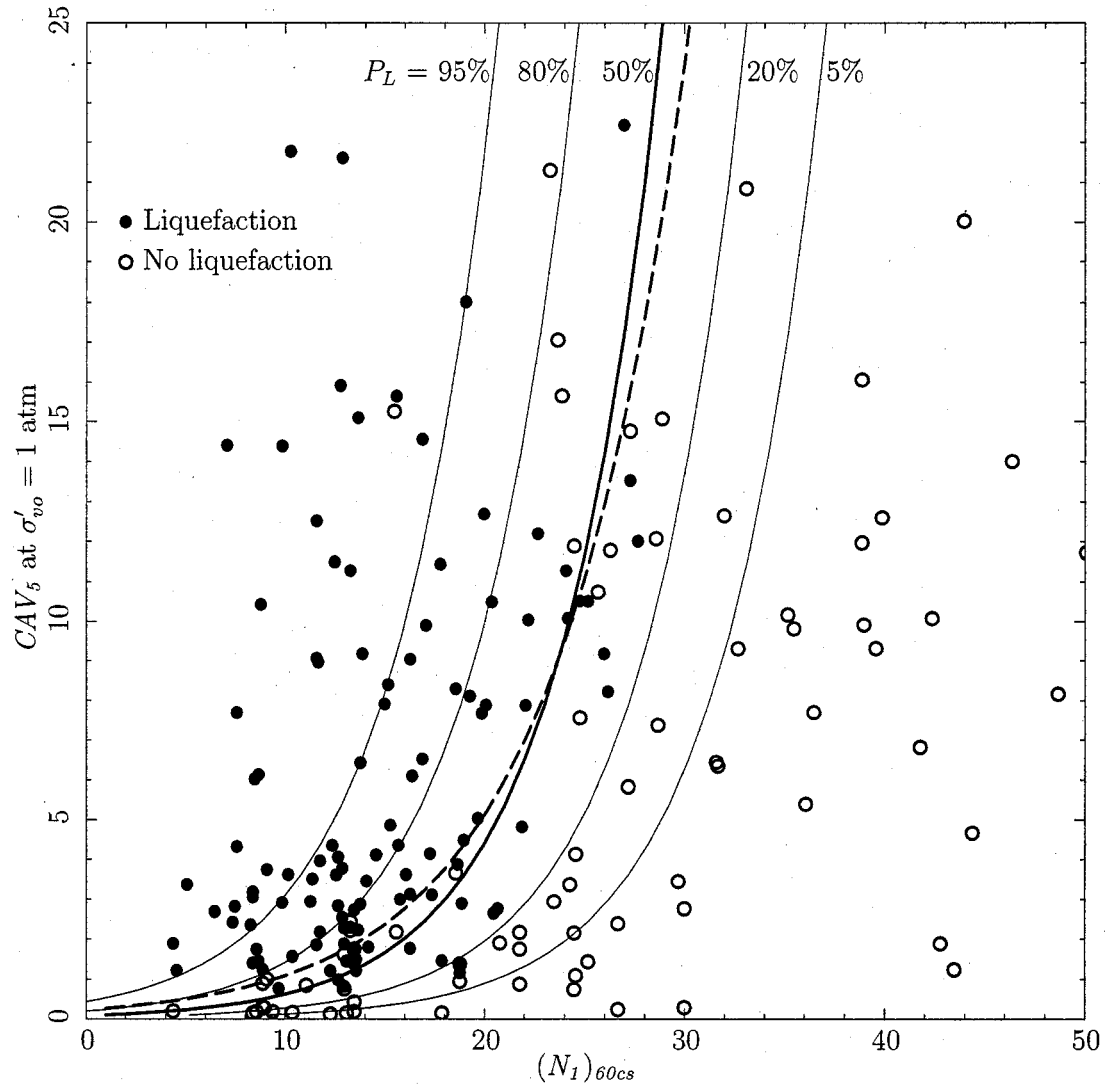


Figure 6.7: Liquefaction state boundary curves with CAV_5 estimated from Kramer and Mitchell's attenuation relationship. The dashed curve is the $P_L = 50\%$ curve from Figure 6.3.

the likelihood function is slightly better for the original data set than for this one. It is not possible to firmly state that the original model is better than this one, but the exclusion of some of the inter-event uncertainty through the use of nearby records suggests that the model from the original data set is preferable. It seems clear, however, that there is little

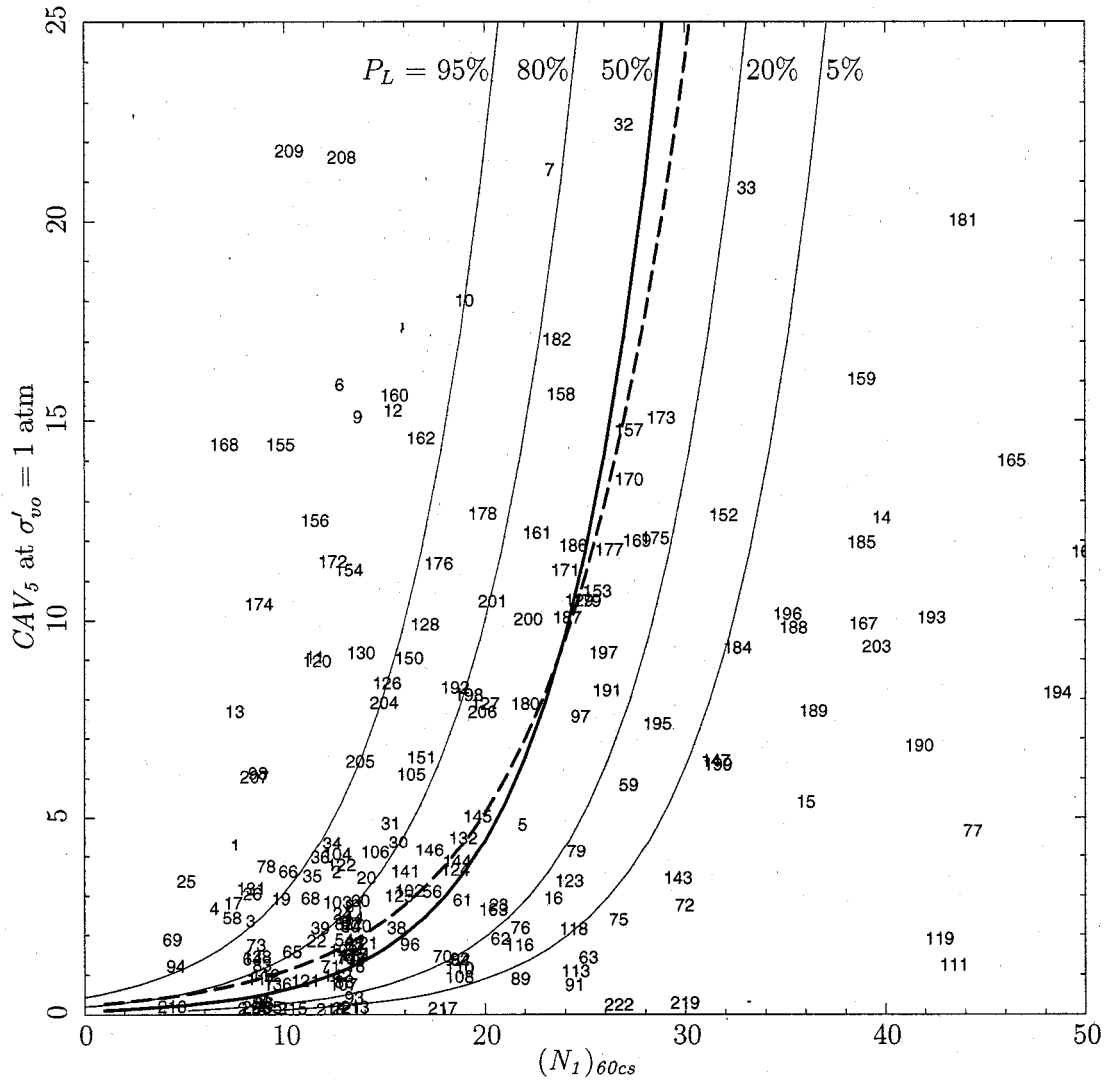


Figure 6.8: Case histories and liquefaction state boundary curves with CAV_5 estimated from Kramer and Mitchell's attenuation relationship. The dashed curve is the $P_L = 50\%$ curve from Figure 6.3.

penalty for using the simpler method of estimating CAV_{5surf} using only an attenuation relationship.

6.8 Estimation of CAV_5 at initial liquefaction

One of the advantages of integral parameters like CAV_5 over peak parameters like a_{max} is the potential for estimating its value at the time when liquefaction is initiated. Once the time of initiation is known, integration of the time history up to that time will produce CAV_5 at the initiation of liquefaction, CAV_{5L} . A well-populated data set of CAV_{5L} , $N_{1,60,cs}$, and σ'_{vo} would allow determination of the liquefaction state boundary by ordinary least squares regression rather than logistic regression, which could lead to less uncertainty in the final result. However, the final dispersion would depend on the number and quality of data points available.

The effect of liquefaction on a recorded time history is apparent. Figure 6.9a presents the north-south component of the acceleration time history from the 1987 Superstition Hills earthquake as recorded at the Wildlife Refuge site. It is apparent that the character of the time history in the first 14 s is different from that after 19 s; piezometric measurements during shaking confirm that this change in character is due to the development of excess pore water pressures and the onset of liquefaction.

An objective determination of the onset of liquefaction from changes in the time history is not easily accomplished. Kostadinov et al. [70] presented a survey of various methods for predicting liquefaction based on the study of strong motions. Most of the methods consider ratios of various parameters such as peak horizontal acceleration, velocity, or displacement; maximum spectral intensity; Arias Intensity; vertical acceleration; or change in frequency content. The primary goal of the methods was to automate the detection of liquefaction in a way that was consistent with subjective visual interpretation. None has been entirely successful, though, and there is no agreement on which method is most appropriate.

Much of the difficulty in developing these methods is due to the scarcity of data. The Wildlife record is ideal: time histories were recorded above and below the layer in which liquefaction occurred, and the record of excess pore water pressures enabled a comparison of the development of liquefaction with the change in character of the recorded motion. Unfortunately, data sets with this type of information are rare.

The database for this chapter includes seven liquefaction cases for which acceleration time histories were recorded at the site:

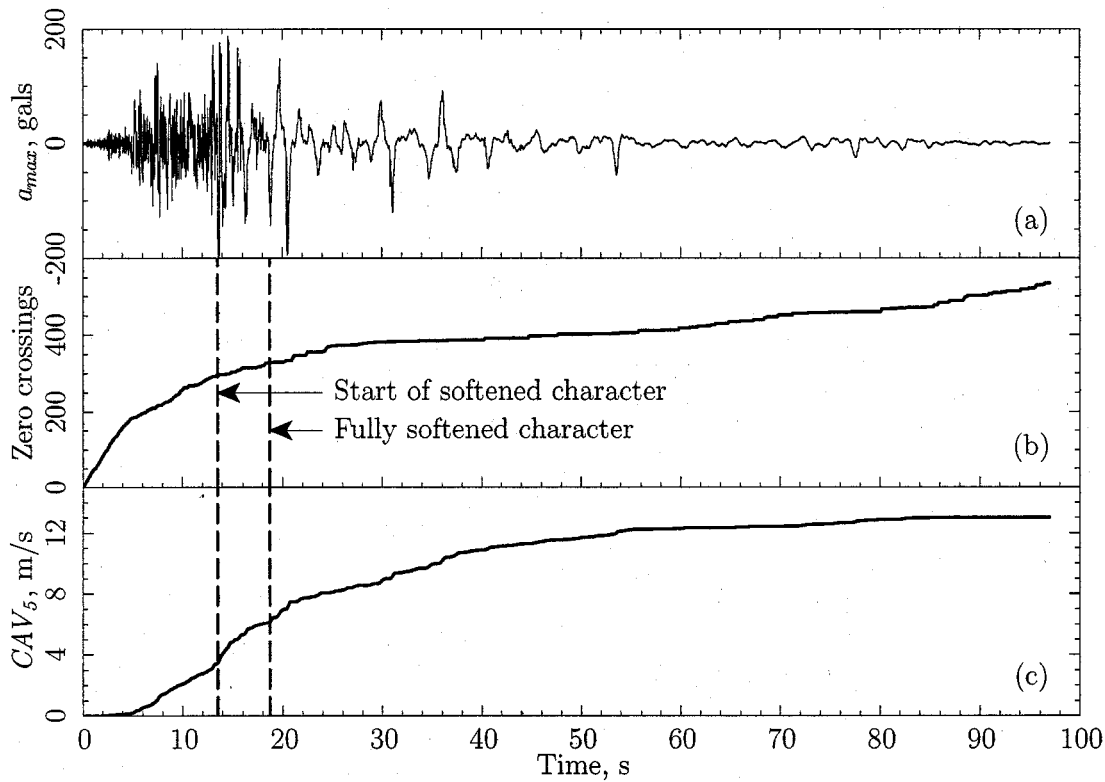


Figure 6.9: Estimation of CAV_5 at the start of liquefaction. (a) North-south component of the acceleration time history from the 1987 Superstition Hills earthquake as recorded at the Wildlife Refuge site; (b) accumulation of the number of crossings of the zero axis; (c) accumulation of CAV_5 .

- Case 110, 1987 Superstition Hills earthquake, Wildlife Refuge;
- Case 142, 1989 Loma Prieta earthquake, Treasure Island;
- Cases 145 and 146, 1993 Kushiro-oki earthquake, Kushiro Port;
- Case 156, 1995 Hyogoken-Nambu earthquake, Port Island;
- Case 208, 1999 Chi-chi earthquake, Chiaya CHY104; and
- Case 209, 1999 Chi-chi earthquake, Yuan-lin TCU110.

CAV_{5L} is estimated for these sites and compared with the liquefaction state boundary illustrated in Figure 6.3. Because the available number of cases is relatively small, CAV_{5L} is estimated subjectively using plots like those in Figure 6.9.

In addition to the time history, plots of accumulated zero crossings and CAV_5 were considered. Accumulated zero crossings is a simple proxy for change in the frequency—soil softening due to liquefaction generally reduces the high frequency content and enhances the low frequency, thus the rate of increase in accumulated zero crossings should decrease. Since CAV_5 is less influenced by high frequency motion than low-frequency motion, the shift in predominantly higher frequency to lower frequency motion should result in an increase in the rate of accumulated CAV_5 .

In Figure 6.9, there are two slope changes in the zero crossings and CAV_5 curves in the first 15 s: one at 4.7 s and one at 13.5 s. The first is not likely due to soil softening but to the first arrival of shear waves at the site. The second is more subtle on these plots but coincides with the start of pore pressure build up as described by Zeghal and Elgamal [130]. As the pore pressures increase there is a corresponding

Table 6.9: CAV_5 at the start of softening and when fully softened for liquefaction sites at which a time history was recorded.

Case	CAV_{5surf} at start of softening	CAV_{5surf} when fully softened
110	3.56	5.46
142	0.61	2.37
145	0.44	8.82
146	0.44	8.82
156	0.79	1.98
208	4.17	7.09
209	0.85	9.10

reduction in soil stiffness and time history frequency that eventually results in the long-period motions after 18.7 s that are typical for liquefied soil. Based on these indications from the zero crossings curve and from visual examination of the time history, the time at which soil softening started in Figure 6.9 is estimated to be 13.5 s, and the time at which liquefaction behavior in the time history is fully developed is estimated to be 18.7 s; the vertical dashed lines in Figure 6.9 illustrate these times.

Appendix D presents the acceleration, zero crossings, and CAV_5 time histories for both horizontal components of the seven cases listed above, and Table 6.9 lists the geometric mean of CAV_{5surf} for the two horizontal components of the record at the start of soil softening and at the development of fully softened behavior (as defined above). To compare this

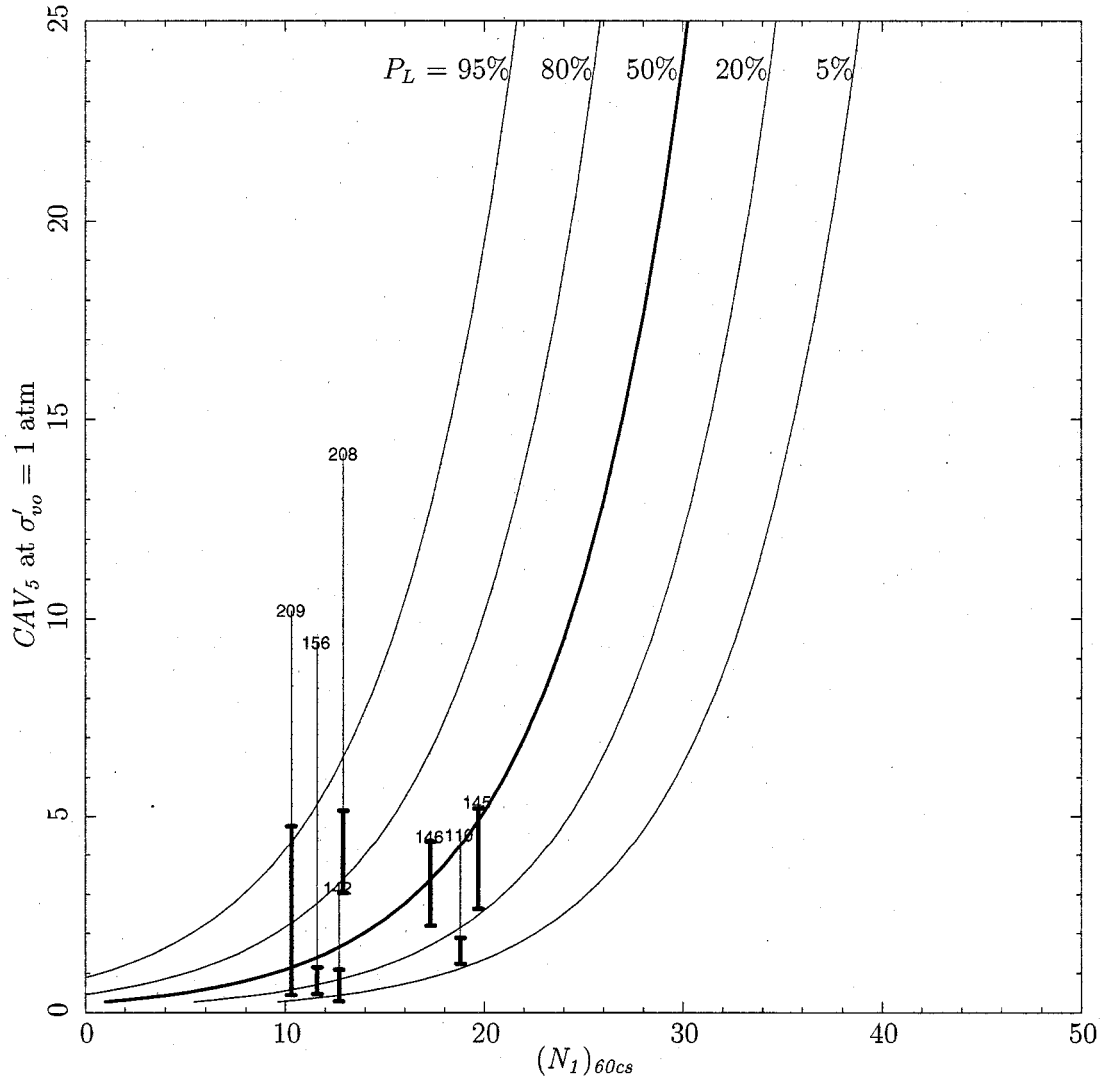


Figure 6.10: CAV_5 at the initiation of liquefaction compared with the liquefaction state boundary curves from Figure 6.3.

information with the liquefaction curves developed from the logistic regression as described in Section 6.5, these ranges of CAV_{5surf} were multiplied by r_c and K_σ (with an exponent of -0.65) and plotted on Figure 6.10. The heavy bars denote the ranges from Table 6.9 after the application of r_c and K_σ ; the location of the case numbers illustrates CAV_5 at the end of the time history.

The data from these seven points generally follow the trend from the logistic regression. The scatter is considerable, though, spanning the range between the 5% and 95% P_L contours. This may be due to the imprecise subjective method used for selecting the times of the character changes in the time history, or to the simplifications inherent in describing liquefaction with only CAV_5 , $N_{1,60,cs}$, and σ'_{vo} , or there may be other considerations that are as yet undefined.

One such possibility has to do with the definition of liquefaction that is associated with each of the methods. In the case histories used in the logistic regression, liquefaction or non-liquefaction was determined from evidence at the ground surface: if sand boils, lateral spreading or other liquefaction features were apparent, the site was classed as one at which liquefaction occurred; if there was no such evidence, it was assumed that no liquefaction occurred. Using this criterion, sites having liquefiable layers deep within the soil profile are more likely to be classed as non-liquefaction sites than sites where the liquefiable layers are close to the ground surface. Estimating the occurrence of liquefaction from changes in the character of the time history is less likely to be dependent on depth: high frequencies will be absorbed at whatever depth the liquefaction occurs, and that change in frequency content will quickly be apparent at the ground surface.

Another possibility has to do with the degree of softening required to cause each definition of liquefaction. A significant volume of water must be expelled to cause a sand boil, and such volume is unlikely to be produced until after fully liquefied behavior is well established. However, the change in frequency content may start to occur much earlier. Youd and Carter [127] noted that fully softened shaking behavior was evident at the Wildlife Refuge site when the pore pressure coefficient, r_u was only about 30%. Disparities such as these must be studied in more detail before it is possible to properly compare the results from different methods of assessing liquefaction occurrence.

6.9 Summary

This chapter presented the development of a relationship between CAV_5 , penetration resistance, and overburden stress that predicts the probability of soil liquefaction. This rela-

tionship was presented in Equation (6.10) and is repeated below:

$$P_L = \Phi \left[-\frac{N_{1,60,cs} - 6.47 \ln(CAV_5) - 4.20 \ln\left(\frac{\sigma'_{v\sigma}}{p_a}\right) - 9.45}{5.25} \right]$$

Figure 6.3 illustrates representative P_L contours from this equation.

A relationship was also developed with the parameter uncertainty separated from the model uncertainty (Tables 6.5 and 6.6, Figure 6.5), but this should only be used for developing replacements to Equation (6.10) based on different levels of parameter uncertainty; it should not be used for assessing liquefaction potential.

In this dissertation, the primary purpose for developing the CAV_5 liquefaction relationship is for computing *IM-EDP* fragility curves. The next chapter describes the implementation of Equation (6.10) into a performance-based framework.

Chapter 7

PERFORMANCE-BASED IMPLEMENTATION OF THE CAV_5 METHOD

This chapter presents the development of a method for assessing soil liquefaction potential in a performance-based framework using CAV_5 as the intensity measure. The organization is generally the same as Chapter 4 for the performance-based CSR method: a site in Seattle is considered, then ten cities across the U. S., and finally Washington State.

Of the two components in the performance-based framework—the IM hazard curve and the IM - EDP fragility curves—the latter are calculated using the CAV_5 liquefaction relationship developed in the two preceding chapters. The procedure for developing CAV_5 hazard curves is presented in the following section.

7.1 IM hazard curve

The availability of results from probabilistic seismic hazard analyses for peak ground acceleration and magnitude greatly eased the development of the CSR hazard curves in Chapter 4. Because CAV_5 is a new IM , however, there is no existing information about its exceedance rate so new PSHAs are required for the development of the CAV_5 hazard curves.

The computer program, EZ-FRISK by Risk Engineering, Inc. [95] provides a broad range of capabilities for seismic hazard analyses. It includes parameters for the seismic source zones used in the USGS PSHAs, the results of which are available on the USGS web site, and it accommodates several dozen different forms of attenuation relationships including the one used by Kramer and Mitchell for CAV_5 [77]. Thus, by incorporating into EZ-FRISK the coefficients listed in Table 6.1 and selecting the seismic source zones used by USGS, it is possible to obtain PSHA results for CAV_5 that are conceptually similar to the a_{max} results published on the USGS web site.

EZ-FRISK computes the mean annual rate of exceedance for given values of the IM . To avoid the extrapolation scheme described in Chapter 4 for the a_{max} hazard curves, 21 values

of CAV_5 from 0.1 m/s to 1000 m/s are used with EZ-FRISK to ensure that the computed return periods span the IM range from very short to at least 10,000 yrs. A cubic spline is then applied to these 21 points in log-log space to interpolate values of CAV_5 and λ_{CAV_5} at intervals of $CAV_5 = 0.2$ m/s.

7.1.1 Soil amplification factor

As noted in the preceding chapter, Kramer and Mitchell's attenuation relationship predicts CAV_5 at the surface of stiff soil or soft rock ($V_s \approx 750$ m/s). Since there is currently no attenuation relationship that directly predicts CAV_5 at the surface of softer soils like those that are normally considered in liquefaction analyses, it is necessary to apply the soil amplification factor, F_A , as described by Stewart et al. [115] to the predicted CAV_{5rock} . As in Chapter 6, F_A for spectral acceleration with a period of one second ($S_a(1.0)$) is used for CAV_5 , and for the soil profiles considered in this chapter, Stewart's coefficients for Quaternary alluvium are considered to be generally representative of a wide range of potentially liquefiable soil.

The soil amplification factor for all IM s depends upon the peak horizontal acceleration at the bedrock surface, PHA_r . Estimates of PHA_r were relatively easy to calculate for the case histories in Chapter 6 because Çetin's database included values of a_{max} . For situations in which the liquefaction potential is predicted using CAV_5 , however, the only way to implement F_A in strict accordance with the description in Stewart et al. is to estimate PHA_r at each site of interest and at each return period considered for CAV_5 . To achieve this, parallel PSHAs for CAV_5 and PHA would be necessary.

Stewart et al. noted that the PHA_r term is statistically insignificant for many of the amplification factors, including F_A for $S_a(1.0)$ and Quaternary alluvium soil. A linear form of F_A excluding PHA_r can be derived by evaluating the published form of F_A at the midpoint of the PHA_r range considered by Stewart et al. (0.01g to 1 g):

$$\ln F_A = a + b\mu_{\ln PHA_r} = \hat{a}$$

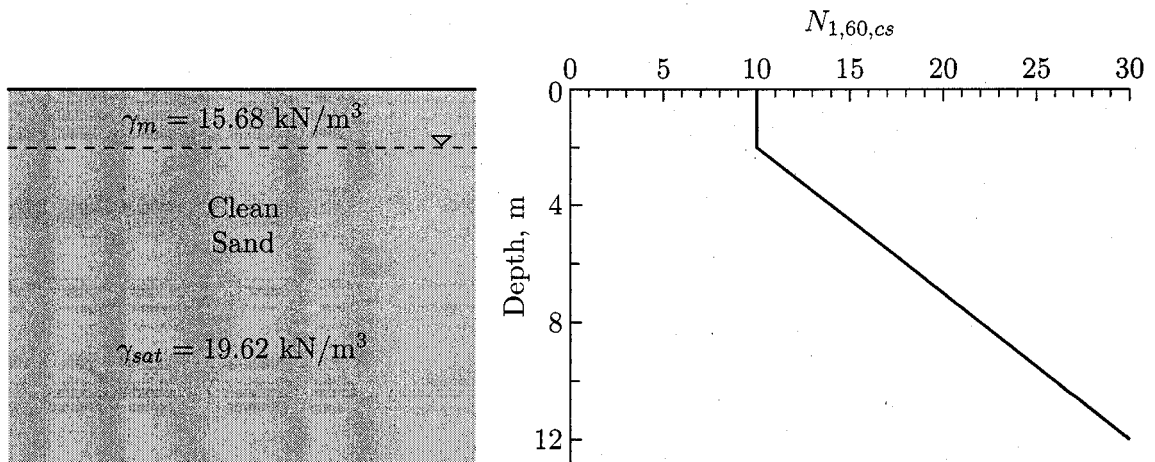


Figure 7.1: Subsurface profile used in assessing the return period of liquefaction in Seattle.

in which $a = 0.20$ and $b = -0.06$ for $S_a(1.0)$ and Quaternary alluvium, $\mu_{\ln PHA_r}$ is the mean value of PHA_r in log space ($= 0.1 \text{ g}$), and \hat{a} is the equivalent coefficient for F_A excluding PHA_r . Now,

$$\ln F_A = 0.20 - 0.06 \ln(0.1) = 0.338$$

$$F_A = 1.40$$

Thus, because of the statistical insignificance of the PHA_r term in F_A for $S_a(1.0)$ and, by inference CAV_{5surf} , a constant of 1.40 can be used to convert the value of CAV_5 at the bedrock surface from Kramer and Mitchell's attenuation relationship, CAV_{5rock} , to a value of CAV_5 at the soil surface, CAV_{5surf} . Hence, the desired CAV_{5surf} hazard curve is computed by multiplying the values of CAV_{5rock} in the hazard curve described in the previous section by 1.40.

7.2 The return period of soil liquefaction in Seattle

The site in Seattle that was analyzed using the performance-based CSR method is now analyzed using a performance-based CAV_5 method. Figure 7.1 repeats the soil profile from Chapter 4, and Figure 7.2 presents the CAV_{5surf} hazard curve for this site. For comparison, the a_{max} hazard curve is also included in Figure 7.2.

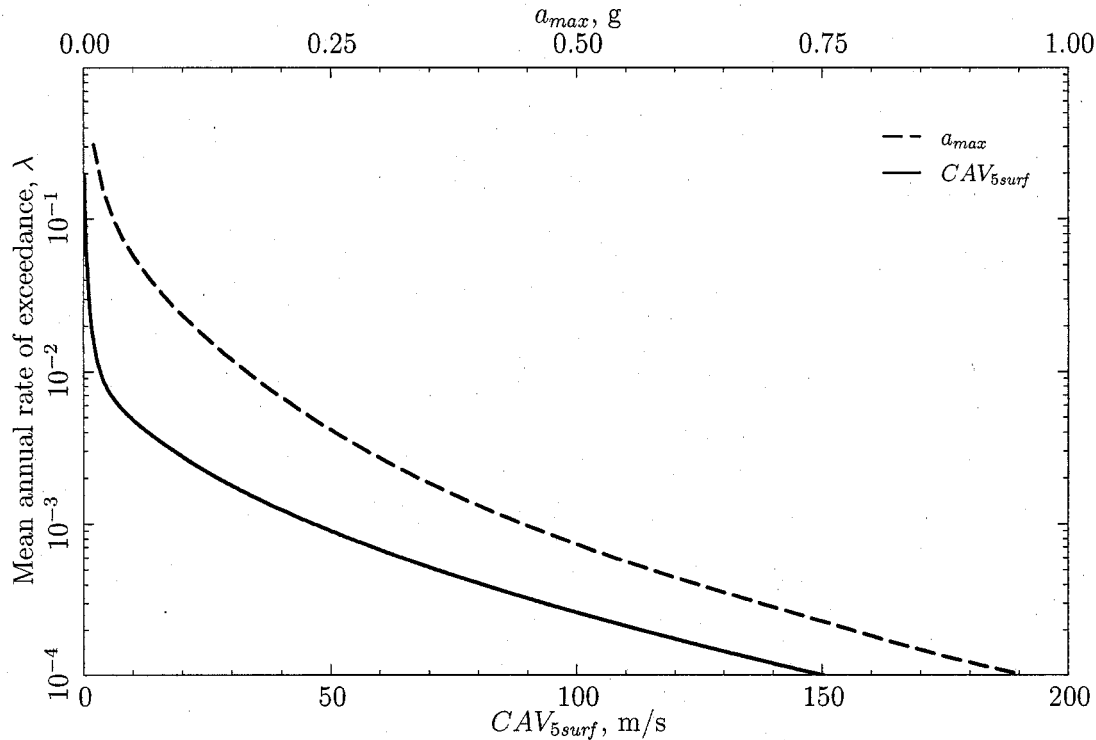


Figure 7.2: CAV_{5surf} and a_{max} hazard curves for Seattle.

The CAV_{5surf} hazard curve has much greater curvature at large exceedance rates than the a_{max} hazard curve. This is likely a result of the CAV_5 threshold: portions of the acceleration time history that are below the 5 cm/s^2 acceleration threshold contribute nothing to CAV_5 or to its hazard. For weak motions, the threshold can be significant but for stronger motions, the threshold has little effect.

One surprising result from comparing the CAV_{5surf} and a_{max} hazard curves is their ratio at a given λ : at the 475-yr and 2475-yr return periods, CAV_{5surf} is approximately 27 and 82 m/s while a_{max} is 0.34 and 0.63 g, respectively, and CAV_{5surf}/a_{max} is 80 and 130—much higher than the ratio of 22 presented in Figure 5.15. This is likely due to the CAV_5 attenuation relationship used in the PSHA rather than a problem with the predictability of CAV_5 itself. Kramer and Mitchell [77] developed the CAV_5 attenuation relationship

using records from 40 earthquakes with magnitudes ranging from 4.7 to 7.4. This is a reasonable range for most parts of the U. S.; however, the USGS currently models the Cascadia subduction zone off the west coast with earthquakes as large as M9.0, which release 250 times more energy than an M7.4 earthquake over 40 times the area. Thus, estimates of CAV_{5surf} from Kramer and Mitchell's attenuation relationship may not be reliable for areas potentially affected by large subduction earthquakes like the Seattle site. This issue will be examined in greater detail later in the chapter.

Integrating the CAV_{5surf} hazard curve from Figure 7.2 and the fragility curves computed from Equation (6.10) according to the PEER framework produces the FS_L and N_{req} hazard curves in Figure 7.3a. The hazard curves from the CSR method in Figure 4.7 are also presented for comparison. Overall, the curves from the two methods show the same trends. The greater spread in the FS_L hazard curves from the CAV_5 method suggests that the CAV_5 method is more sensitive to differences in $N_{1,60,cs}$ at this site than Çetin's CSR method. Except at very low exceedance rates, the CAV_5 method predicts lower FS_L at shallow depths with low $N_{1,60,cs}$ and higher FS_L at greater depths with higher $N_{1,60,cs}$. The relatively low values of FS_L at low exceedance rates are likely due to overly high values of CAV_{5surf} predicted by the attenuation relationship as described above.

The tighter spread in the N_{req} hazard curves from the CAV_5 method suggests that it is less sensitive to changes in depth or overburden stress at this site than the CSR method. Since σ'_{vo} is included in both methods, this implies that the combination of r_c and the K_σ correction in the CAV_5 method is more effective at accounting for depth and overburden stress variations.

The N_{req} hazard curves in Figure 7.3a show a slight curvature reversal at $\lambda_{N_{req}^{pb}} \approx 10^{-2}$ that is not apparent in the FS_L hazard curves. An independent check on the consistency of the two sets of curves can be made by recalling that Equation (6.14) relates FS_L to differences in $N_{1,60,cs}$. Starting with Equation (6.14),

$$FS_L = 1.167^{(N_{site} - N_{req})}$$

$$\ln FS_L = (N_{site} - N_{req}) \ln 1.167$$

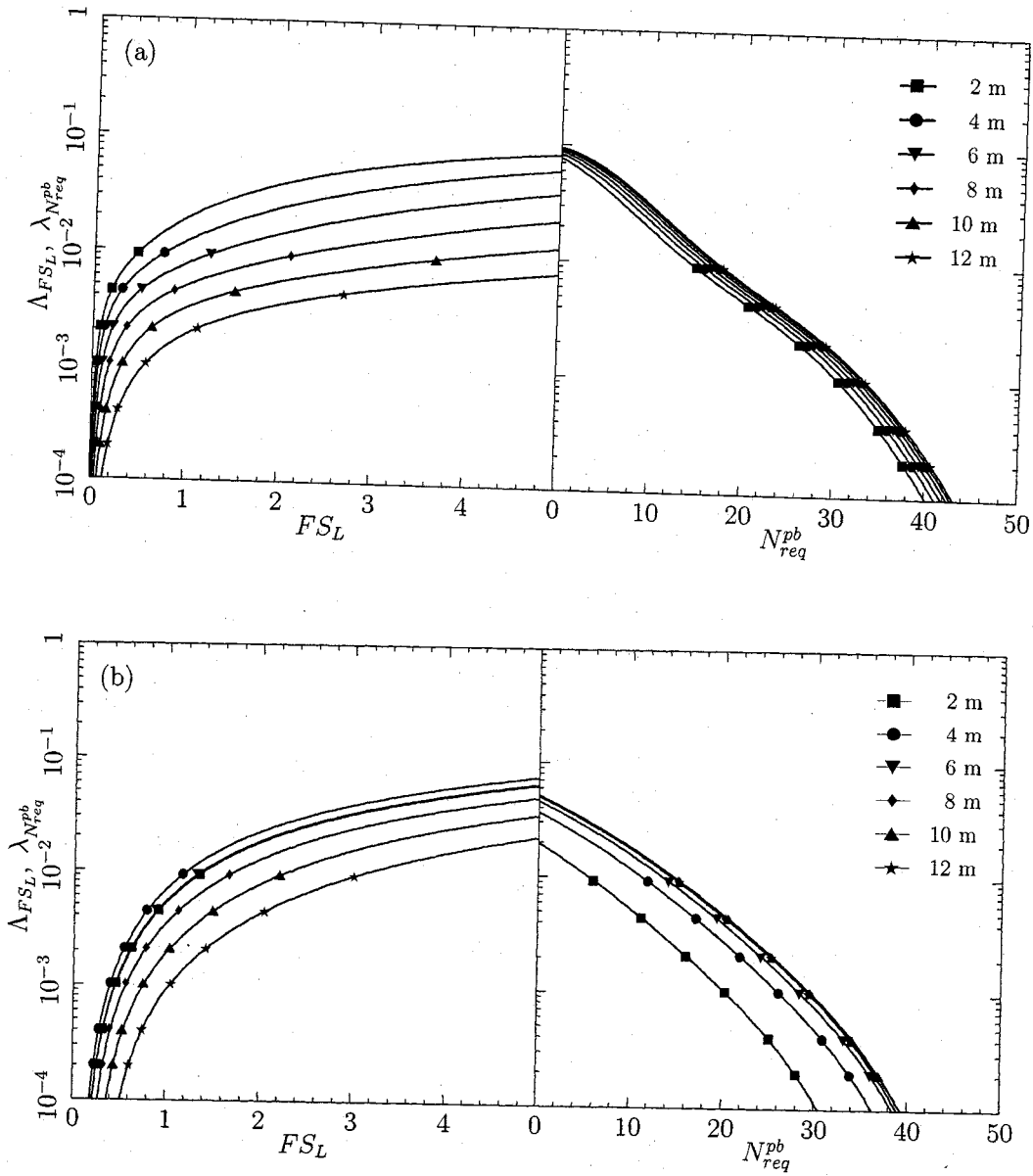


Figure 7.3: FS_L and N_{req} hazard curves at the Seattle site using the (a) CAV_5 and (b) CSR methods.

Rearranging this,

$$N_{req} = 6.47 \ln FS_L - N_{site}$$

in which FS_L and N_{req} are at the same return period and N_{site} is from the $N_{1,60,cs}$ profile in Figure 7.1. This procedure produced exact copies of the N_{req} curves in Figure 7.3a, thus confirming the consistency of the two sets of hazard curves. The presence of the curvature reversal in the N_{req} curves is likely a result of the shape of the CAV_5 hazard curve, which, as noted above, is affected by the CAV_5 threshold. It is also possible that there are differences in the PSHA from USGS and EZ-FRISK.

Figure 7.4 presents the results of the performance-based analysis in the form of depth profiles; the upper pair of plots illustrates the results from the CAV_5 method, and the lower pair repeats the *CSR* results from Figure 4.8. These FS_L curves emphasize the greater influence of increasing $N_{1,60,cs}$ with depth on FS_L from the CAV_5 method over the *CSR* method. This is especially noticeable with the less intense ground motions from shorter return periods. The greater degree of verticality in the CAV_5 N_{req} curves again shows that the stress-corrected CAV_5 method is less affected by changes in depth than Çetin's *CSR* method. At shallow depths, the CAV_5 method produces considerably higher values of N_{req} than the *CSR* method—15 to 38 bpf at 2 m compared to 6 to 28 bpf; the difference is less at greater depths—18 to 50 bpf at 12 m from the CAV_5 method compared to 15 to 36 bpf from the *CSR* method. This difference is at least partially due to the high values of CAV_5 predicted by the attenuation relationship as noted earlier in this section.

7.3 The return period of soil liquefaction across the U. S.

The soil profile in Figure 7.1 is now considered at the 10 U. S. cities from Chapter 4. Figure 7.5 presents the CAV_{5surf} and a_{max} hazard curves for the cities, and Table 7.1 lists their 475-yr and 2475-yr values of CAV_{5surf} , a_{max} , and the ratios of CAV_{5surf} to a_{max} . It is interesting to note that five highest $CAV_{5surf}:a_{max}$ ratios are for cities influenced by large magnitude earthquakes from the Cascadia subduction zone. As noted for the Seattle hazard curves, this is likely a result of the limited range of magnitudes used to develop the attenuation relationship resulting in overprediction of CAV_5 .

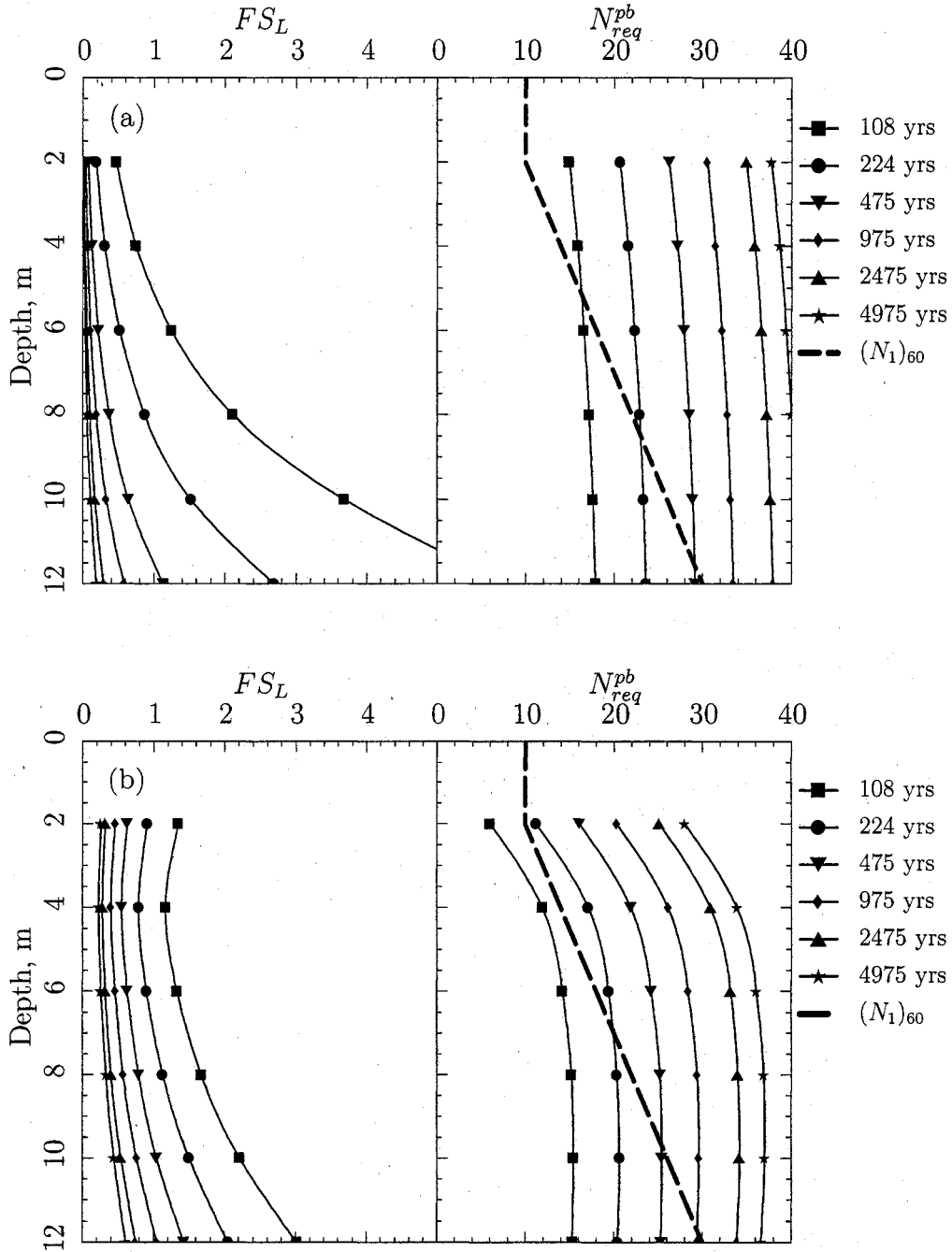


Figure 7.4: Performance-based FS_L and N_{req} depth profiles at the Seattle site from the (a) CAV5 and (b) CSR methods.

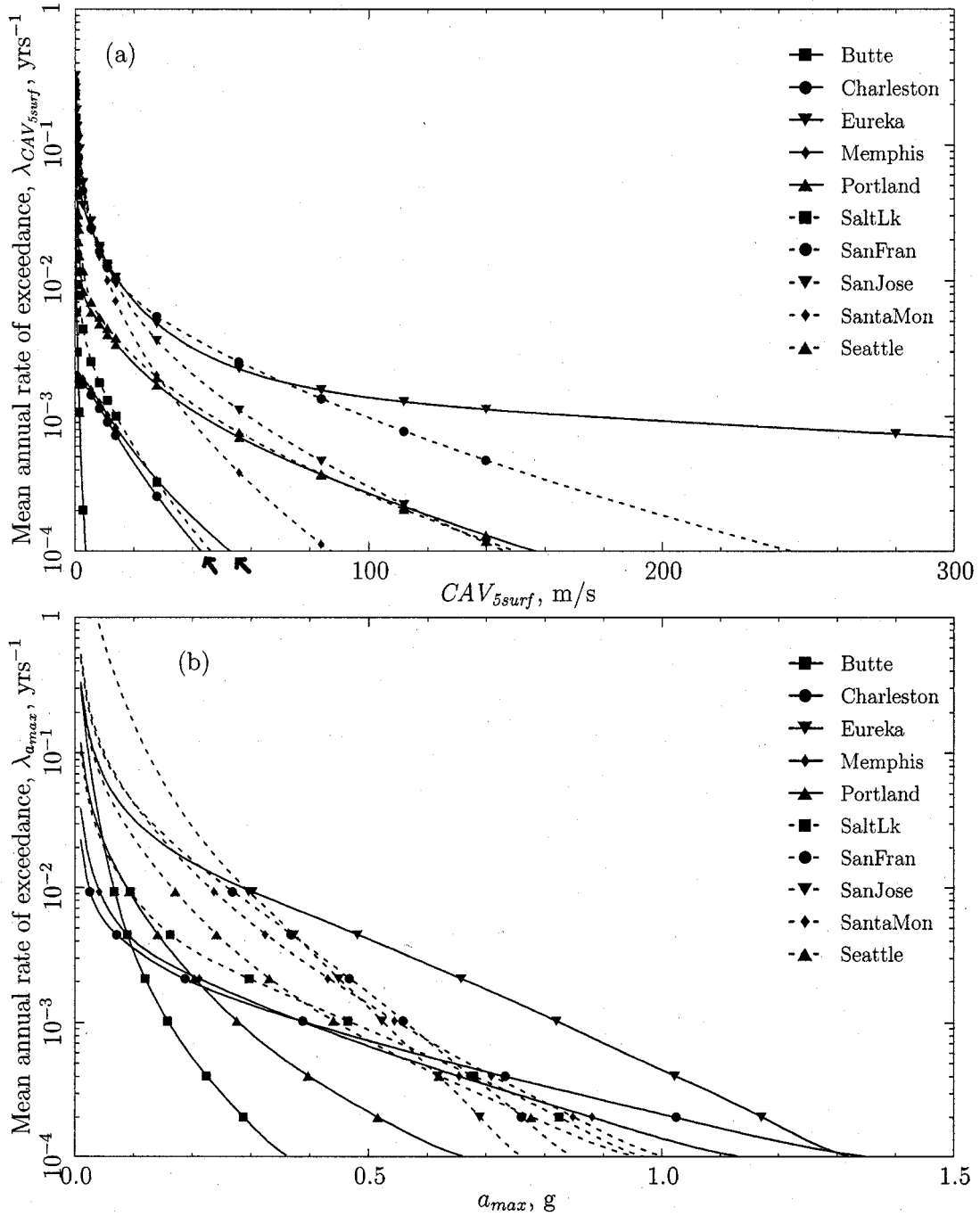


Figure 7.5: (a) CAV_{5surf} and (b) total a_{max} hazard curves for ten cities across the U. S. Both IMs have been modified by their respective rock-soil amplification factors per Stewart et al. [115]. The two small arrows along the CAV_5 axis identify the Charleston and Memphis hazard curves.

Table 7.1: CAV_{5surf} and a_{max} for 10 U. S. cities. CAV_{5surf} values are from the EZ-FRISK program; a_{max} values are from the USGS deaggregation web site.

Location	475-yr		2475-yr		a_{max}	$\frac{CAV_{5surf}}{a_{max}}$
	CAV_{5surf}	a_{max}	$\frac{CAV_{5surf}}{a_{max}}$	CAV_{5surf}		
Butte, MT	1.01	0.120	8.4	2.13	0.225	9.5
Charleston, SC	0.00	0.189	0.0	21.51	0.734	29.3
Eureka, CA	59.32	0.658	90.2	508.97	1.023	497.5
Memphis, TN	0.00	0.214	0.0	24.77	0.655	37.8
Portland, OR	23.21	0.204	84.1	79.56	0.398	199.9
Salt Lake City, UT	6.94	0.298	23.3	25.02	0.679	36.8
San Francisco, CA	63.63	0.468	136.0	149.22	0.675	221.1
San Jose, CA	39.33	0.449	87.6	88.85	0.618	143.8
Santa Monica, CA	27.35	0.432	63.3	54.82	0.710	77.2
Seattle, WA	26.01	0.332	78.3	80.46	0.620	129.8

Integrating the CAV_5 hazard curves from Figure 7.5 and the fragility curves computed from Equation (6.10) according to the PEER framework produces the FS_L and N_{req} hazard curves in Figure 7.6a. The hazard curves from the CSR method in Figure 4.13 are also presented for comparison. As noted for the Seattle site, the CAV_5 FS_L curves have greater curvature at low FS_L and are flatter at high FS_L than the CSR curves, suggesting that the CAV_5 method is more sensitive to differences in $N_{1,60,cs}$ than the CSR method. The relative positions of some of the curves are different for the two methods. For example, the Seattle FS_L and N_{req} curves from the CSR method are significantly higher than the Portland curves; according to the CAV_5 method the two are much closer. Since both cities are affected by large magnitude events from the Cascadia subduction zone, this change in relative position is more likely due to differences in the USGS and EZ-FRISK PSHAs and the behavior of the IMs than to limitations of the attenuation relationship.

The CAV_5 depth profiles for the 475-yr return period in Figure 7.7 are consistent with the interpretation above: the CAV_5 method is more sensitive to changes in $N_{1,60,cs}$ than Cetin's CSR method. As noted in the commentary for Figures 7.3 and 7.4, the CAV_5 method appears to be less sensitive to changes in depth or overburden pressure than the CSR method.

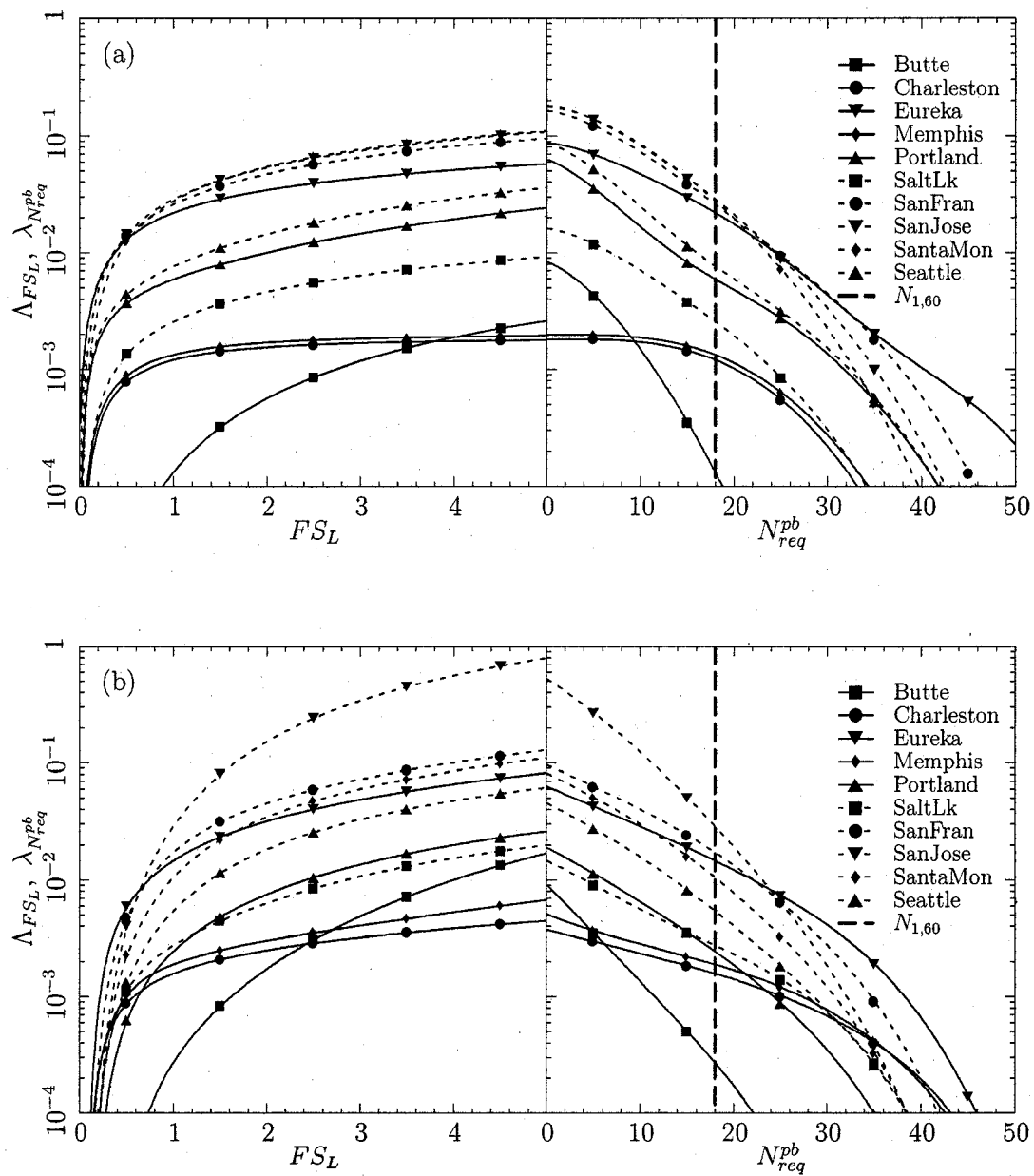


Figure 7.6: FS_L and N_{req} hazard curves at 6-m depth for ten U. S. cities using the (a) CAV_5 and (b) CSR methods.

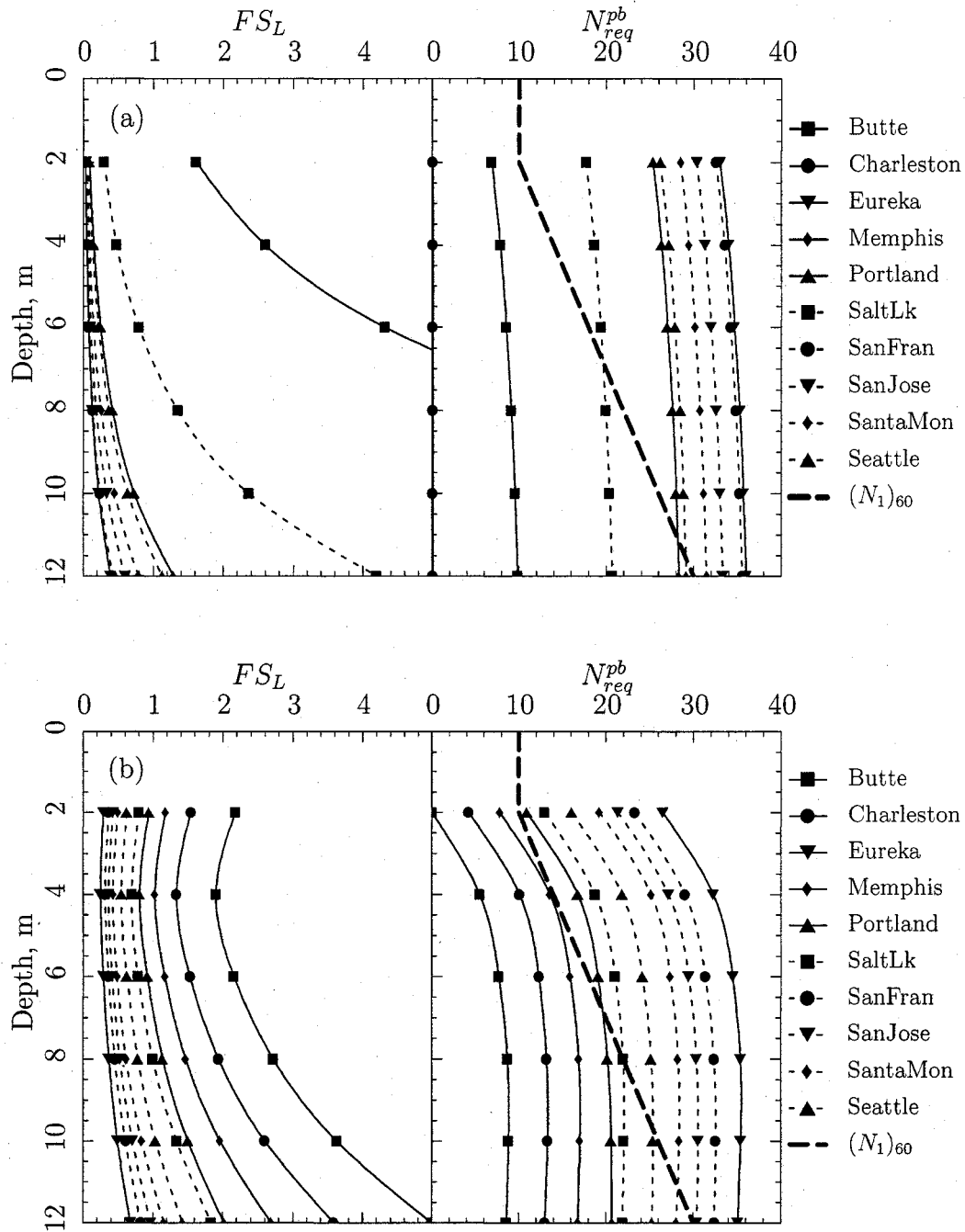


Figure 7.7: Performance-based FS_L and N_{req}^{pb} depth profiles at ten U. S. cities for the 475-yr return period from the (a) CAV_5 and (b) CSR methods.

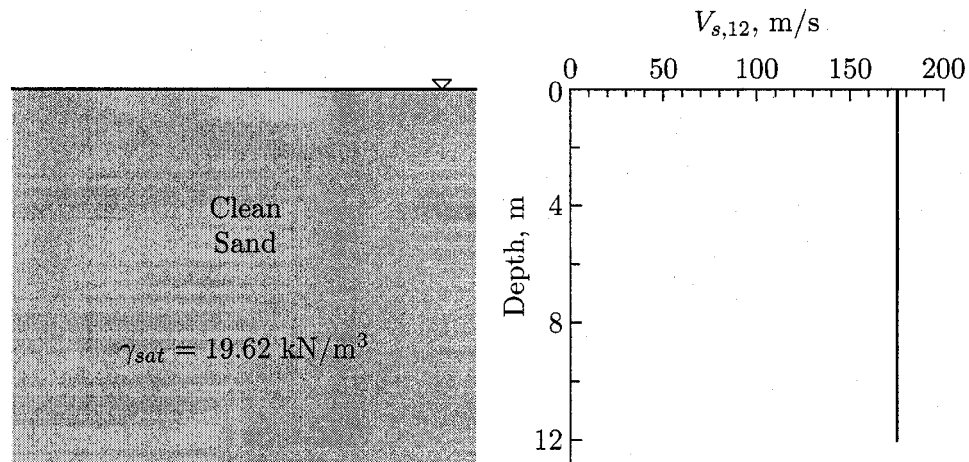


Figure 7.8: Reference soil profile for the performance-based analyses across Washington State.

The curves for Charleston and Memphis are not readily apparent in Figure 7.7a because they are aligned down the $FS_L = 5$ and $N_{req} = 0$ axes. A review of the CAV_5 hazard curves for these two cities in Figures 7.5a (denoted by arrows in the x-axis) and 7.6 shows that this occurs because the mean annual rates of exceedance of a_{max} , FS_L , and N_{req}^{pb} never exceed 0.0021 (1/475). While this implies that there is no liquefaction potential for return periods less than 475 yrs, it is actually a result of using *mean* annual rate of exceedance as the parameter for describing the hazard. Some combinations of magnitude and distance in the source zones affecting Charleston and Memphis result in higher levels of liquefaction potential, but when they are combined with all other possibilities in the PHSAs weighted averaging process, the *mean* annual rate of liquefaction is less than 1/475 yrs.

7.4 Liquefaction hazard maps for Washington State

In this section, the performance-based CAV_5 method is used to develop N_{req} maps across the state of Washington as a comparison to the maps in Chapter 4 based on the CSR method. The same reference profile (Figure 7.8) is assumed to be located at the same grid of 247 points across the state. The 475-yr and 2475-yr N_{req} contours in Figures 7.9 and 7.10 illustrate several obvious differences in the results from the two methods. Along the west

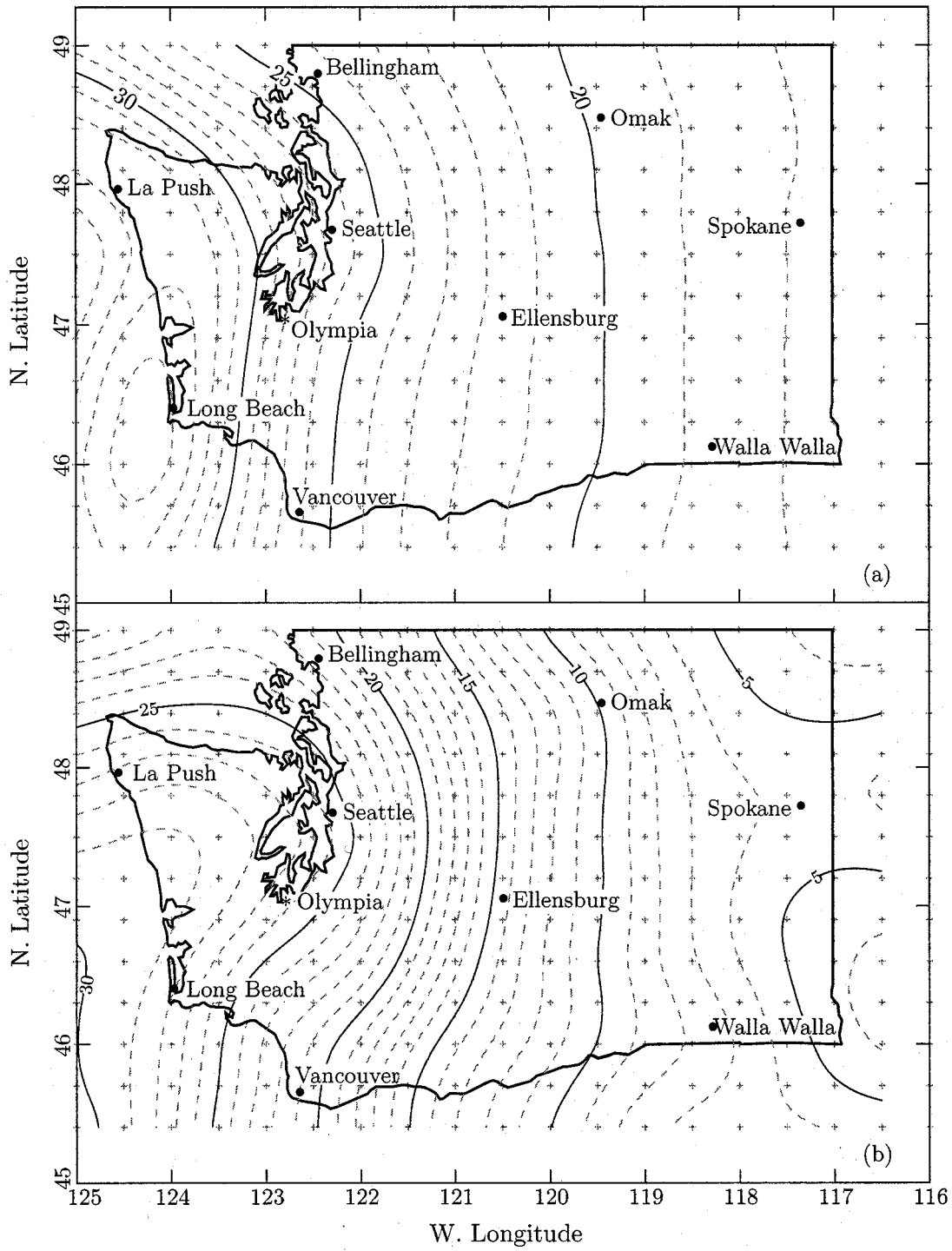


Figure 7.9: 475-yr N_{req} at 6-m depth in reference profile for Washington State from the (a) CAV_5 and (b) CSR methods.

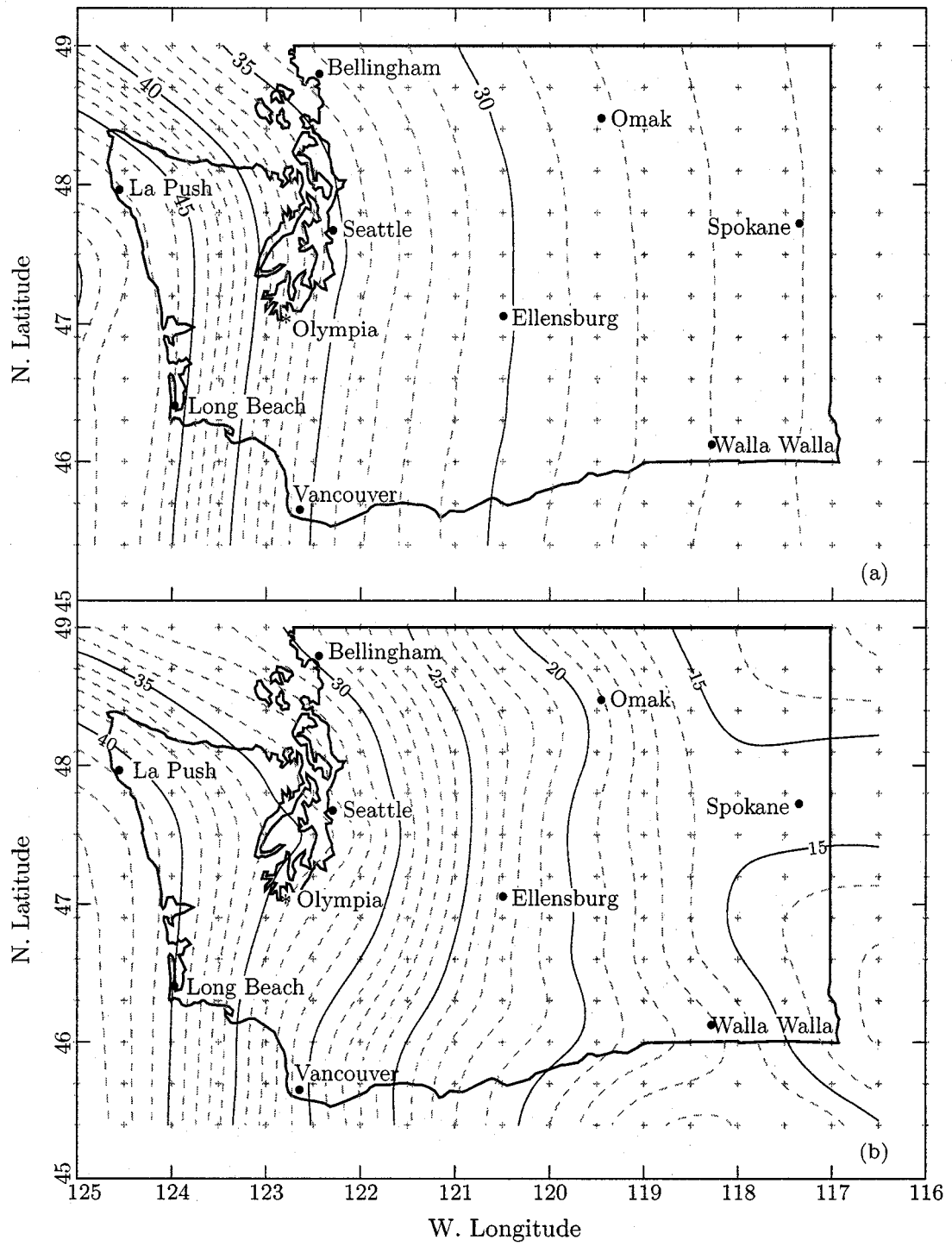


Figure 7.10: 2475-yr N_{req} at 6-m depth in reference profile for Washington State from the (a) CAV_5 and (b) CSR methods.

coast there is a local high in the contours from the CAV_5 method just offshore from Long Beach. This is not evident in the contours from the CSR method, which instead push inland further north. North of La Push, the contours from the CAV_5 method gradually sweep from a north-south orientation to a northwest-southeast direction, while the direction change in the contours from the CSR method is more extreme, especially for the 475-yr return period in which the contours actually curl back to the southwest-northeast. In the eastern part of the state, the contours from the CSR method indicate that there are local increases in seismic activity in the northeast and southeast corners of the state; these are not apparent in the contours from the CAV_5 method. It is unlikely that these overall differences in the shape of the contours are due to the different characteristics of the CAV_5 and CSR parameters or their respective attenuation relationships. Rather, they are more likely due to different interpretations of the seismic source zone characteristics by USGS and the EZ-FRISK program. This complicates a detailed comparison of the performance-based results from the two methods. Nevertheless, general observations are possible.

First, N_{req} along the coast is considerably higher from the CAV_5 method than from the CSR method—33 to 34 bpf versus 27 to 29 bpf for the 475-yr return period. Given the steepness of the upper portion of the $CAV_5-N_{1,60,cs}$ curve in Figure 6.3, this blow count difference represents a very large increase in loading intensity. While variations in the overall shape of the contours can be attributed to differences in seismic source zone characteristics, differences in the actual values of IM and the resulting N_{req} are more likely due to the performance of the attenuation relationship: the high values of N_{req} along the west coast in Figures 7.9 and 7.10 are consistent with an overprediction of CAV_{5rock} from large magnitude earthquakes.

N_{req} in the eastern portion of the state is also considerably higher from the CAV_5 method than from the CSR method—18 bpf vs. about 6 bpf near Spokane for the 475-yr return period. The absolute difference is greater than on the coast and the percentage difference is much greater. Again, the difference in N_{req} from the two methods is likely due to the CAV_5 attenuation relationship.

In general, the CAV_5 method predicts significantly higher values of N_{req} than the CSR method across the entire state of Washington except around Puget Sound. The N_{req} contours

from the *CSR* method push eastward in this area giving values of N_{req} that are nearly the same as those from the CAV_5 method. For example, the CAV_5 method predicts a 475-yr N_{req} of about 27 bpf in Seattle compared to about 26 bpf from the *CSR* method. In this area, the overprediction of CAV_{5surf} and N_{req} from the attenuation relationship is partially masked by differences in the USGS and EZ-FRISK PSHAs.

7.5 Adjustment of mapped N_{req} values for site-specific conditions

The CAV_5 -based N_{req} maps in Figures 7.9 and 7.10 were developed for the simple reference profile illustrated in Figure 7.8. To account for site-specific conditions different from those in the reference profile, an adjustment factor is developed that is similar to the *CSR* adjustment factor in Chapter 4. The adjustment, ΔN_{req} , is an additive value based on the following rearrangement of Equation (6.10):

$$N_{req} = N_{1,60,cs} = 6.47 \ln(CAV_{5surf} \cdot r_c) + 4.20 \ln \frac{\sigma'_{vo}}{p_a} + 9.45 - \sigma_E \Phi^{-1}(P_L)$$

If the site-specific constituents of this equation are evaluated in terms of the reference profile (denoted by the subscript, *ref*) an expression for the required clean sand SPT resistance for the reference soil profile can be written as

$$N_{1,60,cs,ref} = 6.47 \ln(CAV_{5surf} \cdot r_{c,ref}) + 4.20 \ln \frac{\sigma'_{vo,ref}}{p_a} + 9.45 - \sigma_E \Phi^{-1}(P_L)$$

Recalling the CAV_5 soil amplification factor from Stewart et al. [115] that was described earlier in this chapter,

$$F_A = \frac{CAV_{5surf}}{CAV_{5rock}}$$

$$N_{1,60,cs,ref} = 6.47 \ln(F_{A,ref} CAV_{5rock} \cdot r_{c,ref}) + 4.20 \ln \frac{\sigma'_{vo,ref}}{p_a} + 9.45 - \sigma_E \Phi^{-1}(P_L)$$

The required clean sand SPT resistance for a soil profile other than the reference profile can be expressed as the sum of the required clean sand SPT resistance for the reference profile and the site-specific adjustment value, ΔN_{req} ,

$$N_{1,60,cs} = N_{1,60,cs,ref} + \Delta N_{req}$$

Therefore,

$$\begin{aligned}
 \Delta N_{req} &= N_{1,60,cs} - N_{1,60,cs_{ref}} \\
 &= 6.47 \ln(F_A CAV_{5rock} \cdot r_c) + 4.20 \ln \frac{\sigma'_{vo}}{p_a} + 9.45 - \sigma_E \Phi^{-1}(P_L) - \\
 &\quad \left[6.47 \ln(F_{Aref} CAV_{5rock} \cdot r_{cref}) + 4.20 \ln \frac{\sigma'_{vo_{ref}}}{p_a} + 9.45 - \sigma_E \Phi^{-1}(P_L) \right] \\
 &= 6.47 \ln \left(\frac{F_A}{F_{Aref}} \frac{r_c}{r_{cref}} \right) + 4.20 \ln \frac{\sigma'_{vo}}{\sigma'_{vo_{ref}}} \\
 &= 6.47 \ln \frac{F_A}{F_{Aref}} + 6.47 \ln \frac{r_c}{r_{cref}} + 4.20 \ln \frac{\sigma'_{vo}}{\sigma'_{vo_{ref}}} \\
 &= \Delta N_F + \Delta N_{r_d} + \Delta N_{\sigma'_{vo}}
 \end{aligned}$$

Thus, there are three components of the site-specific N_{req} adjustment: the first based on the amplification of CAV_5 up through the soil column, the second based on the r_c profile, and the third based on the initial vertical effective stress profile. Figure 7.11 presents charts for ΔN_{r_c} and $\Delta N_{\sigma'_{vo}}$; ΔN_F can be calculated as follows:

$$\Delta N_F = 6.47 \ln \frac{F_A}{F_{Aref}} = 6.47 \ln \frac{F_A}{1.4} \quad (7.1)$$

in which F_A is the amplification factor for the specific conditions at the site.

7.6 Modification of the CAV_5 attenuation relationship

As noted earlier in this chapter, Kramer and Mitchell based their attenuation relationship for CAV_{5rock} on a suite of ground motion records from earthquakes with moment magnitudes ranging from 4.7 to 7.4. Values of N_{req} from the performance-based analyses using the CAV_5 method suggest that their attenuation relationship overestimates CAV_{5rock} at sites that are affected by larger magnitudes. While it is beyond the scope of this project to develop a new attenuation relationship for CAV_{5rock} , a modification of Kramer and Mitchell's equation for large magnitude earthquakes is examined here.

There are no available time histories from large earthquakes occurring along the Cascadia subduction zone and very few from other large subduction earthquakes. However, in 1998

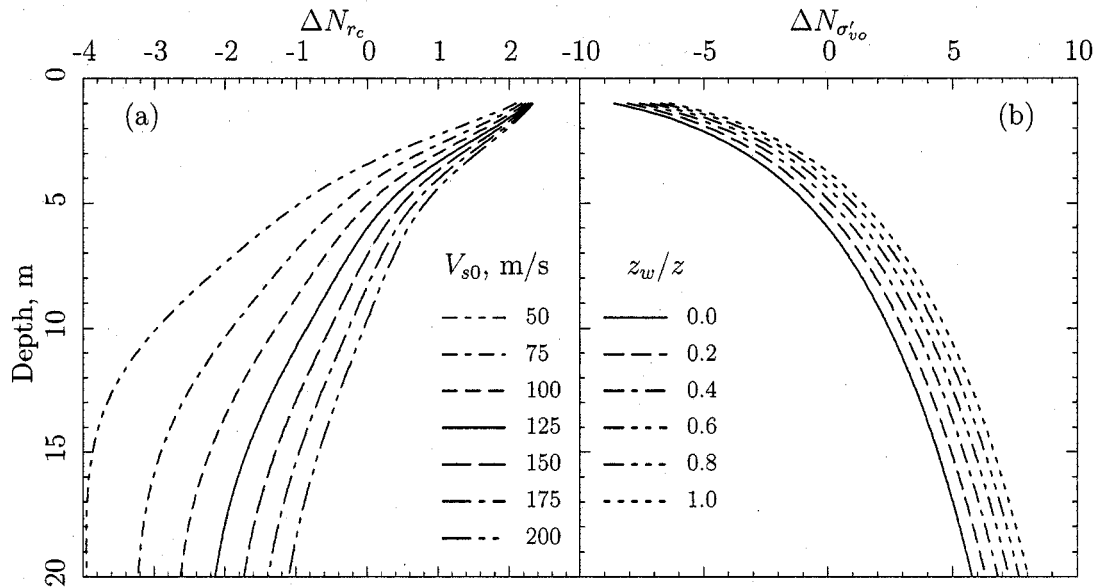


Figure 7.11: Correction factors for changes in (a) depth and shear wave velocity, ΔN_{rc} , and (b) changes in depth and groundwater table, $\Delta N_{\sigma'_{vo}}$, for CAV_5 -based N_{req} maps.

Kramer et al. [78] simulated the motion from Cascadia subduction zone earthquakes using a Green's function approach. For Magnitude 8.0, 8.5, and 9.0 events, they divided the assumed rupture surface into discrete elements and estimated time histories at 17 sites across Washington State for 30 predetermined rupture sequences using a Brune ω -square point source model. The dots in Figure 7.12 illustrate the values of CAV_{5rock} from these time histories at the rupture distances of the various sites, and the solid lines illustrate CAV_{5rock} predicted by Kramer and Mitchell's attenuation relationship for the appropriate magnitude. It is clear that CAV_{5rock} from Kramer and Mitchell's equation is greater than that from the Green's function estimates and that the overestimation becomes progressively greater as the magnitude increases. It should be noted, that the Green's function data were not available at the time the CAV_5 attenuation relationship was developed.

To investigate a potential modification of the attenuation relationship, the magnitude used in the attenuation relationship is varied until the attenuation curve fits the Green's function data; the results are illustrated with dashed lines in Figure 7.12. It is clear,

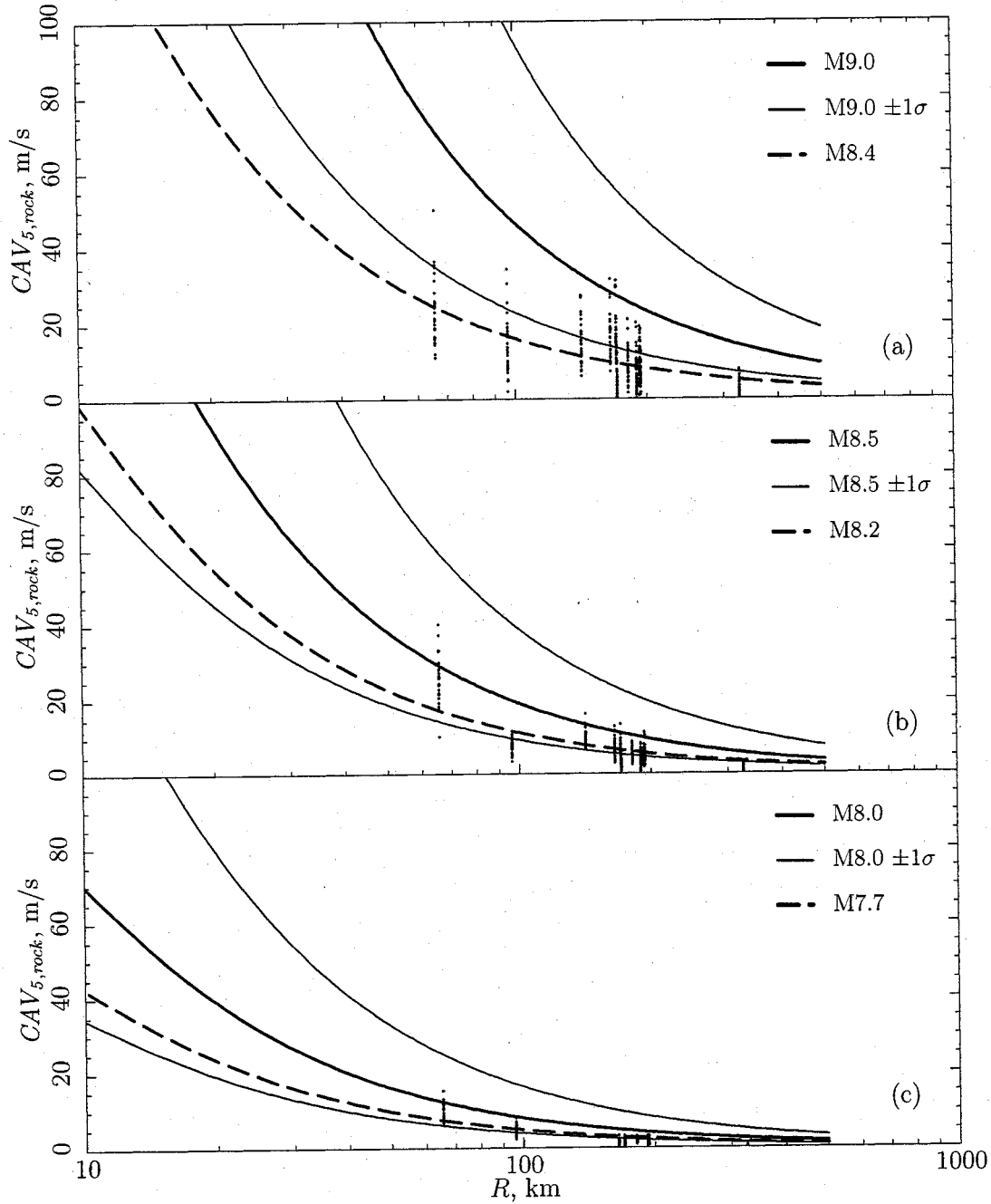


Figure 7.12: Comparison of the Kramer and Mitchell attenuation relationship (solid lines) with $CAV_{5,rock}$ estimates from (a) M9.0, (b) M8.5, and (c) M8.0 earthquakes in the Cascadia subduction zone. The dashed lines are from the Kramer and Mitchell attenuation relationship for the magnitude that fits the data points.

Table 7.2: Actual and apparent magnitudes from Green's function data for Kramer and Mitchell's CAV_5 attenuation relationship.

Apparent M_w	4.0	4.5	5.0	5.5	6.0	6.5	7.0	7.5	8.0	8.5	9.0
Actual M_w	4.0	4.5	5.0	5.5	6.0	6.5	7.0	7.5	7.7	8.2	8.4

though, that the adjusted magnitude curves do not fit the data at all distances. For the magnitudes selected in Figure 7.12, the modified attenuation curves fit the Green's function data reasonably well for R less than about 200 km, but for greater R the attenuation curve still significantly overestimates CAV_{5rock} . This suggests that a simple recalibration of Kramer and Mitchell's attenuation relationship for larger magnitudes is not entirely satisfactory, and that a full regression with an expanded dataset of earthquake motions should be considered.

By using the three actual and apparent magnitude pairs from Figure 7.12 and by assuming the actual and apparent magnitudes are equal for Magnitude 7.5 and lower, the data in Table 7.2 is compiled. A third-order polynomial regression through these data produces the following relationship for adjusting the magnitude to be used with the Kramer and Mitchell equation:

$$M_{apparent} = 0.0109M_w^3 - 0.309M_w^2 + 3.56M_w - 6.55 \quad (7.2)$$

EZ-FRISK does not have an equation form that can incorporate this adjustment but, as an alternative to attenuation relationships, it is able to interpolate IM values from a lookup table spanning ranges of source-to-site distance and magnitude. Using Equation (7.2) and Kramer and Mitchell's equation, a lookup table of CAV_{5rock} values is entered into EZ-FRISK for $M_w = 4.0$ to 9.0 ($M_{apparent} = 4.0$ to 8.4) in $M0.5$ increments and for $R = 1$ to 1000 km in one-half log cycle increments. The effect of the adjustment on the recomputed CAV_{5rock} hazard curves at the Seattle site is readily apparent in Figure 7.13; CAV_{5surf} for the 475-yr and 2475-yr return periods drops from 26 and 80 m/s, respectively, to 15 and 43 m/s. The adjusted ratios of CAV_{5surf} to a_{max} for the same return periods drop from 78 and 130 to 46 and 69. These ratios are still much higher than the average value of 22 from Figure 5.15 and somewhat higher than the values in Table 7.1 for sites that are

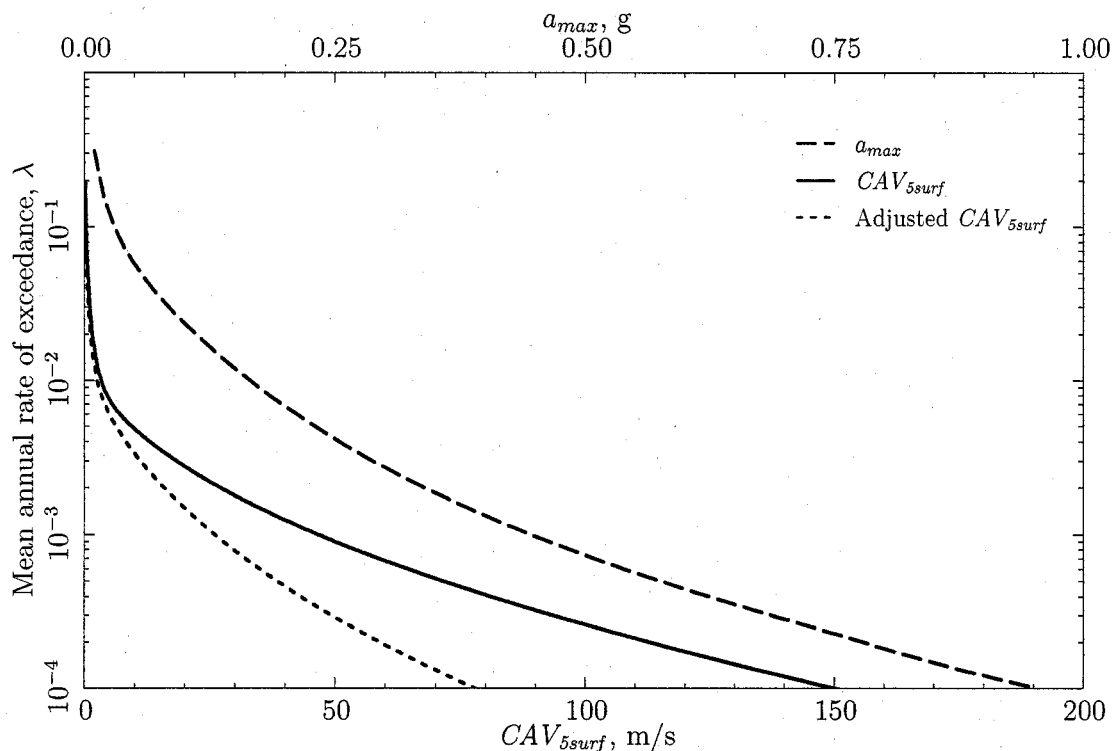


Figure 7.13: Adjusted CAV_{5surf} and a_{max} hazard curves for Seattle.

not influenced by subduction zone earthquakes such as Salt Lake City and Santa Monica. Higher ratios for the larger magnitude subduction zone earthquakes are reasonable because ground motion parameters like a_{max} often saturate at large magnitudes, especially at shorter distances, while parameters that are strongly dependent upon duration—like CAV_5 and Arias Intensity—are less susceptible to saturation [120].

Figures 7.14 and 7.15 present the 475-yr and 2475-yr original and adjusted values of CAV_{5surf} across the state. Again, the effect of the adjustment is apparent, reducing CAV_{5surf} by nearly half along the west coast and a minor amount in the eastern portion of the state. Similar trends are evident from the 475-yr and 2475-yr N_{req} contours in Figures 7.16 and 7.17, although the reduction in N_{req} is not as large along the coast as for CAV_{5surf} . At Long Beach, the 475-yr N_{req} drops from 34 bpf to about 30 bpf with the

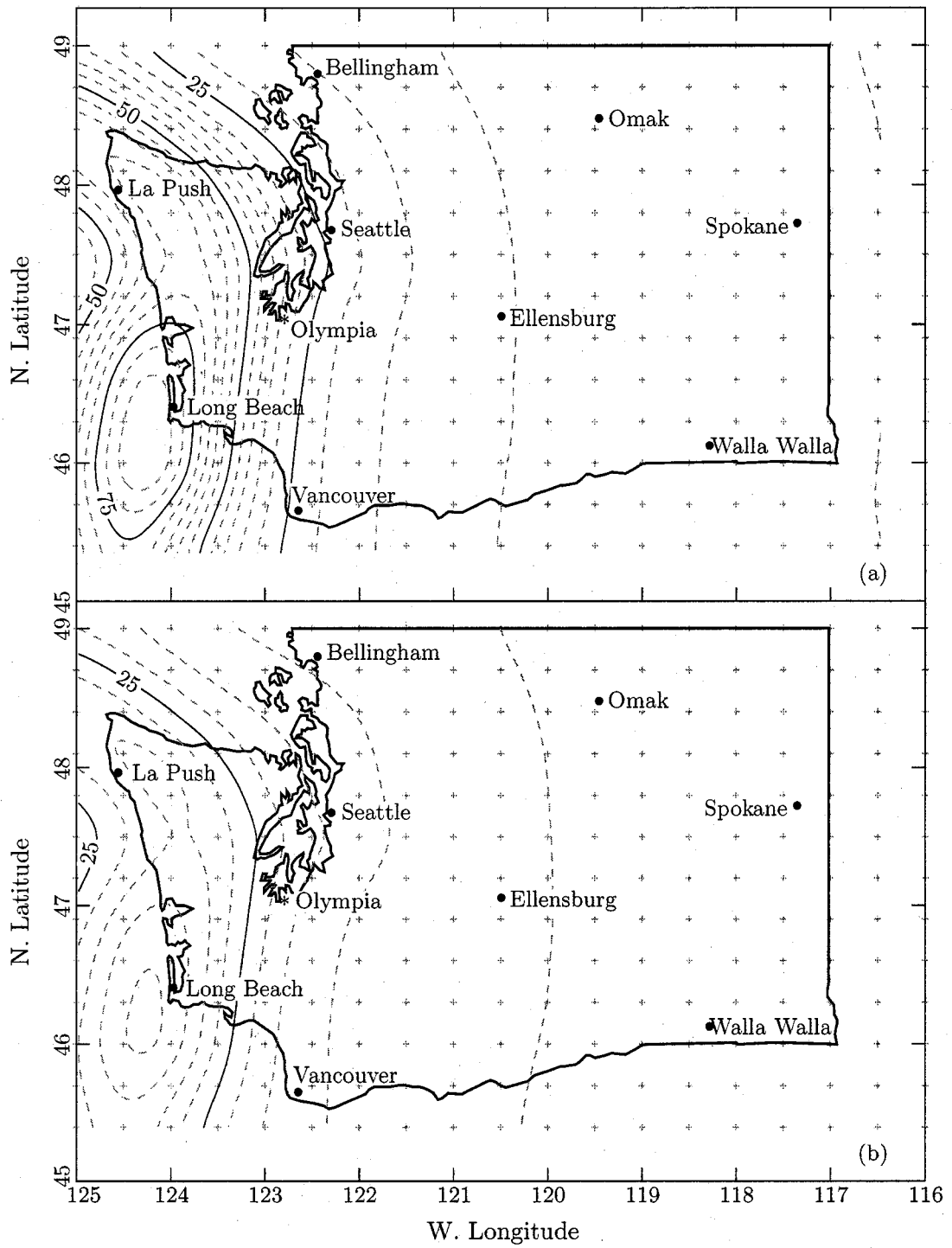


Figure 7.14: 475-yr CAV_{5surf} for Washington State from the original (a) and adjusted (b) Kramer and Mitchell attenuation relationship [77].

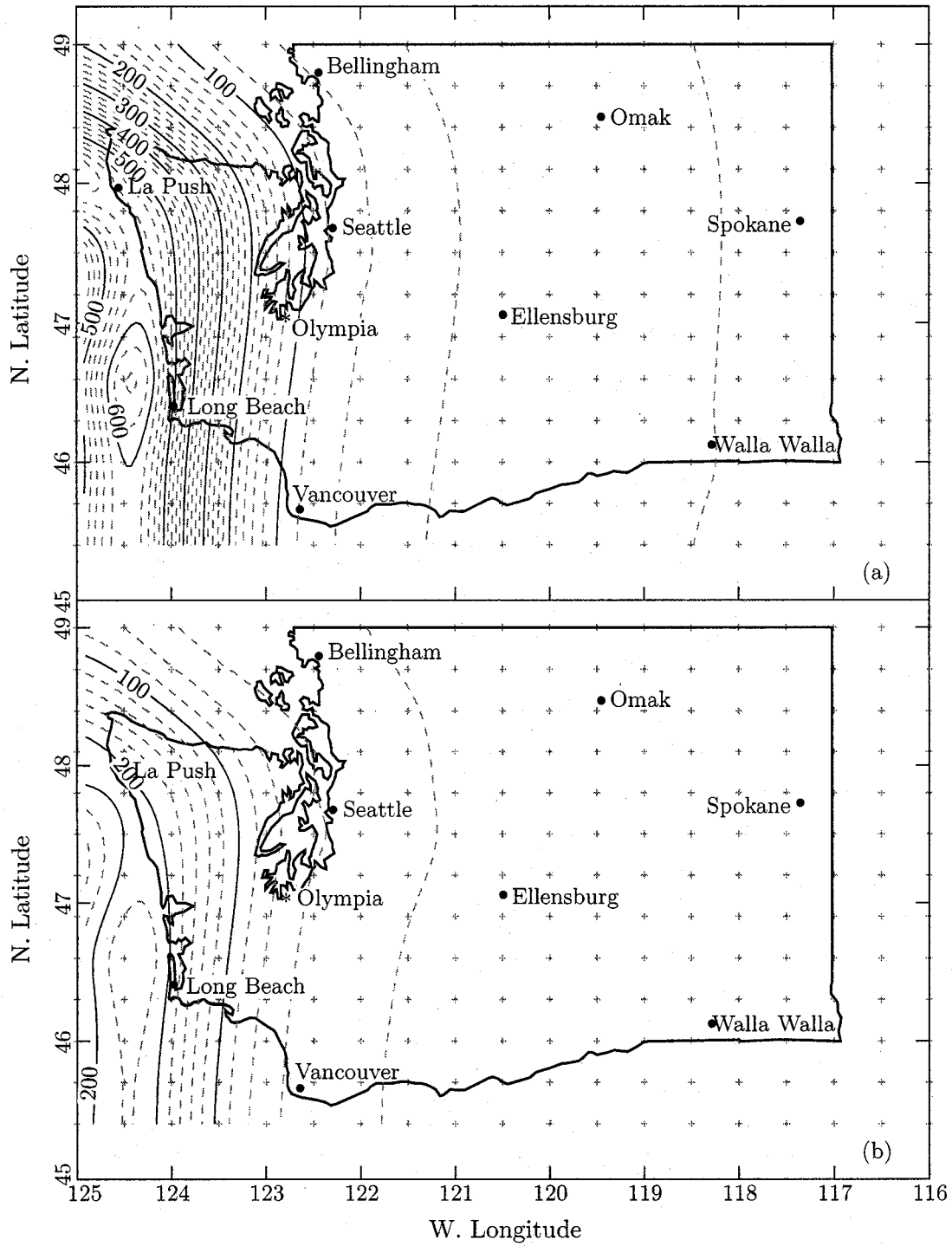


Figure 7.15: 2475-yr CAV_{5surf} for Washington State from the original (a) and adjusted (b) Kramer and Mitchell attenuation relationship.

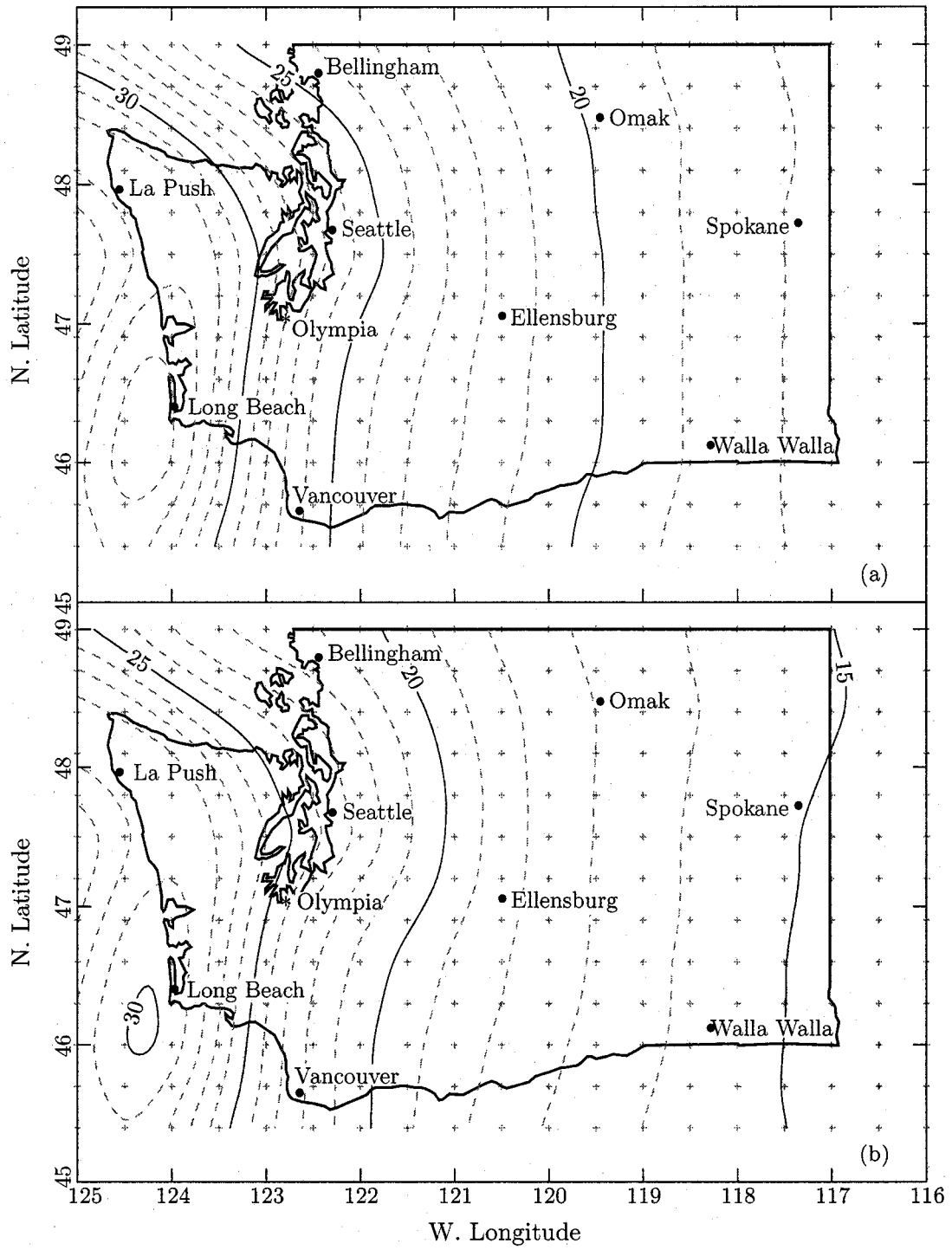


Figure 7.16: 475-yr N_{req} at 6-m depth in reference profile for Washington State from the original (a) and adjusted (b) Kramer and Mitchell attenuation relationship.

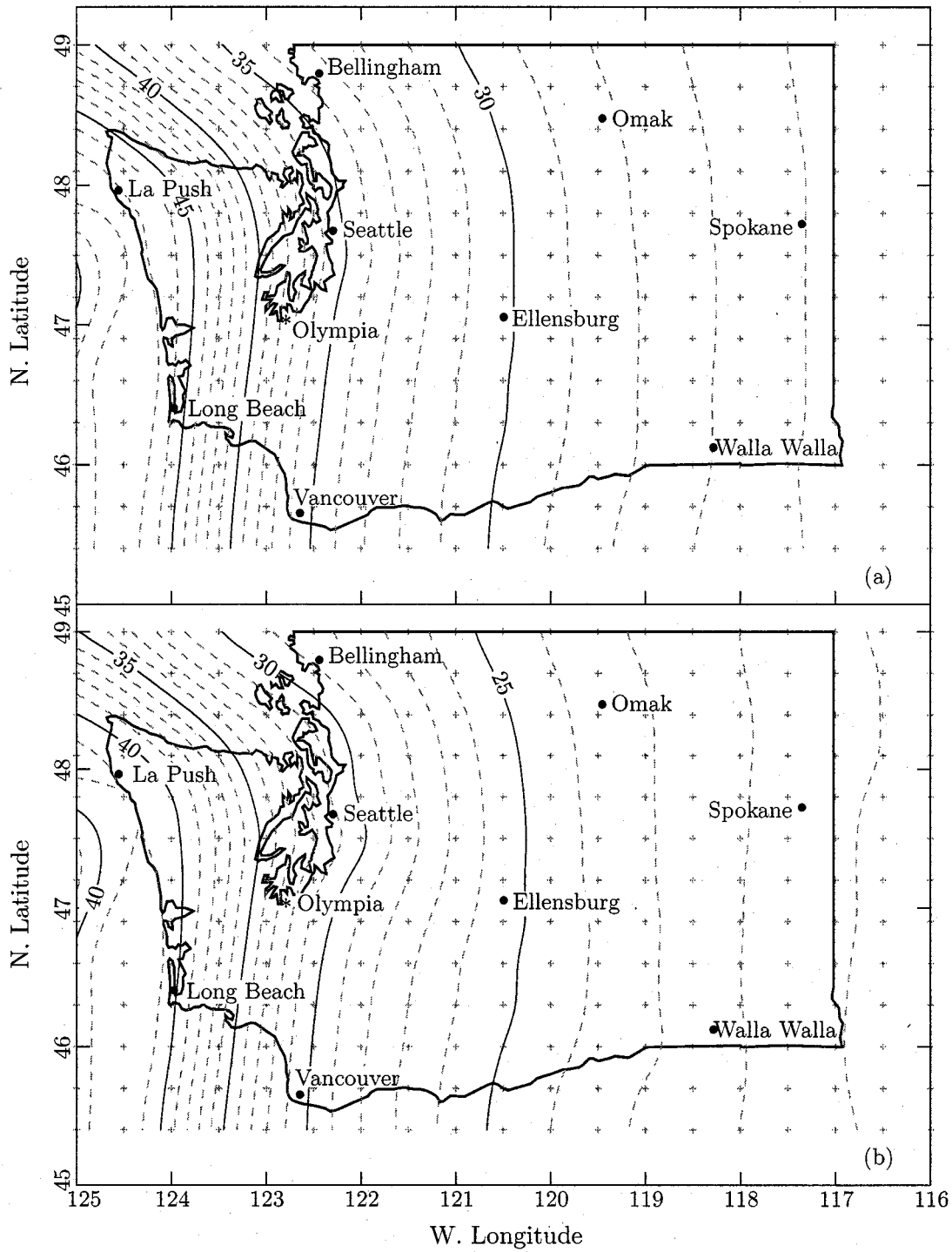


Figure 7.17: 2475-yr N_{req} at 6-m depth in reference profile for Washington State from the original (a) and adjusted (b) Kramer and Mitchell attenuation relationship.

adjusted CAV_{5surf} , which is close to the value of 28 bpf from the *CSR* method. At Spokane, however, the 475-yr N_{req} only drops from 17 bpf to 15 bpf, which is still much higher than the value of about 6 bpf from the *CSR* method.

7.7 Summary of the performance-based CAV_5 approach

In the preceding chapter, CAV_5 was shown to be an effective parameter for discriminating between liquefaction and non-liquefaction case histories, producing results comparable to those from Çetin's equation for *CSR*. Implementing the CAV_5 liquefaction equation into the performance-based framework, however, has not been entirely successful because of limitations in the CAV_5 attenuation relationship for handling large magnitude earthquakes. For sites unaffected by these large events, such as Butte, Salt Lake City, and Santa Monica, the performance-based CAV_5 results are comparable to those from the *CSR* method, producing estimates of N_{req} that are generally within about 2 bpf of those from the *CSR* method. Charleston and Memphis are exceptions to this general statement, however. The near-horizontal *EDP* hazard curves for these two cities imply that there is no mean liquefaction hazard for return periods below about 500 yrs. It is not clear if this effect is due primarily to differences in the behavior of the CAV_5 and *CSR* parameters or to differences in the USGS and EZ-FRISK PSHAs.

For sites that are affected by large magnitude earthquakes, particularly those along the Cascadia subduction zone, values of CAV_{5rock} predicted by Kramer and Mitchell's attenuation relationship [77] appear to be quite high, resulting in high estimates of N_{req} . An attempt at modifying the attenuation relationship to improve the prediction of CAV_5 for large magnitudes reduces the overestimation somewhat but not at all distances. Until there is a CAV_5 attenuation relationship available that properly deals with large magnitude earthquakes over a wide range of distances, the use of the CAV_5 method for predicting liquefaction potential should not be considered for sites that are affected by magnitudes greater than 7.5 unless there are alternate methods for predicting the ground motion intensity.

Chapter 8

SUMMARY, CONCLUSIONS, AND RECOMMENDATIONS

The goal of this research has been to improve the assessment of seismically-induced soil liquefaction potential by incorporating more comprehensively the hazard due to ground shaking and by describing the liquefaction potential in a form that can be more easily used by other stakeholders in hazard and risk analysis. This has been accomplished by implementing the simplified method of liquefaction analysis into the performance-based earthquake engineering framework described by the Pacific Earthquake Engineering Research Center. The PEER framework allows the full range of the ground shaking hazard to be incorporated into a hazard analysis of site response due to the ground shaking, which, in turn, can be incorporated into a hazard analysis of damage and, finally, into an estimate of the risk. Liquefaction assessment fits naturally into this framework because liquefaction is a form of soil response to ground shaking.

The methods of liquefaction analysis most commonly used by geotechnical engineers, including the simplified method, do not provide the information necessary for complete, accurate, and consistent hazard analyses because they consider only a single level of ground shaking and their result is conditional upon that level of shaking. For example, a conventional liquefaction assessment might use the 475-yr return period loading but this does not provide an estimate of the total 475-yr liquefaction hazard because the total liquefaction hazard at that return period is composed of contributions from all return periods of ground shaking—stronger motions that occur less frequently and weaker motions that occur more frequently. Performance-based liquefaction analyses utilize the entire ground motion hazard curve, thus, incorporate the contributions from all return periods of ground shaking into an estimate of the return period of soil liquefaction.

The PEER performance-based approach requires two key sources of information: a hazard curve describing the mean annual rate of exceedance of the full range of ground motion

intensities at the site, and a set of fragility curves describing the probability of liquefaction for a given level of ground motion intensity. The first requirement is satisfied by the results of a probabilistic seismic hazard analysis (PSHA) for the site using the intensity measure of interest, and the second is satisfied by conventional probabilistic liquefaction analyses. The limitations of conventional analyses that were noted in the preceding paragraph are overcome in the performance-based analysis by performing a series of conventional analyses using ground motion intensities across the full range of the *IM* hazard curve and weighting the contribution of each result to the liquefaction hazard according to its probability of liquefaction.

The dispersion of the probability distribution in conventional liquefaction relationships tends to amplify the resulting liquefaction hazard curve; greater dispersion elevates estimates of the liquefaction hazard for a given loading level. Thus, it is important to choose an *IM* with the best possible ability to predict liquefaction: it should have high predictability to reduce uncertainty in *IM* hazard curve, and high efficiency and sufficiency to reduce uncertainty in *IM-EDP* fragility curves. Cyclic stress ratio, cyclic strain amplitude, and a series of energy-based parameters including Arias Intensity and CAV_5 were considered; cyclic stress ratio and CAV_5 were chosen for implementation into the performance-based framework.

The widespread study and use of *CSR* in the geotechnical community for predicting liquefaction has led to a ready source of completed PSHA data for *IM* hazard curves in the continental U. S. and a choice of conventional probabilistic relationships for calculating the fragility curves. With this information, it was much easier to implement *CSR* into the performance-based framework than CAV_5 . Data from the U. S. Geological Survey was available for developing the hazard curves, but the PEER framework had to be modified to accommodate cyclic stress ratio's dependence on the vector of peak acceleration and magnitude. Instead of simply using the PSHA data for the a_{max} hazard curves, the accompanying deaggregations were also required to compute the hazard contribution due to small increments of magnitude.

Çetin's conventional probabilistic method [21, 24] was chosen to compute the fragility curves. However, an examination of Çetin's treatment of uncertainty led to the following conclusion:

The published form of Çetin's conventional probabilistic method of liquefaction assessment excludes parameter variability. This is useful for illustrating the effect of model uncertainty on its own but is not appropriate for direct use in analyzing liquefaction potential. Variability is inherent in all of the parameters associated with liquefaction assessment, and excluding that variability can lead to underestimation of liquefaction hazard.

The traditional measure of liquefaction potential in conventional analysis is either factor of safety against liquefaction, FS_L , or probability of liquefaction, P_L . However, it was concluded that

the penetration resistance (blow count) required to resist liquefaction, N_{req} , is more appropriate for use as the EDP in performance-based analysis than FS_L because the potential for liquefaction in the performance-based method is described by the mean annual rate of exceedance or return period. Including an additional factor of safety is not only redundant but it obscures the actual hazard.

Comparison of the results from the Çetin's conventional analysis and the performance-based analysis (using Çetin's method to compute the fragility curves) led to the most important conclusion from this research:

Conventional methods of liquefaction analysis produce inconsistent estimates of liquefaction hazard across different seismic environments. In Charleston and Memphis, for example, estimates of liquefaction hazard from the conventional method are high relative to the performance-base estimates, so designs in those areas are relatively costly to accommodate the high hazard. Conversely, estimates of hazard in San Jose and Portland from the conventional method are relatively low, so designs in those areas have a relatively low degree of safety.

This occurs because conventional methods consider only a single level of loading from the *IM* hazard curve. In different seismic environments, the *IM* hazard curves have different shapes and positions; thus, a single point from the curve contributes differently to the overall hazard. The performance-based method incorporates the entire *IM* hazard curve, thus providing a consistent estimate of the liquefaction potential across different seismic environments.

The similarities between PEER's performance-based framework and probabilistic seismic hazard analyses suggest that the procedure of deaggregating the hazard from a PSHA could also be done for the hazard from performance-based analyses. From deaggregation of the liquefaction hazard at ten cities across the U. S., the following conclusion was made:

Neither the mean nor the modal earthquake magnitude used in conventional liquefaction analysis consistently represents the mean or the modal (largest) contribution to the liquefaction hazard.

The increased consistency of the performance-based method across different seismic environments led to the following conclusion:

Maps of performance-based N_{req} with a given return period for a reference depth in a reference soil profile provide a clear, concise representation of liquefaction hazard over large areas. A simple procedure allows these mapped values of N_{req} to be adjusted for site-specific conditions different from the reference conditions.

This conclusion motivated the production of N_{req} maps for Washington State for the 475-yr and 2475-yr return periods and a correction procedure based on the form of the liquefaction relationship for site-specific adjustments.

The focus of the research then shifted to CAV_5 , which has several desirable characteristics as an *IM* for liquefaction assessment:

- as an integral parameter, it is influenced by the entire time history, not just the peak value;

- it incorporates a threshold that discards the very weak portions of the time history that are unlikely to contribute to pore pressure rise;
- it seems to be affected less by high frequency motion and more by low frequency motion, which is also a characteristic of pore pressure generation; and,
- as an integral parameter that increases with the progression of the time history, it is possible to compute the value of CAV_5 when liquefaction is initiated if the time of initial liquefaction is known.

As a relatively new *IM*, however, it was necessary to first develop a depth reduction coefficient, r_c , for computing CAV_5 at the depth of interest within the soil profile from CAV_5 at the ground surface. The relationship for r_c was then used with the CAV_5 attenuation relationship by Kramer and Mitchell [77] to compute CAV_5 from assembled time histories at or near Çetin's case history sites. The resulting CAV_5 database was combined with information about the penetration resistance, shear wave velocity, and overburden stress in a logistic regression model to produce a probabilistic liquefaction relationship similar in nature to Çetin's but based on CAV_5 instead of *CSR*. This provided the means for computing the fragility curves, and Kramer and Mitchell's attenuation relationship used with the computer program, EZ-FRISK, provided the means to perform the PSHAs for the CAV_5 hazard curves.

Comparison of results from the CAV_5 and *CSR* performance-based methods identified a problem with the CAV_5 attenuation relationship. For sites affected by earthquake magnitudes greater than about 7.5, the N_{req} hazard from the CAV_5 method was considerably greater than from the *CSR* method. An investigation using time histories from simulated large magnitude earthquakes along the Cascadia subduction zone confirmed the apparent overprediction of CAV_5 by the attenuation relationship and suggested that a more robust version is required.

The inability of the CAV_5 attenuation relationship to perform properly limits the application of the current form of the performance-based CAV_5 method to areas that are not affected by large magnitude ($M_w > 7.5$) earthquakes. Nonetheless, it is possible to make

the following conclusion about the suitability of CAV_5 as an IM for assessing liquefaction potential:

The overall behavior of the new probabilistic CAV_5 relationship as shown in Figure 6.3 is consistent with that from accepted CSR relationships. The uncertainty in the CAV_5 relationship as described by the denominator term in the equation for P_L , Equation (6.10), is about 25% greater than that in Çetin's CSR relationship. Because of the newness of this IM and the questionable performance of the CAV_5 attenuation relationship, this is an encouraging result, and suggests that CAV_5 still has the potential to make a valuable contribution in the assessment of liquefaction hazard as understanding of its behavior increases with use, and as improved attenuation relationships become available.

The significant effect on liquefaction potential that was caused by the CAV_5 attenuation relationship's inability to deal with large magnitude earthquakes underscores the additional demands that are imposed by the performance-based approach. Unlike conventional analyses, which use only one point on the IM hazard curve, performance-based analyses use the hazard curve across a wide range of ground motion intensities, from the very weak to the very strong. Thus, if a portion of the IM hazard curve is unreliable, the performance-based results are unreliable. This same concern applies to the IM - EDP fragility curve, which is invoked across the same range of ground motion intensities as the IM hazard curve. Thus,

the hazard and fragility curves used in performance-based analyses must be reliable across the entire range of ground motions that are of interest. This is a formidable challenge, especially for portions of the curves that are affected by large magnitude earthquakes. The scarcity of data for these large events inevitably increases the uncertainty, and yet, as the study on the CAV_5 attenuation relationship showed, the variation in predicted ground motions caused by this uncertainty can significantly affect the calculated liquefaction potential.

8.1 Recommendations for future work

The research for this dissertation has identified several issues that would benefit from future work:

1. Results from performance-based methods are different than those from conventional analyses, and the degree of difference varies across different seismic environments. Current standards for acceptable factors of safety are based on experience from the conventional method and need to be adapted for the performance-based method. This adaptation will require discussion and concurrence within the geotechnical community.
2. Because CAV_5 is an integral parameter, it offers the potential to estimate CAV_5 at the time of initial liquefaction, thus significantly reducing the uncertainty of the CAV_5 liquefaction relationship. However, there are relatively few time histories that have been recorded at liquefaction sites on which this procedure can be applied. More of these records will become available as more recording stations are installed in a variety of site conditions, and the CAV_5 liquefaction relationship should be periodically updated to incorporate the new information. Also, the potential for generating additional CAV_5 data using physical modeling (e. g. centrifuge or blast-induced loading) with suitable SPT correlations should be explored.
3. In a related matter, the current methods for examining an accelerogram and estimating the time at which liquefaction first occur are poorly established. Improved procedures are needed for accurately and repeatably identifying the time at which liquefaction is initiated to further exploit the potential of the CAV_5 method.
4. Soil amplification factors, like those described by Stewart et al. [115], are useful for estimating the effect of different soil conditions on ground motion parameters. A soil amplification factor specifically for CAV_5 should be developed to confirm or adjust the estimates of CAV_{5surf} in Section 6.2.3.

5. The existing attenuation relationship for CAV_5 appears to perform reasonably well for earthquake magnitudes less than about 7.5 but not very well for larger magnitudes like those from the Cascadia subduction zone. A more robust relationship is needed to accommodate these large earthquakes and to account for different site conditions (soil types or shear wave velocity profiles), faulting mechanisms, and near-source considerations. When this becomes available, estimates of CAV_5 for the case histories in Chapter 6 should be recomputed and the logistic regression and PSHAs rerun.

BIBLIOGRAPHY

- [1] N. N. Ambraseys. Engineering seismology. *Earthquake Engineering and Structural Dynamics*, 17(1):1–105, 1988.
- [2] R. D. Andrus and K. H. Stokoe II. Liquefaction resistance based on shear wave velocity. In T. L. Youd and I. M. Idriss, editors, *Proceedings, NCEER Workshop on Evaluation of Liquefaction Resistance of Soils*, pages 89–128, Buffalo, NY, 1997.
- [3] R. D. Andrus and K. H. Stokoe II. Liquefaction resistance of soils from shear-wave velocity. *Journal of Geotechnical and Geoenvironmental Engineering, ASCE*, 126(11):1015–1025, November 2000.
- [4] Applied Technology Council. Methodology for evaluation and upgrade of reinforced concrete buildings. Technical Report No. ATC-40, California Seismic Safety Commission, Redwood City, California, 1996.
- [5] I. Arango. Magnitude scaling factors for soil liquefaction evaluations. *Journal of the Geotechnical Engineering Division, ASCE*, 122(11):929–936, 1996.
- [6] I. Arango, F. Ostadan, J. Cameron, C. L. Wu, and C. Y. Chang. Liquefaction probability of the BART Transbay Tube backfill. In *Proceedings, 11th International Conference on Soil Dynamics and Earthquake Engineering, and 3rd International Conference on Earthquake Geotechnical Engineering*, volume 1, pages 456–462. Stallion Press, 2004.
- [7] R. J. Archuleta. Analysis of data from the Yokohama dense array and its applicability for understanding variability of ground motion in Seattle. Report for Award 03HQGR0053, Element II: Evaluate Urban Hazard and Risk, Institute for Crustal Studies, University of California, Santa Barbara, Santa Barbara, California, 2003. Accessed electronically at <http://erp-web.er.usgs.gov/reports/abstract/2003/niw/03hqgr0053.pdf>.
- [8] A. Arias. A measure of earthquake intensity. In R. J. Hansen, editor, *Seismic design for nuclear power plants*, Cambridge, Massachusetts, 1970. MIT Press.
- [9] G. M. Atkinson, W. D. L. Finn, and R. G. Charlwood. Simple computation of liquefaction probability for seismic hazard application. *Earthquake Spectra*, 1(1):107–123, 1984.

- [10] G. B. Baecher and J. T. Christian. *Reliability and statistics in geotechnical engineering*. John Wiley & Sons Inc., Chichester, West Sussex, England, 2003.
- [11] J. B. Berrill and R. O. Davis. Energy dissipation and seismic liquefaction of sands: revised model. *Soils and Foundations*, 25(2):106–118, 1985.
- [12] W. A. Bieganousky and W. F. Marcusson III. Liquefaction potential of dams and foundations, Report 2: Laboratory standard penetration test on Platte River sand and standard concrete sand. *WES Report No. 76-2*, March 1977.
- [13] D. M. Boore, W. B. Joyner, and T. E. Fumal. Equations for estimating horizontal response spectra and peak acceleration from western North American earthquakes: a summary of recent work. *Seismological Research Letters*, 68(1):128–153, 1997.
- [14] R. I. Borja, B. G. Duvernay, and C. H. Lin. Ground response in Lotung: total stress analyses and parametric studies. *Journal of Geotechnical and Geoenvironmental Engineering*, 128(1):54–63, January 2002.
- [15] R. W. Boulanger. High overburden stress effects in liquefaction analyses. *Journal of Geotechnical and Geoenvironmental Engineering*, 129(12):1071–1082, December 2003.
- [16] R. W. Boulanger. Relating K_α to relative state parameter index. *Journal of Geotechnical and Geoenvironmental Engineering*, 129(8):770–773, August 2003.
- [17] R. W. Boulanger and I. M. Idriss. State normalization of penetration resistance and the effect of overburden stress on liquefaction resistance. In *Proceedings, 11th International Conference on Soil Dynamics and Earthquake Engineering, and 3rd International Conference on Earthquake Geotechnical Engineering*, volume 2, pages 484–491. Stallion Press, 2004.
- [18] L. Cabañas, B. Benito, and M. Herraiz. An approach to the measurement of the potential structural damage of earthquake ground motions. *Earthquake Engineering and Structural Dynamics*, 26(1):79–92, January 1997.
- [19] A. Casagrande. Liquefaction and cyclic deformation of sands, a critical review. Harvard Soil Mechanics Series No. 81, Harvard University Press, Cambridge, Mass., 1976.
- [20] G. Castro. *Liquefaction of sands*. PhD dissertation, Harvard University, Cambridge, Massachusetts, 1969.
- [21] K. Ö. Çetin. *Reliability-based assessment of seismic soil liquefaction initiation hazard*. PhD dissertation, University of California, Berkeley, California, 2000.

- [22] K. Ö. Çetin, A. Der Kiureghian, and R. B. Seed. Probabilistic models for the initiation of seismic soil liquefaction. *Structural Safety*, 24(1):67–82, 2002.
- [23] K. Ö. Çetin and R. B. Seed. Nonlinear shear mass participation factor (r_d) for cyclic shear stress ratio evaluation. *Soil Dynamics and Earthquake Engineering*, 24(2):103–113, 2004.
- [24] K. Ö. Çetin, R. B. Seed, A. Der Kiureghian, K. Tokimatsu, L. F. Harder Jr., R. E. Kayen, and R. E. S. Moss. Standard penetration test-based probabilistic and deterministic assessment of seismic soil liquefaction. *Journal of Geotechnical and Geoenvironmental Engineering*, 130(12):1314–1340, 2004.
- [25] Y. Choi and J. P. Stewart. Nonlinear site amplification as a function of 30 m shear wave velocity. *Earthquake Spectra*, 21(1):1–30, February 2005.
- [26] J. T. Christian and W. F. Swiger. Statistics of liquefaction and SPT results. *Journal of the Geotechnical Engineering Division, ASCE*, 101(GT11):1135–1150, November 1975.
- [27] C. A. Cornell. Engineering seismic risk analysis. *Bulletin of the Seismological Society of America*, 58(5):1583–1606, 1968.
- [28] C. A. Cornell and H. Krawinkler. Progress and challenges in seismic performance assessment. *PEER News*, 3(2):1–3, Spring 2000. Accessed electronically at <http://peer.berkeley.edu/news/2000spring/performance.html>.
- [29] M. B. Darendeli. *A new family of normalized modulus reduction and material damping curves*. PhD dissertation, University of Texas, Austin, Texas, 2001.
- [30] R. O. Davis and J. B. Berrill. Energy dissipation and seismic liquefaction in sands. *Earthquake Engineering and Structural Dynamics*, 10(1):59–68, 1982.
- [31] R. Dobry and R. S. Ladd. Discussion to Soil liquefaction and cyclic mobility evaluation for level ground during earthquakes by H. B. Seed. *Journal of the Geotechnical Engineering Division, ASCE*, 106(GT6):720–724, 1980.
- [32] R. Dobry, R. S. Ladd, F. Y. Yokel, R. M. Chung, and D. Powell. Prediction of pore water pressure buildup and liquefaction of sands during earthquakes by the cyclic strain method. NBS Building Science Series 138, National Bureau of Standards, 1982.
- [33] EduPro Civil Systems Inc. *ProShake, version 1.1*. Accessed electronically at <http://www.proshake.com/userman.pdf>.

- [34] J. A. Egan and D. Rosidi. Assessment of earthquake-induced liquefaction using ground-motion energy characteristics. In *Proceedings, Pacific Conference on Earthquake Engineering, New Zealand*, pages 313–324, November 20–23 1991.
- [35] Electric Power Research Institute. A criterion for determining exceedance of the operating basis earthquake. Technical Report NP-5930, Palo Alto, California, July 1988.
- [36] Electric Power Research Institute. Standardization of the cumulative absolute velocity. Technical Report TR-100082, Tier 1, Palo Alto, California, December 1991.
- [37] Federal Emergency Management Agency. NEHRP guidelines for seismic rehabilitation of buildings. Technical Report No. FEMA-73, Federal Emergency Management Agency, Washington, D. C., 1997.
- [38] H. J. Gibbs and W. G. Holtz. Research on determining the density of sand by spoon penetration test. In *Proceedings, 4th International Conference on Soil Mechanics and Foundation Engineering*, volume 1, pages 35–39, 1957.
- [39] R. Golesorkhi. *Factors influencing the computational determination of earthquake-induced shear stresses in sandy soils*. PhD dissertation, University of California, Berkeley, California, 1989.
- [40] R. A. Green. *Energy-based evaluation and remediation of liquefiable soils*. PhD dissertation, Virginia Polytechnic Institute and State University, Blacksburg, Virginia, 2001.
- [41] A. Halder and W. H. Tang. Probabilistic evaluation of liquefaction potential. *Journal of the Geotechnical Engineering Division, ASCE*, 105(GT2):145–163, 1979.
- [42] R. Hamburger. Performance-based seismic engineering: the next generation of structural engineering practice, 2002.
- [43] T. C. Hanks and A. C. Cornell. Probabilistic seismic hazard analysis: a beginner's guide. In *Proceedings, 5th Symposium on Current Issues Related to Nuclear Power Plant Structures, Equipment and Piping*, volume 1, pages 1.1–1.17. Center for Nuclear Power Structures, Equipment and Piping, North Carolina University, 1994.
- [44] L. F. Harder, Jr. *Use of penetration tests to determine the cyclic loading resistance of gravelly soils during earthquake shaking*. PhD dissertation, University of California, Berkeley, California, 1988.

- [45] L. F. Harder, Jr. and R. W. Boulanger. Application of K_σ and K_α correction factors. In *Proceedings, NCEER Workshop on Evaluation of Liquefaction Resistance of Soils*, pages 167–190, State University of New York at Buffalo, 1997. National Center for Earthquake Engineering Research.
- [46] L. F. Harder, Jr. and H. B. Seed. Determination of penetration resistance for coarse-grained soils using the Becker hammer drill. Technical Report No. UCB/EERC-86/06, Earthquake Engineering Research Center, University of California, Berkeley, 1986.
- [47] S. Hardy. *The implementation and application of dynamic finite element analysis to geotechnical problems*. PhD dissertation, Imperial College, University of London, London, England, 2003. Accessed electronically at <http://www.imperial.ac.uk/geotechnics/publications/PhDs/Hardy/hardythesis.htm>.
- [48] R. S. Harichandran and E. H. Vanmarcke. Stochastic variation of earthquake ground motion in space and time. *Journal of Engineering Mechanics*, 112(2):154–174, 1986.
- [49] E. L. Harp and R. C. Wilson. Shaking intensity thresholds for rock falls and slides: Evidence from 1987 Whittier Narrows and Superstition Hills earthquake strong-motion records. *Bulletin of the Seismological Society of America*, 85(6):1739–1757, 1995.
- [50] J. C. Horne. *Effects of liquefaction-induced lateral spreading on pile foundations*. PhD dissertation, University of Washington, Seattle, Washington, 2000.
- [51] J. H. Hwang, C. H. Chen, and C. H. Juang. Liquefaction hazard analysis: a fully probabilistic method. In R. W. Boulanger, M. Dewoolker, N. Gucunski, C. H. Juang, M. E. Kalinski, S. L. Kramer, M. Manzari, and J. Pauschke, editors, *Proceedings of the Sessions of the Geo-Frontiers 2005 Congress*, Earthquake Engineering and Soil Dynamics (GSP 133). ASCE, 2005. Paper no. 22.
- [52] M. E. Hynes and R. S. Olsen. Influence of confining stress on liquefaction resistance. In *Proceedings, International Workshop on Physics and Mechanics of Soil Liquefaction*, pages 145–152, Rotterdam, The Netherlands, 1999. Balkema Publishers.
- [53] I. M. Idriss. Response of soft soil sites during earthquakes. In J. Michael Duncan, editor, *Proceedings, H. Bolton Seed Memorial Symposium*, volume 2, pages 273–289. BiTech Publishers Ltd., May 1990.
- [54] I. M. Idriss. An update to the Seed-Idriss simplified procedure for evaluating liquefaction potential. In *Proceedings, TRB Workshop on New Approaches to Liquefaction*, Publication No. FHWA-RD-99-165. Federal Highways Administration, January 1999.
- [55] I. M. Idriss and R. W. Boulanger. Estimating K_α for use in evaluating cyclic resistance of sloping ground. In *Proceedings, 8th US-Japan Conference on Earthquake Resistant*

- Design of Lifelines and Countermeasures against Liquefaction*, pages 449–468. Multi-disciplinary Center for Earthquake Engineering Research, Buffalo, New York, 2003.
- [56] I. M. Idriss and R. W. Boulanger. Relating K_σ and K_α to SPT blow count and to CPT tip resistance for use in evaluating liquefaction potential. In *Proceedings of the 2003 Dam Safety Conference*. American Society for State Dam Safety Officials, September 7–10 2003.
- [57] I. M. Idriss and R. W. Boulanger. Semi-empirical procedures for evaluating liquefaction potential during earthquakes. In *Proceedings, 11th International Conference on Soil Dynamics and Earthquake Engineering, and 3rd International Conference on Earthquake Geotechnical Engineering*, volume 1, pages 32–56. Stallion Press, 2004.
- [58] I. M. Idriss and J. I. Sun. *User's manual for SHAKE91: a computer program for conducting equivalent linear seismic response analyses of horizontally layered soil deposits*. Center for Geotechnical Modeling, Department of Civil and Environmental Engineering, University of California, Davis, 1993.
- [59] T. Imai, K. Tonouchi, and T. Kanemori. The simple evaluation method of shear stress generated by earthquakes in soil ground. Technical Report No. 3, Bureau of Practical Geological Investigation, 1981.
- [60] K. Ishihara. Simple method of analysis for liquefaction of sand deposits during earthquakes. *Soils and Foundations*, 17(3):1–17, September 1977.
- [61] T. Iwasaki. Soil liquefaction studies in Japan. *Soil Dynamics and Earthquake Engineering*, 5(1):1–68, January 1986.
- [62] T. Iwasaki, F. Tatsuoka, K. I. Tokida, and S. Yasuda. A practical method for assessing soil liquefaction potential based on case studies at various sites in Japan. In *Proceedings, 2nd International Conference on Microzonation for Safer Construction—Research and Application*, volume 2, pages 885–896, San Francisco, California, November 1978.
- [63] F. Jalayer and C. A. Cornell. A technical framework for probability-based demand and capacity factor design (DCFD) seismic formats. PEER 2003/08, Pacific Earthquake Engineering Research Center, College of Engineering, University of California, Berkeley, November 2003. Accessed electronically at <http://peer.berkeley.edu/Products/PEERReports/reports-2003/0308.pdf>.
- [64] A. L. Jones, P. Arduino, and S. L. Kramer. Estimation of uncertainty in geotechnical properties for performance-based earthquake engineering. PEER 2002/16, Pacific Earthquake Engineering Research Center, College of Engineering, University of California, Berkeley, December 2002. Accessed electronically at <http://peer.berkeley.edu/Products/PEERReports/reports-2002/0216.pdf>.

- [65] R. E. Kayen. *Accelerogram-energy approach for prediction of earthquake-induced ground liquefaction*. PhD dissertation, University of California, Berkeley, California, 1993.
- [66] R. E. Kayen and J. K. Mitchell. Assessment of liquefaction potential during earthquakes by Arias intensity. *Journal of Geotechnical and Geoenvironmental Engineering*, 123(12):1162–1174, 1997.
- [67] R. E. Kayen and J. K. Mitchell. Variation of the intensity of earthquake motion beneath the ground surface. In *Proceedings, Sixth US National Conference on Earthquake Engineering, Seismic Design & Mitigation for the Third Millennium*, pages 1162–1174. Earthquake Engineering Research Institute, May 1998. Accessed electronically at <http://walrus.wr.usgs.gov/geotech/variation>.
- [68] R. E. Kayen, J. K. Mitchell, R. B. Seed, A. Lodge, S. Nishio, and R. Coutinho. Evaluation of SPT-, CPT-, and shear wave-based methods for liquefaction potential assessment using Loma Prieta data. In *Proceedings, 4th Japan-US Conference on Earthquake Resistant Design of Lifeline Facilities and Countermeasures against Liquefaction*, volume 1, pages 177–204, 1992.
- [69] M. V. Kostadinov and I. Towhata. Assessment of liquefaction-inducing peak ground velocity and frequency of horizontal ground shaking at onset of phenomenon. *Soil Dynamics and Earthquake Engineering*, 22(4):309–322, June 2002.
- [70] M. V. Kostadinov, F. Yamazaki, and K. Sudo. Comparative study on the methods for detection of liquefaction from strong motion records. In *Proceedings of the 8th Specialty Conference on Probabilistic Mechanics and Structural Reliability*, Notre Dame, Indiana, July 2000. Paper PMC2000-092, accessed electronically at http://www.usc.edu/dept/civil_eng/johnsone/pmc2000/sessions/papers/p092.pdf.
- [71] W. D. Kovacs, J. C. Evans, and A. H. Griffith. Towards a more standardized SPT. In *Proceedings of the IX International Conference on Soil Mechanics and Foundation Engineering*, volume II, pages 269–276, Tokyo, Japan, July 1977. Paper 4-18.
- [72] W. D. Kovacs, A. H. Griffith, and J. C. Evans. An alternative to the cathead and rope for the standard penetration test. *Geotechnical Testing Journal*, 1(2):72–89, June 1978.
- [73] S. L. Kramer. *Geotechnical earthquake engineering*. Prentice-Hall, Inc., Upper Saddle River, N.J., 1996.
- [74] S. L. Kramer and P. Arduino. Constitutive modeling of cyclic mobility and implications for site response. In *Proceedings of the Second International Conference on Earthquake Geotechnical Engineering*, volume 3, pages 1029–1034, Lisboa, Portugal, 1999. Balkema Publishers.

- [75] S. L. Kramer, P. Arduino, D. A. Baska, and M. Malgesini. A practical constitutive model for free-field analysis of liquefiable soils. *Journal of Geotechnical and Geoenvironmental Engineering*, 2004. In review.
- [76] S. L. Kramer and R. T. Mayfield. Performance-based liquefaction hazard evaluation. In R. W. Boulanger, M. Dewoolker, N. Gucunski, C. H. Juang, M. E. Kalinski, S. L. Kramer, M. Manzari, and J. Pauschke, editors, *Proceedings of the Sessions of the Geo-Frontiers 2005 Congress, Earthquake Engineering and Soil Dynamics (GSP 133)*. ASCE, 2005. Paper no. 21.
- [77] S. L. Kramer and R. A. Mitchell. Ground motion intensity measures for liquefaction hazard evaluation. *Earthquake Spectra*, 22(2), May 2006.
- [78] S. L. Kramer, W. J. Silva, and D. A. Baska. Ground motions due to large magnitude subduction zone earthquakes. Research Report WA-RD 450.1, Washington State Transportation Center (TRAC), University of Washington, Seattle, December 1998.
- [79] K. T. Law, Y. L. Cao, and G. N. He. An energy approach for assessing seismic liquefaction potential. *Canadian Geotechnical Journal*, 27(3):320–329, 1990.
- [80] M. K. W. Lee and W. D. L. Finn. DESRA-2, dynamic effective stress response analysis of soil deposits with energy transmitting boundary including assessment of liquefaction potential. Soil Mechanics Series No. 38, Department of Civil Engineering, University of British Columbia, Vancouver, British Columbia, 1978.
- [81] S. S. C. Liao, D. Veneziano, and R. V. Whitman. Regression models for evaluating liquefaction probability. *Journal of Geotechnical Engineering*, 114(4):389–409, 1988.
- [82] S. S. C. Liao and R. V. Whitman. Overburden correction factor for SPT in sand. *Journal of Geotechnical Engineering*, 112(3):389–409, March 1986.
- [83] A. H. Liu, J. P. Stewart, N. A. Abrahamson, and Y. Moriwaki. Equivalent number of uniform stress cycles for soil liquefaction analysis. *Journal of Geotechnical and Geoenvironmental Engineering*, 127(12):1017–1026, 2001.
- [84] N. Luco and A. C. Cornell. Structure-specific scalar intensity measures for near-source and ordinary earthquake ground motions. Submitted to *Earthquake Spectra*, available at http://www.stanford.edu/group/rms/RMS_Papers/pdf/nico/EQ_Spectra01.pdf.
- [85] W. F. Marcusson III and W. A. Bieganousky. Laboratory standard penetration tests on fine sands. *Journal of the Geotechnical Engineering Division, ASCE*, 103(GT6):565–588, June 1977.

- [86] J. Marrone, F. Ostadan, R. Youngs, and J. Litehiser. Probabilistic liquefaction hazard evaluation: method and application. In *Transactions of the 17th International Conference on Structural Mechanics in Reactor Technology (SMiRT 17) Prague, Czech Republic*, 2003. Paper no. M02-1. Accessed electronically at <http://www.iasmirt.org/SMiRT17/M02-1.pdf>.
- [87] G. R. Martin, W. D. L. Finn, and H. B. Seed. Fundamentals of liquefaction under cyclic loading. *Journal of the Geotechnical Engineering Division, ASCE*, 101(GT4):423–438, 1975.
- [88] G. R. Martin and M. Lew, editors. *Recommended procedures for implementation of DMG Special Publication 117 Guidelines for analyzing and mitigating liquefaction hazards in California*. Southern California Earthquake Center, University of Southern California, March 1999. Accessed electronically at <http://www.scec.org/outreach/products/liqreport.pdf>.
- [89] P. J. May. Barriers to adoption and implementation of PBEE innovations. PEER 2002/20, Pacific Earthquake Engineering Research Center, College of Engineering, University of California, Berkeley, August 2002. Accessed electronically at <http://peer.berkeley.edu/Products/PEERReports/reports-2002/0220.pdf>.
- [90] R. K. McGuire. Fortran computer program for seismic risk analysis. USGS Open-File Report 76-67, United States Geological Survey, 1976.
- [91] J. P. Moehle and G. G. Deierlein. A framework for performance-based earthquake engineering. In *Proceedings, Thirteenth World Conference on Earthquake Engineering*, 2004. Paper no. 679.
- [92] S. Nemat-Nasser and A. Shokooh. A unified approach to densification and liquefaction of cohesionless sand in cyclic shearing. *Canadian Geotechnical Journal*, 16(4):659–678, November 1979.
- [93] R. M. Pyke. *TESS: a program for nonlinear ground response analyses*. TAGA Engineering Systems and Software, Lafayette, California, 1992.
- [94] R Development Core Team. *R: a language and environment for statistical computing*. R Foundation for Statistical Computing, Vienna, Austria, 2005. ISBN 3-900051-07-0.
- [95] Risk Engineering, Inc. *EZ-FRISK software, version 7.2*. Boulder, Colorado, 2006.
- [96] P. K. Robertson and C. E. Wride. Evaluating cyclic liquefaction potential using the cone penetration test. *Canadian Geotechnical Journal*, 35(3):442–459, June 1998.

- [97] C. Roblee and B. Chiou. A proposed GeoIndex model for design selection of non-linear properties for site response analyses. In *Proceedings, International Workshop on Uncertainties in Nonlinear Soil Properties and their Impact on Modeling Dynamic Soil Response*. National Science Foundation and PEER Lifelines Program, March 18–19, 2004. Accessed electronically at http://peer.berkeley.edu/lifelines/Workshop304/pdf/geo_Roblee.pdf.
- [98] D. L. Running. *An energy-based model for soil liquefaction*. PhD dissertation, Washington State University, Pullman, Washington, 1996.
- [99] J. H. Schmertmann. Use the SPT to measure dynamic soil properties?—Yes, but...! *Dynamic Geotechnical Testing*, ASTM STP 654:341–355, 1978.
- [100] P. B. Schnabel, J. Lysmer, and H. B. Seed. SHAKE: a computer program for earthquake response analysis of horizontally layered sites. Technical Report No. UCB/EERC-72/12, Earthquake Engineering Research Center, University of California, Berkeley, December 1972.
- [101] H. B. Seed. Earthquake-resistant design of earth dams. In *Proceedings, Symposium on Seismic Design of Embankments and Caverns*, pages 41–64, Pennsylvania, 1983. ASCE.
- [102] H. B. Seed, I. Arango, and C. K. Chan. Evaluation of soil liquefaction potential during earthquakes. Technical Report No. EERC-75/28, Earthquake Engineering Research Center, University of California, Berkeley, 1975.
- [103] H. B. Seed and I. M. Idriss. Simplified procedure for evaluating soil liquefaction potential. *Journal of the Soil Mechanics and Foundations Division, ASCE*, 97(SM9):1249–1273, September 1971.
- [104] H. B. Seed and I. M. Idriss. Evaluation of liquefaction potential of sand deposits based on observations of performance in previous earthquakes. In *Proceedings, International Conference on Recent Advances in Geotechnical Earthquake Engineering and Soil Dynamics*, St. Louis, Missouri, April 26–May 2 1981. ASCE.
- [105] H. B. Seed and I. M. Idriss. Ground motions and soil liquefaction during earthquakes. Technical report, Earthquake Engineering Research Institute, Berkeley, California, 1982.
- [106] H. B. Seed, I. M. Idriss, F. Makdisi, and N. Banerjee. Representation of irregular stress time histories by equivalent uniform stress series in liquefaction analyses. Technical Report No. EERC-75/29, Earthquake Engineering Research Center, University of California, Berkeley, October 1975.

- [107] H. B. Seed and K. L. Lee. Liquefaction of saturated sands during cyclic loading. *Journal of the Soil Mechanics and Foundations Division, ASCE*, 92(SM6):105–134, November 1966.
- [108] H. B. Seed and M. L. Silver. Settlement of dry sands during earthquakes. *Journal of the Soil Mechanics and Foundations Division, ASCE*, 98(SM4):381–397, April 1972.
- [109] H. B. Seed, K. Tokimatsu, L. F. Harder, Jr., and R. Chung. Influence of SPT procedures in soil liquefaction resistance evaluations. *Journal of Geotechnical Engineering*, 111(12):1425–1445, December 1995.
- [110] H. B. Seed, R. T. Wong, I. M. Idriss, and K. Tokimatsu. Moduli and damping factors for dynamic analyses of cohesionless soils. Technical Report No. UCB/EERC-84/14, Earthquake Engineering Research Center, University of California, Berkeley, September 1984.
- [111] R. B. Seed, K. Ö. Çetin, R. E. S. Moss, A. Kammerer, J. Wu, J. Pestana, M. Riemer, R. B. Sancio, J. D. Bray, R. E. Kayen, and A. Faris. Recent advances in soil liquefaction engineering: a unified and consistent framework. Technical Report No. EERC 2003-6, Earthquake Engineering Research Center, University of California, Berkeley, 2003. Accessed electronically at http://eerc.berkeley.edu/reports/2003/eerc_2003_06.pdf.
- [112] R. B. Seed and L. F. Harder, Jr. SPT-based analysis of cyclic pore pressure generation and undrained residual strength. In J. Michael Duncan, editor, *Proceedings, H. Bolton Seed Memorial Symposium*, volume 2, pages 351–376. BiTech Publishers Ltd., May 1990.
- [113] N. Shome and A. C. Cornell. Probabilistic seismic demand analysis of nonlinear structures. RMS 35, Reliability of Marine Structures Group, Stanford University, Stanford, California, 1999.
- [114] A. K. Skempton. Standard penetration test procedures and the effects in sands of overburden pressure, relative density, particle size, aging, and overconsolidation. *Géotechnique*, 36(3):425–447, 1986.
- [115] J. P. Stewart, A. H. Liu, and Y. Choi. Amplification factors for spectral acceleration in tectonically active regions. *Bulletin of the Seismological Society of America*, 93(1):332–352, February 2003.
- [116] J. Sun, R. Golezorkhi, and H. B. Seed. Dynamic moduli and damping ratios for cohesive soils. Technical Report No. UCB/EERC-88/15, Earthquake Engineering Research Center, University of California, Berkeley, August 1988.

- [117] K. Tokimatsu and Y. Yoshimi. Empirical correlation of soil liquefaction based on SPT-N values and fines content. *Soils and Foundations*, 23(4):56–74, 1983.
- [118] S. Toprak, T. L. Holzer, M. J. Bennett, and J. C. Tinsley III. CPT- and SPT-based probabilistic assessment of liquefaction. In *Proceedings, 7th U.S.-Japan Workshop on Earthquake Resistant Design of Lifeline Facilities and Countermeasures Against Liquefaction, Seattle, Washington*, pages 69–86. Multidisciplinary Center for Earthquake Engineering Research, Buffalo, NY, 1999.
- [119] G. R. Toro, N. A. Abrahamson, and J. F. Schneider. Model of strong ground motions from earthquakes in central and eastern North America: best estimates and uncertainties. *Seismological Research Letters*, 68(1):41–57, January/February 1997.
- [120] T. Travararou, J. D. Bray, and N. A. Abrahamson. Empirical attenuation relationship for Arias intensity. *Journal of Earthquake Engineering and Structural Dynamics*, 32(7):1133–1155, June 2003.
- [121] M. D. Trifunac. Empirical criteria for liquefaction in sands via standard penetration tests and seismic wave energy. *Soil Dynamics and Earthquake Engineering*, 14(6):419–426, 1995.
- [122] S. B. Upsall. *An instrumental intensity scale for geotechnical and structural damage in a modern infrastructure*. PhD dissertation, University of Washington, Seattle, Washington, 2006.
- [123] S. Weisberg. *Applied Linear Regression*. John Wiley & Sons, 2nd edition, 1985.
- [124] R. V. Whitman. Resistance of soil to liquefaction and settlement. *Soils and Foundations*, 11(4):59–68, 1971.
- [125] M. K. Yegian and R. V. Whitman. Risk analysis for ground failure by liquefaction. *Journal of the Geotechnical Engineering Division, ASCE*, 104(GT7):921–938, 1978.
- [126] T. L. Youd. Compaction of sands by repeated shear straining. *Journal of the Soil Mechanics and Foundations Division, ASCE*, 98(SM7):709–725, July 1972.
- [127] T. L. Youd and B. L. Carter. Influence of soil softening and liquefaction on spectral acceleration. *Journal of Geotechnical and Geoenvironmental Engineering*, 131(7):811–825, July 2005.
- [128] T. L. Youd, I. M. Idriss, R. D. Andrus, I. Arango, G. Castro, J. T. Christian, R. Dobry, W. D. L. Finn, L. F. Harder Jr., M. E. Hynes, K. Ishihara, J. P. Koester, S. S. C. Liao, W. F. Marcuson III, G. R. Martin, J. K. Mitchell, Y. Moriwaki, M. S. Power, P. K. Robertson, R. B. Seed, and K. H. Stokoe II. Liquefaction resistance of soils: summary

report from the 1996 NCEER/NSF workshops on evaluation of liquefaction resistance of soils. *Journal of Geotechnical and Geoenvironmental Engineering*, 127(10):817–833, 2001.

- [129] T. L. Youd and S. K. Noble. Liquefaction criteria based on statistical and probabilistic analyses. In *Proceedings of the NCEER Workshop on Evaluation of Liquefaction Resistance of Soils*, pages 201–205. National Center for Earthquake Engineering Research, Buffalo, NY, 1997.
- [130] M. Zeghal and A. W. Elgamal. analysis of site liquefaction using earthquake records. *Journal of Geotechnical Engineering*, 120(6):996–1017, June 1994.
- [131] S. G. Zhou. Influence of fines on evaluating liquefaction of sand by SPT. In *Proceedings, International Conference on Recent Advances in Geotechnical Earthquake Engineering and Soil Dynamics*, St. Louis, Missouri, April 26–May 2 1981. ASCE.

Appendix A

ESTIMATES OF PARAMETER VARIANCE IN ÇETIN'S EQUATION
FOR PROBABILITY OF LIQUEFACTION

Çetin et al. [24] described the probability of liquefaction as

$$P_L = \Phi \left[\frac{N_{1,60}(1 + 0.004FC) - 13.32 \ln CSR_{eq} - 29.53 \ln M_w - 3.70 \ln \frac{\sigma'_{vo}}{p_a} + 0.05FC + 16.85}{2.70} \right] \quad (\text{A.1})$$

in which Φ is the standard normal cumulative probability operator, $N_{1,60}$ is the SPT blow-count corrected for energy and overburden stress, FC is the fines content in percent (not as a ratio), CSR_{eq} is the cyclic stress ratio not corrected for magnitude, M_w is the earthquake magnitude, σ'_{vo} is the initial vertical effective stress at the point of interest in the soil profile, and p_a is the atmospheric pressure in the same units as σ'_{vo} . Çetin et al. [22] described how the uncertainty in each of the parameters in Equation (A.1) was quantified and then removed from the equation to leave only the model uncertainty in the final result. This explicit apportionment of uncertainty is an improvement on many of the past probabilistic relationships for liquefaction assessment, but users of Equation (A.1) must be careful to add the parameter uncertainty back into the equation to get results that are reasonable for real-world conditions. This appendix describes the procedure to compute parameter uncertainty and include it in Equation (A.1).

A.1 Overview of the approach

Çetin et al. [22] pointed out that Equation (A.1) is based on the form of the standard normal probability distribution:

$$P = \Phi \left(\frac{x - \mu_x}{\sigma_x} \right)$$

in which P is the probability, x is the probabilistic variable of interest, and μ_x is the mean value of the probabilistic variable. Probabilistic representations of liquefaction potential

generally use case histories to estimate the location of the limit state between liquefaction and non-liquefaction. In structural reliability, the limit state is given a value of zero, states of failure—liquefaction in this case—have values less than zero, and states of non-failure have values greater than zero. Thus, the probability of liquefaction can be written as

$$P_L = \Phi \left(-\frac{x - \mu_x}{\sigma_x} \right) = \Phi \left(\frac{-x}{\sigma_x} \right)$$

The negative sign in the fraction is necessary because the state of liquefaction is represented by negative values, and the simplified second form occurs because the mean value ($P_L = 0.5$) is at the liquefaction limit state, which has a value of zero.

In the simplified *CSR* method, the case history database is presented on a plot of *CSR* and $N_{1,60}$ (Figure 3.1), and

$$f(CSR) = f(N_{1,60}, FC, M_w, \sigma'_{vo})$$

This equation can be rearranged to define a liquefaction state variable, \hat{g} , that is zero at the limit state, negative for liquefaction cases, and positive for non-liquefaction cases:

$$\hat{g} = f(N_{1,60}, FC, M_w, \sigma'_{vo}) - f(CSR)$$

In this form, there is no provision for model or parameter uncertainty. To allow for model uncertainty

$$g = \hat{g} + \varepsilon = f(N_{1,60}, FC, M_w, \sigma'_{vo}) - f(CSR) + \varepsilon$$

By assuming that ε is normally distributed with a mean of zero, Çetin et al. defined the probability of liquefaction as

$$\begin{aligned} P_L &= \Phi \left(\frac{-\hat{g}}{\sigma_\varepsilon} \right) \\ &= \Phi \left(-\frac{f(N_{1,60}) - f(CSR)}{\sigma_\varepsilon} \right) \end{aligned}$$

which is the general form of Equation (4.1). Note that all of the uncertainty is included in the denominator. Thus, when the uncertainty of all the parameters is added back into Equation (4.1), the only term that changes is the denominator, which Çetin et al. named σ_E and defined as

$$\sigma_E^2 = (1 + 0.004FC)^2 \sigma_{N_{1,60}}^2 + (-13.32)^2 \sigma_{\ln CSR_{eq}}^2 + (-29.53)^2 \sigma_{\ln M_w}^2 + (-3.70)^2 \sigma_{\ln \sigma'_{vo}}^2 + (0.004N_{1,60} + 0.05)^2 \sigma_{FC}^2 + 2.70^2 \quad (\text{A.2})$$

in which σ_i^2 represents the variance of parameter i .

A.2 Example condition

The uncertainty of many geotechnical parameters is described as the coefficient of variance, COV, which is the ratio of the standard deviation to the mean. To estimate numerical values of parameter standard deviation and variance, therefore, it is necessary to have mean parameter values. For this dissertation, an example element of soil with the following characteristics is used: depth = 6 m, depth to the ground water table = 2 m, soil specific gravity = 2.67, soil void ratio = 0.67, fines content = 10 percent, and $N_{1,60} = 15$ bpf. The variance estimates are made for relatively large and small levels of uncertainty that are intended to correspond to site investigations for preliminary and final design stages.

A.3 Standard penetration resistance

Jones et al. [64] documented the variability of many geotechnical parameters. For standard penetration resistance, they listed COVs ranging from 19 to 62%, with a mean COV of 54%. This mean is very high, implying that a mean blow count of, for example, 15 could be as low as 7 and as high as 23—a range that is so large as to make the actual standard penetration test unnecessary! It is likely that this large variation comes from comparing tests in different materials or in notoriously difficult soils like gravel. Canvassing a limited number of geotechnical engineers resulted in an upper estimate of 30% for the COV, which is still produces a range of 10–20 for an average blow count of 15. The lower end of the COV range from Jones et al. is consistent with the COV of 20% reported by Çetin [21].

In summary, assuming an average blow count of 15, the high and low estimates of $\sigma_{N_{1,60}}^2$ are 20.3 and 9, respectively, which correspond to COVs of 30% and 20%, respectively. Assuming an average fines content of 10% ($FC = 10$), high and low estimates of the first term of Equation (A.2) are 21.9 and 9.73, respectively.

A.4 Cyclic stress ratio

The cyclic stress ratio has been defined as

$$CSR_{eq} = 0.65 a_{max} \frac{\sigma_{vo}}{\sigma'_{vo}} r_d$$

For cases in which a_{max} for soil is not directly available and must be calculated from the bedrock acceleration,

$$CSR_{eq} = 0.65 F_A \cdot a_{maxr} \cdot \mathcal{R} \cdot r_d$$

in which F_A is Stewart's amplification factor and $\mathcal{R} = \sigma_{vo}/\sigma'_{vo}$.

It is not necessary to include a_{maxr} in the cyclic stress ratio variance because the performance-based method integrates explicitly across the entire IM distribution. Neither is it necessary to include F_A in the CSR variance because the uncertainty of a_{maxs} predictions from attenuation relationships is about the same as the uncertainty of a_{maxr} predictions from similar attenuation relationships [119]. Since the entire distribution of a_{maxr} predictions from the USGS PSHA already incorporate the uncertainty from attenuation relationships, it would be incorrect to add in another level of uncertainty due to the use of F . Stewart et al. [115] seemed to concur, noting that the uncertainty term that they associated with F allows the development of a probabilistic hazard curve from a single earthquake rock record or a deterministic set of earthquake rock records.

The contributions to $\sigma_{\ln CSR_{eq}}^2$, therefore, are from \mathcal{R} and r_d . Using the first order second moment (FOSM) approximation,

$$\begin{aligned} \sigma_{\ln CSR_{eq}}^2 = & \sigma_{\mathcal{R}}^2 \left(\frac{\partial \ln CSR_{eq}}{\partial \mathcal{R}} \right)^2 + \sigma_{r_d}^2 \left(\frac{\partial \ln CSR_{eq}}{\partial r_d} \right)^2 \\ & + 2 \text{cov}(\mathcal{R}, r_d) \left(\frac{\partial \ln CSR_{eq}}{\partial \mathcal{R}} \right) \left(\frac{\partial \ln CSR_{eq}}{\partial r_d} \right) \quad (\text{A.3}) \end{aligned}$$

In the first two terms, the partial derivatives are straightforward:

$$\frac{\partial \ln CSR_{eq}}{\partial \mathcal{R}} = \frac{1}{\mathcal{R}}, \quad \frac{\partial \ln CSR_{eq}}{\partial r_d} = \frac{1}{r_d}$$

For the variance terms, Çetin et al. [24] defined $\hat{\sigma}_{r_d} = 0.0198z^{0.85}$ for depth, z , less than 20 m; for a typical depth of 6 m, $\hat{\sigma}_{r_d} = 0.0908$. For a profile of constant density, the relationship for $\sigma_{\mathcal{R}}$ is

$$\begin{aligned} \mathcal{R} &= \frac{\sigma_{vo}}{\sigma'_{vo}} \\ &= \frac{\gamma_d z_w + \gamma_{sat}(z - z_w)}{\gamma_d z_w + \gamma_b(z - z_w)} \\ &= \frac{\gamma_d z_w + \gamma_b(z - z_w) + \gamma_w(z - z_w)}{\gamma_d z_w + \gamma_b(z - z_w)} \\ &= 1 + \frac{\gamma_w(z - z_w)}{\gamma_d z_w + \gamma_b(z - z_w)} \end{aligned}$$

in which γ_d , γ_{sat} , and γ_b are the dry, saturated, and buoyant unit weights of the soil, respectively, and z_w is the depth to the groundwater table. To ensure that $(z - z_w) \geq 0$, this equation for \mathcal{R} is only applicable below the groundwater table. Since liquefaction only occurs in saturated soil, this is not an onerous restriction. Note that this formulation assumes that the moisture content in the zone above the water table is low enough to be ignored. This assumption may be dubious for calculating the actual vertical stresses, but for estimating the variance of $\ln CSR_{eq}$, it is reasonable. Continuing,

$$\begin{aligned} \gamma_d &= \frac{G_s \gamma_w}{1 + e} \\ \gamma_b &= \gamma_{sat} - \gamma_w \\ &= \frac{(G_s + e)\gamma_w}{1 + e} - \gamma_w = \left(\frac{G_s + e}{1 + e} - 1 \right) \gamma_w \\ &= \left(\frac{G_s - 1}{1 + e} \right) \gamma_w \end{aligned}$$

in which G_s is the specific gravity and e is the void ratio of the soil. Using these relationships,

$$\begin{aligned}
\mathcal{R} &= 1 + \frac{\gamma_w(z - z_w)}{\frac{G_s \gamma_w z_w}{1 + e} + \left(\frac{G_s - 1}{1 + e} \right) \gamma_w(z - z_w)} \\
&= 1 + \frac{(1 + e)(z - z_w)}{G_s z_w + (G_s - 1)(z - z_w)} \\
&= 1 + \frac{(1 + e)(z - z_w)}{(G_s - 1)z + z_w}
\end{aligned}$$

The variance of G_s and z is small relative to the variance of e and z_w so

$$\sigma_{\mathcal{R}}^2 = \sigma_e^2 \left(\frac{\partial \mathcal{R}}{\partial e} \right)^2 + \sigma_{z_w}^2 \left(\frac{\partial \mathcal{R}}{\partial z_w} \right)^2 + 2 \text{cov}(e, z_w) \left(\frac{\partial \mathcal{R}}{\partial e} \right) \left(\frac{\partial \mathcal{R}}{\partial z_w} \right)$$

The void ratio and the groundwater depth should be uncorrelated so $\text{cov}(e, z_w) = 0$. Thus,

$$\begin{aligned}
\frac{\partial \mathcal{R}}{\partial e} &= \frac{z - z_w}{(G_s - 1)z + z_w} \\
\frac{\partial \mathcal{R}}{\partial z_w} &= (1 + e) \frac{-[(G_s - 1)z + z_w] - (z - z_w)}{[(G_s - 1)z + z_w]^2} \\
&= (1 + e) \frac{-G_s z + z - z_w - z + z_w}{[(G_s - 1)z + z_w]^2} \\
&= \frac{-G_s z(1 + e)}{[(G_s - 1)z + z_w]^2}
\end{aligned}$$

Now,

$$\sigma_{\mathcal{R}}^2 = \frac{\sigma_e^2 (z - z_w)^2}{[(G_s - 1)z + z_w]^2} + \frac{\sigma_{z_w}^2 (G_s z_w)^2 (1 + e)^2}{[(G_s - 1)z + z_w]^4}$$

Jones et al. noted the average coefficients of variation of unit weight are in a relatively tight range around 8 percent. For a loose to medium dense sand with $e = 0.67$ and $G_s = 2.67$, $\gamma_d = 15.7 \text{ kN/m}^3$ and the corresponding standard deviation, $\sigma_{\gamma_d} \approx 1.25 \text{ kN/m}^3$, which results in $\sigma_e = 0.124$. Typical variations in z_w were not found, so for this work a high estimate of $\sigma_{z_w} = 2 \text{ m}$ and a low estimate of 0.5 m were assumed. For $z = 6 \text{ m}$, Çetin et al. [24] showed an average value of $r_d = 0.82$. With these values, high and low estimates of $\sigma_{\mathcal{R}}^2$ are 0.0169 and 0.00265, respectively.

The parameters listed in the previous paragraphs also allow the calculation of the remaining values needed for the first two terms of Equation A.3. For the standard reference profile, $\mathcal{R} = \sigma_{vo}/\sigma'_{vo} = 1.556$. As noted above, an average value of r_d is 0.82. Now the first two terms of Equation (A.3) can be written as

$$\begin{aligned} \sigma_{\mathcal{R}}^2 \left(\frac{\partial \ln CSR_{eq}}{\partial \mathcal{R}} \right)^2 + \sigma_{r_d}^2 \left(\frac{\partial \ln CSR_{eq}}{\partial r_d} \right)^2 = \\ \frac{\sigma_{\mathcal{R}}^2}{\mathcal{R}^2} + \frac{\sigma_{r_d}^2}{r_d^2} = \frac{[0.0169, 0.00265]}{1.556^2} + \frac{0.0908^2}{0.82^2} = [0.0193, 0.0134] \end{aligned} \quad (\text{A.4})$$

in which [0.0193, 0.0134] are the high and low estimates, respectively.

The covariance term of Equation (A.3) is more complicated but can be simplified somewhat by considering the relationship between parameter pairs. The depth-dependence of r_d suggests that it should be correlated with σ_{vo} and σ'_{vo} . Its correlation with the ratio, \mathcal{R} , however, should be very small because \mathcal{R} is controlled primarily by the ground depth.

With all the covariance terms set to zero,

$$\begin{aligned} \sigma_{\ln CSR_{eq}}^2 &= \sigma_{\mathcal{R}}^2 \left(\frac{\partial \ln CSR_{eq}}{\partial \mathcal{R}} \right)^2 + \sigma_{r_d}^2 \left(\frac{\partial \ln CSR_{eq}}{\partial r_d} \right)^2 \\ &= \frac{\sigma_{\mathcal{R}}^2}{\mathcal{R}^2} + \frac{\sigma_{r_d}^2}{r_d^2} = \frac{[0.0169, 0.00265]}{1.556^2} + \frac{0.0908^2}{0.82^2} \\ &= [0.0193, 0.0134] \end{aligned} \quad (\text{A.5})$$

These result in high and low estimates of the second term in Equation A.2 of 3.42 and 2.37, respectively.

A.5 Earthquake magnitude

There is no need to include the variance of the earthquake magnitude, $\sigma_{\ln M_w}^2$, in Equation (A.2) because the performance-based method explicitly integrates across the entire distribution of magnitudes. Thus, the third term of Equation (A.2) can be omitted.

A.6 Effective vertical stress

As noted in Section A.4, if the moisture content in the soil above the water table is small, the effective vertical stress can be written as

$$\begin{aligned}\sigma'_{vo} &= \gamma_d z_w + \gamma_b (z - z_w) \\ &= \frac{G_s \gamma_w z_w}{1+e} + \left[\frac{(G_s + e) \gamma_w}{1+e} - \gamma_w \right] (z - z_w) \\ &= \gamma_w \left(\frac{G_s z}{1+e} + \frac{ez}{1+e} - \frac{ez_w}{1+e} - z + z_w \right) \\ \ln \sigma'_{vo} &= \ln \gamma_w + \ln \left(\frac{G_s z}{1+e} + \frac{ez}{1+e} - \frac{ez_w}{1+e} - z + z_w \right)\end{aligned}$$

As stated earlier, the variance of G_s , z , and γ_w will be insignificant and e and z_w will be uncorrelated,

$$\begin{aligned}\sigma_{\ln \sigma'_{vo}}^2 &= \sigma_e^2 \left(\frac{\partial \ln \sigma'_{vo}}{\partial e} \right)^2 + \sigma_{z_w}^2 \left(\frac{\partial \ln \sigma'_{vo}}{\partial z_w} \right)^2 \\ &= \sigma_e^2 \left(\frac{-1}{1+e} \right)^2 + \sigma_{z_w}^2 \left(\frac{1}{(G_s - 1)z + z_w} \right)^2 \\ &= \frac{\sigma_e^2}{(1+e)^2} + \frac{\sigma_{z_w}^2}{[(G_s - 1)z + z_w]^2}\end{aligned}$$

Using the values from Section A.4, $e = 0.67$, $G_s = 2.67$, $z = 6$ m, $z_w = 2$ m, $\sigma_e = 0.124$, and high and low estimates for σ_{z_w} of 2 m and 0.5 m, respectively,

$$\begin{aligned}\sigma_{\ln \sigma'_{vo}}^2 &= 0.359 \sigma_e^2 + 0.00692 \sigma_{z_w}^2 \\ &= \begin{cases} 0.0332, & \text{high estimate;} \\ 0.00722, & \text{low estimate.} \end{cases}\end{aligned}$$

These result in high and low values for the fourth term of Equation A.2 of 0.454 and 0.0988, respectively.

A.7 Fines content

Jones et al. did not list an estimate of the fines content uncertainty, but Çetin [21] suggested a single value for the standard deviation of 2%. This results in a value for the fifth term of Equation (A.2) of 4.84×10^{-6} .

A.8 Model uncertainty

As noted earlier, Çetin et al. [22] determined that the standard deviation of the model error is 2.70. Thus, the final term in Equation (A.2) is 7.29.

A.9 Putting it all together

All that remains in computing the new standard deviation for Equation (A.1) is to combine the terms from each section above:

$$\begin{aligned}\sigma_{E_{high}} &= \sqrt{21.9 + 3.42 + 0.454 + 4.84 \times 10^{-6} + 7.29} \\ &= 5.75 \\ \sigma_{E_{low}} &= \sqrt{9.73 + 2.37 + 0.0988 + 4.84 \times 10^{-6} + 7.29} \\ &= 4.41\end{aligned}$$

From this calculation, the largest contributor to the uncertainty of liquefaction probability is the penetration resistance. The variance contributions are then followed in decreasing order by model uncertainty, cyclic stress ratio, effective vertical stress, and finally fines content. Ignoring the uncertainty from effective vertical stress and fines content reduces both the low and high estimate of σ_E by an insignificant amount.

Appendix B

ADJUSTMENT OF LIQUEFACTION HAZARD MAPS FOR SITE SPECIFIC CONDITIONS

The liquefaction hazard maps presented in Chapter 4 are based on a standard reference soil profile. To account for site-specific conditions different from those of the reference profile, a correction procedure is required to allow determination of an adjustment to the blowcount required to resist liquefaction, N_{req} , which will be referred to herein as ΔN_{req} . This appendix describes the development and application of a procedure for determining ΔN_{req} .

B.1 Components of the adjustment

From Çetin et al. [24] the value of the cyclic stress ratio, CSR , required to resist liquefaction with probability, P_L , can be expressed in terms of a cyclic resistance ratio,

$$CRR = \exp \left[\frac{N_{1,60}(1 + 0.004FC) - 29.53 \ln M_w - 3.70 \ln \frac{\sigma'_{vo}}{p_a} + 0.05FC + 16.85 + \sigma_E \Phi^{-1}(P_L)}{13.32} \right] \quad (B.1)$$

in which $N_{1,60}$ is the SPT resistance corrected for overburden pressure and energy variation, FC is the fines content in percent, M_w is the earthquake moment magnitude, σ'_{vo} is the initial vertical effective stress, p_a is the atmospheric pressure in the same units as σ'_{vo} , σ_E is a measure of the uncertainty in the relationship, Φ^{-1} is the inverse standard normal cumulative distribution operator, and P_L is the probability of liquefaction. Applying the fines correction to $N_{1,60}$ and rearranging Equation (B.1),

$$\begin{aligned} N_{req} &= N_{1,60,cs} = N_{1,60}(1 + 0.004FC) + 0.05FC \\ &= 13.32 \ln CSR + 29.53 \ln M_w + 3.70 \ln \frac{\sigma'_{vo}}{p_a} - 16.85 - \sigma_E \Phi^{-1}(P_L) \end{aligned}$$

Note that σ_E has a value of 2.70 when no parametric uncertainty exists, and higher values when parametric uncertainty is accounted for.

The cyclic stress ratio is defined as

$$CSR = 0.65 a_{max} \frac{\sigma_{vo}}{\sigma'_{vo}} r_d$$

in which a_{max} is the peak acceleration at the ground surface as a fraction of gravitational acceleration. The USGS database gives the peak bedrock acceleration so it is necessary to allow for amplification through the soil column to the ground surface. Stewart et al. [115] described a simple multiplicative factor that can be applied to bedrock accelerations,

$$F_a = \frac{a_{max}}{a_{max_{rock}}} = \exp(a + b \ln a_{max_{rock}}) \quad (B.2)$$

in which $a = -0.15$ and $b = -0.13$ for quaternary alluvium. Now,

$$N_{1,60,cs} = 13.32 \ln \left(0.65 F_a a_{max_{rock}} \frac{\sigma_{vo}}{\sigma'_{vo}} r_d \right) + 29.53 \ln M_w + 3.70 \ln \frac{\sigma'_{vo}}{p_a} - 16.85 - \sigma_E \Phi^{-1}(P_L)$$

If the site-specific constituents of this equation are evaluated in terms of the reference profile (denoted by the subscript, *ref*), an expression for the required clean sand SPT resistance for the reference soil profile can be written as

$$N_{1,60,cs,ref} = 13.32 \ln \left(0.65 F_{A_{ref}} a_{max_{rock}} \frac{\sigma_{vo_{ref}}}{\sigma'_{vo_{ref}}} r_{d_{ref}} \right) + 29.53 \ln M_w + 3.70 \ln \frac{\sigma'_{vo_{ref}}}{p_a} - 16.85 - \sigma_E \Phi^{-1}(P_L)$$

The required clean sand SPT resistance for a soil profile other than the reference profile can be expressed as the sum of the required clean sand SPT resistance for the reference profile and a site-specific adjustment value, ΔN_{req} ,

$$N_{1,60,cs} = N_{1,60,cs,ref} + \Delta N_{req}$$

Therefore,

$$\begin{aligned}
\Delta N_{req} &= N_{1,60,cs} - N_{1,60,cs,ref} \\
&= 13.32 \ln \left(0.65 F_a a_{maxrock} \frac{\sigma_{vo}}{\sigma'_{vo}} r_d \right) + 29.53 \ln M_w + 3.70 \ln \frac{\sigma'_{vo}}{p_a} \\
&\quad - 16.85 - \sigma_E \Phi^{-1}(P_L) - \left[13.32 \ln \left(0.65 F_{Aref} a_{maxrock} \frac{\sigma_{vo,ref}}{\sigma'_{vo,ref}} r_{d,ref} \right) \right. \\
&\quad \left. + 29.53 \ln M_w + 3.70 \ln \frac{\sigma'_{vo,ref}}{p_a} - 16.85 - \sigma_E \Phi^{-1}(P_L) \right] \\
&= 13.32 \ln \left(\frac{F_a}{F_{Aref}} \frac{\sigma_{vo}/\sigma'_{vo}}{\sigma_{vo,ref}/\sigma'_{vo,ref}} \frac{r_d}{r_{d,ref}} \right) + 3.70 \ln \frac{\sigma'_{vo}}{\sigma'_{vo,ref}} \\
&= \left[13.32 \ln \frac{\sigma_{vo}/\sigma'_{vo}}{\sigma_{vo,ref}/\sigma'_{vo,ref}} + 3.70 \ln \frac{\sigma'_{vo}}{\sigma'_{vo,ref}} \right] + 13.32 \ln \frac{F_a}{F_{Aref}} + 13.32 \ln \frac{r_d}{r_{d,ref}} \\
&= \Delta N_\sigma + \Delta N_F + \Delta N_{r_d}
\end{aligned}$$

In this form, there are three components of the site-specific N_{req} adjustment: one based on the initial vertical stress profile, one based on the amplification of acceleration up through the soil profile, and one based on the r_d profile. First consider the stress component.

B.2 Stress component of the adjustment

The densities of most inorganic soils fall within a relatively narrow range, at least compared to many other soil properties. If each site consists of soil with a constant void ratio, e , it will have only a single dry unit weight, γ_d , saturated unit weight, γ_{sat} , and buoyant unit weight, γ_b . For a groundwater table at depth, z_w and assuming that the water content of the soil above the groundwater table is a negligible part of the moist unit weight, the vertical stresses are

$$\sigma_{vo} = \gamma_d z_w + \gamma_{sat}(z - z_w)$$

$$\sigma'_{vo} = \gamma_d z_w + \gamma_b(z - z_w)$$

Note that these expressions are only applicable below the groundwater table to ensure that $(z - z_w)$ remains positive. This is not an onerous restriction since liquefaction only occurs in saturated soils.

The relationships for the unit weights are

$$\begin{aligned}\gamma_d &= \frac{G_s \cdot \gamma_w}{1 + e} \\ \gamma_{sat} &= \frac{(G_s + e)\gamma_w}{1 + e} \\ \gamma_b &= \gamma_{sat} - \gamma_w = \left(\frac{G_s + e}{1 + e} - 1 \right) \gamma_w \\ &= \frac{(G_s - 1)\gamma_w}{1 + e}\end{aligned}\tag{B.3}$$

Substituting these into the relationships for vertical stresses,

$$\sigma_{vo} = [G_s z_w + (G_s + e)(z - z_w)] \frac{\gamma_w}{1 + e} = [G_s z + e(z - z_w)] \frac{\gamma_w}{1 + e}\tag{B.4}$$

$$\sigma'_{vo} = [G_s z_w + (G_s - 1)(z - z_w)] \frac{\gamma_w}{1 + e} = [G_s z - (z - z_w)] \frac{\gamma_w}{1 + e}\tag{B.5}$$

These stress relations allow the first part of ΔN_σ to be written as

$$\frac{\sigma_{vo}}{\sigma'_{vo}} = \frac{G_s z + e(z - z_w)}{G_s z - (z - z_w)} = \frac{G_s + e(1 - \frac{z_w}{z})}{G_s - 1 + \frac{z_w}{z}}$$

This can also be written as

$$\frac{\sigma_{vo}}{\sigma'_{vo}} = \frac{1 + w_{sat}(1 - \frac{z_w}{z})}{1 - \frac{1}{G_s}(1 - \frac{z_w}{z})}$$

in which $w_{sat} = e/G_s$ is the saturated moisture content, which can be determined from moisture contents of SPT samples taken below the groundwater table.

The soil properties of the reference section were chosen so that $G_s = 2.67$, $e_{ref} = 0.67$, $z_w = 0$, and $\sigma_{vo_{ref}}/\sigma'_{vo_{ref}} = 2$ so

$$\frac{\sigma_{vo}/\sigma'_{vo}}{\sigma_{vo_{ref}}/\sigma'_{vo_{ref}}} = \frac{G_s + e(1 - \frac{z_w}{z})}{2(G_s - 1 + \frac{z_w}{z})} = \frac{1 + w_{sat}(1 - \frac{z_w}{z})}{2[1 - \frac{1}{G_s}(1 - \frac{z_w}{z})]}$$

Now consider the second part of ΔN_σ . From Equation (B.5),

$$\begin{aligned}\frac{\sigma'_{vo}}{\sigma'_{vo_{ref}}} &= \frac{G_s z - (z - z_w)}{G_{s_{ref}} z_{ref} - (z_{ref} - z_{w_{ref}})} \frac{1 + e_{ref}}{1 + e} \\ &= \frac{G_s - (1 - \frac{z_w}{z})}{G_{s_{ref}} - (1 - \frac{z_{w_{ref}}}{z_{ref}})} \frac{1 + e_{ref}}{1 + e} \frac{z}{z_{ref}}\end{aligned}$$

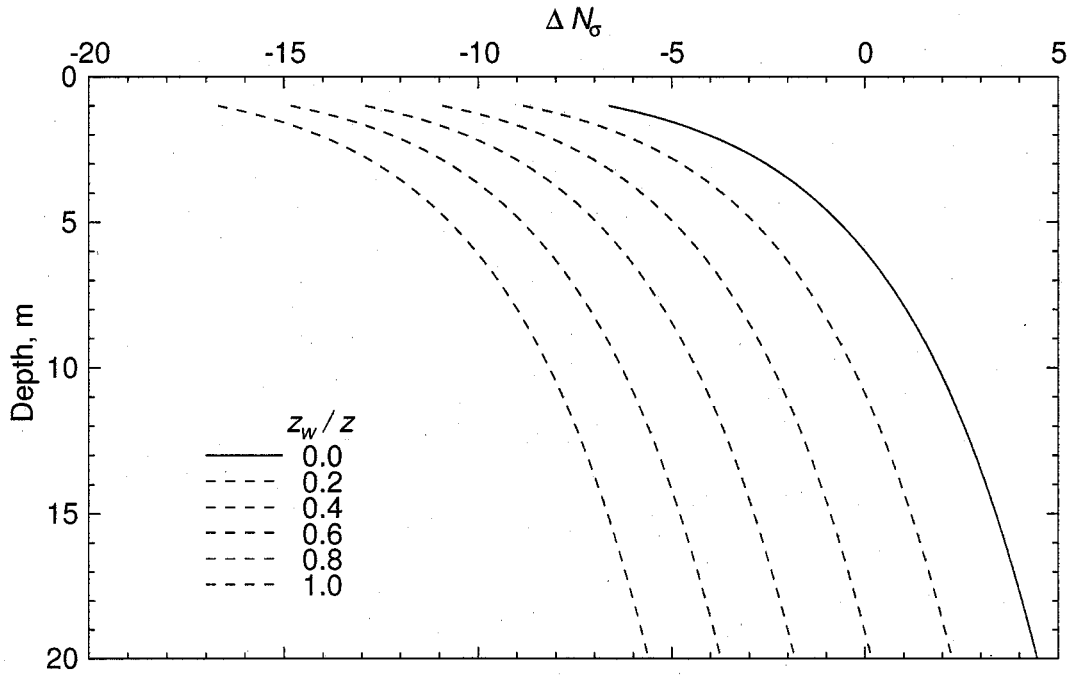


Figure B.1: The ΔN_σ adjustment factor for a range of depths and groundwater depth ratios.

For $z_{ref} = 6$ m,

$$\frac{\sigma'_{vo}}{\sigma'_{vo,ref}} = \frac{z(G_s - 1 + \frac{z_w}{z})}{6(1 + e)}$$

With these two parts,

$$\Delta N_\sigma = 13.32 \ln \left[\frac{G_s + e(1 - \frac{z_w}{z})}{2(G_s - 1 + \frac{z_w}{z})} \right] + 3.70 \ln \left[\frac{z(G_s - 1 + \frac{z_w}{z})}{6(1 + e)} \right]$$

This form can be simplified by invoking another assumption. Earlier it was noted that the densities of most inorganic soils fall within a relatively narrow range. If e and G_s are the same in the reference section and in the section of interest, then

$$\Delta N_\sigma = 13.32 \ln \left(\frac{1 - 0.2 \frac{z_w}{z}}{1 + 0.6 \frac{z_w}{z}} \right) + 3.70 \ln \left[\frac{z}{6} \left(1 + 0.6 \frac{z_w}{z} \right) \right]$$

Figure B.1 illustrates the ΔN_σ factor for a range of depths and z/z_w ratios.

B.3 Soil amplification adjustment

The second adjustment component, ΔN_F , accounts for a site-specific amplification factor different than Stewart's quaternary factor:

$$\begin{aligned}\Delta N_F &= 13.32 \ln \frac{F_a}{F_{A_{ref}}} \\ &= 13.32 (\ln F_a - \ln F_{A_{ref}})\end{aligned}$$

Substituting in the form of Stewart's factor,

$$\begin{aligned}&= 13.32 (a + b \ln a_{max_{rock}} - a_{ref} - b_{ref} \ln a_{max_{rock}}) \\ &= 13.32 [(a - a_{ref}) + (b - b_{ref}) \ln a_{max_{rock}}]\end{aligned}$$

Now, substituting in the values of the coefficients for the reference section (quaternary alluvium),

$$= 13.32 [(a + 0.15) + (b + 0.13) \ln a_{max_{rock}}]$$

When $F_a = F_{A_{ref}}$, $\Delta N_F = 0$.

B.4 Adjustment for depth reduction factor

Now for the third adjustment component, ΔN_{r_d} :

$$\Delta N_{r_d} = 13.32 \ln \frac{r_d}{r_{d_{ref}}}$$

From Çetin et al. [24],

$$r_d = \frac{1 + \frac{-23.013 - 2.949a_{max} + 0.999M_w + 0.0525V_s}{16.258 + 0.201 \exp[0.341(-z + 0.0785V_s + 7.586)]}}{1 + \frac{-23.013 - 2.949a_{max} + 0.999M_w + 0.0525V_s}{16.258 + 0.201 \exp[0.341(0.0785V_s + 7.586)]}} \pm \sigma_{\epsilon_{r_d}}$$

Ignoring the uncertainty term, which is included in σ_E of the probability of liquefaction, this can be restated as

$$r_d = \frac{1 + \frac{a + b}{c + df g}}{1 + \frac{a + b}{c + df}}$$

in which $a = -23.013 - 2.949a_{max} + 0.999M_w$, $b = 0.0525V_s$, $c = 16.258$, $d = 0.201e^{0.341 \cdot 7.586} = 2.671$, $f = e^{0.341 \cdot 0.0785V_s} = e^{0.0268V_s}$, and $g = e^{-0.341z}$. Rearranging this,

$$r_d = \frac{a + b + c + df}{a + b + c + df} \frac{c + df}{c + df}$$

Of these terms, b , f , and g involve parameters that are site-specific, while c and d are constants, and a is constant at any particular site. It is desirable to remove a from consideration so the site-specific correction procedure does not require maps of a_{max} and M_w .

Across the state of Washington, the mean values for a_{max} and M_w from deaggregating the liquefaction hazard range from 0.05g–0.5g and 6.5–8.5, respectively. In general, sites with low a_{max} also have low M_w , and vice versa. Using these ranges, a has the relatively tight limits of -16.667 to -15.998, which is very close to the negative of c . This is very convenient because all terms that include a also include c . To confirm that the residual of $a + c$ is small enough to be ignored, the other terms were evaluated with typical site parameters: for $V_s = 200$ m/s and $z = 5$ m, $b = 10.5$, $d \cdot f = 564.6$, and $d \cdot f \cdot g = 102.8$. Thus, $a + c$ is small compared to the other terms and can be safely ignored. This assumption may not be valid outside the state of Washington.

The relationship for r_d is now

$$r_d = \frac{b + df}{b + df} \cdot \frac{c + df}{c + df}$$

$$\Delta N_{r_d} = \ln \left(\frac{r_d}{r_{d_{ref}}} \right) = 13.32 \left[\ln \left(\frac{b + df}{b + df} \right) - \ln \left(\frac{c + df}{c + df} \right) - \ln r_{d_{ref}} \right]$$

For the reference section, $V_s = 175$ m/s, $z = 6$ m, and $r_{d_{ref}} = 0.889$ so

$$\Delta N_{r_d} = 13.32 \left[\ln \left(\frac{0.0525V_s + 2.671e^{0.0268V_s}e^{-0.341z}}{0.0525V_s + 2.671e^{0.0268V_s}} \right) - \ln \left(\frac{16.258 + 2.671e^{0.0268V_s}e^{-0.341z}}{16.258 + 2.671e^{0.0268V_s}} \right) + 0.118 \right]$$

Figure B.2 illustrates the ΔN_{r_d} relationship for a range of depths and V_s .

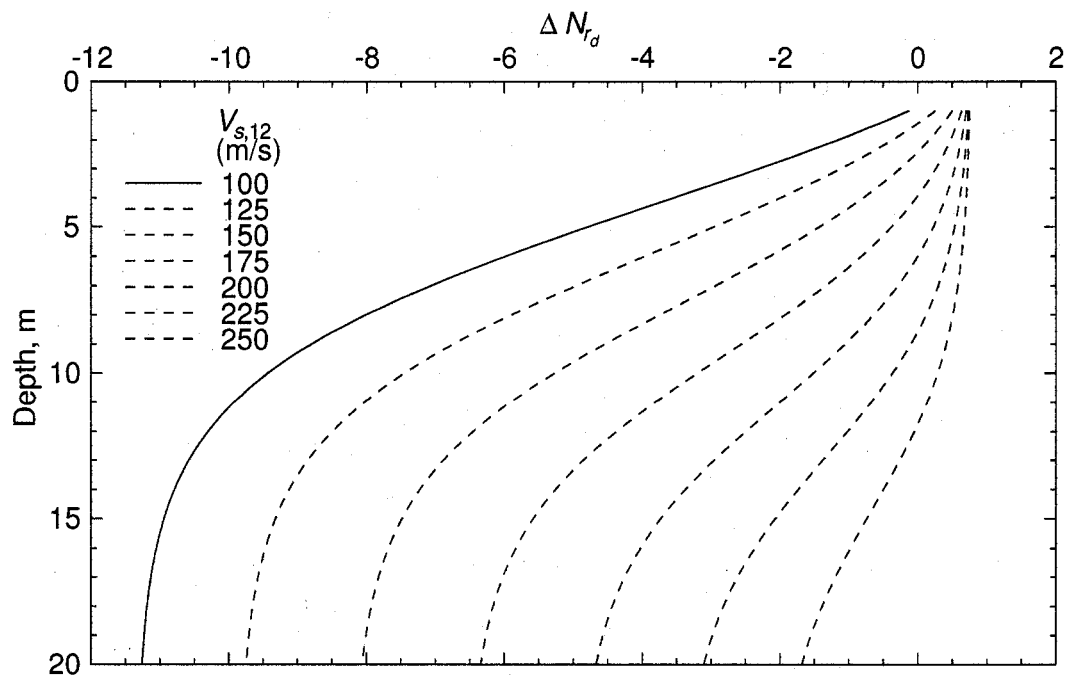


Figure B.2: The ΔN_{rd} adjustment factor for a range of depths and shear wave velocities.

B.5 Calculating the shear wave velocity

Table B.1 lists the methods that Çetin [21] used for correlating blowcounts with shear wave velocity in his calculations of V_s . He stated that the results from all of these methods were reasonably close and that he averaged the results to get his estimate of V_s . It seems reasonable then, that any of these methods could be used to estimate V_s for calculating ΔN_{rd} . From a brief review using a limited set of typical values, the relationship by Sykora and Stokoe (1983) appears to be closest to the middle of the range of results from all of these equations.

B.6 Prediction error of adjustment

Figures B.3 to B.6 illustrate the prediction error of the site-specific adjustment factor, $\varepsilon_{\Delta N_{req}}$, for various depths, shear wave velocities, soil densities, return periods, groundwater levels, and parameter uncertainties, where

Table B.1: Correlations between SPT blowcount and shear wave velocity. After Çetin [21].

Study	Soil	Relationship
Seed et al. (1983)	Sand and silty sand	$V_s = 185N_{60}^{0.5}$
Sykora and Stokoe (1983)	Granular soil	$V_s = 330N_{60}^{0.29}$
Dickenson (1994)	Sand	$V_s = 290(N_{60} + 1)^{0.30}$
Ohta and Goto (1978)	Holocene sand	$V_s = 194N^{0.173}z^{0.195}$
Ohta and Goto (1978)	Pleistocene sand	$V_s = 254N^{0.173}z^{0.195}$
Seed et al. (1984)	Sand	$V_s = 220N^{0.17}z^{0.2}$

$$\varepsilon_{\Delta N_{req}} = N_{1,60,cs,ref} + \Delta N_{req} - N_{reqPBEE}$$

Each individual box plot on the figures shows the distribution of prediction errors for 45 points: 5 depths (2, 6, 10, 15, and 20 m) at each of 9 sites representing the full range of seismic loading across Washington State (La Push, Long Beach, Bellingham, Seattle, Vancouver, Ellensburg, Omak, Walla Walla, and Spokane). The box contains the interquartile points (points in the first and third quartile), the “whiskers” extend out to 1.5 times the interquartile range, and the open circles beyond the whiskers are individual points within 3 times the interquartile range. No points were found beyond this range.

These figures show that the adjustment factor works very well. Most of the prediction errors are within 0.5 bpf of the site-specific PBEE values, and no errors are greater than 2 bpf. While 2 bpf can represent a significant difference when estimating, for example, remediation costs, it is a relatively minor amount compared to the precision of the standard penetration test.

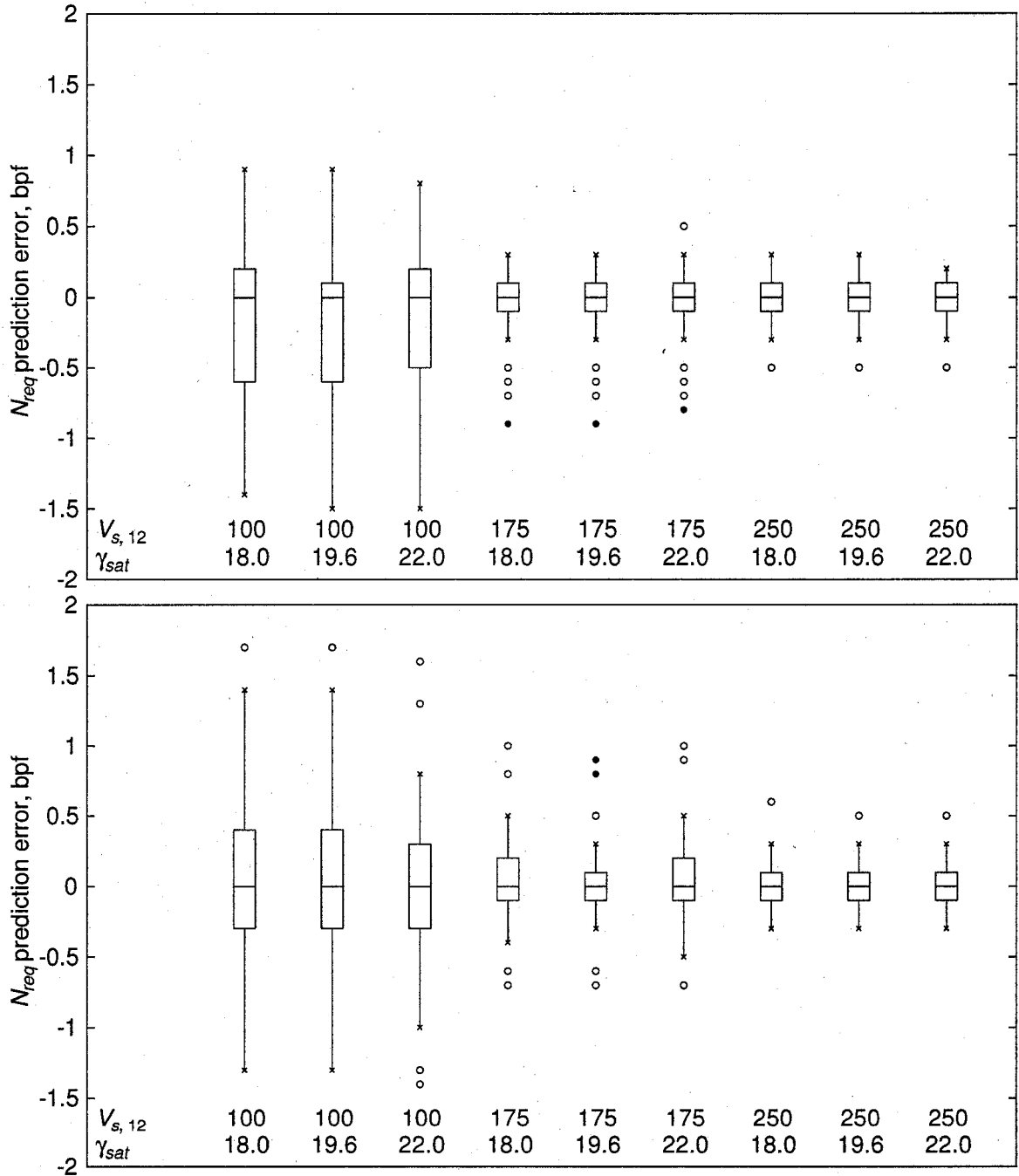


Figure B.3: N_{req} prediction error of site-specific adjustment factor for (a) 475-yr and (b) 2475-yr return periods, $z_w/z = 0$, and parameter uncertainty corresponding to a detailed site investigation ($\sigma_E = 4.21$).

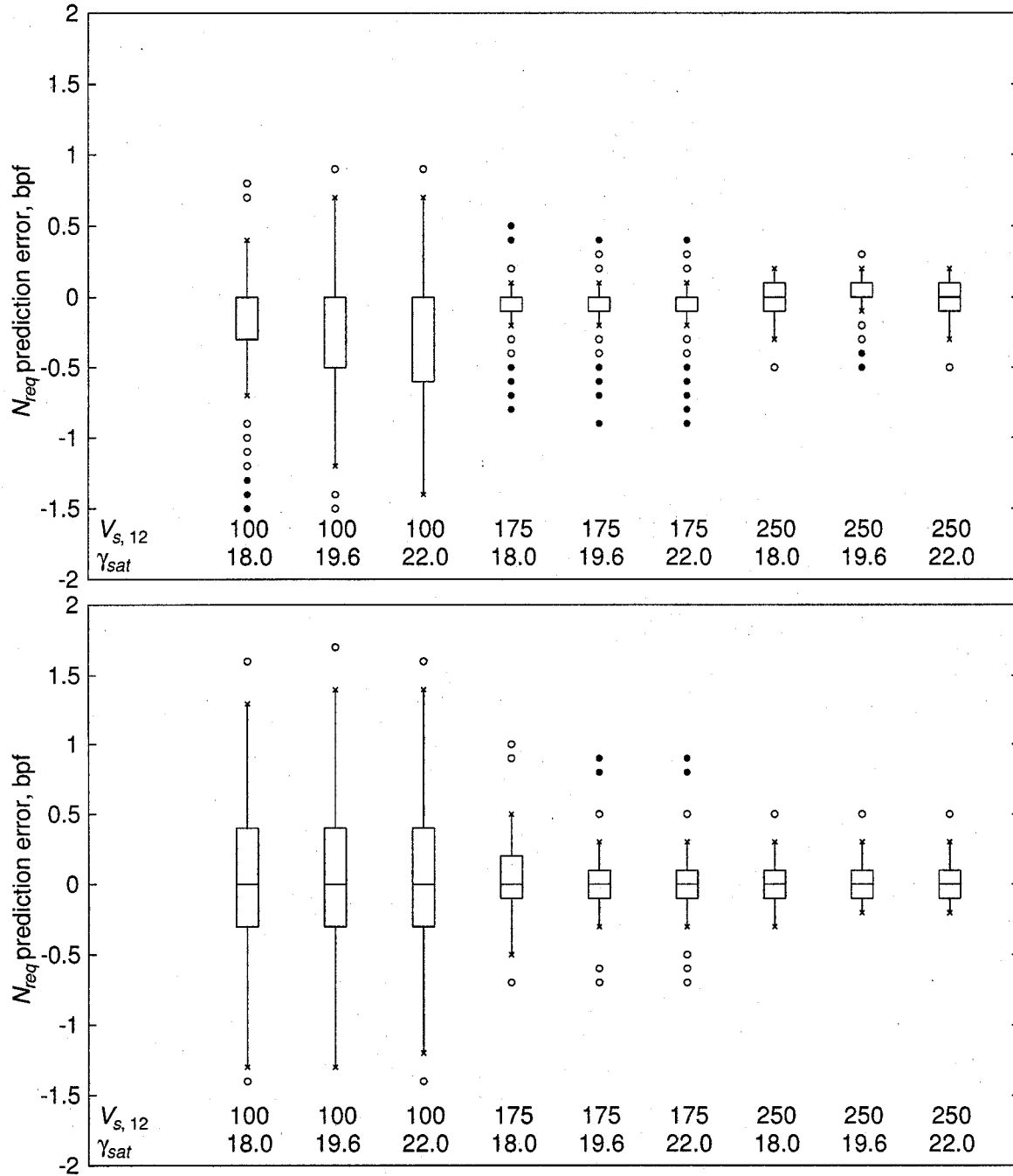


Figure B.4: N_{req} prediction error of site-specific adjustment factor for (a) 475-yr and (b) 2475-yr return periods, $z_w/z = 1$, and parameter uncertainty corresponding to a detailed site investigation ($\sigma_E = 4.21$).

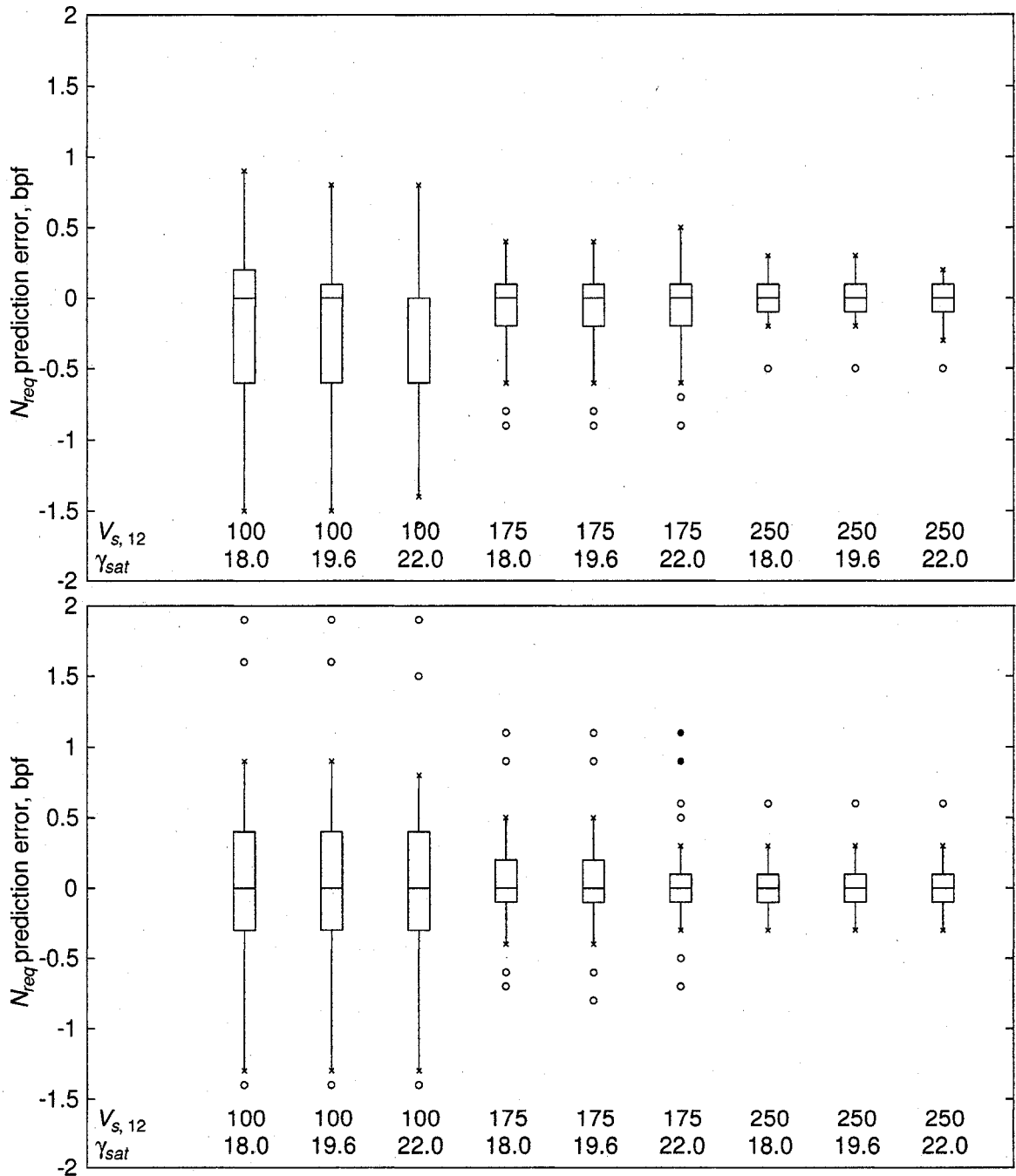


Figure B.5: N_{req} prediction error of site-specific adjustment factor for (a) 475-yr and (b) 2475-yr return periods, $z_w/z = 0$, and no parameter uncertainty ($\sigma_E = 2.70$).

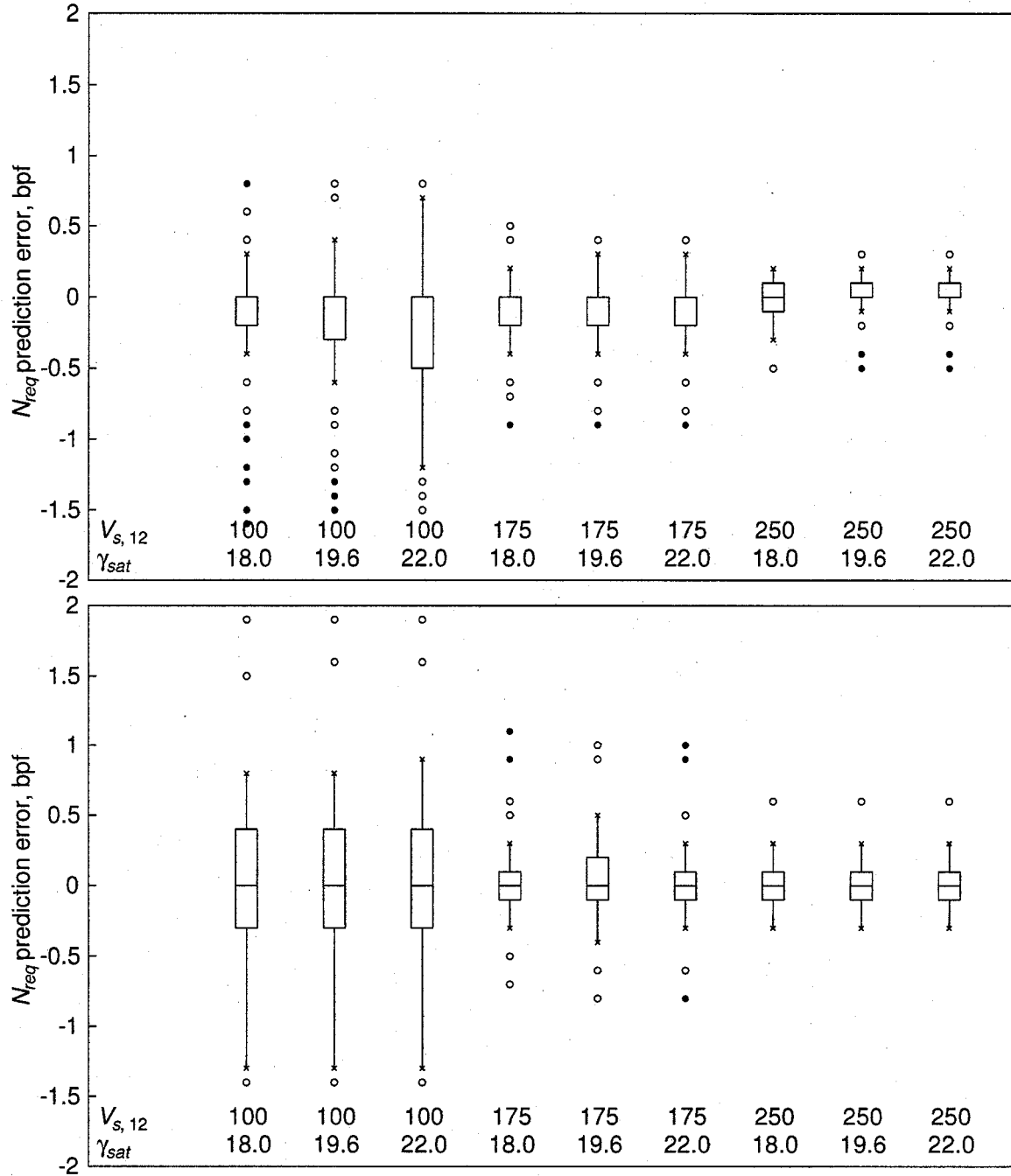


Figure B.6: N_{req} prediction error of site-specific adjustment factor for (a) 475-yr and (b) 2475-yr return periods, $z_w/z = 1$, and no parameter uncertainty ($\sigma_E = 2.70$).

Appendix C

DATA FOR CAV_5 LOGISTIC REGRESSION

The case history data that was used in the logistic regression for the CAV_5 liquefaction relationship is presented in this appendix. Because of the size of the database, it has been divided into three separate tables below. The first includes data relating to the depth and overburden pressure of the layer under consideration, the second includes data relating to the penetration resistance of the layer, and the third includes data relating to CAV_5 . All of the tables include the case number, information about the earthquake and site, and whether or not liquefaction was observed at the site.

Table C.1: Vertical effective stress parameters for CAV_5 logistic regression.

Case	Year	Earthquake	Site	Liq	z_{top} , m	z_{bot} , m	z_w , m	$\pm \sigma'_{vo}$, kPa	\pm	
1	1944	Tohnankai M8.0	Ienaga	Y	2.4	6.1	2.4	0.3	47.19	5.36
2	1944	Tohnankai M8.0	Komei	Y	2.0	5.0	2.0	0.3	38.20	4.69
3	1944	Tohnankai M8.0	Meiko	Y	0.5	3.5	0.5	0.3	16.28	4.16
4	1948	Fukui M7.3	Shonenji Temple	Y	1.2	5.5	1.2	0.3	32.21	5.63
5	1948	Fukui M7.3	Takaya 45	Y	3.7	12.2	3.7	0.3	90.83	12.95
6	1964	Niigata M7.5	Cc17-1	Y	5.0	11.0	0.9	0.3	61.06	9.82
7	1964	Niigata M7.5	Old Town 1	N	5.0	10.0	1.8	0.3	80.04	8.66
8	1964	Niigata M7.5	Old Town 2	N	10.0	13.0	1.8	0.3	116.24	7.93
9	1964	Niigata M7.5	Rail Road 1	Y	5.0	10.0	0.9	0.3	57.72	8.76
10	1964	Niigata M7.5	Rail Road 2	?	9.0	11.0	0.9	0.3	82.30	9.30
11	1964	Niigata M7.5	River Site	Y	4.0	13.0	0.6	0.3	61.82	11.49
12	1964	Niigata M7.5	Road Site	N	4.0	9.0	2.5	0.3	67.22	7.98
13	1964	Niigata M7.5	Showa Br 2	Y	1.4	6.1	0.0	0.0	24.99	5.77
14	1964	Niigata M7.5	Showa Br 4	N	5.0	7.0	1.2	0.3	61.46	4.76
15	1968	Tokachioki M7.9	Hachinohe 2	N	3.0	7.9	2.1	0.3	71.52	8.76
16	1968	Tokachioki M7.9	Hachinohe 4	N	0.9	4.0	0.9	0.3	26.96	5.06
17	1968	Tokachioki M7.9	Hachinohe 6	Y	2.0	6.1	0.6	0.3	32.15	6.79
18	1968	Tokachioki M7.9	Nanaehama 1, 2, 3	Y	0.9	5.0	0.9	0.3	25.71	5.31
19	1971	San Fernando M_w 6.6	Juvenile Hall	Y	4.4	6.3	4.3	0.6	70.93	6.11
20	1971	San Fernando M_w 6.6	Van Norman	Y	5.2	7.3	5.2	0.6	84.47	6.47
21	1975	Haicheng M_s 7.3	Panjin Chemical Fertilizer Plant	Y	3.5	12.5	1.5	0.3	66.05	11.16
22	1975	Haicheng M_s 7.3	Shuang Tai Zi River	Y	6.0	11.0	1.5	0.3	69.39	7.58
23	1975	Haicheng M_s 7.3	Ying Kou Glass Fiber Plant	Y	5.0	9.0	1.5	0.3	63.66	7.59
24	1975	Haicheng M_s 7.3	Ying Kou Paper Plant	Y	4.5	10.5	1.5	0.3	62.70	8.13
25	1976	Guatemala M7.5	Amatitlan B1	Y	3.0	15.2	1.5	0.3	47.40	9.65
26	1976	Guatemala M7.5	Amatitlan B2	?	3.0	6.1	2.4	0.3	32.23	2.98
30	1976	Tangshan M_s 7.8	Coastal Region	Y	3.0	6.0	1.2	0.3	40.16	4.73
31	1976	Tangshan M_s 7.8	Le Ting I8-14	Y	3.5	6.0	1.1	0.3	47.19	4.77
32	1976	Tangshan M_s 7.8	Qing Jia Ying	Y	4.5	6.5	0.9	0.3	52.15	4.63
33	1976	Tangshan M_s 7.8	Tangshan City	N	3.5	5.5	3.0	0.3	60.70	4.20
34	1976	Tangshan M_s 7.8	Yao Yuan Village	Y	3.5	5.0	1.0	0.3	40.01	3.79
35	1977	Argentina M7.4	San Juan B1	Y	7.9	8.5	4.6	0.3	95.58	4.39
36	1977	Argentina M7.4	San Juan B3	Y	10.2	13.1	6.7	0.3	133.22	6.65
37	1977	Argentina M7.4	San Juan B4	N	1.2	3.7	1.2	0.3	27.31	3.95
38	1977	Argentina M7.4	San Juan B5	N	2.1	3.7	2.1	0.3	38.14	3.25
39	1977	Argentina M7.4	San Juan B6	Y	3.7	5.5	1.8	0.3	46.37	3.69
54	1978	Miyagiken-Oki M7.4	Nakajima 18	Y	2.4	6.1	2.4	0.3	53.42	5.99
55	1978	Miyagiken-Oki M7.4	Arahama	Y	2.0	8.0	0.9	0.3	44.91	8.31
56	1978	Miyagiken-Oki M7.4	Hiyori 18	Y	2.5	4.0	2.4	0.3	44.37	3.57

Table C.1: Vertical effective stress parameters for CAV_5 logistic regression (cont.)

Case	Year	Earthquake	Site	Liq	z_{top} , m	z_{bot} , m	z_w , m	m	\pm	σ'_{vo} , kPa	\pm
58	1978	Miyagiken-Oki M7.4	Ishinomaki 2	Y	1.4	6.0	1.4	0.3		36.28	5.96
59	1978	Miyagiken-Oki M7.4	Ishinomaki 4	N	1.4	7.0	1.4	0.3		105.94	7.67
60	1978	Miyagiken-Oki M7.4	Kitawabuchi 2	Y	3.0	4.0	3.0	0.2		48.51	2.57
61	1978	Miyagiken-Oki M7.4	Kitawabuchi 3	Y	3.0	5.5	3.0	0.9		54.66	7.74
62	1978	Miyagiken-Oki M7.4	Nakajima 2	N	3.0	6.1	2.4	0.3		55.93	5.40
63	1978	Miyagiken-Oki M7.4	Nakamura 1	N	2.0	4.0	0.9	0.3		29.14	3.66
64	1978	Miyagiken-Oki M7.4	Nakamura 4	Y	3.0	5.0	0.5	0.3		30.88	4.03
65	1978	Miyagiken-Oki M7.4	Nakamura 5	Y	2.7	4.0	1.3	0.3		33.26	3.26
66	1978	Miyagiken-Oki M7.4	Oiri 1	Y	4.3	7.6	4.3	0.6		74.90	8.51
68	1978	Miyagiken-Oki M7.4	Shiomi 6	Y	3.0	6.0	2.4	0.3		53.72	5.14
69	1978	Miyagiken-Oki M7.4	Yuriage Br 1	Y	3.0	4.0	1.7	0.3		37.35	3.16
70	1978	Miyagiken-Oki M7.4	Yuriage Br 2	Y	1.8	3.0	1.3	0.3		27.02	3.05
71	1978	Miyagiken-Oki M7.4	Yuriage Br 3	Y	2.0	4.0	0.3	0.2		22.22	3.09
72	1978	Miyagiken-Oki M7.4	Yuriage Br 5	N	6.0	9.0	1.3	0.3		70.63	7.48
73	1978	Miyagiken-Oki M7.4	Yuriagekami 1	Y	1.8	4.9	1.8	0.3		39.24	5.09
74	1978	Miyagiken-Oki M7.4	Yuriagekami 2	Y	2.0	5.5	0.9	0.3		32.09	5.01
75	1978	Miyagiken-Oki M7.4	Yuriagekami 3	N	4.5	7.5	2.2	0.3		63.90	5.37
76	1979	Imperial Valley M_L 6.6	Radio Tower B2	N	2.0	3.0	2.0	0.3		30.84	3.16
77	1979	Imperial Valley M_L 6.6	Heber Road A1	N	1.8	5.0	1.8	0.9		44.01	7.66
78	1979	Imperial Valley M_L 6.6	Heber Road A2	Y	1.8	4.6	1.8	0.9		32.72	8.70
79	1979	Imperial Valley M_L 6.6	Heber Road A3	N	1.8	4.9	1.8	0.9		37.24	8.42
80	1979	Imperial Valley M_L 6.6	Kornbloom B	N	2.6	5.2	2.7	0.3		48.59	4.26
81	1979	Imperial Valley M_L 6.6	McKim Ranch A	Y	1.5	4.0	1.5	0.3		29.94	3.85
82	1979	Imperial Valley M_L 6.6	Radio Tower B1	Y	3.0	5.5	2.0	0.3		39.80	3.96
83	1979	Imperial Valley M_L 6.6	River Park A	Y	0.3	1.8	0.3	0.2		8.14	1.94
84	1979	Imperial Valley M_L 6.6	Wildlife B	N	2.7	6.7	0.9	0.3		35.43	6.69
85	1980	Mid-Chiba M6.1	Owi 1	N	4.0	7.0	0.9	0.3		45.06	4.92
86	1980	Mid-Chiba M6.1	Owi 2	N	13.0	16.0	0.9	0.3		105.30	7.78
87	1981	WestMorland M_L 5.6	Kornbloom B	Y	2.6	5.2	2.7	0.3		48.59	4.26
88	1981	Westmorland M_L 5.6	Radio Tower B1	Y	3.0	5.5	2.0	0.3		32.31	3.55
89	1981	Westmorland M_L 5.6	Radio Tower B2	N	2.0	3.0	2.0	0.3		30.84	3.05
90	1981	Westmorland M_L 5.6	River Park A	N	0.3	1.8	0.3	0.2		8.14	1.94
91	1981	WestMorland M_L 5.6	River Park C	N	3.4	5.2	0.3	0.2		33.94	3.53
92	1981	WestMorland M_L 5.6	Wildlife A	Y	2.7	6.7	0.9	0.3		35.43	5.25
93	1981	Westmorland M_L 5.6	McKim Ranch A	N	1.5	4.0	1.5	0.3		29.94	3.85
94	1964	Niigata M7.5	Arayamotomachi	Y	2.0	4.5	1.0	0.3		30.77	4.21
96	1968	Tokachi-Oki M7.9	Aomori Station	Y	4.0	7.5	0.0	0.3		38.48	5.88
97	1976	Tangshan M_s 7.8	Luan Nan L1	N	1.5	5.5	1.1	0.3		38.13	6.51
98	1976	Tangshan M_s 7.8	Luan Nan L2	Y	1.5	5.5	1.1	0.3		32.48	5.38

Table C.1: Vertical effective stress parameters for CAV_5 logistic regression (cont.)

Case	Year	Earthquake	Site	Liq	z_{top} , m	z_{bot} , m	z_w , m	\pm	σ'_{vo} , kPa	\pm
102	1983	Nihonkai-Chubu $M_{7.7}$	Aomori Station	Y	4.0	7.5	0.0	0.3	38.48	5.88
103	1983	Nihonkai-Chubu $M_{7.7}$	Arayamotomachi	Y	1.0	7.5	1.0	0.3	37.46	8.04
104	1983	Nihonkai-Chubu $M_{7.7}$	Gaiko Wharf B2	Y	2.5	12.5	0.4	0.3	53.40	12.28
105	1983	Nihonkai-Chubu $M_{7.7}$	Noshiro Section N7	Y	2.0	5.0	1.7	0.3	37.83	4.46
106	1983	Nihonkai-Chubu $M_{7.7}$	Takeda Elementary School	Y	2.5	6.5	0.3	0.3	33.27	5.86
107	1987	Elmore Ranch M_w 6.2	Radio Tower B1	N	3.0	5.5	2.0	0.3	39.80	3.87
108	1987	Elmore Ranch M_w 6.2	Wildlife B	N	2.7	6.7	0.9	0.3	35.43	5.25
109	1987	Superstition Hills M_w 6.7	Radio Tower B1	N	3.0	5.5	2.0	0.3	39.80	3.87
110	1988	Superstition Hills M_w 6.7	Wildlife B	Y	2.7	6.7	0.9	0.3	35.43	5.25
111	1987	Superstition Hills M_w 6.7	Heber Road A1	N	1.8	5.0	1.8	0.9	44.01	7.66
112	1987	Superstition Hills M_w 6.7	Heber Road A2	N	1.8	4.6	1.8	0.9	32.72	9.04
113	1987	Superstition Hills M_w 6.7	Heber Road A3	N	1.8	4.9	1.8	0.9	37.24	8.42
114	1987	Superstition Hills M_w 6.7	Kornbloom B	N	2.6	5.2	2.7	0.3	48.59	4.26
115	1987	Superstition Hills M_w 6.7	McKim Ranch A	N	1.5	4.0	1.5	0.3	29.94	3.85
116	1987	Superstition Hills M_w 6.7	Radio Tower B2	N	2.0	3.0	2.0	0.3	30.84	3.50
117	1987	Superstition Hills M_w 6.7	River Park A	N	0.3	1.8	0.3	0.3	8.14	3.07
118	1987	Superstition Hills M_w 6.7	River Park C	N	3.4	5.2	0.3	0.2	33.94	3.53
119	1989	Loma Prieta M_w 7.0	Alameda BF Dike	N	6.0	7.0	3.0	0.9	90.97	8.89
120	1989	Loma Prieta M_w 7.0	Farris Farm	Y	5.0	7.0	4.5	0.9	71.30	10.32
121	1989	Loma Prieta M_w 7.0	Hall Avenue	N	3.5	5.8	3.5	0.6	57.01	5.68
122	1989	Loma Prieta M_w 7.0	Marine Laboratory B1	Y	2.4	5.5	2.4	0.9	46.19	8.47
123	1989	Loma Prieta M_w 7.0	MBARI No 3 EB1	N	2.0	3.0	2.0	0.3	34.37	2.68
124	1989	Loma Prieta M_w 7.0	MBARI No 3 EB5	N	1.8	6.4	1.8	0.3	45.87	6.90
125	1989	Loma Prieta M_w 7.0	Sandholdt UC-B10	Y	1.8	3.7	1.7	0.3	32.06	3.49
126	1989	Loma Prieta M_w 7.0	Miller Farm	Y	4.0	8.0	4.0	0.3	66.79	5.20
127	1989	Loma Prieta M_w 7.0	Miller Farm CMF10	Y	7.0	8.4	3.0	0.3	66.37	4.55
128	1989	Loma Prieta M_w 7.0	Miller Farm CMF3	Y	5.8	7.5	5.7	0.9	87.50	7.42
129	1989	Loma Prieta M_w 7.0	Miller Farm CMF5	Y	5.5	8.5	4.7	0.3	92.84	5.75
130	1989	Loma Prieta M_w 7.0	Miller Farm CMF8	Y	5.0	8.0	4.9	0.3	82.58	5.18
131	1989	Loma Prieta M_w 7.0	State Beach UC-B1	Y	1.8	3.7	1.8	0.3	32.35	3.54
132	1989	Loma Prieta M_w 7.0	State Beach UC-B2	Y	2.7	6.7	2.7	0.3	56.35	5.62
133	1989	Loma Prieta M_w 7.0	POO7-2	Y	5.5	6.8	3.0	0.6	80.22	6.81
134	1989	Loma Prieta M_w 7.0	POO7-3	Y	6.0	7.0	3.0	0.3	83.12	4.38
136	1989	Loma Prieta M_w 7.0	POR-2, 3, 4	Y	4.0	5.8	3.5	0.3	52.78	3.85
138	1989	Loma Prieta M_w 7.0	SFOBB-1, 2	Y	5.5	7.0	3.0	0.3	85.96	4.87
140	1989	Loma Prieta M_w 7.0	WoodMarine UC-B4	Y	1.0	2.5	1.0	0.3	19.35	3.22
141	1989	Loma Prieta M_w 7.0	Marine Laboratory B2	Y	3.0	4.0	2.5	0.3	44.04	3.19
142	1989	Loma Prieta M_w 7.0	Treasure Island	Y	1.5	9.0	1.5	0.6	48.66	10.33
143	1990	Luzon M_w 7.6	Cereenan St B12	N	2.4	7.5	2.3	0.3	59.83	7.78
144	1990	Luzon M_w 7.6	Perez B1v B11	Y	4.0	10.5	2.3	0.3	78.84	9.91

Table C.1: Vertical effective stress parameters for CAV_5 logistic regression (cont.)

Case	Year	Earthquake	Site	Liq	z_{top} , m	z_{bot} , m	z_w , m	\pm	σ'_{vo} , kPa	\pm
145	1993	Kushiro-Oki M_w 8.0	Kushiro Port Seismo Stn	Y	19.0	22.0	1.6	0.3	198.66	12.99
146	1993	Kushiro-Oki M_w 8.0	Kushiro Port Site A	Y	4.0	6.5	2.0	0.3	57.29	4.80
147	1993	Kushiro-Oki M_w 8.0	Kushiro Port Site D	N	7.5	14.0	1.6	0.3	110.44	11.68
150	1994	Northridge M_w 6.7	Potrero Canyon C1	Y	6.0	7.0	3.3	0.3	88.49	4.02
151	1994	Northridge M_w 6.7	Wynne Ave. Unit C1	Y	5.8	6.7	4.3	0.3	93.48	4.08
152	1995	Hyogoken-Nambu M_L 7.2	Ashiyama A (Marine Sand)	N	6.9	9.0	3.5	0.3	98.00	5.28
153	1995	Hyogoken-Nambu M_L 7.2	Ashiyama A (Mountain Sand 1)	N	3.5	6.9	3.5	0.3	71.78	5.85
154	1995	Hyogoken-Nambu M_L 7.2	Ashiyama C, D, E (Marine Sand)	Y	7.5	10.0	3.5	0.3	101.11	5.82
155	1995	Hyogoken-Nambu M_L 7.2	Ashiyama C, D, E (Mountain Sand 2)	Y	12.2	15.0	3.5	0.3	141.19	8.14
156	1995	Hyogoken-Nambu M_L 7.2	Port Island Borehole Array Station	Y	2.4	13.1	2.4	0.3	94.08	18.06
157	1995	Hyogoken-Nambu M_L 7.2	Port Island Improved Site (Ikegaya)	N	5.0	12.0	5.0	0.3	120.82	12.31
158	1995	Hyogoken-Nambu M_L 7.2	Port Island Improved Site (Tanahashi)	N	5.0	15.0	5.0	0.3	135.57	17.13
159	1995	Hyogoken-Nambu M_L 7.2	Port Island Improved Site (Watanabe)	N	5.0	14.0	5.0	0.3	130.65	15.51
160	1995	Hyogoken-Nambu M_L 7.2	Port Island Site I	Y	6.0	14.0	3.0	0.3	115.18	13.22
161	1995	Hyogoken-Nambu M_L 7.2	Rokko Island Building D	Y	4.0	11.0	4.0	0.3	103.54	12.16
162	1995	Hyogoken-Nambu M_L 7.2	Rokko Island Site G	Y	4.0	19.0	4.0	0.3	136.98	23.38
163	1995	Hyogoken-Nambu M_L 7.2	Torishima Dike	Y	3.0	6.5	0.0	0.3	35.52	5.85
164	1995	Hyogoken-Nambu M_L 7.2	1	N	5.0	7.0	2.3	0.3	68.92	4.62
165	1995	Hyogoken-Nambu M_L 7.2	2	N	5.0	12.0	2.9	0.3	94.02	10.72
166	1995	Hyogoken-Nambu M_L 7.2	3	N	3.5	7.5	2.5	0.3	66.02	6.53
167	1995	Hyogoken-Nambu M_L 7.2	4	N	3.0	6.5	2.0	0.3	50.27	5.23
168	1995	Hyogoken-Nambu M_L 7.2	5	Y	6.5	11.0	3.0	0.3	99.53	7.91
169	1995	Hyogoken-Nambu M_L 7.2	6	Y	4.3	7.3	2.3	0.3	68.67	5.62
170	1995	Hyogoken-Nambu M_L 7.2	7	Y	4.3	8.3	3.2	0.3	80.55	6.76
171	1995	Hyogoken-Nambu M_L 7.2	8	Y	4.0	6.0	3.0	0.3	60.06	4.20
172	1995	Hyogoken-Nambu M_L 7.2	9	Y	3.3	5.3	2.8	0.3	58.33	4.22
173	1995	Hyogoken-Nambu M_L 7.2	10	N	6.0	9.0	4.5	0.3	96.30	5.75
174	1995	Hyogoken-Nambu M_L 7.2	11	Y	3.7	9.8	1.5	0.3	58.25	8.02
175	1995	Hyogoken-Nambu M_L 7.2	12	N	4.3	6.3	3.2	0.3	64.32	4.28
176	1995	Hyogoken-Nambu M_L 7.2	13	Y	5.0	8.0	2.3	0.3	64.24	5.27
177	1995	Hyogoken-Nambu M_L 7.2	14	N	4.3	5.3	3.1	0.3	60.08	3.71
178	1995	Hyogoken-Nambu M_L 7.2	15	Y	4.7	6.9	3.7	0.3	71.56	4.57
179	1995	Hyogoken-Nambu M_L 7.2	16	?	4.0	5.0	2.4	0.3	52.20	3.58
180	1995	Hyogoken-Nambu M_L 7.2	17	Y	3.0	6.0	0.8	0.3	36.88	4.95
181	1995	Hyogoken-Nambu M_L 7.2	18	N	9.0	12.0	7.7	0.3	155.74	7.14
182	1995	Hyogoken-Nambu M_L 7.2	19	N	7.0	8.0	6.1	0.3	112.19	4.86
183	1995	Hyogoken-Nambu M_L 7.2	20	N	4.0	8.0	2.0	0.3	66.04	6.67
184	1995	Hyogoken-Nambu M_L 7.2	21	N	3.0	4.0	1.6	0.3	42.50	3.26
185	1995	Hyogoken-Nambu M_L 7.2	22	N	4.0	8.0	2.4	0.3	69.33	6.64

Table C.1: Vertical effective stress parameters for CAV_5 logistic regression (cont.)

Case	Year	Earthquake	Site	Liq	z_{top} , m	z_{bot} , m	z_w , m	$\pm \sigma'_{vo}$, kPa	\pm	
186	1995	Hyogoken-Nambu $M_L 7.2$	23	N	4.0	6.0	3.0	0.3	66.01	4.36
187	1995	Hyogoken-Nambu $M_L 7.2$	24	Y	3.0	4.0	2.3	0.3	48.26	3.30
188	1995	Hyogoken-Nambu $M_L 7.2$	25	N	3.0	4.0	2.2	0.3	46.62	3.28
189	1995	Hyogoken-Nambu $M_L 7.2$	26	N	3.0	4.0	0.9	0.3	34.29	3.48
190	1995	Hyogoken-Nambu $M_L 7.2$	27	N	2.0	3.0	1.0	0.3	26.20	3.17
191	1995	Hyogoken-Nambu $M_L 7.2$	28	Y	4.0	5.0	1.7	0.3	45.89	3.61
192	1995	Hyogoken-Nambu $M_L 7.2$	29	Y	3.0	4.5	2.0	0.3	44.51	3.55
193	1995	Hyogoken-Nambu $M_L 7.2$	30	N	7.0	10.0	1.5	0.3	70.41	6.24
194	1995	Hyogoken-Nambu $M_L 7.2$	31	N	3.0	5.0	1.2	0.3	39.79	4.02
195	1995	Hyogoken-Nambu $M_L 7.2$	32	N	2.0	5.0	1.4	0.3	33.30	4.33
196	1995	Hyogoken-Nambu $M_L 7.2$	33	N	7.0	9.0	2.0	0.3	71.57	5.32
197	1995	Hyogoken-Nambu $M_L 7.2$	34	Y	4.0	10.0	1.8	0.3	63.07	8.02
198	1995	Hyogoken-Nambu $M_L 7.2$	35	Y	3.0	6.0	2.0	0.3	48.60	4.77
199	1995	Hyogoken-Nambu $M_L 7.2$	36	N	3.0	4.0	0.9	0.3	31.90	3.42
200	1995	Hyogoken-Nambu $M_L 7.2$	37	Y	2.0	6.0	4.0	0.3	62.83	5.81
201	1995	Hyogoken-Nambu $M_L 7.2$	38	N	6.0	10.0	3.0	0.3	80.59	6.39
202	1995	Hyogoken-Nambu $M_L 7.2$	39	N	4.0	5.0	2.6	0.3	58.59	3.50
203	1995	Hyogoken-Nambu $M_L 7.2$	40	N	3.0	4.0	2.8	0.3	54.17	3.57
204	1995	Hyogoken-Nambu $M_L 7.2$	41	Y	2.3	6.0	2.0	0.3	48.88	5.72
205	1995	Hyogoken-Nambu $M_L 7.2$	42	Y	4.0	6.0	1.2	0.3	39.90	4.22
206	1995	Hyogoken-Nambu $M_L 7.2$	43	Y	4.1	5.2	2.2	0.3	50.50	3.62
207	1995	Hyogoken-Nambu $M_L 7.2$	44	Y	3.0	5.0	1.6	0.3	37.60	3.84
208	1999	Chi M_w 7.6	Chiaya CHY104	Y	3.0	14.5	2.0	0.5	98.63	18.78
209	1999	Chi M_w 7.6	Yuanlin TCU110 upper	Y	6.0	9.0	1.5	0.5	75.74	4.21
213	1973	Miyagiken-Oki $M6.1$	Arahama	N	2.0	8.0	0.9	0.3	44.91	8.31
214	1973	Miyagiken-Oki $M6.1$	Nakamura 4	N	3.0	5.0	0.5	0.3	30.88	4.03
215	1973	Miyagiken-Oki $M6.1$	Nakamura 5	N	2.7	4.0	1.3	0.3	33.26	3.26
216	1973	Miyagiken-Oki $M6.1$	Yuriage Br 1	N	3.0	4.0	1.7	0.3	37.35	3.16
217	1973	Miyagiken-Oki $M6.1$	Yuriage Br 2	N	1.8	3.0	1.3	0.3	27.02	3.05
218	1973	Miyagiken-Oki $M6.1$	Yuriage Br 3	N	2.0	4.0	0.3	0.2	22.22	3.09
219	1973	Miyagiken-Oki $M6.1$	Yuriage Br 5	N	6.0	9.0	1.3	0.3	70.63	7.48
220	1973	Miyagiken-Oki $M6.1$	Yuriagekami 1	N	1.8	4.9	1.8	0.3	39.24	5.09
221	1973	Miyagiken-Oki $M6.1$	Yuriagekami 2	N	2.0	5.5	0.9	0.3	32.09	5.01
222	1973	Miyagiken-Oki $M6.1$	Yuriagekami 3	N	4.5	7.5	2.2	0.3	63.90	5.37

Table C.2: Penetration resistance parameters for CAV_5 logistic regression.

Case	Year	Earthquake	Site	Liq	FC, %	$\pm N_{60}$	$N_{1,60}$	$\pm N_{1,60,cs}$
1	1944	Tohnankai M8.0	Ienaga	Y	25	3.0	1.5	2.6 0.8 7.6
2	1944	Tohnankai M8.0	Komei	Y	13	1.0	5.9	10.1 2.9 12.6
3	1944	Tohnankai M8.0	Meiko	Y	27	3.0	1.8	3.1 1.6 8.3
4	1948	Fukui M7.3	Shonenji Temple	Y	0	0.0	3.8	6.5 2.2 6.5
5	1948	Fukui M7.3	Takaya 45	Y	4	1.0	20.9	21.9 3.5 21.9
6	1964	Niigata M7.5	Cc17-1	Y	8	2.0	9.6	12.4 3.1 12.8
7	1964	Niigata M7.5	Old Town 1	N	8	2.0	20.8	23.0 0.7 23.3
8	1964	Niigata M7.5	Old Town 2	N	8	2.0	29.8	28.3 3.3 28.6
9	1964	Niigata M7.5	Rail Road 1	Y	8	2.0	10.1	13.4 1.6 13.7
10	1964	Niigata M7.5	Rail Road 2	?	2	2.0	17.4	19.1 2.5 19.1
11	1964	Niigata M7.5	River Site	Y	0	0.0	9.0	11.6 4.3 11.6
12	1964	Niigata M7.5	Road Site	N	0	0.0	12.7	15.5 3.9 15.5
13	1964	Niigata M7.5	Showa Br 2	Y	10	3.0	3.8	6.5 0.6 7.6
14	1964	Niigata M7.5	Showa Br 4	N	0	0.0	34.4	39.9 3.4 39.9
15	1968	Tokachioki M7.9	Hachinohe 2	N	5	2.0	32.2	36.1 2.8 36.1
16	1968	Tokachioki M7.9	Hachinohe 4	N	5	2.0	13.8	23.5 2.6 23.5
17	1968	Tokachioki M7.9	Hachinohe 6	Y	5	2.0	4.4	7.5 0.9 7.5
18	1968	Tokachioki M7.9	Nanaehama 1, 2, 3	Y	20	3.0	5.4	9.2 1.4 13.6
19	1971	San Fernando M _w 6.6	Juvenile Hall	Y	55	5.0	3.5	4.4 1.0 9.9
20	1971	San Fernando M _w 6.6	Van Norman	Y	50	5.0	7.7	8.6 2.8 14.1
21	1975	Haicheng M _s 7.3	Panjin Chemical Fertilizer Plant	Y	67	7.0	6.8	8.7 1.2 14.2
22	1975	Haicheng M _s 7.3	Shuang Tai Zi River	Y	5	2.0	9.5	11.6 1.8 11.6
23	1975	Haicheng M _s 7.3	Ying Kou Glass Fiber Plant	Y	48	5.0	12.1	15.2 1.1 20.7
24	1975	Haicheng M _s 7.3	Ying Kou Paper Plant	Y	5	2.0	10.1	12.9 4.0 12.9
25	1976	Guatemala M7.5	Amatitlan B1	Y	3	1.0	3.2	5.1 1.5 5.1
26	1976	Guatemala M7.5	Amatitlan B2	?	3	1.0	4.9	8.4 1.1 8.4
30	1976	Tangshan M _s 7.8	Coastal Region	Y	12	3.0	8.6	13.6 3.2 15.7
31	1976	Tangshan M _s 7.8	Le Ting L8-14	Y	12	3.0	9.0	13.3 2.6 15.3
32	1976	Tangshan M _s 7.8	Qing Jia Ying	Y	20	3.0	17.1	22.5 2.6 27.0
33	1976	Tangshan M _s 7.8	Tangshan City	N	10	2.0	26.7	32.0 5.8 33.1
34	1976	Tangshan M _s 7.8	Yao Yuan Village	Y	5	3.0	7.7	13.1 5.3 13.1
35	1977	Argentina M7.4	San Juan B1	Y	20	3.0	6.7	6.9 1.5 11.4
36	1977	Argentina M7.4	San Juan B3	Y	20	3.0	8.6	7.3 1.0 11.8
37	1977	Argentina M7.4	San Juan B4	N	4	1.5	7.9	13.5 0.6 13.5
38	1977	Argentina M7.4	San Juan B5	N	3	1.0	9.2	15.6 0.1 15.6
39	1977	Argentina M7.4	San Juan B6	Y	50	5.0	4.0	6.3 0.2 11.8
54	1978	Miyagiken-Oki M7.4	Nakajima 18	Y	3	1.0	9.4	13.0 5.3 13.0
55	1978	Miyagiken-Oki M7.4	Arahama	Y	0	0.0	9.0	13.5 3.6 13.5
56	1978	Miyagiken-Oki M7.4	Hiyori 18	Y	20	3.0	8.5	12.9 2.7 17.4

Table C.2: Penetration resistance parameters for CAV_5 logistic regression (cont.)

Case	Year	Earthquake	Site	Liq	FC, %	$\pm N_{60}$	$N_{1,60}$	$\pm N_{1,60,cs}$	
58	1978	Miyagiken-Oki M7.4	Ishinomaki 2	Y	10	2.0	3.7	6.3 0.7	7.4
59	1978	Miyagiken-Oki M7.4	Ishinomaki 4	N	10	2.0	26.5	26.1 2.4	27.2
60	1978	Miyagiken-Oki M7.4	Kitawabuchi 2	Y	5	2.0	9.6	13.8 2.9	13.8
61	1978	Miyagiken-Oki M7.4	Kitawabuchi 3	Y	0	0.0	14.3	18.9 7.3	18.9
62	1978	Miyagiken-Oki M7.4	Nakajima 2	N	26	5.0	11.8	15.6 3.1	20.8
63	1978	Miyagiken-Oki M7.4	Nakamura 1	N	4	1.0	14.8	25.2 7.2	25.2
64	1978	Miyagiken-Oki M7.4	Nakamura 4	Y	5	1.0	4.9	8.4 0.7	8.4
65	1978	Miyagiken-Oki M7.4	Nakamura 5	Y	7	2.0	6.1	10.3 2.0	10.4
66	1978	Miyagiken-Oki M7.4	Oiiri 1	Y	5	3.0	8.7	10.2 2.2	10.2
68	1978	Miyagiken-Oki M7.4	Shiomi 6	Y	10	2.0	7.2	10.2 2.3	11.3
69	1978	Miyagiken-Oki M7.4	Yuriage Br 1	Y	5	1.0	2.6	4.4 1.8	4.4
70	1978	Miyagiken-Oki M7.4	Yuriage Br 2	Y	7	1.0	10.5	17.8 2.8	17.9
71	1978	Miyagiken-Oki M7.4	Yuriage Br 3	Y	12	2.0	6.0	10.2 2.1	12.3
72	1978	Miyagiken-Oki M7.4	Yuriage Br 5	N	17	3.0	22.7	26.1 8.6	30.0
73	1978	Miyagiken-Oki M7.4	Yuriagekami 1	Y	60	5.0	1.8	3.1 1.2	8.6
74	1978	Miyagiken-Oki M7.4	Yuriagekami 2	Y	0	0.0	7.7	13.1 5.2	13.1
75	1978	Miyagiken-Oki M7.4	Yuriagekami 3	N	0	0.0	22.4	26.7 2.5	26.7
76	1979	Imperial Valley M _L 6.6	Radio Tower B2	N	30	5.0	9.7	16.4 2.8	21.8
77	1979	Imperial Valley M _L 6.6	Heber Road A1	N	25	4.0	30.5	39.3 3.6	44.4
78	1979	Imperial Valley M _L 6.6	Heber Road A2	Y	29	4.5	2.2	3.8 2.4	9.1
79	1979	Imperial Valley M _L 6.6	Heber Road A3	N	37	5.0	12.2	19.1 6.1	24.6
80	1979	Imperial Valley M _L 6.6	Kornbloom B	N	92	10.0	5.1	7.8 3.5	13.3
81	1979	Imperial Valley M _L 6.6	McKim Ranch A	Y	31	3.0	4.7	8.1 4.2	13.5
82	1979	Imperial Valley M _L 6.6	Radio Tower B1	Y	75	10.0	4.4	7.5 5.2	13.0
83	1979	Imperial Valley M _L 6.6	River Park A	Y	80	10.0	2.0	3.4 3.4	8.9
84	1979	Imperial Valley M _L 6.6	Wildlife B	N	40	3.0	7.8	13.3 5.7	18.8
85	1980	Mid-Chiba M6.1	Owi 1	N	13	1.0	4.3	6.9 0.6	9.4
86	1980	Mid-Chiba M6.1	Owi 2	N	27	1.0	3.9	3.8 0.6	9.0
87	1981	WestMorland M _L 5.6	Kornbloom B	Y	92	10.0	5.1	7.8 3.5	13.3
88	1981	WestMorland M _L 5.6	Radio Tower B1	Y	75	10.0	4.4	7.5 5.2	13.0
89	1981	WestMorland M _L 5.6	Radio Tower B2	N	30	5.0	9.7	16.4 2.8	21.8
90	1981	WestMorland M _L 5.6	River Park A	N	80	10.0	2.0	3.4 3.4	8.9
91	1981	WestMorland M _L 5.6	River Park C	N	18	3.0	12.0	20.4 7.7	24.5
92	1981	WestMorland M _L 5.6	Wildlife A	Y	40	3.0	7.8	13.3 5.7	18.8
93	1981	WestMorland M _L 5.6	McKim Ranch A	N	31	3.0	4.7	8.1 4.2	13.5
94	1964	Niigata M7.5	Arayamotomachi	Y	5	2.0	2.7	4.6 2.6	4.6
96	1968	Tokachi-Oki M7.9	Aomori Station	Y	3	1.0	10.3	16.3 1.6	16.3
97	1976	Tangshan M _s 7.8	Luan Nan L1	N	5	3.0	16.8	24.8 3.6	24.8
98	1976	Tangshan M _s 7.8	Luan Nan L2	Y	3	2.0	5.1	8.7 0.9	8.7

Table C.2: Penetration resistance parameters for CAV₅ logistic regression (cont.)

Case	Year	Earthquake	Site	Liq	FC, %	\pm	N_{60}	$N_{1,60}$	\pm	$N_{1,60,cs}$
102	1983	Nihonkai-Chubu M_w 7.7	Aomori Station	Y	3	1.0	10.3	16.3	1.6	16.3
103	1983	Nihonkai-Chubu M_w 7.7	Arayamotomachi	Y	15	4.0	5.6	9.5	4.9	12.7
104	1983	Nihonkai-Chubu M_w 7.7	Gaiko Wharf B2	Y	1	1.0	9.2	12.7	2.9	12.7
105	1983	Nihonkai-Chubu M_w 7.7	Noshiro Section N7	Y	1	1.0	10.3	16.4	3.6	16.4
106	1983	Nihonkai-Chubu M_w 7.7	Takeda Elementary School	Y	0	1.0	8.6	14.6	1.6	14.6
107	1987	Elmore Ranch M_w 6.2	Radio Tower B1	N	75	10.0	4.4	7.5	5.2	13.0
108	1987	Elmore Ranch M_w 6.2	Wildlife B	N	40	3.0	7.8	13.3	5.7	18.8
109	1987	Superstition Hills M_w 6.7	Radio Tower B1	N	75	10.0	4.4	7.5	5.2	13.0
110	1988	Superstition Hills M_w 6.7	Wildlife B	Y	40	3.0	7.8	13.3	5.7	18.8
111	1987	Superstition Hills M_w 6.7	Heber Road A1	N	25	4.0	29.7	38.4	3.6	43.5
112	1987	Superstition Hills M_w 6.7	Heber Road A2	N	29	4.5	2.2	3.8	2.4	9.1
113	1987	Superstition Hills M_w 6.7	Heber Road A3	N	37	5.0	12.2	19.1	6.1	24.6
114	1987	Superstition Hills M_w 6.7	Kornbloom B	N	92	10.0	5.1	7.8	3.5	13.3
115	1987	Superstition Hills M_w 6.7	McKim Ranch A	N	31	3.0	4.7	8.1	4.2	13.5
116	1987	Superstition Hills M_w 6.7	Radio Tower B2	N	30	5.0	9.7	16.4	2.8	21.8
117	1987	Superstition Hills M_w 6.7	River Park A	N	80	10.0	2.0	3.4	3.4	8.9
118	1987	Superstition Hills M_w 6.7	River Park C	N	18	3.0	12.0	20.4	7.7	24.5
119	1989	Loma Prieta M_w 7.0	Alameda BF Dike	N	7	2.0	41.4	42.6	1.8	42.8
120	1989	Loma Prieta M_w 7.0	Farris Farm	Y	8	2.0	9.4	11.3	2.5	11.7
121	1989	Loma Prieta M_w 7.0	Hall Avenue	N	30	7.0	4.1	5.8	3.7	11.1
122	1989	Loma Prieta M_w 7.0	Marine Laboratory B1	Y	3	1.0	8.7	12.9	0.9	12.9
123	1989	Loma Prieta M_w 7.0	MBARI No 3 EB1	N	1	2.0	14.3	24.3	3.5	24.3
124	1989	Loma Prieta M_w 7.0	MBARI No 3 EB5	N	1	2.0	13.0	18.6	3.5	18.6
125	1989	Loma Prieta M_w 7.0	Sandholdt UC-B10	Y	2	2.0	9.3	15.8	1.0	15.8
126	1989	Loma Prieta M_w 7.0	Miller Farm	Y	22	3.0	8.3	10.4	4.4	15.2
127	1989	Loma Prieta M_w 7.0	Miller Farm CMF10	Y	20	3.0	13.2	16.1	2.5	20.6
128	1989	Loma Prieta M_w 7.0	Miller Farm CMF3	Y	27	5.0	11.0	11.9	4.1	17.1
129	1989	Loma Prieta M_w 7.0	Miller Farm CMF5	Y	13	2.0	21.5	22.3	3.5	24.8
130	1989	Loma Prieta M_w 7.0	Miller Farm CMF8	Y	15	2.0	9.5	10.6	1.0	13.9
131	1989	Loma Prieta M_w 7.0	State Beach UC-B1	Y	2	2.0	4.9	8.4	1.6	8.4
132	1989	Loma Prieta M_w 7.0	State Beach UC-B2	Y	1	2.0	14.6	19.0	2.5	19.0
133	1989	Loma Prieta M_w 7.0	POO7-2	Y	3	1.0	11.9	13.4	3.1	13.4
134	1989	Loma Prieta M_w 7.0	POO7-3	Y	5	1.0	12.3	13.6	4.1	13.6
135	1989	Loma Prieta M_w 7.0	POR-2, 3, 4	Y	50	5.0	2.8	4.2	1.2	9.7
136	1989	Loma Prieta M_w 7.0	SFOB-1, 2	Y	8	3.0	7.6	8.4	2.2	8.7
137	1989	Loma Prieta M_w 7.0	WoodMarine UC-B4	Y	35	5.0	4.8	8.2	0.3	13.7
138	1989	Loma Prieta M_w 7.0	Marine Laboratory B2	Y	3	1.0	10.8	16.1	3.5	16.1
139	1989	Loma Prieta M_w 7.0	Treasure Island	Y	20	4.0	5.4	8.2	4.6	12.7
140	1989	Loma Prieta M_w 7.0	Cereenan St B12	N	19	2.0	20.6	25.4	5.3	29.7
141	1990	Luzon M_w 7.6	Perez B1v B11	Y	19	2.0	12.7	14.4	2.8	18.7

Table C.2: Penetration resistance parameters for CAV_5 logistic regression (cont.)

Case	Year	Earthquake	Site	Liq	FC, %	\pm	N_{60}	\pm	$N_{i,60}$	\pm	$N_{i,60,cs}$
145	1993	Kushiro-Oki M_w 8.0	Kushiro Port Seismo Stn	Y	10	3.0	10.4	7.1	1.9	8.2	
146	1993	Kushiro-Oki M_w 8.0	Kushiro Port Site A	Y	2	1.0	13.3	17.3	4.2	17.3	
147	1993	Kushiro-Oki M_w 8.0	Kushiro Port Site D	N	0	1.0	32.6	31.6	3.6	31.6	
150	1994	Northridge M_w 6.7	Potrero Canyon C1	Y	37	5.0	10.1	10.8	0.7	16.3	
151	1994	Northridge M_w 6.7	Wynne Ave. Unit C1	Y	38	23.0	10.9	11.4	1.6	16.9	
152	1995	Hyogoken-Nambu M_L 7.2	Ashiyama A (Marine Sand)	N	2	1.0	31.6	32.0	5.9	32.0	
153	1995	Hyogoken-Nambu M_L 7.2	Ashiyama A (Mountain Sand 1)	N	18	4.0	18.6	21.6	7.1	25.7	
154	1995	Hyogoken-Nambu M_L 7.2	Ashiyama C, D, E (Marine Sand)	Y	2	1.0	13.3	13.3	3.1	13.3	
155	1995	Hyogoken-Nambu M_L 7.2	Ashiyama C, D, E (Mountain Sand 2)	Y	18	4.0	7.1	5.8	2.8	9.9	
156	1995	Hyogoken-Nambu M_L 7.2	Port Island Borehole Array Station	Y	20	5.0	6.8	7.1	1.7	11.6	
157	1995	Hyogoken-Nambu M_L 7.2	Port Island Improved Site (Ikegaya)	N	20	5.0	24.6	22.9	4.1	27.3	
158	1995	Hyogoken-Nambu M_L 7.2	Port Island Improved Site (Tanahashi)	N	20	5.0	22.1	19.5	3.3	23.9	
159	1995	Hyogoken-Nambu M_L 7.2	Port Island Improved Site (Watanabe)	N	20	5.0	37.4	34.4	7.0	38.9	
160	1995	Hyogoken-Nambu M_L 7.2	Port Island Site I	Y	20	5.0	11.9	11.1	1.8	15.6	
161	1995	Hyogoken-Nambu M_L 7.2	Rokko Island Building D	Y	25	5.0	17.8	17.6	6.9	22.7	
162	1995	Hyogoken-Nambu M_L 7.2	Rokko Island Site G	Y	20	5.0	14.5	12.4	3.5	16.9	
163	1995	Hyogoken-Nambu M_L 7.2	Torishima Dike	Y	20	7.0	9.5	16.1	3.5	20.5	
164	1995	Hyogoken-Nambu M_L 7.2		N	4	1.5	48.9	53.3	3.2	53.3	
165	1995	Hyogoken-Nambu M_L 7.2		N	15	5.0	42.3	43.2	9.6	46.4	
166	1995	Hyogoken-Nambu M_L 7.2		N	4	1.0	45.2	50.1	7.2	50.1	
167	1995	Hyogoken-Nambu M_L 7.2		N	4	1.0	31.5	39.0	5.3	39.0	
168	1995	Hyogoken-Nambu M_L 7.2		Y	2	1.0	7.0	7.1	1.6	7.1	
169	1995	Hyogoken-Nambu M_L 7.2		Y	25	3.0	19.2	22.6	3.9	27.7	
170	1995	Hyogoken-Nambu M_L 7.2		Y	0	0.0	25.0	27.3	1.7	27.3	
171	1995	Hyogoken-Nambu M_L 7.2		Y	0	0.0	19.4	24.1	2.9	24.1	
172	1995	Hyogoken-Nambu M_L 7.2		Y	3	1.0	9.5	12.5	5.3	12.5	
173	1995	Hyogoken-Nambu M_L 7.2		N	9	1.0	27.7	28.2	4.2	28.9	
174	1995	Hyogoken-Nambu M_L 7.2		Y	5	1.0	6.5	8.8	2.3	8.8	
175	1995	Hyogoken-Nambu M_L 7.2		N	13	3.0	21.9	26.1	1.3	28.6	
176	1995	Hyogoken-Nambu M_L 7.2		Y	18	3.0	10.9	13.7	1.5	17.8	
177	1995	Hyogoken-Nambu M_L 7.2		N	18	3.0	17.9	22.3	2.3	26.3	
178	1995	Hyogoken-Nambu M_L 7.2		Y	5	2.0	17.2	20.0	4.4	20.0	
179	1995	Hyogoken-Nambu M_L 7.2		?	5	1.0	19.3	25.2	1.5	25.2	
180	1995	Hyogoken-Nambu M_L 7.2		Y	5	1.0	14.4	22.1	7.9	22.1	
181	1995	Hyogoken-Nambu M_L 7.2		N	0	0.0	49.5	44.0	4.1	44.0	
182	1995	Hyogoken-Nambu M_L 7.2		N	10	1.0	23.6	22.6	1.0	23.7	
183	1995	Hyogoken-Nambu M_L 7.2		N	0	0.0	53.6	58.3	2.0	58.3	
184	1995	Hyogoken-Nambu M_L 7.2		N	0	0.0	24.3	32.7	3.2	32.7	
185	1995	Hyogoken-Nambu M_L 7.2		N	6	2.0	34.6	38.8	2.2	38.9	

Table C.2: Penetration resistance parameters for CAV_5 logistic regression (cont.)

Case	Year	Earthquake	Site	Liq	FC, %	$\pm N_{60}$	$N_{1,60}$	$\pm N_{1,60,cs}$
186	1995	Hyogoken-Nambu $M_L 7.2$	23	N	8	2.0	20.2	24.1 1.0 24.5
187	1995	Hyogoken-Nambu $M_L 7.2$	24	Y	0	0.0	17.9	24.2 1.4 24.2
188	1995	Hyogoken-Nambu $M_L 7.2$	25	N	4	1.0	27.6	35.5 1.2 35.5
189	1995	Hyogoken-Nambu $M_L 7.2$	26	N	0	0.0	25.8	36.5 6.8 36.5
190	1995	Hyogoken-Nambu $M_L 7.2$	27	N	10	2.0	27.3	40.7 5.7 41.8
191	1995	Hyogoken-Nambu $M_L 7.2$	28	Y	10	2.0	18.3	25.1 4.0 26.2
192	1995	Hyogoken-Nambu $M_L 7.2$	29	Y	0	0.0	12.8	18.6 3.4 18.6
193	1995	Hyogoken-Nambu $M_L 7.2$	30	N	10	1.0	37.1	41.2 6.6 42.4
194	1995	Hyogoken-Nambu $M_L 7.2$	31	N	0	0.0	38.6	48.7 6.3 48.7
195	1995	Hyogoken-Nambu $M_L 7.2$	32	N	6	2.0	18.9	28.7 3.5 28.7
196	1995	Hyogoken-Nambu $M_L 7.2$	33	N	50	5.0	26.1	29.7 2.1 35.2
197	1995	Hyogoken-Nambu $M_L 7.2$	34	Y	9	1.0	21.0	25.3 3.7 26.0
198	1995	Hyogoken-Nambu $M_L 7.2$	35	Y	8	2.0	13.6	18.9 2.6 19.3
199	1995	Hyogoken-Nambu $M_L 7.2$	36	N	3	1.0	21.2	31.7 1.5 31.7
200	1995	Hyogoken-Nambu $M_L 7.2$	37	Y	0	0.0	18.1	22.2 3.1 22.2
201	1995	Hyogoken-Nambu $M_L 7.2$	38	Y	5	1.0	18.4	20.4 2.8 20.4
202	1995	Hyogoken-Nambu $M_L 7.2$	39	N	0	0.0	51.6	57.6 4.4 57.6
203	1995	Hyogoken-Nambu $M_L 7.2$	40	N	0	0.0	32.8	39.6 0.8 39.6
204	1995	Hyogoken-Nambu $M_L 7.2$	41	Y	0	0.0	10.5	15.0 2.9 15.0
205	1995	Hyogoken-Nambu $M_L 7.2$	42	Y	10	1.0	7.9	12.7 0.5 13.8
206	1995	Hyogoken-Nambu $M_L 7.2$	43	Y	20	2.0	11.0	15.4 0.3 19.9
207	1995	Hyogoken-Nambu $M_L 7.2$	44	Y	5	1.0	5.0	8.5 2.0 8.5
208	1999	Chi Chi $M_w 7.6$	Chiaya CHY104	Y	84	8.0	7.3	7.4 0.0 12.9
209	1999	Chi Chi $M_w 7.6$	Yuanlin TCU110 upper	Y	87	9.0	4.1	4.8 0.0 10.3
213	1973	Miyagiken-Oki M6.1	Arahama	N	0	0.0	9.0	13.5 3.6 13.5
214	1973	Miyagiken-Oki M6.1	Nakamura 4	N	5	1.0	4.9	8.4 0.7 8.4
215	1973	Miyagiken-Oki M6.1	Nakamura 5	N	7	2.0	6.1	10.3 2.0 10.4
216	1973	Miyagiken-Oki M6.1	Yuriage Br 1	N	5	1.0	2.6	4.4 1.8 4.4
217	1973	Miyagiken-Oki M6.1	Yuriage Br 2	N	7	1.0	10.5	17.8 2.8 17.9
218	1973	Miyagiken-Oki M6.1	Yuriage Br 3	N	12	2.0	6.0	10.2 2.1 12.3
219	1973	Miyagiken-Oki M6.1	Yuriage Br 5	N	17	3.0	22.7	26.1 8.6 30.0
220	1973	Miyagiken-Oki M6.1	Yuriagekami 1	N	60	5.0	1.8	3.1 1.2 8.6
221	1973	Miyagiken-Oki M6.1	Yuriagekami 2	N	0	0.0	7.7	13.1 5.2 13.1
222	1973	Miyagiken-Oki M6.1	Yuriagekami 3	N	0	0.0	22.4	26.7 2.5 26.7

Table C.3: CAV_5 parameters for CAV_5 logistic regression.

Case	Year	Earthquake	Site	Liq	R, km	V_{s0} , m/s	τ_c	\pm	Record	R, km	$CAV_{5,surf}$	\pm
1	1944	Tohnankai M8.0	Ienaga	Y	90.8	54	0.656	0.090	Attenuation		12.00	9.69
2	1944	Tohnankai M8.0	Komei	Y	91.6	36	0.653	0.083	Attenuation		11.90	9.60
3	1944	Tohnankai M8.0	Meiko	Y	91.2	46	0.831	0.061	Attenuation		11.95	9.64
4	1948	Fukui M7.3	Shonenji Temple	Y	28.0	39	0.674	0.082	Attenuation		9.81	7.92
5	1948	Fukui M7.3	Takaya 45	Y	31.4	82	0.592	0.106	Attenuation		8.87	7.16
6	1964	Niigata M7.5	Cc17-1	Y	10.8	86	0.600	0.106	Attenuation		39.50	31.88
7	1964	Niigata M7.5	Old Town 1	N	10.9	119	0.659	0.105	Attenuation		38.91	31.40
8	1964	Niigata M7.5	Old Town 2	N	10.9	119	0.585	0.109	Attenuation		38.91	31.40
9	1964	Niigata M7.5	Rail Road 1	Y	10.8	77	0.595	0.105	Attenuation		39.50	31.88
10	1964	Niigata M7.5	Rail Road 2	?	10.8	77	0.537	0.108	Attenuation		39.50	31.88
11	1964	Niigata M7.5	River Site	Y	14.6	38	0.567	0.106	Attenuation		30.93	24.96
12	1964	Niigata M7.5	Road Site	N	14.5	120	0.683	0.102	Attenuation		30.86	24.90
13	1964	Niigata M7.5	Showa Br 2	Y	12.0	37	0.636	0.086	Attenuation		36.38	29.36
14	1964	Niigata M7.5	Showa Br 4	Y	12.0	37	0.517	0.100	Attenuation		36.09	29.12
15	1968	Tokachioki M7.9	Hachinohe 2	N	92.4	132	0.721	0.098	Hachinoe Harbor		22.23	14.32
16	1968	Tokachioki M7.9	Hachinohe 4	N	92.4	89	0.842	0.069	Hachinoe Harbor		22.23	14.32
17	1968	Tokachioki M7.9	Hachinohe 6	Y	92.4	72	0.705	0.089	Hachinoe Harbor		22.23	14.32
18	1968	Tokachioki M7.9	Nanaehama 1, 2, 3	Y	202.6	86	0.797	0.077	Muroran Harbor		17.76	11.44
19	1971	San Fernando M _w 6.6	Juvenile Hall	Y	16.9	56	0.613	0.097	NGA-57, 68, 70, 88		19.33	12.45
20	1971	San Fernando M _w 6.6	Van Norman	Y	17.0	84	0.636	0.101	NGA-57, 68, 70, 88		18.41	11.86
21	1975	Haicheng M _s 7.3	Panjin Chemical Fertilizer Plant	Y	72.0	91	0.609	0.106	Attenuation		4.18	3.37
22	1975	Haicheng M _s 7.3	Shuang Tai Zi River	Y	67.0	70	0.544	0.106	Attenuation		4.57	3.69
23	1975	Haicheng M _s 7.3	Ying Kou Glass Fiber Plant	Y	48.0	109	0.657	0.104	Attenuation		6.07	4.90
24	1975	Haicheng M _s 7.3	Ying Kou Paper Plant	Y	48.0	87	0.613	0.105	Attenuation		6.07	4.90
25	1976	Guatemala M7.5	Amatitlan B1	Y	40.0	96	0.592	0.107	Attenuation		10.31	8.32
26	1976	Guatemala M7.5	Amatitlan B2	?	40.0	107	0.727	0.093	Attenuation		10.31	8.32
30	1976	Tangshan M _s 7.8	Coastal Region	Y	73.0	78	0.692	0.092	Attenuation		13.05	10.53
31	1976	Tangshan M _s 7.8	Le Ting L8-14	Y	68.0	63	0.653	0.094	Attenuation		13.60	10.97
32	1976	Tangshan M _s 7.8	Qing Jia Ying	Y	15.0	95	0.679	0.098	Attenuation		55.72	44.97
33	1976	Tangshan M _s 7.8	Tangshan City	N	21.0	156	0.776	0.092	Attenuation		40.19	32.43
34	1976	Tangshan M _s 7.8	Yao Yuan Village	Y	78.0	130	0.764	0.090	Attenuation		11.85	9.56
35	1977	Argentina M7.4	San Juan B1	Y	70.0	113	0.636	0.106	INPRES Building	45.0	9.26	5.96
36	1977	Argentina M7.4	San Juan B3	Y	70.0	102	0.556	0.109	INPRES Building	45.0	9.26	5.96
37	1977	Argentina M7.4	San Juan B4	N	70.0	100	0.852	0.069	INPRES Building	45.0	9.26	5.96
38	1977	Argentina M7.4	San Juan B5	N	70.0	99	0.816	0.076	INPRES Building	45.0	9.26	5.96
39	1977	Argentina M7.4	San Juan B6	Y	70.0	86	0.701	0.093	INPRES Building	45.0	9.26	5.96
54	1978	Miyagiken-Oki M7.4	Nakajima 18	Y	92.9	93	0.724	0.090	Shiogama	62.9	11.10	7.15
55	1978	Miyagiken-Oki M7.4	Arahama	Y	79.5	76	0.667	0.096	Shiogama	62.9	13.14	8.46
56	1978	Miyagiken-Oki M7.4	Hiyori 18	Y	53.7	111	0.803	0.081	Shiogama	62.9	19.21	12.37

Table C.3: CAV_5 parameters for CAV_5 logistic regression (cont.)

Case	Year	Earthquake	Site	Liq	R, km	V_{50} , m/s	τ_c	\pm	Record	R, km	CAV_{5surf}	\pm
58	1978	Miyagiken-Okii M7.4	Ishinomaki 2	Y	53.7	74	0.727	0.085	Shiogama	62.9	19.45	12.53
59	1978	Miyagiken-Okii M7.4	Ishinomaki 4	N	53.7	114	0.751	0.090	Shiogama	62.9	19.45	12.53
60	1978	Miyagiken-Okii M7.4	Kitawabuchi 2	Y	53.7	88	0.761	0.083	Shiogama	62.9	17.42	11.22
61	1978	Miyagiken-Okii M7.4	Kitawabuchi 3	Y	58.6	73	0.696	0.090	Shiogama	62.9	17.42	11.22
62	1978	Miyagiken-Okii M7.4	Nakajima 2	N	92.9	93	0.710	0.093	Shiogama	62.9	11.10	7.15
63	1978	Miyagiken-Okii M7.4	Nakamura 1	N	75.6	53	0.741	0.077	Shiogama	62.9	13.38	8.62
64	1978	Miyagiken-Okii M7.4	Nakamura 4	Y	75.6	64	0.784	0.088	Shiogama	62.9	13.38	8.62
65	1978	Miyagiken-Okii M7.4	Nakamura 5	Y	75.6	61	0.787	0.082	Shiogama	62.9	13.38	8.62
66	1978	Miyagiken-Okii M7.4	Oiiri 1	Y	57.6	94	0.663	0.100	Shiogama	62.9	17.91	11.54
68	1978	Miyagiken-Okii M7.4	Shiomi 6	Y	53.7	57	0.665	0.092	Shiogama	62.9	19.21	12.37
69	1978	Miyagiken-Okii M7.4	Yuriage Br 1	Y	75.2	109	0.814	0.083	Shiogama	62.9	13.72	8.84
70	1978	Miyagiken-Okii M7.4	Yuriage Br 2	Y	75.2	45	0.778	0.068	Shiogama	62.9	13.72	8.84
71	1978	Miyagiken-Okii M7.4	Yuriage Br 3	Y	75.2	58	0.752	0.077	Shiogama	62.9	13.72	8.84
72	1978	Miyagiken-Okii M7.4	Yuriage Br 5	Y	75.2	149	0.691	0.105	Shiogama	62.9	13.72	8.84
73	1978	Miyagiken-Okii M7.4	Yuriagekami 1	Y	75.6	56	0.699	0.085	Shiogama	62.9	13.65	8.79
74	1978	Miyagiken-Okii M7.4	Yuriagekami 2	Y	75.6	50	0.678	0.086	Shiogama	62.9	13.65	8.79
75	1978	Miyagiken-Okii M7.4	Yuriagekami 3	N	75.6	87	0.651	0.100	Shiogama	62.9	13.65	8.79
76	1979	Imperial Valley M _L 6.6	Radio Tower B2	N	12.5	134	0.872	0.070	Brawley Airport	11.7	4.58	2.41
77	1979	Imperial Valley M _L 6.6	Heber Road A1	N	4.3	132	0.843	0.082	Agrarias	3.6	7.45	3.47
78	1979	Imperial Valley M _L 6.6	Heber Road A2	Y	4.3	130	0.819	0.080	Agrarias	3.6	7.45	3.47
79	1979	Imperial Valley M _L 6.6	Heber Road A3	N	4.3	136	0.812	0.082	Agrarias	3.6	7.45	3.47
80	1979	Imperial Valley M _L 6.6	Kornbloom B	N	16.1	110	0.744	0.087	Calipatria Fire Stn	21.5	4.04	2.60
81	1979	Imperial Valley M _L 6.6	McKim Ranch A	Y	8.0	159	0.833	0.074	El Centro 4	9.5	8.46	5.45
82	1979	Imperial Valley M _L 6.6	Radio Tower B1	Y	12.5	121	0.745	0.090	Brawley Airport	11.7	4.54	2.39
83	1979	Imperial Valley M _L 6.6	River Park A	Y	7.3	130	0.969	0.038	Brawley Airport	11.7	6.83	4.40
84	1979	Imperial Valley M _L 6.6	Wildlife B	N	18.1	80	0.685	0.094	Calipatria Fire Stn	21.5	3.62	2.33
85	1980	Mid-Chiba M6.1	Owi 1	N	164.2	115	0.703	0.098	Attenuation		0.50	0.40
86	1980	Mid-Chiba M6.1	Owi 2	N	164.2	115	0.538	0.110	Attenuation		0.50	0.40
87	1981	WestMorland M _L 5.6	Kornbloom B	Y	3.6	110	0.744	0.087	Salton Sea, Westmorland		8.89	5.72
88	1981	Westmorland M _L 5.6	Radio Tower B1	Y	13.5	121	0.783	0.086	Brawley Airport	10.5	2.45	1.57
89	1981	Westmorland M _L 5.6	Radio Tower B2	N	13.5	134	0.872	0.070	Brawley Airport	10.5	2.46	1.58
90	1981	Westmorland M _L 5.6	River Park A	N	15.5	130	0.969	0.038	Brawley Airport	10.5	2.18	1.40
91	1981	WestMorland M _L 5.6	River Park C	N	15.5	130	0.745	0.091	Brawley Airport	10.5	2.18	1.40
92	1981	WestMorland M _L 5.6	Wildlife A	Y	5.4	80	0.685	0.094	Salton Sea Refuge	6.8	5.72	3.68
93	1981	Westmorland M _L 5.6	McKim Ranch A	N	15.5	159	0.833	0.074	Brawley Airport	10.5	1.24	0.80
94	1964	Niigata M7.5	Arayamotomachi	Y	117.5	62	0.738	0.081	Attenuation		4.26	3.44
96	1968	Tokachi-Okii M7.9	Aomori Station	Y	150.5	158	0.737	0.099	Aomori	75.8	36.88	19.36
97	1976	Tangshan M _s 7.8	Luan Nan L1	N	46.0	151	0.731	0.083	Attenuation		19.93	16.09
98	1976	Tangshan M _s 7.8	Luan Nan L2	Y	46.0	82	0.735	0.083	Attenuation		19.93	16.09

Table C.3: CAV_5 parameters for CAV_5 logistic regression (cont.)

Case	Year	Earthquake	Site	Liq	R, km	V_{50} , m/s	r_c	Record	R, km	CAV_{5surf}	\pm	
102	1983	Nihonkai-Chubu M_w 7.7	Aomori Station	Y	75.0	158	0.737	0.099	Aomori	75.8	13.73	7.21
103	1983	Nihonkai-Chubu M_w 7.7	Arayamotomachi	Y	71.8	62	0.675	0.090	Akita	15.7	14.25	9.17
104	1983	Nihonkai-Chubu M_w 7.7	Gaiko Wharf B2	Y	62.6	108	0.645	0.105	Akita	15.7	16.21	10.44
105	1983	Nihonkai-Chubu M_w 7.7	Noshiro Section N7	Y	37.4	92	0.766	0.083	Hachirogata	48.0	49.17	31.66
106	1983	Nihonkai-Chubu M_w 7.7	Takeda Elementary School	Y	47.1	101	0.724	0.092	Aomori	75.8	20.55	13.24
107	1987	Elmore Ranch M_w 6.2	Radio Tower B1	N	24.3	121	0.745	0.086	Wildlife Array	17.9	3.11	2.00
108	1987	Elmore Ranch M_w 6.2	Wildlife B	N	17.9	80	0.685	0.094	Wildlife Array	17.9	4.02	0.20
109	1987	Superstition Hills M_w 6.7	Radio Tower B1	N	18.9	121	0.745	0.086	Brawley Airport	18.3	3.60	1.47
110	1988	Superstition Hills M_w 6.7	Wildlife B	Y	25.3	80	0.685	0.094	Wildlife Array, 7.5 m	17.9	13.07	1.52
111	1987	Superstition Hills M_w 6.7	Heber Road A1	N	34.1	132	0.843	0.082	Brawley Airport	18.3	2.09	1.35
112	1987	Superstition Hills M_w 6.7	Heber Road A2	N	34.1	130	0.819	0.080	Brawley Airport	18.3	2.10	1.35
113	1987	Superstition Hills M_w 6.7	Heber Road A3	N	34.1	136	0.812	0.082	Brawley Airport	18.3	2.12	1.36
114	1987	Superstition Hills M_w 6.7	Kornbloom B	N	18.5	110	0.744	0.087	Kornbloom	18.5	4.38	0.22
115	1987	Superstition Hills M_w 6.7	McKim Ranch A	N	21.7	159	0.833	0.074	Brawley Airport	18.3	3.22	2.07
116	1987	Superstition Hills M_w 6.7	Radio Tower B2	N	18.9	134	0.872	0.070	Brawley Airport	18.3	3.62	1.47
117	1987	Superstition Hills M_w 6.7	River Park A	N	13.8	130	0.969	0.038	Brawley Airport	18.3	4.76	3.07
118	1987	Superstition Hills M_w 6.7	River Park C	N	13.8	130	0.745	0.091	Brawley Airport	18.3	4.76	3.07
119	1989	Loma Prieta M_w 7.0	Alameda BF Dike	N	64.6	186	0.741	0.102	Alameda NAS Hangar	70.9	8.17	5.26
120	1989	Loma Prieta M_w 7.0	Farris Farm	Y	8.6	127	0.702	0.100	Watsonville Telephone	9.2	9.10	3.69
121	1989	Loma Prieta M_w 7.0	Hall Avenue	N	86.0	46	0.616	0.093	Richmond City Hall	87.7	4.31	2.77
122	1989	Loma Prieta M_w 7.0	Marine Laboratory B1	Y	19.9	157	0.801	0.088	Watsonville Telephone	9.2	4.73	3.05
123	1989	Loma Prieta M_w 7.0	MBARI No 3 EBI	N	19.8	184	0.897	0.070	Watsonville Telephone	9.2	4.75	3.06
124	1989	Loma Prieta M_w 7.0	MBARI No 3 EB5	N	19.7	137	0.778	0.089	Watsonville Telephone	9.2	4.74	3.05
125	1989	Loma Prieta M_w 7.0	Sandholdt UC-B10	Y	19.9	127	0.804	0.074	Watsonville Telephone	9.2	4.71	3.03
126	1989	Loma Prieta M_w 7.0	Miller Farm	Y	8.9	138	0.713	0.100	Watsonville Telephone	9.2	8.81	2.01
127	1989	Loma Prieta M_w 7.0	Miller Farm CMF10	Y	8.9	134	0.672	0.105	Watsonville Telephone	9.2	8.83	2.01
128	1989	Loma Prieta M_w 7.0	Miller Farm CMF3	Y	8.9	123	0.683	0.103	Watsonville Telephone	9.2	8.76	2.00
129	1989	Loma Prieta M_w 7.0	Miller Farm CMF5	Y	8.9	136	0.688	0.104	Watsonville Telephone	9.2	8.83	2.01
130	1989	Loma Prieta M_w 7.0	Miller Farm CMF8	Y	8.9	104	0.663	0.102	Watsonville Telephone	9.2	8.76	2.00
131	1989	Loma Prieta M_w 7.0	State Beach UC-B1	Y	18.6	125	0.799	0.074	Watsonville Telephone	9.2	4.97	3.20
132	1989	Loma Prieta M_w 7.0	State Beach UC-B2	Y	18.7	157	0.775	0.094	Watsonville Telephone	9.2	5.01	3.23
133	1989	Loma Prieta M_w 7.0	POO7-2	Y	74.1	125	0.696	0.101	Oakland Outer Harbor	74.3	7.16	1.04
134	1989	Loma Prieta M_w 7.0	POO7-3	Y	74.1	156	0.717	0.102	Oakland Outer Harbor	74.3	7.16	1.04
136	1989	Loma Prieta M_w 7.0	POR-2, 3, 4	Y	85.6	58	0.588	0.095	Richmond City Hall	87.7	4.22	2.72
138	1989	Loma Prieta M_w 7.0	SFOBB-1, 2	Y	75.3	141	0.695	0.101	Oakland Outer Harbor	74.3	6.72	4.33
140	1989	Loma Prieta M_w 7.0	WoodMarine UC-B4	Y	19.4	119	0.919	0.056	Watsonville Telephone	9.2	4.83	3.11
141	1989	Loma Prieta M_w 7.0	Marine Laboratory B2	Y	19.9	127	0.801	0.083	Watsonville Telephone	9.2	4.71	3.03
142	1989	Loma Prieta M_w 7.0	Treasure Island	Y	77.4	147	0.779	0.097	Oakland Outer Harbor	74.3	6.86	4.42
143	1990	Luzon M_w 7.6	Cereenan St B12	N	65.0	119	0.726	0.095	Attenuation	7.18	7.18	5.80
144	1990	Luzon M_w 7.6	Perez B1v B11	Y	65.0	113	0.657	0.104	Attenuation	7.18	7.18	5.80

Table C.3: CAV_5 parameters for CAV_5 logistic regression (cont.)

Case	Year	Earthquake	Site	Liq	R, km	V_{50} , m/s	τ_c	\pm	Record	R, km	CAV_{5surf}	\pm
145	1993	Kushiro-Oki M_w 8.0	Kushiro Port Seismo Stn	Y	15.0	129	0.517	0.110	Attenuation		9.08	7.32
146	1993	Kushiro-Oki M_w 8.0	Kushiro Port Site A	Y	15.0	120	0.716	0.097	Attenuation		9.08	7.32
147	1993	Kushiro-Oki M_w 8.0	Kushiro Port Site D	N	15.0	175	0.663	0.109	Attenuation		9.08	7.32
150	1994	Northridge M_w 6.7	Potrero Canyon C1	Y	5.1	69	0.604	0.102	NGA1045		7.25	4.67
151	1994	Northridge M_w 6.7	Wynne Ave. Unit C1	Y	11.3	118	0.686	0.101	NGA1048		14.60	3.33
152	1995	Hyogoken-Nambu M_L 7.2	Ashiyama A (Marine Sand)	N	5.5	170	0.702	0.106	Kobe JMA		13.72	8.83
153	1995	Hyogoken-Nambu M_L 7.2	Ashiyama A (Mountain Sand 1)	N	5.5	170	0.762	0.097	Kobe JMA		13.72	8.83
154	1995	Hyogoken-Nambu M_L 7.2	Ashiyama C, D, E (Marine Sand)	Y	6.2	130	0.647	0.107	Kobe JMA		12.95	8.34
155	1995	Hyogoken-Nambu M_L 7.2	Ashiyama C, D, E (Mountain Sand 2)	Y	5.9	170	0.620	0.110	Kobe JMA		13.28	8.55
156	1995	Hyogoken-Nambu M_L 7.2	Port Island Borehole Array Station	Y	3.5	89	0.609	0.105	Kobe JMA		16.19	10.42
157	1995	Hyogoken-Nambu M_L 7.2	Port Island Improved Site (Ikegaya)	N	5.0	144	0.668	0.106	Kobe JMA		14.28	9.20
158	1995	Hyogoken-Nambu M_L 7.2	Port Island Improved Site (Tanahashi)	N	5.0	148	0.647	0.108	Kobe JMA		14.28	9.20
159	1995	Hyogoken-Nambu M_L 7.2	Port Island Improved Site (Watanabe)	N	5.0	177	0.683	0.108	Kobe JMA		14.28	9.20
160	1995	Hyogoken-Nambu M_L 7.2	Port Island Site 1	Y	3.2	139	0.636	0.108	Kobe JMA		16.52	10.64
161	1995	Hyogoken-Nambu M_L 7.2	Rokko Island Building D	Y	5.6	115	0.654	0.105	Kobe JMA		13.61	8.76
162	1995	Hyogoken-Nambu M_L 7.2	Rokko Island Site G	Y	4.8	117	0.582	0.109	Kobe JMA		14.67	9.45
163	1995	Hyogoken-Nambu M_L 7.2	Torishima Dike	Y	16.0	66	0.661	0.094	Fukushima		14.91	9.60
164	1995	Hyogoken-Nambu M_L 7.2	1	N	2.3	125 ¹	0.700	0.100	Kobe JMA		18.50	11.91
165	1995	Hyogoken-Nambu M_L 7.2	2	N	2.5	125 ¹	0.646	0.106	Kobe JMA		18.30	11.78
166	1995	Hyogoken-Nambu M_L 7.2	3	N	2.5	125 ¹	0.714	0.098	Kobe JMA		18.30	11.78
167	1995	Hyogoken-Nambu M_L 7.2	4	N	2.3	125 ¹	0.740	0.094	Kobe JMA		18.50	11.91
168	1995	Hyogoken-Nambu M_L 7.2	5	Y	2.8	125 ¹	0.642	0.107	Kobe JMA		18.14	11.68
169	1995	Hyogoken-Nambu M_L 7.2	6	Y	2.4	125 ¹	0.705	0.100	Kobe JMA		18.40	11.85
170	1995	Hyogoken-Nambu M_L 7.2	7	Y	2.2	125 ¹	0.693	0.101	Kobe JMA		18.60	11.98
171	1995	Hyogoken-Nambu M_L 7.2	8	Y	2.0	125 ¹	0.730	0.096	Kobe JMA		18.50	11.91
172	1995	Hyogoken-Nambu M_L 7.2	9	Y	1.9	125 ¹	0.758	0.091	Kobe JMA		18.58	11.97
173	1995	Hyogoken-Nambu M_L 7.2	10	N	1.5	125 ¹	0.666	0.105	Kobe JMA		18.66	11.03
174	1995	Hyogoken-Nambu M_L 7.2	11	Y	1.7	125 ¹	0.682	0.103	Kobe JMA		18.75	6.28
175	1995	Hyogoken-Nambu M_L 7.2	12	N	1.3	125 ¹	0.720	0.097	Kobe JMA		19.03	12.26
176	1995	Hyogoken-Nambu M_L 7.2	13	Y	1.5	125 ¹	0.688	0.102	Kobe JMA		18.90	2.95
177	1995	Hyogoken-Nambu M_L 7.2	14	N	1.1	125 ¹	0.737	0.094	Kobe JMA		19.15	12.33
178	1995	Hyogoken-Nambu M_L 7.2	15	Y	1.4	125 ¹	0.706	0.100	Kobe JMA		18.97	12.22
179	1995	Hyogoken-Nambu M_L 7.2	16	?	1.4	125 ¹	0.749	0.092	Kobe JMA		18.73	12.06
180	1995	Hyogoken-Nambu M_L 7.2	17	Y	2.0	125 ¹	0.749	0.092	Kobe JMA		18.50	11.91
181	1995	Hyogoken-Nambu M_L 7.2	18	N	1.4	125 ¹	0.610	0.108	Kobe JMA		18.53	11.94
182	1995	Hyogoken-Nambu M_L 7.2	19	N	1.4	125 ¹	0.666	0.105	Kobe JMA		18.73	12.06
183	1995	Hyogoken-Nambu M_L 7.2	20	N	1.7	125 ¹	0.700	0.100	Kobe JMA		18.63	12.00
184	1995	Hyogoken-Nambu M_L 7.2	21	N	2.0	125 ¹	0.800	0.083	Kobe JMA		18.27	11.76
185	1995	Hyogoken-Nambu M_L 7.2	22	N	2.0	125 ¹	0.700	0.100	Kobe JMA		18.27	11.76

¹ Insufficient data to determine V_{50} . The average of the dataset, 125 m/s assumed.

Table C.3: CAV_5 parameters for CAV_5 logistic regression (cont.)

Case	Year	Earthquake	Site	Liq	R, km	V_{s0} , m/s	τ_c	\pm	Record	R, km	CAV_{surf}	\pm
186	1995	Hyogoken-Nambu $M_L7.2$	23	N	2.2	125^1	0.730	0.096	Kobe JMA	1.1	18.08	11.65
187	1995	Hyogoken-Nambu $M_L7.2$	24	Y	2.6	125^1	0.800	0.083	Kobe JMA	1.1	17.91	11.54
188	1995	Hyogoken-Nambu $M_L7.2$	25	N	2.2	125^1	0.800	0.083	Kobe JMA	1.1	17.89	11.52
189	1995	Hyogoken-Nambu $M_L7.2$	26	N	2.4	125^1	0.800	0.083	Kobe JMA	1.1	17.89	11.52
190	1995	Hyogoken-Nambu $M_L7.2$	27	N	2.2	125^1	0.866	0.070	Kobe JMA	1.1	18.08	11.65
191	1995	Hyogoken-Nambu $M_L7.2$	28	Y	4.2	125^1	0.749	0.092	Kobe JMA	1.1	16.30	10.49
192	1995	Hyogoken-Nambu $M_L7.2$	29	Y	4.4	125^1	0.785	0.086	Kobe JMA	1.1	16.05	10.33
193	1995	Hyogoken-Nambu $M_L7.2$	30	N	3.7	125^1	0.646	0.106	Kobe JMA	1.1	16.45	10.59
194	1995	Hyogoken-Nambu $M_L7.2$	31	N	2.8	125^1	0.772	0.088	Kobe JMA	1.1	17.48	11.25
195	1995	Hyogoken-Nambu $M_L7.2$	32	N	2.9	125^1	0.799	0.083	Kobe JMA	1.1	17.59	11.33
196	1995	Hyogoken-Nambu $M_L7.2$	33	N	4.1	125^1	0.656	0.106	Kobe JMA	1.1	16.17	10.41
197	1995	Hyogoken-Nambu $M_L7.2$	34	Y	4.7	125^1	0.677	0.104	Kobe JMA	1.1	15.67	10.09
198	1995	Hyogoken-Nambu $M_L7.2$	35	Y	4.8	125^1	0.749	0.092	Kobe JMA	1.1	15.31	9.86
199	1995	Hyogoken-Nambu $M_L7.2$	36	N	4.4	125^1	0.800	0.083	Kobe JMA	1.1	15.60	10.05
200	1995	Hyogoken-Nambu $M_L7.2$	37	Y	5.3	125^1	0.772	0.088	Kobe JMA	1.1	15.08	9.71
201	1995	Hyogoken-Nambu $M_L7.2$	38	Y	4.9	125^1	0.656	0.106	Kobe JMA	1.1	15.19	9.78
202	1995	Hyogoken-Nambu $M_L7.2$	39	N	4.5	125^1	0.749	0.092	Kobe JMA	1.1	15.48	9.97
203	1995	Hyogoken-Nambu $M_L7.2$	40	N	4.8	125^1	0.800	0.083	Kobe JMA	1.1	15.12	9.74
204	1995	Hyogoken-Nambu $M_L7.2$	41	Y	5.6	125^1	0.766	0.090	Kobe JMA	1.1	14.58	9.39
205	1995	Hyogoken-Nambu $M_L7.2$	42	Y	5.6	125^1	0.730	0.096	Kobe JMA	1.1	14.58	9.39
206	1995	Hyogoken-Nambu $M_L7.2$	43	Y	6.0	125^1	0.743	0.093	Kobe JMA	1.1	14.24	9.17
207	1995	Hyogoken-Nambu $M_L7.2$	44	Y	6.5	125^1	0.772	0.088	Kobe JMA	1.1	13.54	8.72
208	1999	Chi Chi M_w 7.6	Chiaya CHY104	Y	20.7	239	0.605	0.107	CHY102	25.0	19.44	12.52
209	1999	Chi Chi M_w 7.6	Yuanlin TCU110 upper	Y	12.6	98	0.631	0.105	TCU123	14.9	19.51	12.56
213	1973	Miyagiken-Oki $M6.1$	Arahama	N	124.5	76	0.667	0.096	Shiogama	103.9	1.62	1.04
214	1973	Miyagiken-Oki $M6.1$	Nakamura 4	N	117.6	64	0.784	0.088	Shiogama	103.9	1.71	1.10
215	1973	Miyagiken-Oki $M6.1$	Nakamura 5	N	117.6	61	0.787	0.082	Shiogama	103.9	1.71	1.10
216	1973	Miyagiken-Oki $M6.1$	Yuriage Br 1	N	117.5	109	0.814	0.083	Shiogama	103.9	1.71	1.10
217	1973	Miyagiken-Oki $M6.1$	Yuriage Br 2	N	117.5	45	0.778	0.068	Shiogama	103.9	1.71	1.10
218	1973	Miyagiken-Oki $M6.1$	Yuriage Br 3	N	117.5	58	0.752	0.077	Shiogama	103.9	1.71	1.10
219	1973	Miyagiken-Oki $M6.1$	Yuriage Br 5	N	117.5	149	0.691	0.105	Shiogama	103.9	1.71	1.10
220	1973	Miyagiken-Oki $M6.1$	Yuriagekami 1	N	117.6	56	0.699	0.082	Shiogama	103.9	1.71	1.10
221	1973	Miyagiken-Oki $M6.1$	Yuriagekami 2	N	117.6	50	0.678	0.086	Shiogama	103.9	1.71	1.10
222	1973	Miyagiken-Oki $M6.1$	Yuriagekami 3	N	117.6	87	0.651	0.100	Shiogama	103.9	1.71	1.10

¹ Insufficient data to determine V_{s0} . The average of the dataset, 125 m/s assumed.

Appendix D

 CAV_5 AT THE START OF LIQUEFACTION

This appendix presents the acceleration, zero crossing, and CAV_5 time histories for the two horizontal components of the following case histories:

- Case 110, 1987 Superstition Hills earthquake, Wildlife Refuge;
- Case 142, 1989 Loma Prieta earthquake, Treasure Island;
- Cases 145 and 146, 1993 Kushiro-oki earthquake, Kushiro Port;
- Case 156, 1995 Hyogoken-Nambu earthquake, Port Island;
- Case 208, 1999 Chi-chi earthquake, Chiaya CHY104; and
- Case 209, 1999 Chi-chi earthquake, Yuan-lin TCU110.

The dashed vertical lines in the time histories indicate the estimated time at which there is a change in the nature of the ground motion that suggests the start of softening and the time when the nature of the ground motion suggests fully softened behavior.

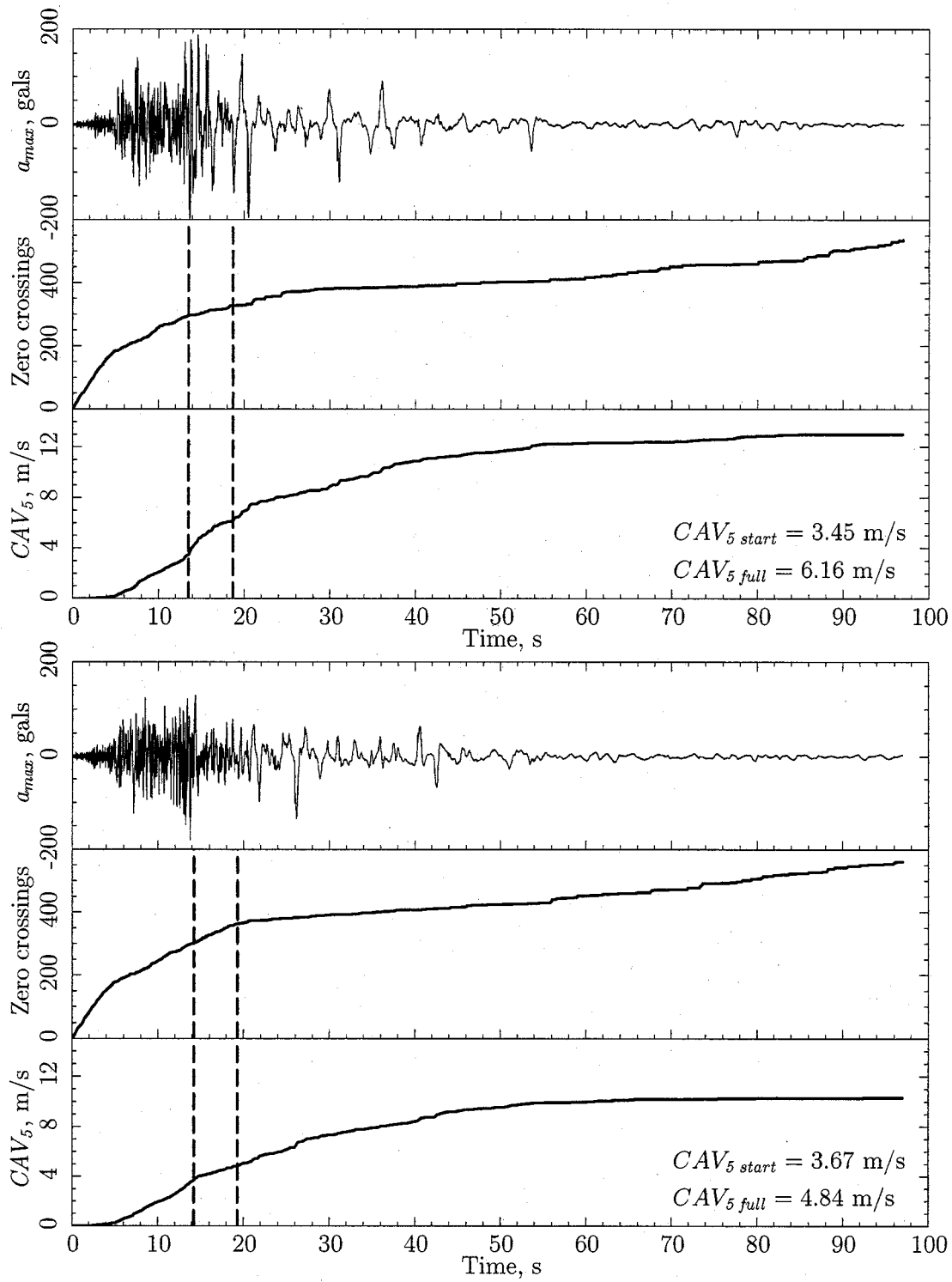


Figure D.1: Case 110, 1987 Superstition Hills earthquake, Wildlife Refuge: (top) NS component, (bottom) EW component.

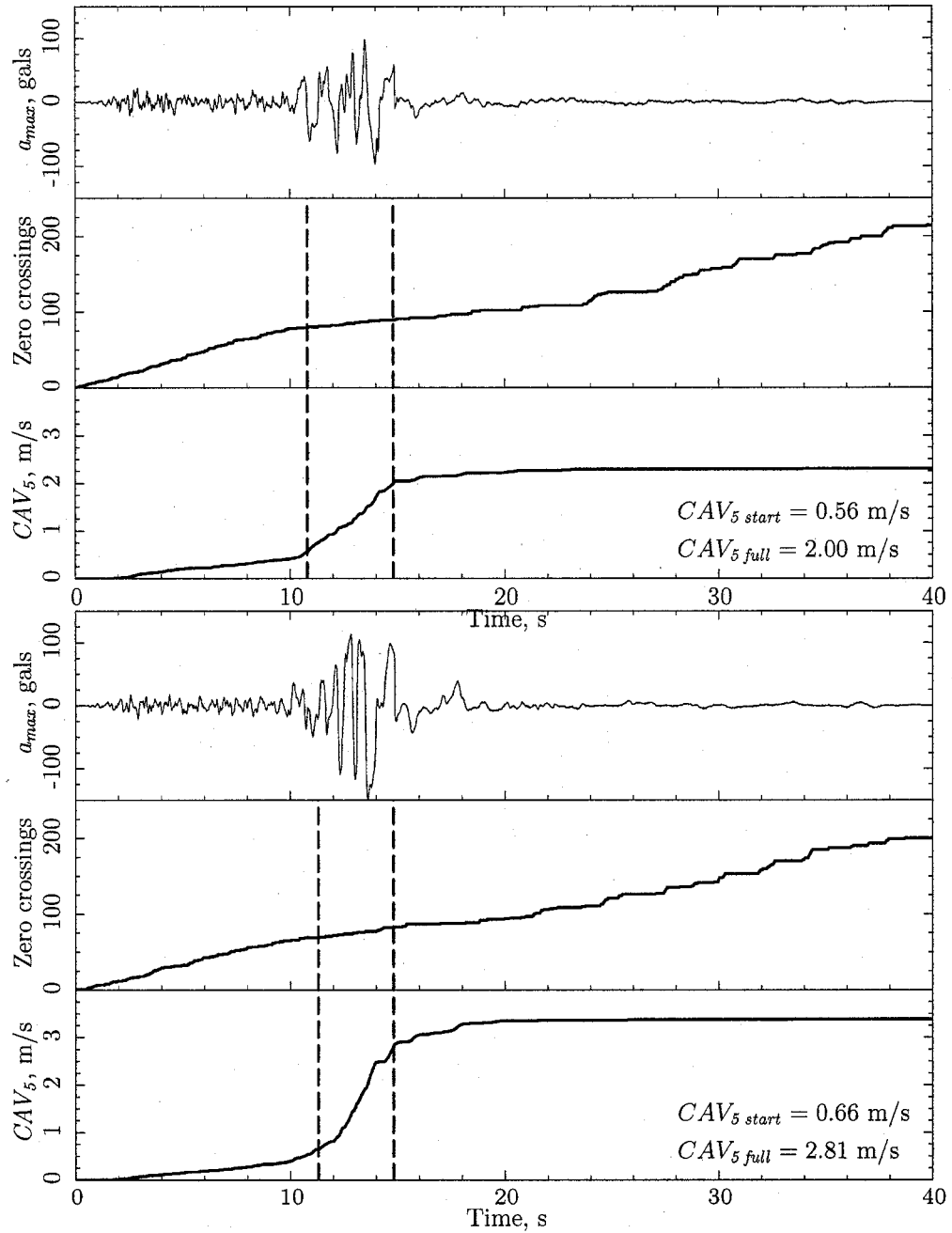


Figure D.2: Case 142, 1989 Loma Prieta earthquake, Treasure Island: (top) NS component, (bottom) EW component.

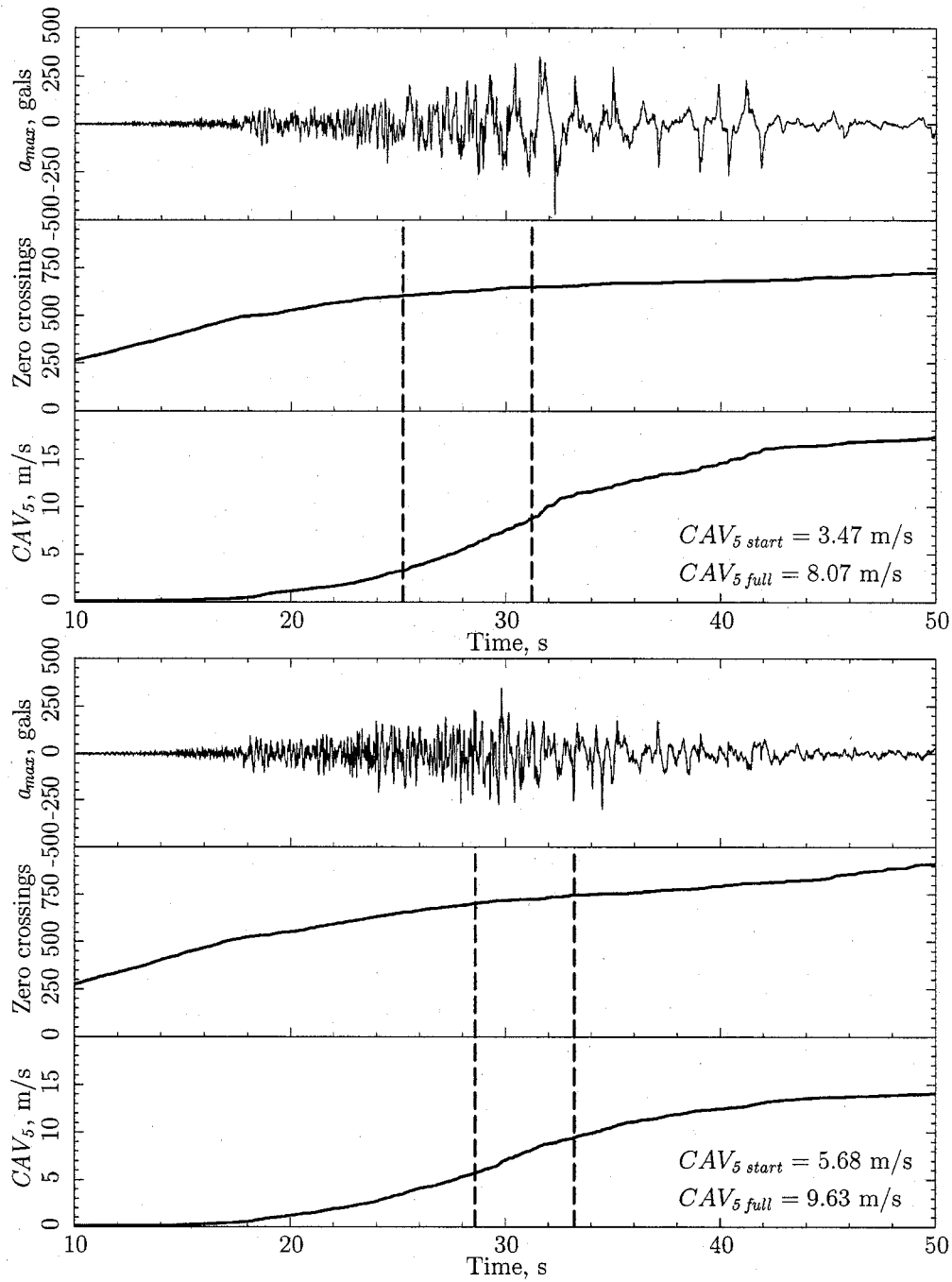


Figure D.3: Cases 145 and 146, 1993 Kushiro-oki earthquake, Kushiro Port: (top) NS component, (bottom) EW component.

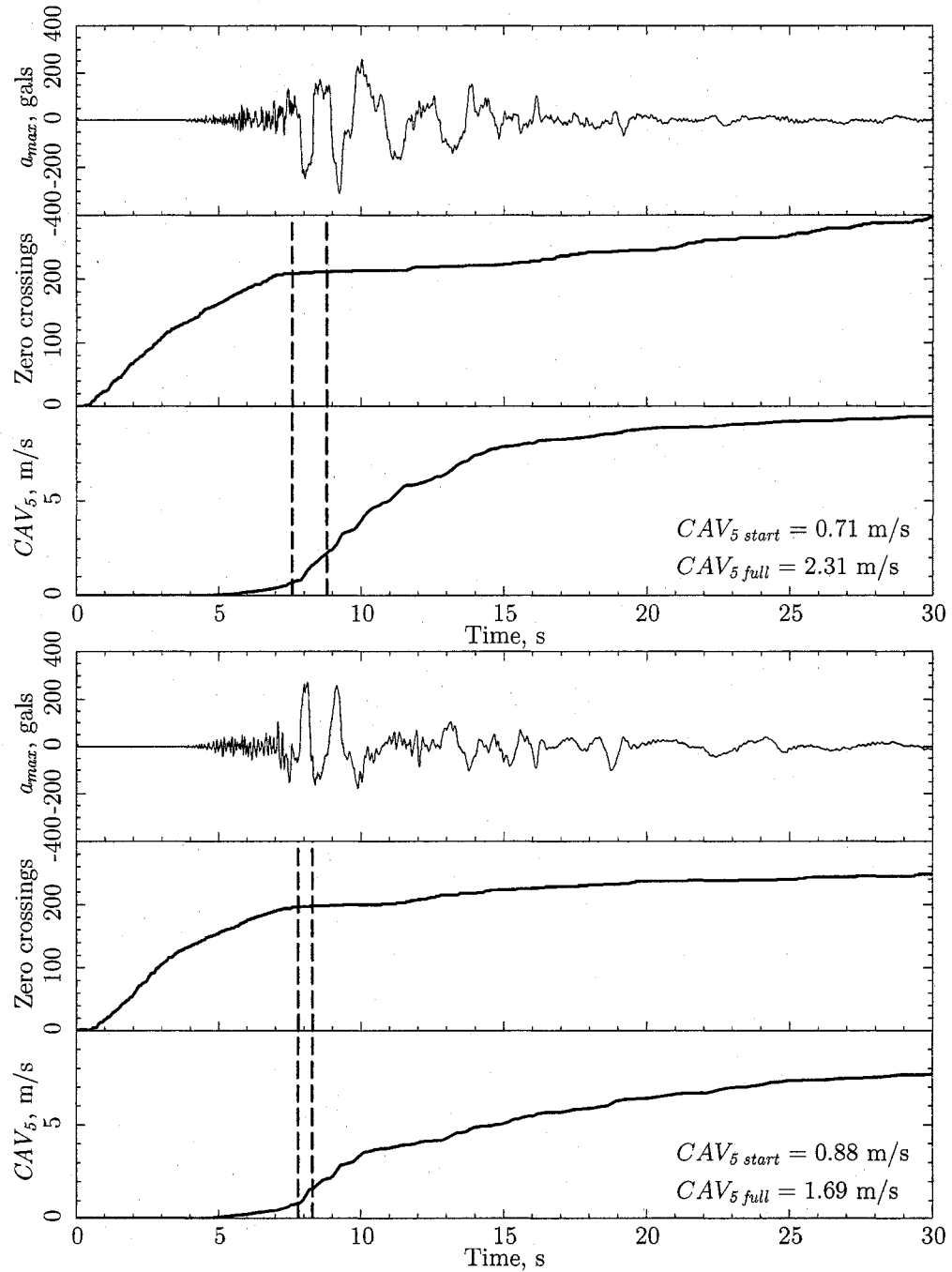


Figure D.4: Case 156, 1995 Hyogoken-Nambu earthquake, Port Island: (top) NS component, (bottom) EW component.

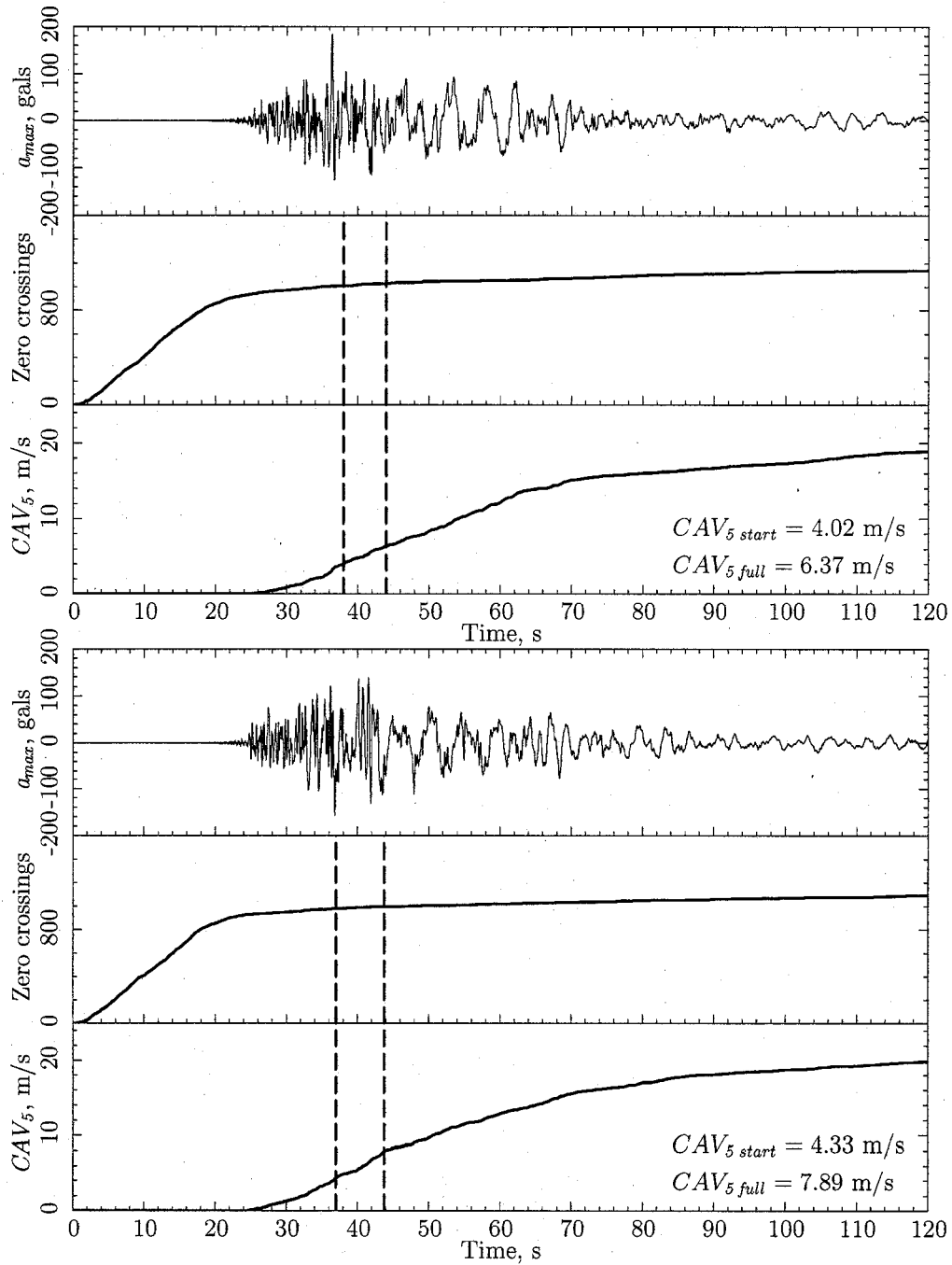


Figure D.5: Case 208, 1999 Chi-chi earthquake, Chiaya CHY104: (top) NS component, (bottom) EW component.

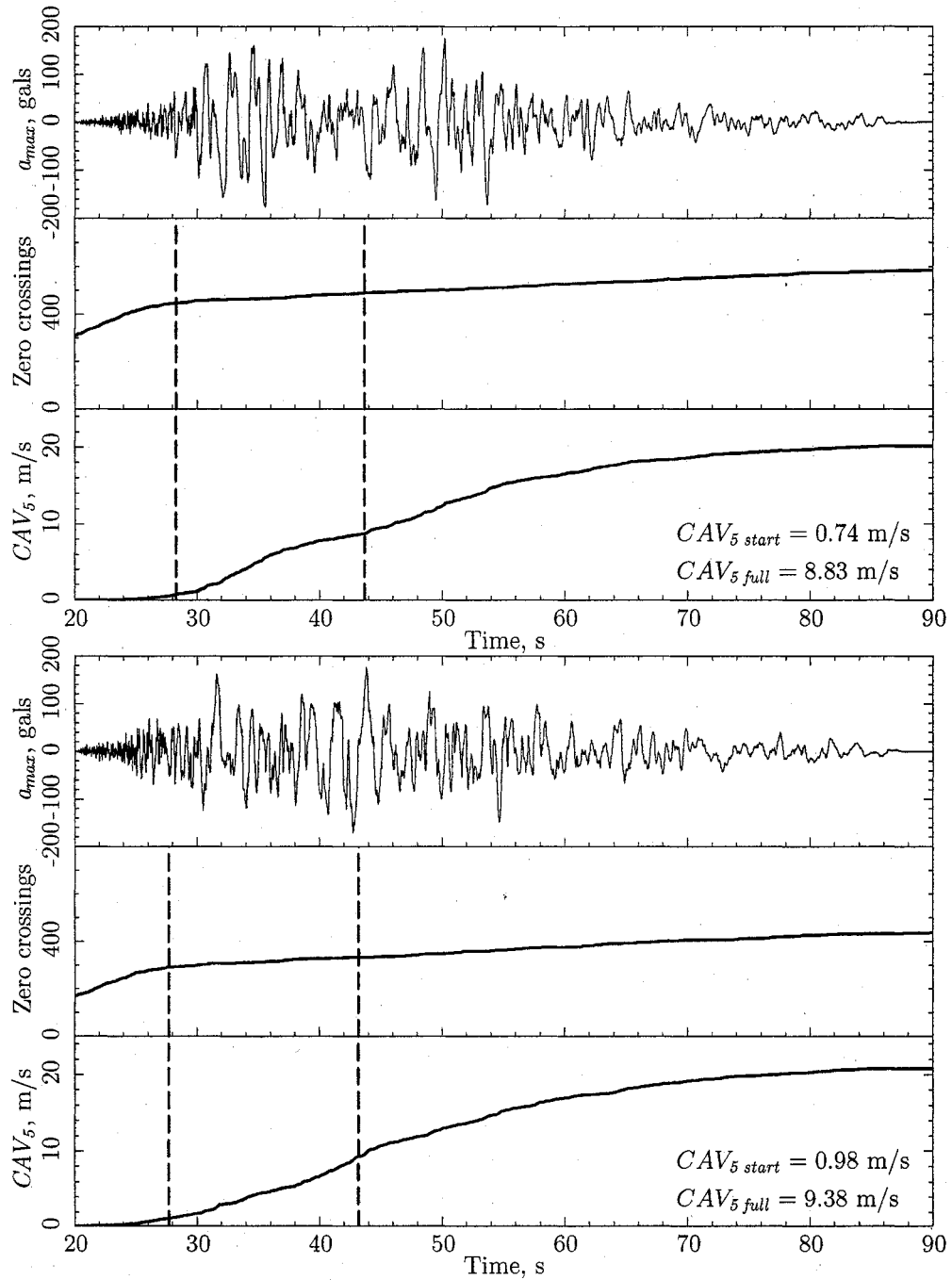


Figure D.6: Case 209, 1999 Chi-chi earthquake, Yuan-lin TCU110: (top) NS component, (bottom) EW component.

VITA

Roy Mayfield was born and raised in Williams Lake, British Columbia, Canada. After receiving his Bachelor's degree in Applied Science (Civil Engineering) from the University of British Columbia in 1980, he worked as a geotechnical consultant in Canada and the United States. In 2001, he was admitted to the University of Washington to study for a Master's degree in Science (Civil Engineering) under Professor Steven Kramer, and he completed his research on *Measuring post-liquefaction soil behavior in a cyclic triaxial system* in 2004. He continued working with Professor Kramer until he earned his Doctor of Philosophy in 2007.